

REMOVAL OF ASPHALTENE AND PARAFFIN DEPOSITS  
USING MICELLAR SOLUTIONS AND FUSED REACTIONS

Final Report  
1995-1997

By  
Dr. Chia-Lu Chang  
Vaibhav Nalwaya  
Probjot Singh  
Dr. H. Scott Fogler

RECEIVED

JUL 2 / 1998

OSTI

May 1998

Performed Under Contract No. DE-AC22-94PC91008  
Subcontract G4S40807

The University of Michigan  
Ann Arbor, Michigan

FOR  
S  
H  
H  
E  
Z  
E  
R  
O  
M



National Petroleum Technology Office  
U. S. DEPARTMENT OF ENERGY  
Tulsa, Oklahoma

DISTRIBUTION OF THIS DOCUMENT IS UNLIMITED *pc* MASTER

#### DISCLAIMER

This report was prepared as an account of work sponsored by an agency of the United States Government. Neither the United States Government nor any agency thereof, nor any of their employees, makes any warranty, expressed or implied, or assumes any legal liability or responsibility for the accuracy, completeness, or usefulness of any information, apparatus, product, or process disclosed, or represents that its use would not infringe privately owned rights. Reference herein to any specific commercial product, process, or service by trade name, trademark, manufacturer, or otherwise does not necessarily constitute or imply its endorsement, recommendation, or favoring by the United States Government or any agency thereof. The views and opinions of authors expressed herein do not necessarily state or reflect those of the United States Government.

This report has been reproduced directly from the best available copy.

Available to DOE and DOE contractors from the Office of Scientific and Technical Information, P.O. Box 62, Oak Ridge, TN 37831; prices available from (615) 576-8401.

Available to the public from the National Technical Information Service, U.S. Department of Commerce, 5285 Port Royal Rd., Springfield VA 22161

## **DISCLAIMER**

**Portions of this document may be illegible in electronic image products. Images are produced from the best available original document.**

DOE/PC/91008-6  
Distribution Category UC-122

Removal Of Asphaltene And Paraffin Deposits Using Micellar Solutions And Fused  
Reactions

By  
Dr. Chia-Lu Chang  
Vaibhav Nalwaya  
Probjot Singh  
Dr. H. Scott Fogler

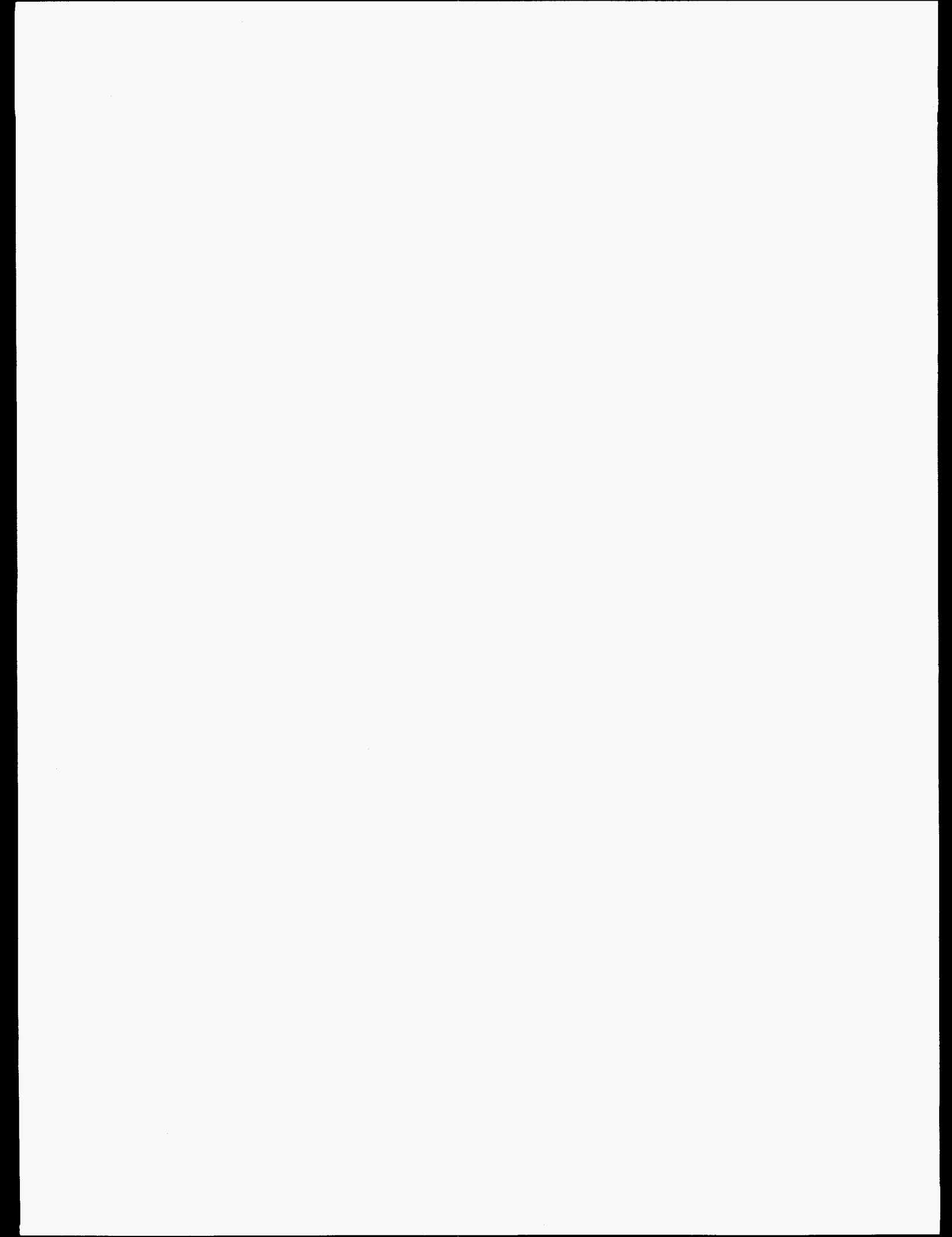
May 1998

Work Performed Under Contract No. DE-AC22-94PC91008  
Subcontract G4S40807

Prepared for  
U.S. Department of Energy  
Assistant Secretary for Fossil Energy

Jerry Casteel, Project Manager  
National Petroleum Technology Office  
P.O. Box 3628  
Tulsa, OK 74101

Prepared by:  
Department of Chemical Engineering  
The University of Michigan  
3168 H. H. Dow Building  
2300 Hayward Street  
Ann Arbor, MI 48109-2136



## Table of Contents

Table of contents	iii
List of Tables	vi
List of Figures	vii
Abstract	xiv
Executive Summary	xvii
I : Asphaltenes	xviii
II: Paraffins	xxiii
Technology Transfer	xxvii
Acknowledgments	xxviii
<b>1. Objective</b>	<b>1</b>
<b>2. Research on Asphaltenes</b>	<b>2</b>
2.1 Project Description	2
2.2 Preparation of Asphaltene Materials	2
2.3 Characterization of Asphaltenes	3
2.3.1 <i>Molecular Weight of Asphaltenes</i>	3
2.3.2 <i>Functional Group of Asphaltenes</i>	3
2.3.3 <i>Acid/Base Properties of Asphaltenes</i>	4
2.3.4 <i>Morphology of the Precipitates of Asphaltenes</i>	4
2.3.5 <i>Morphology of Asphaltene Deposits in Porous Media</i>	5
2.4 Stabilization of Asphaltenes Using Amphiphile/Alkane Solutions	5
2.4.1 <i>Effect of amphiphiles' head group on amphiphile adsorption</i>	6
2.4.2 <i>Effect of tail group of amphiphiles on asphaltene stabilization</i>	7
2.4.3 <i>Effect of alkane solvent on asphaltene stabilization</i>	8
2.5 Stability of Different Asphaltenes in Amphiphile/Alkane Solutions	8
2.6 Kinetics of Dissolution of Asphaltene Deposits by Amphiphile/Alkane	9
	Solutions
2.6.1 <i>Effect of amphiphile concentration</i>	11
2.6.2 <i>Effect of the type of amphiphiles</i>	13
2.6.3 <i>Effect of alkane solvent</i>	13
2.6.4 <i>Effect of flow rate of micellar fluid</i>	14
2.6.5 <i>Effect of temperature</i>	14
2.7 Discussion of First-Order Model for Asphaltene Dissolution	16
2.8 Visualization of Asphaltene Dissolution in Micromodel	18

2.8.1 <i>Results</i>	18
2.9 Dissolution of Asphaltenes in Model Porous Media	20
2.9.1 <i>Results</i>	21
2.10 Fractionation of Asphaltenes	22
2.10.1 <i>Fractionation procedure</i>	23
2.10.2 <i>Characterization of fractions</i>	23
2.10.3 <i>Dissolution studies</i>	24
2.10.4 <i>Discussion of results</i>	25
2.11 Sludge Precipitation Using Acid System	25
2.11.1 <i>Experimental</i>	26
2.11.2 <i>Results</i>	26
2.11.3 <i>Discussion</i>	28
<b>3. Paraffin Research</b>	29
3.1 Project Description	29
3.2 Preparation of Paraffin Wax	30
3.3 Characterization of Wax Material	30
3.3.1 <i>Molecular weight of wax</i>	30
3.3.2 <i>Melting point temperature of wax</i>	30
3.3.3 <i>Functional groups of wax</i>	31
3.3.4 <i>Acid/base titration of wax</i>	31
3.3.5 <i>Morphology of wax</i>	31
3.3.6 <i>Crystal structure of wax</i>	31
3.4 Inhibition of Paraffin Precipitation Using Chemicals	32
3.5 Dissolution of Paraffins Using Exothermically Reacting Fluids	34
3.6 Kinetics of the Exothermic Reaction Between $\text{NH}_4\text{Cl}$ and $\text{NaNO}_2$	35
3.6.1 <i>Effect of the concentration of acid catalyst</i>	35
3.6.2 <i>Effect of the concentration of <math>\text{NH}_4\text{Cl}</math> reactant</i>	36
3.6.3 <i>Effect of the concentration of <math>\text{NaNO}_2</math> reactant</i>	36
3.6.4 <i>Application of kinetic study to the <math>\text{NH}_4\text{NO}_3</math>-<math>\text{NaNO}_2</math> reaction</i>	37
3.7 Other Factors: Surfactant and Oil	38
3.7.1 <i>Effect of type of surfactant</i>	38
3.7.2 <i>Effect of water-to-oil volume ratio</i>	38
3.7.3 <i>Effect of surfactant concentration</i>	39
3.7.4 <i>Effect of type of oil</i>	39
3.7.5 <i>Effect of acetic acid concentration</i>	39
3.8 Experimental Investigation of Paraffin Dissolution in Pipelines	39

3.8.1 <i>Evaluation of effect of evolved nitrogen on deposit removal</i>	40
3.9 Simulation of Exothermic Reactive Fluid Flow Inside Pipelines	41
3.9.1 <i>Model Description</i>	41
3.9.2 <i>Simulation Results</i>	43
3.10 Simulation of Exothermic Reactive Fluid Flow in a Pipeline	45
3.10.1 <i>Governing differential equations</i>	46
3.10.2 <i>System of single set of pulses</i>	47
3.10.3 <i>System of multiple set of pulses</i>	48
3.10.4 <i>Results and Discussion</i>	49
3.11 Simulation of $\text{NaNO}_2\text{-NH}_4\text{Cl}$ Reaction (in W/O emulsion) in Pipeline	51
3.11.1 <i>Determination of Kinetics</i>	51
3.11.2 <i>Simulation of alternate pulse flow of the emulsions in a pipeline</i>	52
3.11.3 <i>Simulation results</i>	53
3.12 Encapsulation of the Catalyst	54
3.13 Nomenclature for Sections 3.1 thru 3.9	55
3.14 Nomenclature for Sections 3.10 thru 3.12	56
<b>4. References</b>	58
<b>5. Tables and Figures</b>	60



## List of Tables

1. Asphaltenes used in this study	60
2. Alkylbenzene-derived amphiphiles used in this study	60
3. List of the amphiphiles' functional groups used for quantifying amphiphile concentrations by FTIR spectroscopy	61
4. List of the experimental conditions conducted in this study	61
5. List of $K_s$ and $k_{\infty}$ values	62
6. Amount of asphaltene dissolved using different "good" solvents and flow rates	62
7. Elemental analysis of asphaltenes precipitated in the presence and absence of ferric ions	62
8. BET surface areas and specific reaction rate constants for dissolution of fractions from Mobil #0 crude oil precipitate	63
9. Heteroatom analysis for fractions from sludge and directly from crude oil	63
10. List of the measured cloud point temperatures of Jolliet wax and hexatriacontane in solutions containing inhibitor candidates	64

## List of Figures

1.	Molecular weight distribution of Mobil asphaltenes	65
2.	FTIR spectrum of Mobil asphaltenes	65
3.	Potentiometric titration of the acid quantity of Mobil asphaltenes	66
4.	Light microscopic graph of Mobil asphaltene precipitates	66
5.	Scanning electron micrograph of Mobil asphaltene precipitates	67
6.	Asphaltenes stabilized in heptane solutions containing amphiphiles with different head groups	68
7.	Asphaltenes stabilized in heptane solutions containing alkylphenol amphiphiles with different tail lengths	68
8.	Kuparuk asphaltenes stabilized in heptane solutions containing alkylpyridine amphiphiles	69
9.	Minimum weight percentage of nonylphenol and dodecylbenzene sulfonic acid for completely dissolving 1 wt% asphaltene in different alkanes	69
10.	Amphiphiles with different head groups remaining in supernatant	70
11.	FTIR spectra of alkylphenol amphiphiles with different tail lengths in the supernatant	71
12.	Asphaltenes stabilized in the binary heptane-toluene solution	71
13.	Asphaltenes stabilized in heptane solution with nonylphenol	72
14.	Asphaltenes stabilized in heptane solution with dodecylbenzene sulfonic acid	72
15.	Schematic illustration of the experimental setup used for kinetic study of asphaltene dissolution	73
16.	Detailed schematic drawing the differential reactor used in this study	73
17.	Asphaltene dissolution by heptane-based fluids containing different concentrations of NP	74
18.	Asphaltene dissolution by dodecane-based fluids containing different concentrations of NP	74
19.	Asphaltene dissolution by heptane-based fluids containing different concentrations of DBSA	75
20.	Asphaltene dissolution by dodecane-based fluids containing different concentrations of DBSA	75
21.	Asphaltene dissolution in 5% DBSA solutions containing different types of alkane solvents	76

22.	Kinetic analysis of asphaltene dissolution in 5% DBSA solutions containing different types of alkane solvents	76
23.	Asphaltene dissolution at different temperatures by dodecane-based fluids containing 20% NP	77
24.	Asphaltene dissolution at different temperatures by dodecane-based fluids containing 5% DBSA	77
25.	Asphaltene dissolution by heptane-based fluids containing 20% NP at different flow rates	78
26.	Kinetic analysis of asphaltene dissolution by dodecane-based fluids containing different concentrations of NP	79
27.	Kinetic analysis of asphaltene dissolution by dodecane-based fluids containing different concentrations of DBSA	79
28.	Kinetic analysis of asphaltene dissolution by dodecane-based fluids containing 5% DBSA at different temperatures	80
29.	Specific dissolution rate constant, $k$ , as a function of NP concentration in heptane and dodecane-based fluids	80
30.	Specific dissolution rate constant, $k$ , as a function of DBSA concentration in heptane and dodecane-based fluids	81
31.	Specific dissolution rate constant, $k$ , as a function of solution temperature	81
32.	Specific dissolution rate constant, $k$ , as a function of viscosity of alkane solvents	82
33	(a) Schematic of dissolution of asphaltene deposits by amphiphile/alkane fluids	82
33.	(b) Schematic of mass transfer process in asphaltene dissolution	82
34.	Schematic of glass micromodel apparatus	83
35.	Experimental setup for asphaltene precipitation and plugging in the micromodel	83
36.	Microscopic images showing asphaltene deposition and plugging in the micromodel	84
37.	Experimental setup for dissolution of asphaltene in the micromodel	86
38.	Concentration of asphaltenes in the effluent as a function of elution time	86
39.	Microscopic images showing asphaltene dissolution in the micromodel by 10wt% NP/heptane solution	87
40.	Schematic of packed-bed experimental setup	89

41.	Differential pressure profile and concentration profile for asphaltene dissolution in packed bed (5% NP/heptane, 1ml/min, 25°C)	90
42.	Differential pressure profile and concentration profile for asphaltene dissolution in packed bed (7% NP/heptane, 1 ml/min, 25°C)	90
43.	Differential pressure profile and concentration profile for asphaltene dissolution in packed bed (7% NP/heptane, 5ml/min, 25°C)	91
44.	Differential pressure profile and concentration profile for asphaltene dissolution in packed bed (13% NP/heptane, 1 ml/min, 25°C)	91
45.	Differential pressure profile and concentration profile for asphaltene dissolution in packed bed (5% DBSA/heptane, 1ml/min, 25°C)	92
46.	Differential pressure profile and concentration profile for asphaltene dissolution in packed bed (5% DBSA/heptane, 5ml/min, 25°C)	92
47.	Differential pressure profile and concentration profile for asphaltene dissolution in packed bed (10% DBSA/heptane, 1ml/min, 25°C)	93
48.	Differential pressure profile for silica gel in packed bed	93
49.	Yield of asphaltene fractions as wt% of asphaltenes originally dissolved in CH <sub>2</sub> Cl <sub>2</sub>	94
50.	Light microscope pictures of unfractionated asphaltenes and fractions	95
51.	SEM of unfractionated asphaltenes and fractions F1 and F4	96
52.	SEM of unfractionated asphaltenes and fractions F1 and F4 (higher magnification)	97
53.	Dissolution curves for asphaltene fractions and unfractionated asphaltene	98
54.	Kinetic analysis of dissolution rates of unfractionated asphaltene and fractions F1 and F4	98
55.	Dissolution curves for fraction F1 using 10wt% DBSA in heptane at different temperatures	99
56.	Asphaltene yield in the presence and absence of ferric iron	99
57.	Distribution of fractions precipitated from crude oil and from sludge	100
58.	Effect of aerobic aging on the distribution of fractions from sludge	100
59.	Effect of ferric ion concentration on fraction yield from sludge	101
60.	Effect of acid concentration on fraction yield in the absence of ferric ions	101
61.	Effect of acid concentration on fraction yield in the presence of ferric ions	102
62.	Molecular weight distribution of Joliet wax	102

63.	FTIR spectrum of Jolliet wax	103
64.	Light microscope graph of Jolliet wax precipitates	103
65.	Scanning electron microscope graph of Jolliet wax precipitates	104
66.	X-ray diffraction profiles of Jolliet wax precipitates	105
67.	Cooling temperature profile of heptane solution containing 1% Jolliet wax	105
68.	Schematic comparison of the temperature profile of hot-oiling fluids with that of exothermically reacting fluids	106
69.	Schematic of the criteria for effective dissolution of paraffin deposits using in-situ exothermic reactions conducted in the cleaning fluids	106
70.	Schematic of the process of the exothermic reaction between $\text{NH}_4\text{Cl}$ and $\text{NaNO}_2$	107
71.	Schematic of the adiabatic batch reactor for studying exothermic reaction kinetics	107
72.	Effect of acetic acid concentration on temperature rise in the adiabatic batch reactor	108
73.	Rate of exothermic reaction as a function of proton concentration	108
74.	$\text{NH}_4\text{Cl}$ concentration and reaction rate deduced from data in Fig. 73	109
75.	Temperature profile of aqueous solutions conducting the exothermic reaction under adiabatic conditions (varying $\text{NH}_4\text{Cl}$ concentration)	109
76.	Rate of exothermic reaction as a function of $\text{NH}_4\text{Cl}$ concentration	110
77.	Temperature profile of aqueous solutions conducting the exothermic reaction under adiabatic conditions (varying $\text{NaNO}_2$ concentration)	110
78.	Rate of exothermic reaction as a function of $\text{NaNO}_2$ concentration	111
79.	Temperature profile of aqueous solutions conducting the exothermic reaction under adiabatic conditions (varying $\text{NH}_4\text{Cl}$ and $\text{NaNO}_2$ concs.)	111
80.	Temperature profiles of water/heptane emulsions containing SMO and SML by different proportions	112
81.	Temperature profiles of SMO emulsions containing different proportions of water and heptane	112
82.	Temperature profiles of SML emulsions containing different proportions of water and heptane	113
83.	Additional temperature profiles of SML emulsions containing different proportions of water and heptane	113
84.	Temperature profiles of water/heptane emulsions containing different concentrations of SML	114

85.	Rate of $\text{NaNO}_2\text{-NH}_4\text{Cl}$ reaction, $dT/dt$ , as a function of concentration of SML in water/heptane emulsions	114
86.	Temperature profiles of SMO emulsions containing different types of alkane	115
87.	Temperature profiles of water/heptane SML emulsions containing different concentrations of acetic acid	115
88.	Schematic of pipe flow experimental setup	116
89.	Temperature of pipe wall at four different positions	116
90.	Photographs of the process of paraffin dissolution	117
91.	Overall view of the solution process	119
92.	Schematic of two different injection cases	120
93.	Concentration profile of $\text{NaNO}_2$ in simultaneous injection model	121
94.	Concentration profile of $\text{NH}_4\text{Cl}$ in simultaneous injection model	122
95.	Temperature profile in simultaneous injection model	123
96.	Concentration profile of $\text{NaNO}_2$ in sequential injection model	124
97.	Concentration profile of $\text{NH}_4\text{Cl}$ in sequential injection model	125
98.	Temperature profile in sequential injection model	126
99.	Fluid temperature along the centerline of pipe with simultaneous injection of $\text{NaNO}_2$ and $\text{NH}_4\text{Cl}$	127
100.	Fluid temperature along the centerline of pipe with sequential injection of $\text{NaNO}_2$ and $\text{NH}_4\text{Cl}$ with a liquid spacer	127
101.	Temperature evolution of fluid at position 2m of pipe inlet for the simultaneous injection case	128
102.	Temperature evolution of fluid at position 2m of pipe inlet for the sequential injection case	128
103.	$\text{NaNO}_2$ concentration profile at position 2m from pipe inlet for the simultaneous injection case	129
104.	$\text{NaNO}_2$ concentration profile at position 2m from pipe inlet for the sequential injection case	129
105.	(a) Schematic of an offshore platform with a pipeline which is partially plugged by wax deposition	130
	(b) Schematic of a tubular reactor with system of pulses	130
106.	(a) Schematic of pipeline with pulses of reactants, with values used for Fig. 106b	131
	(b) Effect of length of inert spacing on the plot of maximum temperature vs. location inside the pipeline	131

107.	(a) Schematic of pipeline with pulses of reactants, with values used for Fig. 107b	132
	(b) Effect of inlet temperature on the maximum temperature vs. location inside the pipeline	132
108.	Temperature trajectory at the location of 5 and 10 km from the inlet end inside the pipeline	133
109.	Distribution of temperature and concentration of the reactants after the entire system has traveled 30 km.	134
110.	Local dimensionless concentration and temperature profiles at the entrance of the pipeline	135
111.	Local dimensionless concentration and temperature profiles at a location of 3 km from the entrance of the pipeline for a pulse size 30 m.	136
112.	Local dimensionless concentration and temperature profiles at a location of 5 km. from the entrance of the pipeline for a pulse size 30 m.	137
113.	Local dimensionless concentration and temperature profiles at a location of 10 km. from the entrance of the pipeline for a pulse size 30 m.	138
114.	Local dimensionless concentration and temperature profiles at a location of 20 km from the entrance of the pipeline for a pulse size 30 m.	139
115.	Volume average temperature as a function of location down the pipeline for various pulse sizes	140
116.	Volume average temperature as a function of location down the pipeline for various reactant concentrations	140
117.	Volume average temperature as a function of location down the pipeline for various catalyst concentrations	141
118.	Plots of average temperature of one set of pulses vs. location inside the pipeline for various concentrations of catalyst	141
119.	Temperature profiles of water/heptane emulsions containing SML with differing parameters for different stirring rates	142
120.	Temperature profiles of water/heptane emulsions containing SML with differing parameters for different stirring rates	142
121.	Temperature profiles of water/heptane emulsions containing SML with differing parameters for different stirring rates	143

122.	Temperature profiles of water/heptane emulsions containing SML with differing parameters for different stirring rates	143
123.	Temperature profiles of water/heptane emulsions containing SML with differing parameters for different stirring rates	144
124.	Temperature profiles of water/heptane emulsions containing SML with differing parameters for different stirring rates	144
125.	Temperature profiles of water/heptane emulsions containing SML with no stirring	145
126.	Temperature profile of mixture of the two emulsions flowing inside the pipeline with equal concentrations of both reactants	146
127.	Schematic of pipeline with continuous alternate pulses of emulsions of the two aqueous reactants	146
128.	Local temperature wave inside the pipeline due to dispersion and reaction at the location of 5000 m.	147
129.	Local temperature wave inside the pipeline due to dispersion and reaction at the location of 10000 m.	147
130.	Local temperature wave inside the pipeline due to dispersion and reaction at the location of 20000 m.	148
131.	Local temperature wave inside the pipeline due to dispersion and reaction at the location of 30000 m.	148
132.	Average temperature profile inside the pipeline when continuous alternate pulses of the two emulsions are injected	149
133.	Temperature-time trajectory for the case of encapsulated catalyst	149



## Abstract

Chemical treatments of paraffin and asphaltene deposition by means of cleaning fluids were carried out in this research project. Research focused on the characterization of asphaltene and paraffin materials and dissolution of asphaltene and paraffin deposits using surfactant/micellar fluids developed early in the project. The key parameters controlling the dissolution rate were identified and the process of asphaltene/paraffin dissolution were examined using microscopic apparatus. Numerical modeling was also carried out to understand the dissolution of paraffin deposits.

In the treatment of asphaltene deposition problems, the effectiveness of alkane-based solvents containing alkylphenol (nonylphenol, NP) and alkylbenzene sulfonic acid (dodecylbenzene sulfonic acid, DBSA) amphiphiles on the dissolution of asphaltenes was evaluated. The results indicate that the rate of asphaltene dissolution can be influenced by the type and concentration of amphiphiles, the type of solvents, fluid temperature and flow rates. On the basis of this result, it was deduced that asphaltene dissolution is rate-controlled by the reactions involving the hydrogen-bonding associations between asphaltenes and amphiphiles and by the mass transfer of reacting species between the precipitated asphaltene surface and bulk fluids. In micromodel experiments, it was observed that asphaltenes precipitated to form cluster-like deposits which plugged the fluid flow in porous media. In the silica-gel packed column experiments, it was found that a sharp differential pressure peak appeared at the initial stage of asphaltene dissolution because the highly concentrated asphaltenes dissolved in the amphiphile fluid front temporarily plugged the pack bed. Amphiphile-based alkane fluids were shown to be effective cleaning fluids for asphaltene deposits.

Asphaltene fractionation was found to be a convenient and reliable tool in quantifying the polarity-and therefore the degree of difficulty in dissolution of asphaltenes. The nature of asphaltene varies strongly depending on crude oil source, and it is difficult to find a common characteristic on the basis of which they can be directly compared with each other. Asphaltene polarity, through fractionation, is one characteristic which can be used for this purpose.

It was found that the heteroatom content (iron, nickel, vanadium etc.) of the precipitated asphaltene plays the strongest role in determining the polarity of the precipitated asphaltene. The kinetics of dissolution of asphaltenes with different polarities were investigated. In a separate approach, the effect of the presence of ferric iron on the precipitation of asphaltenes from crude was studied. It was found that the presence of ferric ions increased the amount and the polarity of the precipitated asphaltenes. The effect of

various factors such as ferric ion concentration, acid concentration etc. was also studied.

In the treatment of paraffin deposition problems, the focus was on the dissolution of paraffin deposits using water/oil/surfactant emulsion fluids containing reactants, ammonium chloride ( $\text{NH}_4\text{Cl}$ ) and sodium nitrite ( $\text{NaNO}_2$ ), that underwent highly exothermic reactions. The results showed that the rate of this exothermic reaction was influenced by the type of surfactant, the water-to-oil volume ratio, the concentration of surfactant, and the type of oil media. These findings indicate that the desirable temperature profile for emulsion fluids to treat paraffin deposit in oil pipelines can be controlled not only by the reactant concentrations but also by the type and concentrations of surfactant and oil. A numerical simulation was also performed to investigate the flow of aqueous fluids with  $\text{NaNO}_2$  and  $\text{NH}_4\text{Cl}$  into pipes. Both simultaneous and sequential injections of aqueous fluids containing  $\text{NaNO}_2$  and  $\text{NH}_4\text{Cl}$  into an elbow-shaped pipe were studied numerically. The results show that when  $\text{NaNO}_2$  and  $\text{NH}_4\text{Cl}$  are injected sequentially along the pipe with a liquid spacer, the initiation time of this  $\text{NaNO}_2$  and  $\text{NH}_4\text{Cl}$  reaction can be delayed in a controlled manner. The simultaneous and sequential reactant-injection strategy was investigated in order to achieve both a complete usage of reactants and a sufficiently high temperature of fluids for paraffin dissolution. The effect of factors such as surfactant type, surfactant concentration and the acid concentration in the emulsion system was further studied. The method of encapsulation of the catalyst to delay the initiation of the exothermic reaction was also studied.

The results show that fused chemical reaction systems are a promising way of removing paraffin deposits in subsea pipelines. The fused system may be in the form of alternate pulses, emulsions systems or encapsulated catalyst systems. Fused reaction systems, in fact, are extremely cost-effective - less than 10% of the cost of replacing entire sections of the blocked pipeline.

This report can be of value in establishing new techniques for dealing effectively with asphaltene and paraffin deposits. Such deposits have caused oil companies millions of dollars in terms of remediation technologies, manpower and lost production time and in extreme cases have caused complete abandonment of formations which still contain millions of barrels of usable crude oil. The results presented in this report can have a real impact on the petroleum industry and the National Oil Program, if it is realized that the remediation technologies developed here can substantially delay abandonment (due to asphaltene/paraffin plugging) of domestic petroleum resources. The report also sheds new light on the nature and properties of asphaltenes and paraffin deposits which will ultimately help the scientific and research community to develop effective methods in eliminating asphaltene/ paraffin deposition problems. It must also be realized that asphaltene

remediation technologies developed and presented in this report are a real alternative to aromatic cleaning fluids currently used by the petroleum industry. Government legislation is becoming increasingly restrictive on the type and quantity of fluids being introduced into the formation depending on their environmental impact. The toxic nature of aromatic cleaning fluids places them in a category which may be restricted from use in the near future; it is only then that the usefulness and the impact of amphiphile-based alkane fluids will be evident to the petroleum industry.

## Executive Summary

Heavy organics deposition during oil production and processing is a very serious problem in many areas throughout the world [1]. In the Prinos field in the North Aegean sea, some wells completely ceased producing oil in a matter of a few days after the start of production after an initial production rate of up to 3000 BPD. The economic implications of this problem are tremendous considering the fact that the problem well workover can cost well over half a million dollars today. In Venezuela, the formation of heavy organics (asphaltic sludges) after shutting in a well temporarily (after stimulation treatment by acid) resulted in partial or complete plugging of the well. At the Hassi Messaoud field in Algeria, deposition of heavy organics in tubing was a very serious production problem [2].

Wax deposition in production tubing and transport pipelines drastically reduces operating efficiency and its removal requires significant additional operating costs. The direct cost of removing paraffin blockage from a pipeline 40,000 ft. long and diameter 6 in. is about \$1,000,000 (source: Elf Aquitaine). The overall procedure for removal of the wax deposit using conventional mechanical methods requires nearly 40 days of downtime. During this period, the production loss is nearly 1.2 million barrels of crude, which translates to approximately \$26,000,000 (at February 1997 OPEC barrel prices). Usually the deposit consists of a mix of asphaltenes and paraffins.

Tatham Offshore, Texas and Lasmo, UK replaced flow lines plugged by paraffins for two different oil fields at a cost of US\$1,000,000 each. However, the replaced pipelines were plugged again within one year. As a result, Lasmo abandoned the field at a loss of \$100,000,000.

Because oil drilling is moving further offshore, it is clear that asphaltene and paraffin deposition is a very important and costly problem. Developing solutions for this problem is critical to maintaining the oil supply of the United States as well as the world. The United States Government, therefore, must continue to take an active part in encouraging research directed towards developing better remediation technologies for such problems.

The United States Government's initial support for this project encouraged further financial contributions by the oil industry. Valuable results from the first year of research in this project prompted funding from oil companies participating in the Industrial Affiliates Program at the University of Michigan.

## I : Asphaltenes

Asphaltene precipitation manifests itself in almost all facets of production, transportation and processing of the crude (in-situ formation damage deep inside the reservoir, precipitation at the wellhead and in pumps and tubing). Precipitation normally occurs due to change in system parameters such as temperature/pressure and pH. Reservoir flooding by light hydrocarbons (LHG) and carbon dioxide (CO<sub>2</sub>) and matrix acidization (where ferric ions dissolved from pipes and instruments, in the presence of acid, cause asphaltene polymerization) are commonly encountered processes which cause asphaltene precipitation.

Asphaltenes are the most polar and heaviest component of crude oil [4,5]. Operationally defined on the basis of solubility, asphaltenes are the component of crude oil soluble in aromatics such as benzene and naphthalene, but are insoluble in light aliphatics such as pentane and heptane. Asphaltene particles are thought to be stabilized in crude oil by resins, another components of the crude. Resin molecules resemble surfactant molecules, having a polar head group and a long hydrocarbon tail. The head groups of the molecules orient themselves towards the polar surface of the asphaltene particle, with their hydrocarbon tails extending into the oil phase, thus forming a micellar structure. Light alkanes preferentially dissolve resins, thus breaking the micellar structures. The asphaltene particles then aggregate due to attractive forces between them and subsequently precipitate out of the crude oil.

Due to the serious economic nature of these problems, numerous studies have been carried out on asphaltene precipitation and a lesser number on asphaltene dissolution. Aromatic-based fluids (polyaromatics, naphthalene, xylenes, toluene) are effective in cleaning asphaltene deposits in reservoirs. However, aromatic fluids prove to be very expensive due to the large volumes required to treat the formation. Moreover, in laboratory tests of purified asphaltene in contact with pure toluene, a further increase in asphaltene content after the start of micelle formation was shown to lead to the formation of larger micelles, then of coacervate, and finally to the separation of asphaltene into a distinct phase [7]. Recent environmental concerns about the toxicity of aromatic fluids have further prompted researchers to develop alternate fluid systems for asphaltene dissolution. Studies on the stabilization of asphaltenes using non aromatic-based liquids have been undertaken in recent years. Chang and Fogler [10-11] found that asphaltene could be completely stabilized in alkane-based solutions containing a sufficient amount of alkylbenzene-derived amphiphiles. de Boer and coworkers [21] found that alkylbenzene sulphonic acid with a sufficiently long alkyl tail could effectively reduce the precipitation of asphaltenes in near-

wellbore regions. In a later study, Permsukarome and Fogler [22] studied the effects of type and concentration of amphiphiles, type of solvents and fluid temperature and type of fluid on the dissolution of asphaltenes with amphiphile/alkane solutions.

The research work on the stabilization and dissolution of asphaltenes conducted in this project includes the preparation and characterization of asphaltene materials, the evaluation of the effectiveness of a series of amphiphiles and alkane solvents on the stabilization of amphiphiles, the rate of asphaltene dissolution with amphiphile/alkane solutions, characterization of asphaltene polarity by fractionation and studying the effect of the presence of ferric ( $\text{Fe}^{3+}$ ) ions in the system on the properties of the precipitated asphaltenes.

The basic physical properties of Mobil #0 asphaltenes were characterized. The number-averaged molecular weight of solubilized asphaltenes is approximately 1000 from a size exclusion chromatographic measurement. The FTIR spectroscopic measurement shows that asphaltenes contain aliphatic groups, aromatic (including  $\pi$  bonding) groups and hydrogen-bonding groups, such as amine (N-H). The UV/vis spectra of asphaltenes indicate the existence of electronic-transition structure such as alternating  $\pi$ -bonding. The experiments of the potentiometric titration of asphaltenes further provide evidence of acid-base interactions among asphaltene molecules. These acid-base interactions in asphaltenes support the feasibility of stabilization and dissolution of asphaltenes using solutions containing amphiphiles with acid/base functional groups. In addition, microscopic measurements showed that asphaltene precipitates appear as branched clusters of spheres and not having any specific patterns, such as fibrillar, lamellar, etc., indicating that asphaltene molecules tend to associate together with no specific direction or orientation.

The stability of asphaltenes in alkane media containing a series of acidic alkylbenzene-derived amphiphiles and a homologue of basic alkylpyridine amphiphiles was extensively evaluated. In addition, the adsorption of alkylbenzene-derived amphiphiles to asphaltenes was also quantified. These studies show clearly that asphaltenes can be stabilized in alkane media by alkylbenzene-derived amphiphiles. Two factors are found to be important in stabilizing asphaltenes by amphiphiles, which are: the adsorption of amphiphiles to asphaltene surfaces by the head group of amphiphiles and the establishment of a stable steric alkyl layer around asphaltene molecules by the tail group of amphiphiles. The influences of the chemical structure of amphiphiles as well as the properties of oil solvent on the stabilization of asphaltenes are summarized as follows:

(1) Effect of amphiphile's head group: increasing the polarity (or more specifically, the acidity, in this study) of the amphiphile's head group strengthens the attraction of

amphiphiles to asphaltenes through acid-base interaction; therefore, the amphiphile's effectiveness on asphaltene stabilization is increased.

(2) Effect of amphiphile's tail length: increasing the tail length of an amphiphile can improve its effectiveness to sterically stabilize asphaltenes even though this increase may reduce their affinity to asphaltenes by a small amount.

(3) Effect of solvent: the influence of alkane solvents on the ability of amphiphiles to stabilize asphaltenes is dependent on the types of amphiphiles. For example, the ability of NP amphiphiles on asphaltene stabilization is reduced in pentane while that of DBSA amphiphiles is not.

The kinetics of dissolution of asphaltene deposits by fluids composed of amphiphiles and alkanes was also investigated using a differential reactor apparatus. The results show that asphaltenes can be dissolved by alkane-based fluids containing two alkylbenzene-derived amphiphiles, nonylphenol (NP) and dodecylbenzene sulfonic acid (DBSA). The factors influencing the rate of asphaltene dissolution by amphiphile/alkane fluids are summarized as follows:

(1) Effect of type and concentration of amphiphile: The rate of asphaltene dissolution appears to follow Langmuir-Hinshelwood kinetics with respect to the concentration of amphiphiles; that is, the dissolution rate increases steadily at low amphiphile concentrations and reaches a plateau at higher amphiphile concentrations where asphaltenes are completely dissolved. The rate increment in asphaltene dissolution by micellar solutions with DBSA amphiphile is more significant than that with NP amphiphile.

(2) Effect of type of solvent: The rate of asphaltene dissolution by the heptane-based micellar fluids is higher than that of dodecane-based fluids because heptane penetrates into asphaltene deposits more easily. Thus light alkanes are more effective in asphaltene dissolution with amphiphiles.

(3) Effect of temperature: The rate of asphaltene dissolution increases with increasing the fluid temperature and follows an Arrhenius temperature dependence yielding an activation energy of approximately 4-7 kcal/mole. On the basis of this result, it is deduced that asphaltene dissolution is rate-controlled by the reactions involving the transition from asphaltene-asphaltene associations to asphaltene-amphiphile associations through the redistribution of inter-molecular hydrogen-bonding and charge transfer interactions as well as by the mass transfer of reacting species between the precipitated asphaltene surface and bulk fluids.

(4) Effect of flow rate: Higher flow rates of amphiphile/alkane fluids can also increase the rate of asphaltene dissolution by enhancing the penetration of fluids into

porous asphaltene precipitates as well as reducing the boundary layer that control the mass transfer of reacting species between asphaltenes and fluids.

The phenomenon of asphaltene deposition and dissolution in porous media was observed by microscopic visualization of the deposition and plugging of asphaltenes in glass micromodels in which etched conducting channels form a two-dimensional model porous medium. The results showed that during the deposition of asphaltenes, the less soluble asphaltenes are first precipitated in the micromodel to form cluster-like deposits. Then, these cluster-like deposits block the flow of asphaltenes that flow pass by to form island-like deposits. The solubility of cluster-like deposits appears lower than that of island-like deposits. As a result, the NP/heptane fluid can only remove the island-like asphaltene deposits and leaves cluster-like deposits undissolved inside micromodel. These cluster-like deposits can then be dissolved by the more effective DBSA/hexane solution which cleans up the entire micromodel.

The study of asphaltene dissolution in a silica gel packed-bed column using micellar solution was also carried out to further understand asphaltene dissolution in porous media. The time evolution profiles of the differential pressure across the bed and the asphaltene concentration in the effluent were measured. The results showed that asphaltene deposited in the bed were dissolved by amphiphile/alkane solutions. The elution of asphaltenes with amphiphile solutions out of the bed caused the decrease in the differential pressure across the bed. The rate of asphaltene dissolution was greater with NP/heptane solutions than with DBSA/heptane solutions. The amount of asphaltenes removed from the packed bed in general increased with increasing the concentration of amphiphiles in the solution. It was also found that a sharp differential pressure peak appeared at the initial stage of asphaltene dissolution because the highly concentrated asphaltenes dissolved in the amphiphile fluid front temporarily plugged the packed bed.

Characterization of asphaltenes by fractionation of the asphaltenes into components of different polarities was carried out. Studies were performed on asphaltene fractions obtained by varying the amount of pentane ( $n\text{-C}_5\text{H}_{12}$ ) in a binary mixture of methylene chloride ( $\text{CH}_2\text{Cl}_2$ ) and pentane in which the asphaltene powder was initially dissolved. The fractions varied in physical appearance, varying from dense, shiny black particles (the most polar fraction) to light, dull brown powder (less polar fraction). did not yield conclusive results. Dissolution studies were carried out on the unfractionated asphaltene and two of the fractions (the most polar and the least polar) using an amphiphile/alkane solution (dodecylbenzene sulphonic acid in heptane). The rates of dissolution for the unfractionated asphaltenes and the two fractions were very different : the most polar fraction showed the lowest rate of dissolution, while the least polar fraction had the highest rate of dissolution.



Even after taking the surface area of the fractions into account, the least polar fraction still showed a higher specific first-order reaction rate constant.

Effect of temperature on the dissolution behavior of the most polar fraction F1 (or F40/60) was studied using 10% DBSA in heptane at a flow rate of 5 ml/min. At low temperatures (1-7°C), no dissolution takes place. Dissolution can be noticed at 12.8°C. At slightly higher temperatures (14-17°C), the kinetics deviate from first-order behavior, displaying a "lag" phase where the rate of dissolution is slow at first and then picks up. At still higher temperatures (22,58 °C) the "lag" phase disappears and the kinetics obey first order behavior. The different behavior at low temperatures may be due to lower values of mass transfer coefficients, which causes the system to take a finite amount of time for saturation of the asphaltene surface with the amphiphilic species.

Formation damage caused by the precipitation of asphaltic sludge when crude oil is contacted by acid is a common problem during matrix acidizing treatments [13]. The formation of asphaltic sludges has become more widely recognized over the years. Asphaltic sludge problems have been identified with crudes of Western Canada such as the Beaverhill Lake crude, crudes of Alaska and California, San Andres crudes of West Texas and the Smackover crudes of Mississippi. Asphaltic sludge precipitation is considerably worse in the presence of ferric iron, especially in crudes with high asphaltene resin to asphaltene ratios. This phenomenon may be due to oxidative polymerization processes in the resin layer surrounding the asphaltene particles or charge neutralization in the resin layer [13,14]. The effect of the presence of iron in the precipitating system was studied by adding a mixture of aqueous ferric chloride and hydrochloric acid to the crude prior to precipitation. The sludge formed was then mixed with heptane and the asphaltenes were precipitated. These asphaltenes were compared to the asphaltenes precipitated directly from crude by the addition of heptane by analyzing the C:H ratio and the heteroatom content (mainly iron, nickel and vanadium). Results show that the asphaltene(sludge) has a greater yield (based on weight of crude) and also possesses higher levels of unsaturation/aromaticity and total heteroatom concentration. It was observed that longer contact times tended to increase the polarity of the precipitated asphaltene. These asphaltenes were also further fractionated into different components and the effects of varying the ferric ion concentration and the acid concentration were observed.

### **Suggested Future Work**

The micellar fluids which were developed using alkylbenzene derived amphiphiles have been shown to be effective in dissolving asphaltenes in model systems such as differential reactors, micromodels and silica-asphaltene packed beds. Future work should

be directed at confirming the ability of these micellar fluids in dissolving asphaltene deposits under reservoir conditions

A comprehensive study needs to be undertaken on the effectiveness of these micellar fluids in dissolving asphaltenes from different crude oils and different precipitating conditions. This study would determine the universal applicability of these micellar fluids in treating asphaltene deposition problems.

Aromatic fluids (xylenes, toluene etc.) which are currently used for treating asphaltene deposits are extremely toxic to plant, animal and human life. Developing alternative cleaning fluids is therefore of great interest to the government, the oil industry as well as the general public. The authors strongly feel that the indicated micellar fluids are viable and much less toxic alternatives to aromatic cleaning fluids.

## **II: Paraffins**

The rate of wax deposition depends not only on the nature of the crude oil (like viscosity, wax content, wax solubility, tendency to retain wax particles, etc.) but also on the operating conditions such as temperature gradient, pressure, flow rate, etc. in the wellbore or pipeline. Different mechanisms of wax deposition have previously been reported; for example molecular diffusion, shear dispersion, Brownian diffusion and gravity settling [20]. The difficulty in predicting wax deposition arises due to the presence of various components such as asphaltenes, hydrates, and other impurities in the oil. The effect of each of these components on the nature of the deposited wax and the deposition rate has not been well studied. The other difficulty in predicting wax deposition is due to the presence of a high percentage of the oil in the total immobile wax deposited on the pipeline wall. It has also been observed that deposits obtained at high shear rates are hard and brittle, whereas deposits at low shear rates are soft and pliable which is due to the fact that high shear rate decreases the amount of oil trapped in the deposit.

The major research work on the stabilization and dissolution of paraffins conducted in the years 1995-1997 includes the preparation and characterization of paraffin materials, the evaluation of the effectiveness of paraffin inhibitors in preventing paraffins from precipitation, the dissolution of paraffin deposits by fused reaction systems using exothermic reactive fluids and the preliminary investigation of the method of catalyst encapsulation in fused reaction systems.

The basic physical properties of Joliet wax were characterized. The FTIR spectroscopic study and the potentiometric titration indicate Joliet wax is mainly composed

of paraffin molecules with very low content of acid/base functional groups. The number of carbon atoms of these molecules range from 24 to 76. The X-ray diffraction study verifies the existence of a crystalline phase in Joliet wax. It was also found that Joliet wax readily precipitated as the temperature was reduced below its melting point approximately in the range of 40°C.

In the study of preventing paraffin precipitation from solution, it was found that both natural and synthetic paraffin wax could not be stabilized in the organic media by the so-called paraffin inhibitors such as those used in this study. Effective paraffin inhibitors may require a sufficiently long aliphatic chain structure to form strong van der Waals attractions with paraffin molecules to prevent or modify their crystallization. The long aliphatic chain of the inhibitors may result in the instability of inhibitors themselves in the heptane solution, which is especially true about monomeric inhibitors. Although polymeric molecules such as poly(ethylene vinyl acetate) can slightly reduce the precipitation temperature of paraffin wax materials, the feasibility and the optimal molecular design of this polymer for preventing wax from precipitation needs to be further studied.

In the research on the removal of paraffin deposits, exothermic reacting emulsion fluids were used as paraffin cleaning fluids. These fluids are, in fact, water-in-oil emulsions containing an oil phase for accommodating the dissolved paraffin and an aqueous phase for hosting the aqueous exothermic reactions to produce heat for melting paraffin deposits. This aqueous exothermic reaction involves the reaction between ammonium chloride and sodium nitrite carried out with an acid catalyst. The feasibility of this thermal treatment method on the dissolution of paraffin deposits was verified by a preliminary study using a video-enhanced microscopic apparatus. Results demonstrate that paraffin deposits can be either dissolved or dispersed at temperature about 55-60°C.

The kinetics of the exothermic reaction between ammonium chloride( $\text{NH}_4\text{Cl}$ ) and sodium nitrite( $\text{NaNO}_2$ ) were analyzed using the temperature evolution profile of the reaction which was conducted in an adiabatic reactor. Results show that the kinetics of the reaction between ammonium chloride and sodium nitrite can be expressed by a power law (equation [22] in text of report). In addition, a further experiment indicates that the reaction between ammonium nitrate and sodium nitrite is also similar to that between ammonium chloride and sodium nitrite. The results of these kinetic studies provide guidelines for controlling the rate of exothermic reactions currently selected for the dissolution of paraffin deposits.

The kinetics of the exothermic reaction between the emulsified ammonium chloride and the emulsified sodium nitrite taking place inside the dispersed phase were determined. Further variables investigated included the type of surfactant, the water-to-oil volume ratio,

the concentration of surfactant, and the type of oil medium. It was found that the sorbitan mono-laurate (SML) surfactant is significantly more effective than the sorbitan mono-oleate (SMO) surfactant in reducing the rate of the  $\text{NaNO}_2\text{-NH}_4\text{Cl}$  reaction. Increasing the concentration of surfactant in general reduces the  $\text{NaNO}_2\text{-NH}_4\text{Cl}$  reaction rate in emulsions, and the type of alkane media also affects this reaction rate. These findings indicate that the desirable temperature profile for emulsion fluids to treat paraffin deposit in oil pipelines has to be achieved by controlling not only the reactant and acid concentrations but also the type and concentrations of surfactant and oil. In addition, the potential influence of nitrogen produced by the  $\text{NaNO}_2\text{-NH}_4\text{Cl}$  reaction was assessed. It seems likely that nitrogen evolved in-situ from paraffin treatment fluids can increase the speed of fluids in pipelines and thus leads to the rupture of paraffin deposits.

A numerical simulation using a computational fluid dynamics solver, FLUENT (see page 42 of report), was also performed to investigate the flow of aqueous fluids with  $\text{NaNO}_2$  and  $\text{NH}_4\text{Cl}$  into pipes. Both the simultaneous and sequential injections of aqueous fluids containing  $\text{NaNO}_2$  and  $\text{NH}_4\text{Cl}$  into an elbow-shaped pipe were studied numerically. The results show the reaction between  $\text{NaNO}_2$  and  $\text{NH}_4\text{Cl}$  occurs immediately and significantly as they flow into pipe simultaneously. When  $\text{NaNO}_2$  and  $\text{NH}_4\text{Cl}$  are injected sequentially along the pipe with a liquid spacer, the time of this  $\text{NaNO}_2$  and  $\text{NH}_4\text{Cl}$  reaction can be delayed in a controlled manner. The flow dispersion along the axial direction results in the mixing and exothermic reaction between the sequentially injected  $\text{NaNO}_2$  and  $\text{NH}_4\text{Cl}$ , leading to a rise in temperature at a position between these two slugs of reactants.

This sequential reactant-injection strategy was continued for long straight pipelines. This technique was achieved by feeding pulses of aqueous reactants into the pipeline separated by an inert. Dispersed plug flow model was used to solve this problem. The technique was verified for both single set of pulses and multiple set of pulses. This method of melting the wax deposited on the pipeline wall was found promising and results from the mathematical simulation showed that heat can be released at locations as far as 30 km from the entrance of the pipeline.

This sequential reactant-injection strategy was continued for the emulsified reacting system. This technique was achieved by alternately feeding pulses of the two emulsions into the pipeline. This method was also found promising in delaying the exothermic reaction.

The catalyst of the reaction between  $\text{NaNO}_2$  and  $\text{NH}_4\text{Cl}$  is an acid. Acid anhydride was encapsulated in gelatin capsules and added to the reactive mixture of the two reactants. The exothermic reaction started only when the gelatin capsule was dissolved and acid anhydride contacted the reacting aqueous solution. Further investigations are needed to

understand the dissolution kinetics of the capsule which will be used in designing the thickness of the capsule for a desired delay in the heat release.

### **Suggested Future Work**

Better technologies for paraffin dissolution can only be developed when the nature of the deposits can be fully understood. As mentioned before, the paraffin deposits are wax-oil gels with a high oil content. The processes of paraffin deposition and formation of the wax-oil gel need to be examined in much detail.

The use of fused reaction systems for melting wax deposits in subsea pipelines appears feasible. This statement is based largely on computer simulations and has been corroborated to a certain extent by simple experiments. Flow-loop experiments need to be carried out to study the actual performance and effectiveness of these reaction systems. The method of encapsulation to delay the release of the catalyst seems to be extremely promising.

The authors strongly feel that fused reaction systems may hold the key to removing paraffin deposits in subsea oil pipelines at costs which are insignificant when compared to the cost of replacing blocked sections of the pipeline. As a result, the authors have embarked on research aimed at studying formation of wax-oil gels and studying the technique of encapsulation in a flow-loop system. Experimental setups for this purpose have been recently installed at the Porous Media Laboratories at the University of Michigan.

It is hoped that results from future experiments will shed meaningful light on the two "black boxes" which are asphaltene and paraffin deposits.

## Technology Transfer

The publications and presentations that resulted from the research in this report are listed below.

### Publications

1. Permsukarome, Pornruedee, Chang, Chialu and Fogler, H. Scott, "Kinetic Study of Asphaltene Dissolution in Amphiphile/Alkane Solutions", *Ind. & Eng. Chem. Res.*, 36, 3960-67, 1997.
2. Singh Probjot, Fogler, H. Scott, "Fused Chemical Reactions: The Use of Dispersion to Delay Reaction Time in Tubular Reactors", accepted for publication in *Ind. & Eng. Chem. Res.*, Doraiswamy special issue, June 1998.
3. Tangtayakom, Veerapat, "Asphaltic Sludge Study", M.S. thesis submitted to the Petroleum and Petrochemical College, Chulalongkorn University, Thailand, March 1998.

### Presentations

1. Chang, Chialu, Nalwaya, V. and Fogler, H. Scott, "Dissolution of Asphaltenes Using Amphiphile/Alkane Solutions: Asphaltene Fractionation"; presentation made at the Annual Meeting of the Industrial Affiliates Group, University of Michigan, Ann Arbor, June 1997.
2. Singh, Probjot, Fogler, H. Scott, "Dissolution of Wax Using Fused Chemical Reactions", presentation made at the Annual Meeting of the Industrial Affiliates Group, University of Michigan, Ann Arbor, June 1997.
3. Fredd, C.N., "Surfactant-Micellar Techniques for Near-Wellbore Paraffin and Asphaltene Damage Remediation", presentation made at the Extraction Research session of the Oil Technology & Gas Environmental Review, U.S. Department of Energy, Tulsa, OK, June 1997.
4. Nalwaya, V., Fogler, H. Scott, "Characterization of Asphaltenes for Effective Dissolution Using Micellar Solutions", presentation made to researchers at Chevron R&D, Los Angeles, CA, November 1997.

## **Acknowledgment**

The authors would like to gratefully acknowledge the financial support for this three-year study provided by the Department of Energy, United States Government under BDM-Oklahoma subcontract BDM-OKL G4S40807. The authors would also like to express their thanks to Dr. Michael Madden, BDM Program Manager for his insightful comments and suggestions which helped to bring this report to its present form.

## 1. Objective

The objective of this project is to design and evaluate new chemical treatments using surfactant/micellar technology alone or in combination with other chemical methods to prevent, alleviate, and minimize damage resulting from paraffin and asphaltene deposition in oil production reservoirs and oil pipelines.

The general research work of this project includes:

- Testing methodology development of protocols to characterize paraffin and asphaltene components in the crude oil in order to provide a basis for selecting effective functional chemicals in stabilization and removing deposits;
- Evaluation of chemical systems - identification of the major chemical structural effects of functional chemicals on the solubilization or dispersion of paraffin/asphaltene materials in organic-based fluids; and
- Rock-fluid studies - visualization of the process of dissolving or dispersing paraffin and asphaltene deposits in porous media, and quantification of the damage removal of these organic deposits from both porous media and pipelines through core flood and pipe flow experiments.

This final report describes the results of the project study carried out in the years 1995-1997.



## **2. Research on Asphaltenes**

### **2.1. Project Description**

Research was conducted on the characterization of asphaltenes and their stabilization and dissolution in alkane media. The research done includes:

- Preparation of asphaltene materials from different crude oil samples.
- Characterization of asphaltenes, including the molecular weight, the functional group and the acid/base number of asphaltenes, as well as the morphology of asphaltene precipitates.
- Quantification of the stability of asphaltenes in alkane-based micellar solutions containing asphaltene stabilizers such as amphiphiles, in order to select amphiphile/alkane solutions effective to the dissolution of asphaltene deposits.
- Investigation of the adsorption of amphiphiles to precipitated asphaltene samples, in order to elucidate the mechanism that asphaltenes are stabilized in alkane media by amphiphiles.
- Investigation of the stability of different asphaltene materials in the selected amphiphile/alkane solutions, in order to examine the general feasibility of asphaltene dissolution by amphiphile/alkane fluids.
- Fractionation of asphaltenes into components of different polarities and subsequent characterization of these fractions.
- Study of the kinetics of dissolution of asphaltene deposits by fluids composed of amphiphiles and alkane solvent as a function of the flow rate, temperature and composition of fluids.

### **2.2 Preparation of asphaltene materials**

Asphaltenes used in this project, as listed in Table 1, are isolated from different crude oil samples. The asphaltene sample used in the first study was a pentane-insoluble fraction of crude oil provided by Mobil Research and Development (Mobil #0). This asphaltene sample was prepared from crude oil according to a modified procedure described in ASTM 2007D (1983) [8]. In brief, one volume of crude oil was first mixed with ten volumes of warm pentane solvent for approximately one hour to precipitate asphaltenes out of solution. Afterwards, asphaltene precipitates were collected from solution by passing the solution media through a fritted glass filter with Whatman No.1 filter papers and were dried at 60°C. This precipitated Mobil asphaltene sample appeared as fine powder with a dark brown to black color. The solubility of this asphaltene sample was found to be 8.4 (cal/cm<sup>3</sup>)<sup>0.5</sup> in the scale of Hildebrand solubility

parameter. The elemental composition and chemical characterization of this asphaltene sample was also reported previously (Chang and Fogler)[10-11].

### 2.3 Characterization of Asphaltenes

An extensive characterization of the properties of an asphaltene material, Mobil asphaltenes, was carried out. This characterization includes the molecular weights, the functional groups, and the acid/base number of asphaltenes, as well as the morphology of asphaltene precipitates.

**2.3.1 Molecular Weight of Asphaltenes** : The molecular weights of Mobil asphaltenes were measured using size exclusion chromatography (SEC). To measure the molecular weight of asphaltenes, asphaltenes were dissolved in tetrahydrofuran (THF) and injected into a SEC apparatus equipped with an ultra-violet (254 nm) detector. The obtained elution time of asphaltenes was converted to the molecular weight of asphaltenes using the calibration curve of polystyrene standards with known molecular weights. Figure 1 illustrates the resultant molecular weight distribution of Mobil asphaltenes. The molecular weight of Mobil asphaltenes ranging from 200 to 20000 indicates a broad size distribution of asphaltene molecules. The number average molecular weight of Mobil asphaltenes is approximately 1000.

**2.3.2 Functional Groups of Asphaltenes** : The functional groups of the Mobil asphaltene sample was investigated by FTIR spectroscopy using carbon tetrachloride ( $\text{CCl}_4$ ) and carbon disulfide ( $\text{CS}_2$ ) as solvents. These solvents were used because  $\text{CCl}_4$  and  $\text{CS}_2$  have a low IR absorption background above and below  $1400\text{ cm}^{-1}$ , respectively. As illustrated by the FTIR spectrum in Figure 2, strong absorption of  $\text{CH}_2$  symmetric and asymmetric stretching bands located at  $2850$  and  $2920\text{ cm}^{-1}$ , respectively, indicates that Mobil asphaltenes contain a major portion of  $\text{CH}_2$  group. However, it also contains a significant portion of aromatics and/or  $\text{C}=\text{C}$  bonds as illustrated by the absorption peak at  $1600\text{ cm}^{-1}$ . The broad band ranging from  $1700$  to  $1000\text{ cm}^{-1}$  suggests that Mobil asphaltenes may have various functional groups. These functional groups are very likely to form hydrogen-bonding as illustrated by the broad hydrogen-bonding band in the range of  $3100\text{-}3600\text{ cm}^{-1}$ . The appearance of a sharp peak located at  $3480\text{ cm}^{-1}$  should be due to the vibrational stretching of the free N-H group of asphaltenes. This FTIR study indicates that the hydrogen-bonding interactions may partially contribute to the solubility of asphaltenes in solution.

**2.3.3 Acid/Base Properties of Asphaltenes** : The acid/base quantities of Mobil asphaltenes were measured using a potentiometric titration method described in ASTM D664 [9]. In short, a sample was mixed with a titration solvent consisting of toluene and anhydrous isopropyl alcohol and then heated until a homogeneous solution was formed. The Mobil asphaltene was dissolved in the solvent at room temperature. During titration, the electric potential of the solution was measured using an electrode probe. Solutions of 0.1N of HCl or KOH were added to 125 ml titration solvent containing 0.5g asphaltenes until the end point was reached. The end point was taken as the inflection point of the titration curve plotted as electric potential versus volume of titration solvent added. If no definite inflection point was found, the end point was assumed to be where the volume of acid (or base) had the same electric potential difference as the nonaqueous buffer.

An example of the potentiometric titration is illustrated in Figure 3. The acid (base) quantity of sample is described by the so-called acid (base) number (unit: mg KOH/g sample) as follows:

$$\text{Total acid (base) number} = \frac{(A - B) \times N \times 56.1}{W}$$

where A = milliliters of alcoholic KOH (HCl) solution used to titrate sample to end point, B = volume corresponding to A for blank titration, N = normality of alcoholic KOH (HCl) solution, W = gram of sample, and 56.1 = molecular weight of KOH.

It was found that Mobil asphaltenes had significant values of acid and base numbers, 13.90 and 6.30, respectively. These acid/base values support the hypothesis that asphaltenes can precipitate out of solution by the attractive acid-base interactions among different asphaltene molecules. Therefore, the feasibility of preventing asphaltenes from precipitation using surfactant-like stabilizers with an acidic or basic group was conducted. This acid/base titration method provides an easy way to quantify the acid/base properties of crude oil precipitates. However, it was noticed that the base numbers of asphaltenes are ill-defined because of the lack of inflection points in the titration curve. This trend might be caused by a wide variety of weak basic groups of asphaltenes, leading to the formation of many conjugate acids when HCl is added to the titrated solution.

**2.3.4 Morphology of the Precipitates of Asphaltenes** : The molecular weights of individual molecules of asphaltenes are no more than the order of  $10^4$ . However, the flocculation of asphaltenes results in precipitates sufficiently large to be observable visually. The precipitates of asphaltenes were made by the addition of an excessive amount of alkane to the toluene medium containing dissolved asphaltenes. While asphaltene precipitates were still wet with the precipitating solution, a stereo zoom microscope was used to observe their morphology. The

length scale of this light microscopic study is between 1 to 100  $\mu\text{m}$ . Figure 4 illustrates the light microscopic graphs of Mobil asphaltene precipitates. One observes that these asphaltene precipitates appear as branched cluster patterns without any other specific patterns, such as fibrillar, lamellar etc. Subsequently, a scanning electron microscope was used to further examine asphaltene precipitates which were completely dried. The resolution of this electron microscopic measurement was about 0.1  $\mu\text{m}$ . As shown in Figure 5, the micrograph of asphaltene precipitates appears as branched clusters which are composed of asphaltene particles with the diameter as small as 0.1  $\mu\text{m}$ . Similar to the light microscopic measurement, no other specific pattern such as fibrillar was observed. In fact, asphaltene aggregates in the wet state, as shown in Figure 4, appear as the fractal pattern generated by the computer simulation of the cluster-cluster aggregation of particles under random motion, indicating that asphaltene molecules may flocculate and aggregate into fractals under a cluster-cluster aggregation process. This precipitate was dissolved in toluene and further precipitated by the addition of heptane.

**2.3.5 Morphology of Asphaltene Deposits in Porous Media** : Asphaltene deposits in a model porous medium, a two-dimensional glass micromodel, were observed in this study. In this study, asphaltenes were induced to in-situ precipitate out of solution and deposit on the pore surface of glass micromodels. Through a deep-bed filtration process, asphaltenes preferentially deposit in the pore throat. The accumulation of deposited asphaltenes results in an apparent blocking of pore throats. In addition, it is clear that the extent of blocking of pore throats is also influenced by the temperature of solution. The asphaltene precipitates at higher temperatures (80°C) are more dense than those at lower temperatures (room temperature). Dense precipitates suggest that asphaltene blocking may be worse in high temperature oil reservoirs.

## 2.4 Stabilization of Asphaltenes Using Amphiphile/Alkane Solutions

A systematic investigation of the stability of asphaltenes was carried out using a series of alkane-based solutions with oil-soluble amphiphiles. From this study, the effect of the molecular structure of amphiphiles and the type of alkane solvent on the stabilization of asphaltenes is identified.



Mobil asphaltenes were used in the major part of this study. The solubility parameter of the Mobil asphaltene sample was estimated by the solubility of asphaltenes in the binary toluene-heptane solution. Asphaltenes start to precipitate when the composition of heptane attains 30-40 vol% which corresponds to the Hildebrand solubility parameter of approximately 8.4 (cal/cm<sup>3</sup>)<sup>0.5</sup>. A variety of amphiphiles were used in this study, including a series of acidic alkylbenzene-derived amphiphiles ( $\text{C}_n\text{H}_{2n+1}$  -X, where X = SO<sub>3</sub>H, OH, O(C<sub>2</sub>H<sub>4</sub>)<sub>2</sub>OH) and a homologue of basic alkylpyridine amphiphiles ( $\text{C}_n\text{H}_{2n+1}$  ). Information about these amphiphiles is detailed in

Table 2. While all of the amphiphiles have a common alkylbenzene (or alkylpyridine) group, they have at least one of the following two structural differences: (1) different polar head groups and (2) different length of alkyl tails. Consequently, the effect of the amphiphile's chemical structure on the stabilization of asphaltenes can be systematically investigated.

The purpose of the investigation of the adsorption of amphiphiles to precipitated asphaltene samples in this study is to elucidate the mechanism by which asphaltenes are stabilized in alkane media by amphiphiles. Alkylbenzene-derived amphiphiles were used in this study. Adsorption of amphiphiles to asphaltenes was carried out using Fourier transform infrared spectroscopic (FTIR) techniques. Experiments were conducted by preparing samples containing a fixed amount of amphiphiles but different amounts of asphaltenes. In this task, the amphiphile concentration was approximately 0.3 - 0.5 mole/dm<sup>3</sup>. Concentrations of asphaltenes ranged from 0 to 4 wt% in the solution. Samples were centrifuged at 3000 rpm for 20 minutes in a Beckman TJ-6 centrifuge. Next, the concentrations of asphaltenes and amphiphiles remained in the supernatant were measured by the absorbance of light at the wavelength of 400 nm and by the absorbance of a characteristic infrared band of each amphiphiles, as listed in Table 3.

In the following, the results of the study on the effect of the head and tail groups of alkylbenzene-derived amphiphiles on the adsorption of amphiphiles to asphaltenes are described.

**2.4.1 Effect of the Amphiphiles' Head Group on Amphiphile Adsorption to Asphaltenes :** The amphiphiles tested were n-dodecylbenzene sulphonic acid (DBSA), n-nonylphenol (NP), n-nonylbenzene (NB) and n-nonylbenzene di-oxyethylene (NBDO). Figure 6 shows that the effectiveness of amphiphiles in stabilizing asphaltenes follows the order: DBSA>NP>NBDO>NB. Without a polar head group, NB does not have any ability whatsoever to stabilize asphaltenes; the concentration of solubilized asphaltenes in a heptane solution containing up to 6 wt% NB remains almost as low as that in pure heptane. 7 wt% NP can completely stabilize asphaltenes but 7 wt% NBDO stabilizes only 50% asphaltenes. With 1-2 wt% DBSA, asphaltenes can be totally solubilized in heptane solvent. Figure 10 shows the amount of amphiphiles and asphaltenes retained in the supernatants. The higher the amount of amphiphiles adsorbed to the surface of asphaltene precipitates (acting as adsorbent), the lower the percentage of amphiphiles remained in the supernatant. This clearly demonstrates that the extent of the amphiphile's adsorption to asphaltenes follows the order: DBSA > NP > NBDO > NB. Figures 6 and 10 show that the effectiveness of amphiphile's head group on the asphaltene stabilization and on the asphaltene-amphiphile interaction is: sulfonic acid group > phenol group > di-oxyethylene group. This trend also follows the acidity order of these groups, suggesting that asphaltenes are stabilized by these amphiphiles through the acid-base interaction (note: hydrogen-bonding belongs to a weak acid-base interaction). DBSA is a significantly strong acid

that can readily undergo an almost irreversible acid-base reaction by donating its proton to the C=C bonds and/or specific basic groups of asphaltenes. Consequently, dilute solutions of DBSA can effectively stabilize asphaltenes (which are also dilute). For alkylphenol molecules, its aromatic benzene group can de-localize the electrons bonded between O and H elements of the hydroxyl group to make its phenol group moderately acidic. Therefore, 7 wt% NP is needed to completely stabilize asphaltenes. On the other hand, amphiphiles with a strong self-association such as NBDO or with an extremely weak acidity such as NB cannot stabilize asphaltenes thoroughly in alkane media.

**2.4.2 Effect of the Tail Group of Amphiphiles on Asphaltene Stabilization** : Alkylphenols with tail length ranging from one carbon to twelve carbons were used in this study. Figure 7 shows the percentage of solubilized asphaltenes in heptane solutions containing different alkyl phenols. When the carbon number of the amphiphile's tail is less than 6, the amphiphile's ability to stabilize asphaltenes decreases significantly with decreasing the tail length. The effectiveness of alkyl phenols on asphaltene stabilization is: n-hexylphenol > n-butylphenol > sec-butylphenol > ethylphenol > p-cresol. However, the effectiveness of alkylphenols with alkyl chains longer than 6 carbons are quite similar. It suggests that a minimum alkyl chain length is necessary for an amphiphile to provide sufficient ability to stabilize asphaltenes in the solution. This minimum chain length for alkyl phenol amphiphiles is about 6 carbons.

Alkylpyridine amphiphiles with different tail lengths, including 4-ethylpyridine, 4-isopropylpyridine and 4-butylpentyl pyridine, were also tested for stabilizing asphaltenes in heptane. Figure 8 shows that these basic alkylpyridine amphiphiles are of similar ability to stabilize asphaltenes, requiring about 20 wt% for completely stabilize Kuparuk asphaltenes in heptane. One observes that the effectiveness of alkylpyridine amphiphiles in stabilizing asphaltenes is significantly less than that of alkylphenol amphiphiles even though pyridine has a permanent dipole moment 2.2D (Debye) which is higher than that of phenol which is 1.6D. This result may be attributed to the fact that basic alkylpyridine molecules can only associate with acidic asphaltene functional groups as opposed to alkylphenol molecules which are able to interact with both acidic and basic groups of asphaltenes.

Figure 11 shows that the extent of the adsorption of alkylphenols to asphaltenes increases with decreasing the tail length from C12 to C1. This result demonstrates that the decrease in the ability of alkylphenols to stabilize asphaltenes with decreasing tail length, as illustrated in Figure 7, does not result from the decrease of the attractive interactions between asphaltenes and alkylphenols. Therefore, it is deduced that the major effect of the amphiphile's tail length is to provide a steric-stabilization effect to prevent asphaltenes from aggregation. The alkylphenols with short tails are not only much smaller than asphaltene molecules but also more polar

throughout most of the molecular structure than the surrounding solvent molecules. Consequently, they cannot surround asphaltene particles but instead intercalate with, or are imbedded in, asphaltenes, thereby offering little hindrance to asphaltene flocculation. As the tail length of alkylphenols increases, the size of this apolar moiety becomes larger and tending less to be surrounded by asphaltene molecules. When the alkyl tail has 6 carbon atoms or more, this apolar moiety becomes sufficiently large to form a stable aliphatic layer to prevent asphaltene particles from aggregation.

**2.4.3 Effect of Alkane Solvent on Asphaltene Stabilization** : Studies on the effects of alkane solvents on the amphiphile's ability to stabilize asphaltenes were carried out using the experimental procedures similar to those on the stabilization of asphaltenes using amphiphiles. Here, the minimum concentrations of two oil-soluble amphiphiles, nonylphenol (NP) and dodecylbenzene sulfonic acid (DBSA) needed to completely stabilize 1 wt% asphaltenes in different alkanes were measured. Figure 9 shows that the minimum concentration of NP for complete asphaltene stabilization decreases successively from pentane (24 wt%), to hexane (12 wt%), to heptane (7 wt%) and to dodecane and hexadecane (both 6.5 wt%). As opposed to NP, the effectiveness of DBSA amphiphiles to stabilize asphaltenes apparently increases with increasing the molecular weight of alkane molecules. The minimum concentration of DBSA to completely stabilize 1 wt% asphaltenes increases successively from pentane and heptane (both 3.5 wt%), dodecane (5 wt%) to hexadecane (11 wt%). This trend shows that alkane solvents with different molecular weights can influence the ability of both NP and DBSA amphiphiles to stabilize asphaltenes. These results might be due to the fact that different alkane solvents can contribute different entropic effect on the asphaltene-amphiphile interactions in the solution.

## **2.5 Stability of Different Asphaltenes in Amphiphile/Alkane Solutions**

The stability of different types of asphaltenes in amphiphile/alkane solutions were compared in this study in order to examine the general feasibility in employing amphiphile/alkane solutions to dissolve asphaltene deposits. Asphaltene materials were prepared from crude oil by following the procedures described in ASTM 2007D. Four asphaltene materials from different crude oil resources, called Mobil #0, Villano Field, Kuparuk, and West Sak asphaltenes, are used for this study (Table 1).



The solubility of the above-mentioned four asphaltenes in binary toluene/heptane solutions was measured. As illustrated in Figure 12, these asphaltene samples are gradually solubilized in the toluene/heptane solution as the volume percentage of toluene increases. When the volume percentage of toluene in the solution reaches 40-60 %, all of asphaltene samples

become completely solubilized. This trend suggests that all of the asphaltene samples prepared (by a similar procedure) display similar solubility parameters.

The effectiveness of both nonylphenol (NP) and dodecylbenzene sulfonic acid on the stabilization of three asphaltene samples, Mobil, Kuparuk and West Sak, was investigated. Figure 13 illustrates the solubility of these asphaltenes in heptane media containing different concentrations of NP amphiphile. One observes that the solubility of all of the asphaltene samples follows a similar function of the concentration of NP; that is, the solubility asphaltenes increases gradually with increasing NP concentration, and beyond 6-8 wt% NP in solution a complete solubilization of asphaltenes occurs.

Figure 14 shows the effectiveness of dodecylbenzene sulfonic acid (DBSA) on the stabilization of asphaltenes in heptane. All asphaltene samples, including Mobil, Kuparuk and West Sak asphaltenes, show an increment of solubility in heptane with increasing DBSA concentration. As DBSA concentration reaches 2 wt%, asphaltenes become completely soluble in heptane. Figures 13 and 14 clearly demonstrate that asphaltenes from different crude oils have a similar solubility behavior in NP/heptane and DBSA/heptane solutions. This trend indicates that the dissolution of asphaltene deposits using fluids composed of amphiphiles and alkanes is independent of the crude oil source. Furthermore, the fact that different asphaltenes also have a similar solubility behavior in toluene/heptane solutions further indicates that these asphaltene samples have similar polarities, i.e., solubility parameters. Therefore, asphaltene materials with similar polarities seem to be stabilized equally well in alkane media by amphiphiles.

## 2.6 Kinetics of Dissolution of Asphaltene Deposits by Amphiphile/Alkane Solutions

The purpose of this study is to identify the factors affecting the kinetics of asphaltene dissolution by fluids composed of amphiphiles and alkanes. The influence of the effect of the composition and flow rate of amphiphile/alkane fluids on the rate of dissolution of asphaltene deposits was systematically investigated. The major variables evaluated include the flow rate of micellar fluids, the fluid temperature, the concentration of amphiphiles in the fluid, the type of amphiphiles and solvents in the fluid. Experiments for each variable are detailed in Table 4. Mobil asphaltenes were used in this study. Two alkylbenzene-derived amphiphiles, dodecylbenzene sulfonic acid (DBSA,  $n\text{-C}_{12}\text{H}_{25}$    $\text{SO}_3\text{H}$ ) and nonylphenol (NP,  $n\text{-C}_9\text{H}_{19}$    $\text{OH}$ ), and five alkane solvents, ranging from hexane to hexadecane, were used in this study. These two oil-soluble amphiphiles have been proven to be effective in the stabilization of asphaltenes in alkane media (Chang and Fogler)[10-11]. All chemicals are commercially available and used directly for study without further purification.



In order to carry out this study, an experimental apparatus was established as illustrated in Figure 15. This apparatus includes a differential reactor to accommodate asphaltene deposits and a syringe pump to constantly inject the fluid in the syringe through the differential reactor to dissolve asphaltene deposits. In the dissolution experiments conducted at controlled temperatures, a water bath is used to accommodate the differential reactor. As shown in Figure 17, the differential reactor is modified from a filter holder with a diameter of 25 mm. This differential reactor appears as a circular disk with 22 mm in diameter and 3 mm in thickness. The edge of the reactor is made of an O-ring while both of the front and rear faces of the reactor are made of a pair of 0.45 micron Teflon filter membranes. These Teflon membranes are selected for this study because they are inert to any of the component in the micellar fluid, especially, dodecylbenzene sulfonic acid amphiphile. For each experiment, 0.025 gram of asphaltene powder is first placed in the reactor as the model deposit of asphaltenes. Asphaltene powders are loosely and uniformly placed in the reactor space so they can easily contact the micellar fluid. The micellar fluid is injected vertically upwards into the reactor at a constant flow rate. This upward flow ensures that any air remaining in the reactor can be completely displaced out of reactor by the micellar fluid at the initial stage of the experiment. The filter membranes at both ends of the reactor are permeable to the micellar fluid and the dissolved asphaltenes but impermeable to the undissolved asphaltene powder. Therefore, only the dissolved asphaltenes flow out of the reactor with the micellar fluid and are collected in glass vials. Afterwards, the concentration of asphaltenes in the effluent collected at different elution times is measured by the absorbance of light by the effluents at wavelength 400 nm using a UV/vis spectrophotometer.

**Kinetics Analysis** : In order to further analyze the kinetics and mechanism of asphaltene dissolution, we assumed that the rate of dissolution of asphaltene precipitates,  $r_D$ , was first order with respect to the undissolved asphaltene mass, i.e.,

$$-r_D = \frac{dM}{dt} = -k M \quad (1)$$

Integrating equation (1) gives

$$\ln \frac{M}{M_0} = -k t \quad (2)$$

where  $k$  is the apparent specific rate constant for asphaltene dissolution ( $\text{min}^{-1}$ ).  $M_0$  and  $M$  are the mass of asphaltene precipitates initially placed and that remaining undissolved at time  $t$ , respectively.

The results of these experiments are described below.

**2.6.1 Effect of Amphiphile Concentration** : The influence of the concentration of amphiphiles in the alkane-based fluid on the rate of dissolution of asphaltene deposits was studied using two types of amphiphiles, DBSA and NP, and two types of alkane medium, heptane and dodecane. The rate of fluid flow was fixed at 1 ml/minute and the experimental temperature maintained at 22°C.

Figures 17 and 18 show the profile of asphaltene dissolution as a function of NP concentration in heptane and dodecane, respectively. Both figures show that the rate of asphaltene dissolution in general increases with increasing the concentration of NP amphiphile. However, the trend of asphaltene dissolution with respect to NP concentration appears quite different at the concentrations of NP above and below 7 wt%. When the NP concentration is less than 7 wt%, asphaltene deposits are apparently not completely dissolved in the fluid. For example, the percent of asphaltene dissolved in the first 50 ml of the injected fluid increases gradually from 15%, 30% to 80% as the concentration of NP increases from 0 wt%, 2 wt% to 4 wt% of NP. This result indicates that the asphaltene sample used in this study has a distribution of solubility, and the less soluble fraction can only be dissolved in the fluid with higher NP concentrations. When the NP concentration is above 7 wt%, asphaltene deposits can be dissolved completely in the fluid. The rate of asphaltene dissolution seems to increase slightly with increasing the concentration of NP amphiphile, indicating that the concentrated NP amphiphilic molecules in alkane media expedite the process of dissolution of asphaltene deposits.

Figures 19 and 20 show the profile of asphaltene dissolution as a function of the concentration of DBSA in heptane and dodecane, respectively. Both figures show that the rate of asphaltene dissolution in general increases with increasing the concentration of DBSA amphiphile. Nevertheless, similar to the results of NP amphiphiles shown in Figures 17 and 18, the trend of asphaltene dissolution with respect to DBSA concentration appears quite different at the concentrations of DBSA above and below 3 wt%. When the DBSA concentration is less than 3 wt%, asphaltene deposits are apparently not completely dissolved in the fluid. For example, the percent of asphaltene dissolved in the first 50 ml of the injected fluid increases gradually from 15% to 33% as the concentration of DBSA increases from 0 wt% to 1 wt%. When the DBSA concentration is above 3 wt%, asphaltene deposits can be dissolved completely in the fluid. The rate of asphaltene dissolution apparently increases gradually with increasing the concentration of DBSA amphiphile, indicating that the concentrated DBSA amphiphilic molecules in alkane media expedite the process of dissolution of asphaltene deposits.

Comparing both Figures 17 and 18 with Figures 19 and 20, one observes that both amphiphiles effectively dissolve asphaltene precipitates in dodecane solutions. However, the

minimum concentrations of NP and DBSA for completely dissolving asphaltene deposits are 7 wt% and 3 wt%, respectively. These values are consistent with the stability of asphaltenes in the amphiphile/alkane solutions reported previously by Chang and Fogler (1994). The NP-asphaltene association is significantly weaker than the DBSA-asphaltene association. Therefore, a higher concentration of NP amphiphiles is needed to provide a sufficient attractive interaction with asphaltene molecules to sterically stabilize them in the solution. Figures 17-20 also show that when the concentration of amphiphiles is higher than the minimum value for completely dissolving asphaltenes, the increment in the rate of asphaltene dissolution with increasing the amphiphile concentration appears more pronounced with DBSA solutions than with NP solutions.

The data in the dissolution curves were replotted in Figures 26 thru 28 in terms of the logarithm of undissolved asphaltene mass fraction [ $\ln (M/M_0)$ ] versus time (see equation (2)). As shown in these figures, for most of dissolution curves, [ $\ln (M/M_0)$ ] decreases essentially linearly with time in the early reaction period, indicating the adequacy of the first reaction order assumption. However, for low amphiphile concentrations that asphaltenes are not completely soluble, [ $\ln (M/M_0)$ ] deviates from the linear decay trend as the reaction time is increased. These deviations could be attributed to the fact that the un-dissolved asphaltene fraction is taken into account in equation (2), leading to positive deviations of the dissolution data from the linear curve.

The specific dissolution rate constant,  $k$ , calculated from the slope of linear fitting to the initial [ $\ln (M/M_0)$ ]-versus-time data points for Figures 17 to 20 were plotted in Figures 29 and 30. Figure 30 shows that for both DBSA/heptane and DBSA/dodecane solutions, the  $k$  value increases significantly at low DBSA concentrations and gradually levels off at about  $0.11 \text{ min}^{-1}$  when the DBSA concentration in heptane and dodecane reaches 0.06 M and 0.1 M, respectively. Figure 29 shows that the  $k$  value for both NP/heptane and NP/dodecane solutions also increases with increasing the NP concentration. Above 0.3 M of NP, the  $k$  value becomes virtually constant at 0.25 and  $0.1 \text{ min}^{-1}$  for heptane and dodecane, respectively. Overall, the  $k$  value of each amphiphile solution increases steadily at lower amphiphile concentrations and levels out at higher amphiphile concentrations. This trend suggests that the variation of  $k$  with respect to the amphiphile concentration can be described by a Langmuir-Hinshelwood kinetics (Fogler, 1992)

$$k = \frac{k_{\infty} [S]}{K_s + [S]} \quad (3)$$

where  $[S]$  is the concentration of amphiphile in solution. This Langmuir-Hinshelwood equation shows that  $k$  is first and zero order with respect to  $[S]$  at low and high concentrations,

respectively.  $k_{\infty}$  and  $K_S$  are the adjustable parameters in equation (3). For data points of Figures 29 and 30, the fitted values of  $k_{\infty}$  and  $K_S$  are listed in Table 5.

**2.6.2 Effect of the Type of Amphiphiles** : Two amphiphiles, nonylphenol and dodecylbenzene sulfonic acid, were used in the alkane media for the dissolution of asphaltene deposits. As illustrated in Figures 17 to 20, both amphiphiles are effective to the dissolution of asphaltene deposits. However, the minimum concentration of NP and DBSA for completely dissolving asphaltene deposits is 7 wt% and 3 wt%, respectively. These results are very consistent with the stability of asphaltenes in the amphiphile/alkane solutions studied previously, and they can be explained by the strength of the associative interaction between amphiphiles and asphaltenes. As shown in the third quarter, the NP-asphaltene association is significantly weaker than the DBSA-asphaltene association. Therefore, a higher concentration of NP amphiphilic molecules in solution is needed to provide a sufficient attractive interaction with asphaltene particles in order to dissociate them from asphaltene deposits. Figures 17 to 20 also show that when the concentration of amphiphiles is higher than the minimum value for completely dissolving asphaltenes, the rates of asphaltene dissolution by NP solution and by DBSA solution appear similar. In general, it requires 30-50 ml of both amphiphile solutions to completely dissolve asphaltene deposits in the differential reactor. However, one also observes that the increment of the rate of asphaltene dissolution with increasing the concentration of amphiphiles appears more pronounced with DBSA solutions than with NP solutions.

**2.6.3 Effect of Alkane Solvent** : Two types of alkane solvents, heptane and dodecane, were used to prepare micellar fluids for the dissolution of asphaltene deposits. Figures 17 to 20 show that for both NP and DBSA amphiphiles, the rate of asphaltene dissolution by heptane-based fluids is in general faster than that by dodecane-based fluids. For example, to dissolve 80 % asphaltene deposits requires 5 ml of heptane media with 10 wt% NP while it requires 20 ml of dodecane media containing 10 wt% NP. Similarly, the amount of alkane media with 10 wt% DBSA required to dissolve 80% asphaltene deposits is 8 ml for heptane and 15 ml for dodecane. The fact that the rate of asphaltene dissolution in heptane is faster than that in dodecane can be attributed to the different fluidity of these two alkane solvents. The viscosity of heptane is significantly lower than that of dodecane. Therefore, heptane can penetrate into the porous asphaltene deposits to mobilize the deposits more quickly and easily than dodecane. Overall, the results of this study indicate that the type of alkane solvents has a significant effect on the rate of asphaltene dissolution.

A wider study on the effect of alkane solvent of amphiphile solutions on the rate of asphaltene dissolution was then investigated using a homologue of alkanes, from hexane (C6) to

hexadecane (C16). The profile of asphaltene dissolution by 5 wt% DBSA alkane solutions is shown in Figure 21. These dissolution profiles were replotted in Figure 22 using Equation (2). The values of  $k_{\infty}$  calculated from the rate of asphaltene dissolution were then plotted in logarithm as a function of the viscosity ( $\mu$ ) of alkane solvents (Figure 32, which also includes a similar set of data with 20 wt% NP). As shown in Figure 22, the rate of asphaltene dissolution decreases significantly with increasing the chain length of alkane solvent molecules. From the slope of the plot (Figure 32), we found that  $k_{\infty} \sim \mu^{-0.5}$  where  $\mu$  is the viscosity (in cP) of alkane solvent. Therefore, the rapid rate of asphaltene dissolution occurring in light alkane solvents, such as hexane, can be attributed to the low solvent viscosity compared to that of heavy alkanes, such as dodecane and hexadecane. In the less viscous light alkanes, asphaltenes and amphiphiles have larger diffusivities to undergo faster mass transfer and inter-molecular collisions to facilitate the process of asphaltene dissolution.

**2.6.4 Effect of Flow Rate of Micellar Fluid** : The effect of the flow rate of micellar fluids on the rate of asphaltene dissolution is illustrated in Figure 25. Under two different rates of flow of a heptane-based fluid containing 20 wt% NP amphiphiles, 0.1 and 1 ml/minute, the profiles of asphaltene dissolution appear much more closely overlapped with each other if they are plotted as a function of the dissolution time rather than as a function of the accumulated elution volume of micellar fluids. This result indicates that the flow rate of micellar fluids in this flow rate range does not significantly affect the rate of asphaltene dissolution. Since the internal diffusion of micellar fluids in the porous asphaltene deposit is weakly dependent on the rate of external fluid flows, it is derived that this internal diffusion process is of primary importance in the rate of dissolution of asphaltene deposits. At the same time, the slight increase in the rate of asphaltene dissolution with increasing flow rate of fluids suggests that the convective mass transfer of species between bulk fluids and the surface of asphaltene deposits is also a factor in the rate of asphaltene dissolution. Increasing the flow rate reduces the thickness of fluid boundary layer around the asphaltene precipitates and therefore enhances the rate of mass transfer between fluids and asphaltene surfaces. In addition, higher flow rates may enhance the movement of fluids within porous asphaltene deposits and expedite the mobilization of asphaltene deposits.

**2.6.5 Effect of Temperature** : The effect of temperature on the rate of asphaltene dissolution was studied using amphiphile/alkane solutions which contain sufficient amphiphiles to dissolve asphaltene completely. Figures 23 and 24 show the time evolution profiles of asphaltene dissolution by dodecane-based fluids containing NP and DBSA, respectively. It is clear that the rate of asphaltene dissolution increases significantly with increasing fluid temperature. For example, when the temperature increases from 6°C, 22°C to 58°C, the volume of the injected

fluid required to dissolve 80% asphaltene deposits decreases from 40 ml to 16 ml to 8 ml. The data in Figure 24 are replotted in Figure 28 using the parameter  $[\ln (M/M_0)]$ . One observes that  $[\ln (M/M_0)]$  decreases rapidly with the reaction time as temperature is increased. The  $k_\infty$  value obtained from the slope of linear fitting to the initial data points was then plotted according to the Arrhenius equation as shown below

$$k_\infty = A \exp\left(-\frac{E_A}{RT}\right) \quad (4)$$

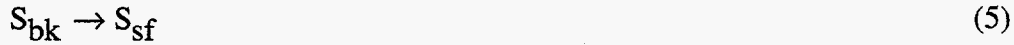
where A is the pre-exponential constant, R is 1.987 cal/mole °K, ideal gas constant, and  $E_A$  is the activation energy.

Figure 31 shows the logarithm of  $k_\infty$  as a function of  $1/T(^{\circ}\text{K})$ . One observes that the experimental data was linearly fitted reasonably well, suggesting the dependence of the  $k_\infty$  value on temperature could be represented by Arrhenius kinetics. The activation energy,  $E_A$ , calculated from the slope of the linear fitting was approximated to be 3.99, 6.92, 3.98 and 3.81 kcal/mole for the dissolution of asphaltene by NP/heptane, NP/dodecane, DBSA/heptane and DBSA/dodecane solutions, respectively. These measured activation energies are fairly close to the typical values of intermolecular hydrogen bonding (in the range of 3-7 kcal/mol) and charge transfer associations (generally less than 8 kcal/mole) that may occur between asphaltene molecules or between asphaltenes and polar molecules, e.g. phenol. Hence, it is inferred that the rate of asphaltene dissolution is significantly affected by reactions on the surface of asphaltene precipitates which involve the transition from asphaltene-asphaltene associations to asphaltene-amphiphile associations through the redistribution of inter-molecular hydrogen bonding and charge transfer interactions. At higher temperatures, asphaltenes and amphiphiles not only possess higher kinetic energies to overcome the reaction activation energy barrier but also have larger diffusivities to undergo higher molecular collisions to bring about asphaltene dissolution. In addition, the mass transfer of asphaltenes and amphiphiles between the precipitated asphaltene surface and the contact fluid may also be a cause of the temperature-dependent asphaltene dissolution rate. This mass transfer process usually has an apparent activation energy of 2-3 kcal/mole due to the temperature-dependent viscosity of solvent and diffusivity of reacting species.

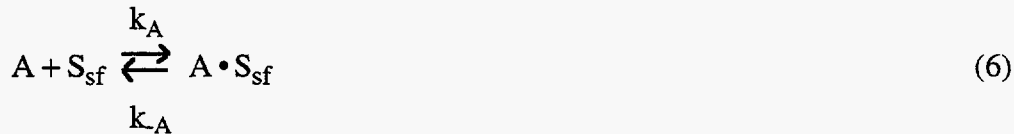
Overall, the results of this study demonstrate that the rate of dissolution of asphaltene precipitates and deposits can be affected significantly by the type and concentration of amphiphiles, the type of solvents, fluid temperature and flow rate. All of these variables have to be considered in designing and evaluating new chemical treatments for alleviating damages resulting from asphaltene precipitation and deposition in oil production reservoirs and pipelines.

## 2.7 Discussion of First Order Model for Asphaltene Dissolution

The dissolution of solid asphaltene precipitates and deposits by amphiphile/alkane fluids involves both mass transfer and surface reaction processes. As shown in Figure 33(a), the dissolution of asphaltenes involves the following steps [12]. For asphaltene dissolution, the amphiphile is first transported from the bulk liquid to the asphaltene surface



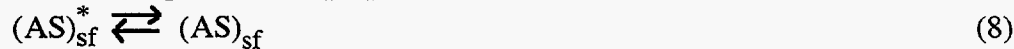
where  $S_{sf}$  and  $S_{bk}$  are amphiphiles at the asphaltene surface and in the bulk fluid, respectively. Subsequently, the amphiphile near asphaltenes adsorbs to the functional site on asphaltene surfaces



where  $A$  represents the functional site on the asphaltene surface to which the amphiphile can adsorb.  $A \cdot S_{sf}$  denotes the amphiphile molecule adsorbed to the surface. After adsorption, the amphiphile may cause the formation of the amphiphile-asphaltene transition state complex,  $(AS)_{sf}^*$ , as shown below



Afterwards, this asphaltene-amphiphile complex desorbs from the asphaltene surface



and transported to the bulk liquid



where  $(AS)_{sf}$  and  $(AS)_{bk}$  are the asphaltene-amphiphile associated complex at the asphaltene surface and in the bulk fluid, respectively.

The fact that the rate of asphaltene dissolution follows a Langmuir-Hinshelwood kinetics as a function of amphiphile concentrations [as shown by experimental results and equation (3)] indicates that the surface reaction step (equation (7)) may be assumed to be rate-limiting with respect to the adsorption and desorption steps (equations (6) and (8)). Hence,

$$[A \cdot S_{sf}] = K_A [A] [S_{sf}] \quad (10)$$

with  $K_A = k_A/k_{-A}$ . For the first order model, we have assumed the total number of functional sites on asphaltene surfaces is proportional to the mass of undissolved asphaltenes and is the sum of the bound and unbound sites. That is,

$$M = [A] + [(AS)_{sf}] = [A] + K_A [A] [S_{sf}] \quad (11)$$

$$[A] = \frac{M}{1 + K_A [S_{sf}]} \quad (12)$$

Then, the rate of asphaltene dissolution becomes

$$-\frac{dM}{dt} = k_r [A \cdot S_{sf}] = k_r K_A [A] [S_{sf}] = k_r K_A \frac{M [S_{sf}]}{1 + K_A [S_{sf}]} = k M \quad (13)$$

which is a Langmuir-Hinshelwood form as that observed experimentally and represented by equation (3). This Langmuir-Hinshelwood model indicates that the extent of amphiphile adsorption to asphaltene surfaces dictates the rate of asphaltenes in amphiphile/alkane solutions. At low amphiphile concentrations, the amount of amphiphiles adsorbing to asphaltenes increases linearly with increasing the concentration of amphiphiles; hence, the rate of asphaltene dissolution increases correspondingly. At sufficiently high amphiphile concentrations, most functional groups having hydrogen bonding or charge transfer interactions on asphaltene surfaces are already bound with amphiphiles; therefore, the rate of asphaltene dissolution cannot be further increased with further raising the amphiphile concentration.

On the other hand, the fact that the asphaltene dissolution rate is influenced by the flow rate and the viscosity of alkane solvents implies that the convective mass transfer of reacting species (asphaltenes and amphiphiles) between bulk fluids and the surface of asphaltene solid (equations (5) and (9)) may also be important to the rate of asphaltene dissolution (Fig 33(b)). The rate of mass transfer for amphiphiles can be described as

$$-\frac{dM}{dt} = k_c ([S_{bk}] - [S_{sf}]) \quad (14)$$

and that for dissolved asphaltenes is

$$-\frac{dM}{dt} = k_c ([AS]_{sf} - [AS]_{bk}) \quad (15)$$

where  $k_c$  is the mass transfer coefficient for amphiphiles and asphaltenes between solid asphaltene surfaces and the bulk fluid. For a spherical solid asphaltene precipitate,  $k_c$  can be approximated as

$$k_c = 2 \frac{D_s}{d_A} + 0.6 \frac{(D_s)^{1/2} (U)^{1/2}}{(v)^{1/6} (d_A)^{1/2}} \quad \text{where } v = \frac{\mu}{\rho} \quad (16)$$

where  $\mu$  is the viscosity of fluid.  $\rho$  is the density of fluid.  $D_s$  is the diffusivity of reacting species.  $U$  is fluid velocity, and  $d_A$  is the size of asphaltene precipitates.

Equation (16) shows that the rate of asphaltene dissolution increases with increasing the velocity of fluid,  $U$ , and the diffusivity of reacting species,  $D_s$ , but decreases with increasing the solvent viscosity,  $\mu$ . The higher rates of asphaltene dissolution at higher temperatures result from the enhancement of mass transfer processes. At higher temperatures, the viscosity of solution is decreased and the diffusivity of amphiphiles and asphaltenes is increased, leading to a higher rate of transport of amphiphiles towards the asphaltene precipitates and a higher rate of transport of the dissolved asphaltenes towards the bulk fluid.



In summary, the results of this experimental study reveal that pentane-insoluble asphaltene precipitates are comprised of asphaltene molecules aggregating together through fairly weak hydrogen bonding or charge transfer associations. As a consequence, dissolution of asphaltenes occurs under a Langmuir-Hinshelwood surface reaction and a mass transfer process.

## 2.8 Visualization of Asphaltene Dissolution in Micromodel

In this experiment, we experimentally simulated in-situ asphaltene plugging phenomena using an etched glass micromodel apparatus as depicted in Figure 34. Etched micromodels are a set of two dimensional inter-connected flow channels imbedded in two fused glass plates. Micromodels offer the advantage in that one can visualize mechanisms actually occurring in (two-dimensional) porous media. The micromodels used for these experiments were fabricated in-house to a desired pore pattern.

All the tubing used in this apparatus was 1/16 in. dia high pressure tubing. The processes occurring in the micromodel were observed through the use of a stereo-zoom microscope and recorded using a super VHS video recorder. The effect of amphiphile solutions on asphaltene dissolution in the glass micromodel was investigated by measuring both the differential pressure across the column and the concentration of asphaltenes in the effluent.

A syringe pump (Harvard Apparatus 22) was used to flow desired fluids into the micromodel via two inlet streams. The temperature of micromodels was controlled by a heating tape connected with a transformer.

**2.8.1 Results** : Asphaltene plugging in the near-wellbore formation results from the continuous accumulation of asphaltenes that become unstable and precipitate inside the pore space of formations where the change of temperature, pressure and fluid compositions of crude oil occurs. The concentration of precipitated asphaltenes may be low in crude oil (or reservoir fluids); however, the massive flow of crude oil toward production wells causes significant accumulation of deposited asphaltenes inside the near-wellbore formation, leading to the eventual blocking of the formation.

**2.8.8.1 Precipitation of Asphaltenes in Micromodel:** As shown in Figure 35, two fluids were injected simultaneously and continuously into two inlets; one fluid (A) is a solution containing stabilized asphaltenes, e.g., 2% asphaltene in 10% NP in dodecane, and the other fluid (B) is a poor solvent to asphaltenes, e.g., dodecane. The flow rates of these two fluids are controlled independently. The mixing of asphaltene solution and poor solvent in the inlet region of micromodels causes asphaltenes to become unstable and precipitate out of solution. Figure 18 illustrates the light micrographs of asphaltene precipitation and deposition inside a glass micromodel at different times. The mixing of two fluids in the inlet zone de-stabilizes

asphaltenes and induce them to flocculate and precipitate out of solution. The size of flocculated asphaltenes are significantly small compared with the size of pore throats. Therefore, in the early stage of asphaltene precipitation, asphaltene flocs are deposited onto pore surfaces mainly by the deep-bed filtration mechanism. That is, asphaltenes are predominately captured at pore throats and eventually shrink and close these pore throats as shown in Figure 36(a). Subsequently, precipitated asphaltenes are easily strained at pore bodies and gradually deposit and fill out the entire pore space as shown in Figure 36(b)-(d). From the difference in pressure across micromodels, it was also found that due to asphaltene plugging the final permeability of micromodels were reduced by about two order of magnitude.

**2.8.8.2 Asphaltene Dissolution in Micromodel.** The micromodel containing asphaltene deposits was then used in the asphaltene dissolution experiment. As shown in Figure 37, two amphiphiles/alkane fluids, NP/heptane and DBSA/hexane solutions, were successively injected into this micromodel at a flow rate about 1 pore volume/min. The concentration of asphaltenes eluted out of micromodels was then measured in conjunction with recording the microscopic image of asphaltene dissolution process inside micromodels.

In the first stage, 10 wt% nonylphenol/heptane solution (Fluid A) was injected into micromodel. As shown in Figure 38, after the NP/heptane solution was injected by 10 pore volumes, the asphaltene deposit starts to dissolve quickly. A dissolution peak appearing at 50 pore volumes corresponds to asphaltenes dissolved by the NP/heptane solution. After the first peak, the concentration of eluted asphaltenes decreases gradually between 60 and 100 pore volumes. The process of asphaltene dissolution by NP/heptane solution was also shown by the pictures in Figure 39. Figure 39(a) shows that a wormhole-like flow channel was first formed across the asphaltene deposit zone. The NP/heptane fluid flows preferentially along this wormhole-like flow channel and asphaltenes deposited next to the channel are gradually dissolved. The continual dissolution of asphaltenes results in the shrinkage of deposited area as well as the formation of new flow channels. At this period, as shown in Figure 39(b) and (d), two types of asphaltene deposits in the micromodel was observed; One deposit appears cluster-like and the other is island-like. The NP/heptane fluid was able to dissolve the island-like asphaltene deposit efficiently; however, it was not effective on the cluster-like asphaltene deposit.

The reason of the presence of two different asphaltene deposits in the micromodel can be realized from the experiment of asphaltene deposition in micromodels. As explained previously, we found that the process of asphaltene deposition can be separated into two stages. Before the permeability of micromodels was significantly reduced (first stage), the more soluble asphaltenes were either still remaining in the fluids, or attached loosely to the deposits and carried away by the fluids. Only the asphaltenes that were less soluble and strongly attached were deposited in

the micromodel. After the pore throats inside micromodel was plugged by deposited asphaltenes, not only the less soluble asphaltenes but also the more soluble asphaltenes were strained at the plugged pore throats (second stage). Therefore, the cluster-like deposits were formed in the first stage, and the island-like deposits were generated in the second stage. This deposition mechanism also explains why the solubility of cluster-like deposits are less soluble than the island-like deposits. It is believed that this deposition mechanism may also occur in the actual damaged reservoir formation around production wells.

Due to the fact that cluster-like asphaltene deposits cannot be dissolved by the NP/heptane fluid, in the second stage of experiment, a 5 wt% DBSA/hexane solution (Fluid B) was injected into micromodel starting at 100 pore volumes. The remaining cluster-like asphaltenes were dissolved immediately and completely, as indicated by the second peak centered at pore volume 125 and by the microscopic pictures shown in Figures 39(a)-(d). After the treatment, the deposited asphaltenes in the micromodel were completely removed.

## **2.9 Dissolution of Asphaltenes in Model Porous Media**

The setup of the experiment, as shown in Figure 40, involved a glass tube acting as the packed bed, a differential pressure transducer, two accumulators and a personal computer with a data acquisition board. The packed bed was filled with asphaltene and silica gel using a ratio of 1:9 in grams. The glass tube and the mixture were first wetted with pure heptane separately, then the mixture was added to the glass tube. The glass tube was well packed to leave no air inside. The fluids used in the experiment were contained in two accumulators. The first accumulator contained 200 ml of poor solvent to asphaltene, pure heptane; the second accumulator contained 300 ml of good solvent (to asphaltene, usually different percentages of DBSA or NP with heptane). The differential pressure between the inlet and outlet of the packed bed was measured by a differential pressure transducer and the data was transmitted through a data acquisition board to a personal computer. The effluent was collected using a fraction collector. The experiments usually lasted about 2 to 3 hours.

The experiments were carried out at room temperature with two different flow rates: 1 ml/min and 5 ml/min. Each set of experiment involved poor and good solvent. The first part of the experiment required the usage of pure heptane. For flow rate of 1 ml/min, pure heptane was usually run for 30 minutes before switching to good solvent and the effluent was collect every 5 minutes. For flow rate of 5 ml/min, pure heptane was usually run for 6 minutes before switching to good solvent, and the effluent was collect every 1 minute.

The concentration of asphaltene was measured from the absorbance of the effluent using a UV spectroscopy with a wavelength of 400 nm. About 15 vials of effluent were used to

construct a concentration profile for a set of experiment, and the concentration profile was plotted along with a differential pressure profile for a given set of experiment.

**2.9.1 Results :** The rate and total amount of asphaltenes dissolved in the solution effluent are shown in Table 6 and Figures 41 to 47. One observes that asphaltenes in the packed-bed column were not dissolved in the heptane fluids; whereas after the fluid was switched to amphiphile solutions, the dissolution of asphaltenes took place. The concentration of asphaltenes in the effluent started to increase after the amphiphile solution was flown through the column for volume of 10-20 ml. This volume corresponded to the fluid space inside the flow system between the accumulator for good solvent and the outlet for effluent. Most of asphaltene dissolution in NP/heptane solutions occurs over a fluid volume of 60 ml (Figures 41 to 44), whereas the dissolution of asphaltenes in DBSA/heptane solutions lasts for 150-200 ml (Figures 45 to 47). This result indicates that the rate of asphaltene dissolution in NP/heptane solutions was faster than that in DBSA/heptane solutions.

The difference in asphaltene dissolution rates between NP and DBSA amphiphile solutions may be due to the interactions between amphiphiles and silica gel. The highly polar DBSA amphiphile attaches strongly to the silica gel surface through acid-base interaction (including hydrogen-bonding). As a result, the residence time distribution of DBSA in the silica gel bed is significantly increased and broadened as to delay the dissolution of asphaltene out of column. As compared to DBSA, the less polar NP amphiphile with a weaker associative interaction with silica gel appears traveling faster inside the bed and accessing the entire pore space of the bed more quickly. Therefore, the rate of asphaltene dissolution out of the column appears faster for NP than for DBSA amphiphiles. In addition, one observes that the maximum asphaltene concentration in the effluent was in general higher for the flow rate of 1 ml/min than for 5 ml/min. This trend may be due to the fact that under a slower flow rate, the amphiphile fluids reside in the bed for a longer time period and thus dissolve more asphaltenes into the solution.

Table 6 summarizes the total amount of asphaltene dissolved in the effluent under different flow rates and different concentration of amphiphiles. The amount of asphaltenes eluted from the packed bed initially containing around 0.85 gram asphaltenes is in the range between 0.2 and 0.8 gram. For both NP and DBSA amphiphiles, the amount of dissolved asphaltene in general increases with increasing the concentration of amphiphile. This trend indicates that the solubility of asphaltenes in fluids was higher at higher concentration of amphiphiles. The adsorption of amphiphiles to silica gel also results in the decrease of amphiphile concentration in the fluid and, hence, reduces the effectiveness of amphiphile solution to the dissolution of asphaltene deposits.

The differential pressure across the packed bed during asphaltene dissolution is shown in Figure 41 to 47. In general, the differential pressure across the bed decreases after asphaltene dissolution. The extent of decrease in differential pressure varies with the type and concentration of amphiphiles. NP/heptane solutions appear more effective to the recovery of packed-bed permeability (i.e., the decrease in differential pressure) than DBSA/heptane solutions.

One also observes that a fairly sharp peak appears in the differential pressure profile after the fluid is switched from heptane to amphiphile/alkane solution. The appearance of this peak can be due to the dissolution and movement of asphaltenes inside the silica gel packed bed. At the start of asphaltene dissolution, the asphaltene near the inlet of the packed bed is first dissolved and carried by the amphiphile/heptane fluids. The front face of amphiphile fluids moves along the bed and accumulates more and more dissolved asphaltenes, which eventually becomes sufficiently concentrated as to reduce the local bed permeability in the down-stream region and, hence, cause a sharp differential pressure peak. Once this fluid front moves out of the packed bed, the permeability is recovered and the differential pressure across the bed further decreases gradually until reaching a final steady value. In a reference study using a silica gel packed bed without containing any asphaltene deposits, the differential pressure across the bed, as shown in Figure 48, is quite stable without the appearance of the sharp peak as the injection fluid switches from heptane to amphiphile/heptane solutions. This result further indicates that the differential pressure peak occurring in Figures 41 to 47 is due to the process of asphaltene dissolution.

These experimental results illustrate that asphaltene deposits can be removed from porous media using oil-soluble amphiphile/alkane solutions. It also indicates that the efficiency of removing asphaltene deposits increases with the strength of the amphiphiles. DBSA has greater ability to dissolve asphaltene deposits than NP. In addition, the type of alkane solvent used with amphiphiles are also important to the asphaltene dissolution efficiency because the lighter alkane, such as hexane, can provide more entropic energy for asphaltene dissolution than the heavier alkane, such as heptane. In addition, the rate of mass transfer in the lighter alkane solvents with low viscosities is significantly higher than that in heavier alkanes with high viscosities, leading to the faster asphaltene dissolution in lighter alkane solutions.

## **2.10 Fractionation of asphaltenes**

Fractionation of asphaltenes into components of different polarities provides a way to characterize asphaltenes. Since asphaltenes are known to be composed of a variety of different functional groups and heteroatoms, separation of the asphaltene sample into components of different polarities provides a methodical way to study asphaltene structure. The additive effects

of the individual fractions may give a better picture of the unfractionated asphaltene. Characterization studies and dissolution experiments were carried out on the fractions obtained.

**2.10.1 Fractionation Procedure** : Asphaltene obtained by precipitation from crude oil by the addition of heptane was fractionated into components of different polarities by using a binary mixture of  $\text{CH}_2\text{Cl}_2$  (polar) and pentane (non-polar). As the amount of the non-polar liquid is increased in the binary mixture, the polar effect of  $\text{CH}_2\text{Cl}_2$  decreases. The asphaltene fractions which precipitate out first are the more polar fractions, followed by precipitation of less polar fractions upon addition of more pentane.

In this procedure, unfractionated asphaltene powder from Mobil #0 crude is completely dissolved in 10 times by weight of  $\text{CH}_2\text{Cl}_2$ . Pentane is now added slowly upto a composition 50%  $\text{CH}_2\text{Cl}_2$  (v/v). No asphaltenes are precipitated upto this composition. More pentane is now added to make the composition 70:30 pentane :  $\text{CH}_2\text{Cl}_2$ . The solution is magnetically stirred for one hour at room temperature. It is then left undisturbed at room temperature for 30 minutes and subsequently vacuum filtered using a Whatman no.4 filter paper on a fritted glass filter. The asphaltenes so precipitated are the first fraction F1 (or F30/70). More pentane is now added to the filtrate to make the composition 75:25 pentane :  $\text{CH}_2\text{Cl}_2$ . After a similar procedure of mixing and settling, the solution is filtered to yield the second fraction of asphaltenes F2 (or F25/75). Similarly, taking the filtrate in each case, the third and fourth fraction F3 (or F20/80) and F4 (or F10/90) are obtained at compositions 80:20 and 90:10 pentane :  $\text{CH}_2\text{Cl}_2$ .

**2.10.2 Characterization of Fractions** : Characterization was carried out for F1 and F4, the most polar and least polar fractions. Since these two fractions are the extremes, comparing them with each other is expected to provide some useful results.

**2.10.2.1 Yield.** The yield of fractions (Fig. 49) shows significant differences in amounts of the fractions. It is noticeable that over 70% of unfractionated asphaltenes originally dissolved in  $\text{CH}_2\text{Cl}_2$  do not precipitate out at 90:10 pentane :  $\text{CH}_2\text{Cl}_2$ . This may be due to the reason that some of the precipitate particles are small enough for Brownian motion to dominate and they do not aggregate in the solution in the time period of 30 minutes.

**2.10.2.2 Physical appearance.** The asphaltene fractions vary in appearance from shiny, dense black particles (F1) to dull, less dense brown powder (F4). Light microscope pictures of unfractionated asphaltene and the fractions can be seen in Fig. 50 (a-f). The pictures reveal the macrostructures of the fractions to be noticeably different from each other.

**2.10.2.3 SEM.** Scanning electron microscope pictures of the asphaltene fractions show clear distinctions in the microstructure of the two fractions as well (Fig. 51). Fig. 51 (a) shows

planar, defined surfaces on the unfractionated asphaltene particle. Fig. 51(b) & 52(a) reveal planar surfaces in the more polar fraction F1, indicating that an ordered structure may be present. Fig 51(c) & 52(b) reveals F4 to have an undefined, highly porous structure. The high porosity of F4 explains its lower density and higher surface area (see below).

**2.10.2.4 B.E.T. Surface Area.** Surface areas of the unfractionated asphaltene and fractions F1 and F4 were measured using a Micromeritics ASAP 2010 apparatus which measures the absorption of  $N_2$  gas at 77K to calculate the surface area by the Brunauer-Emmett-Teller method. The first two columns of Table 8 list the specific surface area for the three samples.  $A_{sp}$  for F4 is much higher than for F1 and for the unfractionated asphaltene, confirming the observations from the SEM about the high porosity of F4.

**2.10.3 Dissolution Studies** : Studies of dissolution kinetics were carried out on unfractionated asphaltene powder and fractions F1 and F4 (most polar and least polar fraction, respectively). The same apparatus described earlier in this report was used for the dissolution studies. 0.025 grams of asphaltene powder was used in each experiment. The solvent used was 10% by wt DBSA in heptane at a flow rate of 5 ml/min. The temperature in each experiment was 22°C.

Fig. 53 shows the asphaltenes dissolved as a function of accumulated volume. The most polar fraction F1 does not dissolve completely, even after 90 ml of accumulated solvent. Fraction F4 dissolves very quickly compared to F1. The rate of dissolution of unfractionated asphaltene is between that of F1 and F4 (the kink in the observation points for F1 is due to changing the syringe at that point). This result indicates that polarity of the asphaltene plays a crucial role in the rate of dissolution of the asphaltene using amphiphile / alkane solutions.

Fig 54 shows data analysis for the rate of asphaltene dissolution using the first-order dissolution model mentioned previously. The first-order model provides a satisfactory fit to the experimental data.

Dissolution runs were conducted at different temperatures for fraction F1 (since F1 is more difficult to dissolve, more effort was concentrated on the behaviour of F1). The apparatus shown in Figures. 15-16 was used. The solvent used was 10% w/w DBSA in heptane at a flow rate of 5 ml/min. An amount of 0.025 g. of asphaltene powder was used in each run. The runs for F1 were conducted at different temperatures (1, 3, 6.8, 12.8, 14.3, 16, 22, 58°C). The results are shown in Fig. 55.

It was observed that at a temperature of 1°C, F1 does not dissolve even partially in the DBSA/ heptane solvent. F1 showed no dissolution at a temperature of 3°C too. This indicates that high energies are required to break the asphaltene-asphaltene bonds in fraction F1. It appears that still enough thermal energy is not available to break these bonds and allow dissolution. There is still no dissolution of F1 at a temperature of 6.8°C. Dissolution of F1 is noticeable but

still quite small at 12.8°C. At 14.3°C, an S-shaped dissolution curve is obtained for F1 which clearly does not represent first-order kinetics. There appears to be a "lag" in the dissolution of F1. This same behaviour appears in the dissolution curve for F1 at 16°C. The dissolution curve of F1 at 22°C does not display this "lag" phase and seems to satisfy first-order kinetics.

The lag observed at 14.3 and 16°C may be caused by the time taken at lower temperatures for surface equilibrium to be attained. Since at lower temperatures the diffusion coefficient would decrease, lowering the mass transfer coefficient, the system would take a longer time to attain surface equilibrium. At higher temperatures (22, 58°C) the system attains surface equilibrium in so short a period of time that the lag phase does not appear in the experimental data.

**2.10.4 Discussion of results** : The two fractions F1 and F4 displayed markedly different properties. F4, the least polar fraction displays the highest surface area. This is partly reflected in the greater rate of dissolution compared to F1 and the unfractionated asphaltene. However, the increase in the rate of dissolution does not correspond to the increase in surface area. Table 8 shows the specific reaction rate constants for the fractions calculated from the experimentally determined rate first order rate constants. After taking the surface area into account, F1 still has a much lower reaction rate constant than F4, proving that the difference in kinetics of dissolution of the two fractions are inherently different and are not purely a result of difference in surface areas. In addition, the pore size distribution in F4 may play a role in limiting the access of the amphiphile species to the entire surface area of F4.

The kinetics of dissolution of F1 at lower temperature display a "lag" phase. It is suggested that this "lag" is due to the lower values of mass transfer coefficients at low temperatures, thus causing the system to take more time to attain full coverage of the asphaltene surface by the amphiphilic species. This effect needs to be studied further to be fully understood.

Fractionation seems to be a good method of characterizing asphaltenes. As seen in the next section, fractionation proves to be a powerful tool in determining the polarity of asphaltene: if an asphaltene yields more of the higher polarity fraction through one procedure than the other, it means the asphaltene itself is more polar when precipitated through the former procedure (due to the additive effect of the fractions).

## **2.11. Sludge precipitation using acid system**

Sludge precipitation from crude oil in the presence of ferric ions during matrix acidizing is an important problem in formations [6, 13,14]. Properties of sludge precipitated from Venezuelan crude by contacting with an acid/  $Fe^{3+}$  system were studied in much detail. The acid system was prepared by adding 3000 ppm of  $FeCl_3$  to 100 ml of acid (HCl) and heating to 85° C.



The acid system was then mixed with 100 ml of crude oil (also at 85°C) and vigorously stirred for 30 minutes. The mixture was allowed to sit for at least one hour. On separation into sludge and a liquid phase, the liquid phase was decanted and the sludge was then mixed with excess of heptane (100 ml) for a minimum of one hour at 80°C; the mixture was then allowed to settle for one hour and subsequently vacuum filtered using Whatman #4 filter paper.

The asphaltenes thus precipitated were fractionated into different components using the fractionation procedure described earlier. Since a greater number of fractions were obtained from the sludge precipitate, the fractions were renamed in accordance with the composition of the precipitating solvent (e.g. F60/40 refers to the fraction precipitated at a solvent composition of 60% methylene chloride and 40% pentane, respectively).

**2.11.1 Experimental** : A number of studies were carried out on the asphaltene(sludge) and its fractions. The same tests were also carried out on asphaltene precipitated by adding heptane directly to the same batch of crude oil (no ferric ions in the system), so that results of the two could be compared directly to show the effect of the presence of the ferric ions during precipitation.

**2.11.2 Results** : All studies in this section were carried out on asphaltenes obtained from Venezuelan crude supplied by INTEVEP.

**2.11.2.1 Yield.** Figure 56 shows that the asphaltene yield is more than doubled in the presence of ferric ions. This may be, in part, due to the weight of iron itself in the precipitate; however, material balances indicate that the presence of iron, by itself, cannot account for the steep rise in the yield.

**2.11.2.2 Fractionation.** Asphaltenes from the sludge were fractionated using the same method described in preceding sections. Asphaltenes were also directly precipitated from the crude oil by addition of heptane and fractionated. The results of the two are presented in Figure 57. The asphaltenes from sludge show about 70% F40/60, while asphaltenes from crude show less than 5% F40/60. Presence of ferric ions greatly increases the relative amount of the higher polarity fraction.

**2.11.2.3 C:H content and ratio.** The asphaltene (sludge) and asphaltene (crude) were analyzed for C:H content and ratio. The results are presented in Table 7. The C:H ratio is higher for asphaltene(sludge), which may indicate either greater aromaticity or a greater degree of unsaturation.

**2.11.2.4 Aging.** The sludge obtained by the addition of ferric ions to the crude oil was allowed to stay in contact with air at room temperature. Samples were extracted at varying times (1 hour, 1 week and 2 weeks from the formation of the sludge). Asphaltene was precipitated

from the sludge and fractionated. The effect of sludge aging on fraction distribution is shown in Figure 58.

The sample which has been exposed to air for a longer period of time shows a greater amount of the higher polarity fraction F50/50. This effect may be due to contact with air, or due to the greater residence time of the  $\text{Fe}^{3+}$  ions in the asphaltenic system, perhaps allowing more association in the asphaltene through these ions.

**2.11.2.5 Metal element analysis.** The asphaltene from sludge and the fractions obtained were analyzed for the presence of metals. The metal element analysis was carried out by XRAL Activation Services Inc., Ann Arbor, Michigan by the ICP-90 method. A comprehensive list is presented in Table 9. The second column shows the metal content of asphaltene precipitated from crude oil by heptane. This asphaltene was fractionated and two of the fractions were analyzed for metal content; those results are shown in the third and fourth column. Finally, asphaltenes were also precipitated from sludge obtained from a 1:1 mixture of 4.4M hydrochloric acid and crude oil (fifth column); and sludge obtained from a 1:1 mixture of 9000ppm  $\text{FeCl}_3$  in 4.4M hydrochloric acid and crude oil (sixth column)

The concentrations for iron, nickel and vanadium are significantly higher in F30/70 than in F10/90. The concentration of iron in F30/70 is three times higher than in F10/90; this is significant keeping in mind that no ferric chloride was added while precipitating these samples: the iron content of these fractions originates from the crude oil. The concentration of nickel and vanadium are also significantly higher in F30/70 than in F10/90. This may be the key to the differences in polarities of the two fractions: the fraction with the higher metal level would show higher polarity.

It is interesting to note that the asphaltene precipitated from sludge (sixth column) has a lower level of nickel and vanadium than that precipitated directly from crude oil by the addition of heptane; however the level of Mn is six times higher in the sludge-derived asphaltene. The lower levels of nickel and vanadium may be due to the fact that the level of iron is almost 200 times higher in the sludge-derived asphaltene than in the crude-oil+heptane asphaltene. Such a relatively high level of one compound may affect the detection of other compounds, especially in the ICP-90 method.

**2.11.2.6 Ferric ion concentration.** The effect of varying the concentration of ferric ions prior to the precipitation is shown in Figure 59. Presence of acid without ferric ions does not seem to have too much an effect on the yield of the higher polarity fractions. Introducing ferric ions at a concentration of 3000 ppm increases the proportion of the fraction F40/60. Surprisingly, addition of ferric ions does not have an effect on the yield of the high polarity fractions F60/40 and F50/50.

**2.11.2.7 Acid concentration.** The effect of changing acid concentration is shown in Figures 60-61. In the absence of ferric ions (Figure 60), there is not a very significant difference in the proportion of the fractions with change in the acid concentration. However, decreasing the acid concentration from 4.4M to 2.2M (in the presence of 9000ppm FeCl<sub>3</sub>, see Figure 61) *increases* the amount of the high polarity fractions F50/50 and F40/60.

**2.11.3 Discussion :** Addition of acid/Fe<sup>3+</sup> system during the precipitation of asphaltenes seems to have a significant effect on the polarity of the precipitated asphaltene. The yield of the high-polarity fractions is increased in the presence of the acid/Fe<sup>3+</sup> system. In addition, the elemental analysis shows a higher degree of aromaticity or unsaturation for the asphaltene (sludge). The residence time of the Fe<sup>3+</sup> ions in the sludge also seems to play an important level on the polarity of the precipitated asphaltene.

The ICP-90 analysis for metals shows higher levels of metals such as iron, nickel and vanadium in the asphaltene(sludge) compared to the levels in asphaltene(crude). Thus these metal ions probably play a direct role in determining the polarity (hence the degree of difficulty in dissolution) of the precipitated asphaltenes.

The effect of acid concentration on the asphaltene polarity is not yet clear. More experiments need to be performed before a logical conclusion can be reached.

These results illustrate that the method of precipitation plays a very important role in determining the properties of the precipitated asphaltene. Asphaltenes precipitated from crude oil by heptane possess different properties than asphaltenes precipitated from crude oil by ferric ions. Similarly, other methods of precipitation such as contact with CO<sub>2</sub> or steam will introduce other parameters which will alter the properties of the precipitated asphaltene.

### **3. Paraffin Research**

#### **3.1. Project Description**

The research work on the stabilization and dissolution of paraffins conducted includes

- Preparation of paraffin wax materials from crude oil samples.
- Characterization of paraffin samples, including the molecular weight, the functional group and the acid/base number of paraffin wax, as well as the morphology and crystalline structure of wax precipitates.
- Investigation of the effectiveness of paraffin inhibitors on preventing or reducing the precipitation of paraffins from alkane solvents, in order to evaluate the feasibility of preventing paraffin deposition.
- Introduction of the method of dissolving paraffin deposits using organic-based fluids with in-situ exothermic reactions.
- Quantification of the kinetics of exothermic reactions with respect to the concentration of reactants and acid catalysts, in order to understand how to control the rate of this reaction to optimize paraffin dissolution by in-situ exothermically reacting fluids.
- Study of the kinetics of the exothermic reaction between ammonium chloride (or ammonium nitrate) and sodium nitrite in emulsion fluids, particularly the effect of the type of surfactant, the concentration of surfactant, and the type of oil media.
- Evaluation of the feasibility of removing paraffin deposits using the currently selected emulsion systems. Characterization of the unfavorable side effects associated with this thermal treatment for paraffin dissolution, particularly, the formation of nitrogen gas phase.
- Investigation of the dissolution of paraffin deposits in pipelines and porous media using exothermic reactive fluids.
- Numerical simulation of the reaction kinetics and fluid temperature in pipeline using a computational fluid dynamics package, FLUENT.
- Modification of currently selected reactive fluid systems or design of other new systems for further improving the thermal treatment of paraffin dissolution.
- Establishment of guidelines for the dissolution of paraffin deposits using organic-based fluids.
- Verification of the technique of delaying the release of energy until the fluid reaches the deposited paraffin by alternately pumping pulses of the two reactants into the pipeline separated by an inert spacer (simulation of the reaction during flow of the reactant pulses inside the pipeline).

- Study of the kinetics of the exothermic reaction between ammonium chloride ( $\text{NH}_4\text{Cl}$ ) (or ammonium nitrate,  $\text{NH}_4\text{NO}_3$ ) and sodium nitrite ( $\text{NaNO}_2$ ) in emulsion fluids, particularly the effect of the stirring rate and the concentration of surfactant, sorbitan mono-laurate (determination of the empirical reaction rate in the emulsion).
- Verification of the technique of delaying the release of heat until the fluid reaches the deposited paraffin by alternately pumping pulses of the emulsion mixtures, consisting of aqueous medium containing one of the reactants stabilized in heptane using surfactant, into the pipeline and numerical simulation of the fluid temperature inside the pipeline.
- Confirmation of the technique of delaying the heat release by encapsulating the catalyst for the exothermic reaction between ammonium chloride ( $\text{NH}_4\text{Cl}$ ) (or ammonium nitrate,  $\text{NH}_4\text{NO}_3$ ) and sodium nitrite ( $\text{NaNO}_2$ ).

### 3.2 Preparation of Paraffin Wax

The paraffin wax used in this project, called Jollier wax, was provided by Conoco. The isolation of Jollier wax from a crude oil source was carried out according to the procedure in UOP Method 46-85. In brief, crude oil was first treated with sulfuric acid to precipitate asphalt. The asphalt-free crude oil sample was dissolved in warm methylene chloride. Subsequently, this solution was cooled to  $-30^\circ\text{C}$  and filtered through a cold fretted glass filter to collect wax precipitates. The isolated Jollier wax sample was paste-like and light brown.

### 3.3 Characterization of Wax Material

**3.3.1 Molecular Weight of Wax:** The measurement of the molecular weight of Jollier wax was made by Conoco using high temperature gas chromatography. The molecular weight distribution of Jollier wax is illustrated in Figure 62 using the number of carbon atom in a wax molecule as the coordinate. One observes that the carbon number of dried Jollier wax ranges from 24 to 76 with the maximum weight fraction located at 50 carbon atoms. The average carbon number of this wax sample is 51.2.

**3.3.2 Melting Point Temperature of Wax:** The melting point temperature of Jollier wax was measured by the cloud point of a slowly cooling heptane solution previously heated to  $80^\circ\text{C}$  to completely dissolve the added Jollier wax. The experimental result indicates that the observed cloud point temperature of Jollier wax increases from 30, 34 to  $39^\circ\text{C}$  as the amount of wax increases from 1, 2 to 4 gram per 100 ml heptane (measured at  $25^\circ\text{C}$ ). This trend might be explained as follows: At the higher wax content in solution, the amount and rate of wax flocculation and precipitation will be higher as the solution is cooled to the wax melting point temperature, leading to a noticeable cloud appearance at the higher temperature. This study shows that the cloud point temperature of Jollier wax is approximately in the range of  $40^\circ\text{C}$ . The

fact that Jolliet wax is a poly-dispersed mixture also suggests that there may exist a broad range of temperatures where Jolliet wax precipitates.

**3.3.3 Functional Groups of Wax:** FTIR spectroscopy was used to characterize the functional groups of Jolliet wax. A thin film of wax was casted on the NaCl window for measurement. The FTIR spectrum of Jolliet wax, illustrated in Figure 63, has a strong absorption of  $\text{CH}_2$  symmetric and asymmetric stretching bands located at 2850 and 2920  $\text{cm}^{-1}$ , respectively. However, as opposed to the broad FTIR spectrum of Mobil asphaltenes, the FTIR spectrum of Jolliet wax in the range between 1000-1700  $\text{cm}^{-1}$  only has two significant bands located at 1453 and 1377  $\text{cm}^{-1}$ , which represent the  $\text{CH}_2$  and  $\text{CH}_3$  deformation bands, respectively. In addition, the existence of a significant portion of paraffinic bonds ( $-\text{CH}_2-$ ) is evidenced by the strong absorption band at 720  $\text{cm}^{-1}$  which stands for the  $(\text{CH}_2)_n$  in-phase rocking. These results suggest that the Jolliet wax sample is mainly composed of paraffinic chain molecules without extra functional groups.

**3.3.4 Acid/Base Titration of Wax:** The acid/base quantities of Jolliet wax were measured using a potentiometric titration method described in ASTM D664 [9]. This titration experiment shows that Jolliet paraffin wax has a virtually undetectable base number of approximately 0.03 and a much lower acid number, 1.76, than Mobil asphaltenes. This trend suggests that Jolliet wax behaves more closely as the pure paraffin material without acid/base functional groups.

**3.3.5 Morphology of Wax:** The morphology of the precipitates of Jolliet wax was studied using light and scanning electron microscopy. Jolliet wax was dissolved in toluene and precipitated by adding heptane. Figure 64 illustrates the light micrograph of Jolliet wax precipitates. Similar to Mobil asphaltenes, the morphology of Jolliet wax precipitates shows no pattern of defined shapes such as spherical, fibril, lamellar, etc., indicating no specific orientation in wax aggregates at the scale well above micrometers. However, Jolliet wax precipitates appear as significantly less branched clusters than Mobil asphaltenes, suggesting that the aggregation of Jolliet wax precipitates might be different from that of Mobil asphaltenes. Figure 65 illustrates the scanning electron micrograph of Jolliet wax precipitates. The wax precipitates appear as flake-like structure with the size about 1  $\mu\text{m}$ . This morphology might be attributed to the chain alignment of paraffin molecules.

**3.3.6 Crystal Structure of Wax:** The structure of Jolliet wax precipitates at the atomic scale were characterized by X-ray diffraction (XRD) methods. A sealed tube copper anode generating X-rays with the wavelength at 1.542 Å was used for the measurement. As illustrated in Figure 66, the XRD profile of Jolliet wax contains two significant crystalline peaks with Bragg angle ( $2\theta$ ) at 21.8° and 24.3° and a broad amorphous band ranging from 12° to 25° with a peak at 19.5°. This result suggests that Jolliet wax precipitates are a semi-crystalline material with both crystalline and amorphous phases. From the Bragg diffraction relation, the molecular spacings

in the wax precipitates were found to be 4.072Å for the 21.8° peak and 3.66Å for the 24.3° peak. However, it was noticed that the number of crystalline peaks in this XRD profile was much less than that from a common crystal.

### 3.4 Inhibition of Paraffin Precipitation Using Chemicals

The influences of wax inhibitor on reducing the cloud point temperature of Joliet wax and hexatriacontane ( $n\text{-C}_{36}\text{H}_{74}$ ) were studied. Along with Joliet wax, hexatriacontane was studied as a model paraffin wax. The first type of paraffin inhibitors selected for study was monomeric chemicals with a long aliphatic chain and a polar head group. Arachidyl alcohol ( $\text{C}_{18}\text{H}_{37}\text{OH}$ ) (m.p.=74-76°C) and behenic (docosanoic) acid ( $\text{C}_{21}\text{H}_{43}\text{COOH}$ ) used in this study belong to this group. These inhibitors have a long aliphatic chain (with  $n>18$ ) which can attach the nuclei of paraffin crystals to co-crystallize with paraffin molecules. The function groups (OH, COOH) of these inhibitors can modify the surface structure of paraffin crystals and inhibit their growth. The functional groups of paraffin inhibitors should favorably interact attractively with the solvent molecules through hydrogen bonding or p-orbital association, and further disperse the paraffin crystals.

The second class of paraffin inhibitors selected for this study was the polymeric chemicals including poly(ethylene vinyl acetate) ( $-(\text{CH}_2\text{CH}_{2,x}-\text{CHOCH}_{3,y})-$ ) with  $x=0.75$  and poly(octadecene maleic anhydride) ( $-(\text{CH}_2\text{CH}(\text{C}_{16}\text{H}_{33})-\text{CH}(\text{OCOCO})\text{CH})-$ ). These polymeric inhibitors might be more effective than monomeric inhibitors because polymers had multiple sites to attach a paraffin crystal. Therefore, the effect of the molecular weight of polymeric inhibitors on the inhibition of paraffin growth can be investigated. In this study, aliphatic solvents such as light alkanes was used preferentially as the organic media for accommodating inhibitor chemicals because of their environmental compatibility. Only if aliphatic solvents do not effectively solubilize the paraffins and the inhibitors, will the use of aromatic solvents such as toluene be considered.

The experimental procedure for quantifying the effectiveness of inhibitors on the solubilization (or dispersion) of paraffin is, in general, as follows: First, samples were prepared by mixing 1 wt% paraffin, different amounts of inhibitor and pure solvent. Samples were heated above the paraffin melting temperature (80°C) and cooled down subsequently while gently shaking the solution. The temperature drop of this continuously stirred solution was measured and recorded as a function of time. The cloud point temperature of this sample was recorded. If the temperature of melting of paraffin decreases with increasing the concentration of inhibitors, the inhibitor will be considered to be effective. The effectiveness of inhibitors will be determined by the extent of decrease of the heat and temperature of melting of paraffin precipitates.

The effectiveness of paraffin inhibitors described above was studied by monitoring the decrease of the cloud point of Jolliet wax with the concentration of inhibitors. The heptane solution containing Jolliet wax and inhibitors was preheated up to 80°C to completely dissolve wax precipitates. Then, the heptane solution was gradually cooled down until the appearance of wax precipitation. Figure 67 illustrates typical cooling curves of wax solutions. In general, it took 8-12 minutes for the solution to reach the cloud point. The cloud point temperatures of both Jolliet wax solutions and hexatriacontane solutions containing different inhibitors were summarized in Table 10. One can see that four proposed inhibitors, arachidyl alcohol, behenic acid, poly(ethylene vinyl acetate) and poly(1-octadecene maleic anhydride), at 1 wt%, 2 wt%, 4 wt% and 8 wt% were tested. The amount of Jolliet wax and hexatriacontane was always kept at 1 wt%.

As illustrated in Table 10, among the four inhibitors used in this study, only poly(ethylene vinyl acetate) (PEVAc) could reduce the cloud point temperature of Jolliet wax by as small as 3°C from 30°C without PEVAc to 26-27°C with PEVAc. For the other three inhibitors, the cloud point temperature of paraffin actually increases with increasing the amount of inhibitors. For the 1% hexatriacontane solutions, again only PEVAc reduces the paraffin precipitation temperature. The paraffin precipitation temperature increases unfavorably to 33-37°C when behenic acid and arachidyl alcohol are used. Poly(1-octadecene maleic anhydride) seemed ineffective to the precipitation temperature of the hexatriacontane. In summary, this experiment indicates that the wax inhibitors used in this study cannot effectively inhibit the precipitation of both natural and manufactured paraffin materials.

The difficulties in stabilizing paraffin molecules in the solution can be realized by their unique linear aliphatic  $((\text{CH}_2)_n)$  structure dominated by the trans-conformation. This conformation strongly favors the alignment of different paraffin chains together to form paraffin crystals through van der Waals attractive interaction. The longer the aliphatic chain, the higher the attractive force will be. The chain lengths of both Jolliet wax and hexatriacontane are significantly higher than those of behenic acid, arachidyl alcohol and poly(1-octadecene maleic anhydride), which may account for the ineffectiveness of these inhibitors. In addition, behenic acid and arachidyl alcohol will precipitates at about 30-40°C, leading to the increase of the cloud point of the wax solution.

The slight effective paraffin inhibitor, poly(ethylene vinyl acetate), has an extremely long linear chain structure with a random alternation of both ethylene and vinyl acetate groups. The arrangement and the number ratio of these two groups strongly affect the effectiveness of poly(ethylene vinyl acetate) to inhibit wax precipitation. However, even though the percentage of ethylene group in the poly(ethylene vinyl acetate) can be controlled (75% ethylene group,



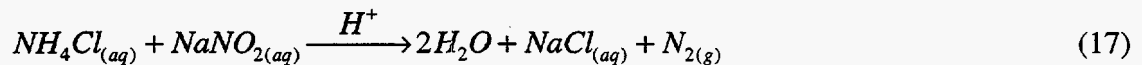
here), the difficulty in controlling the actual arrangement of functional groups may significantly limit the feasibility of poly(ethylene vinyl acetate) as effective paraffin wax inhibitors.

### 3.5 Dissolution of Paraffins Using Exothermically Reacting Fluids

Because of the ineffectiveness of preventing paraffin dissolution by paraffin inhibitors, the dissolution of paraffin deposits using exothermically reacting fluids was introduced in this project. This method appears to provide an advantage over the hot-oiling method for thermally treating the distant paraffin deposits in that the exothermic reaction carried by fluids is possible to be delayed long enough to generate sufficient heat at the distant deposition zone to dissolve paraffin deposits. A typical example of the distant paraffin deposits takes place during the transportation of crude oil through pipelines, as shown in Figure 68. Once paraffins deposit in the pipeline, the fluids, such as hot oils, have to be injected into the pipelines to dissolve paraffin deposits. However, the heat loss of hot oils to the cold environment during the travel of hot oils through pipelines is usually too much such that the injected oils become no longer hot enough to heat paraffin deposits up to their melting point temperature. On the other hand, the fluids which conduct in-situ exothermic reactions can generate heat to overcome the heat loss to environment and eventually raise the fluid temperature beyond the paraffin melting point temperature.

There are two criteria for the exothermically reacting fluid to be effect to the dissolution of paraffin deposits; namely, as illustrated in Figure 69, (1) the amount of heat generated by the exothermic reaction is sufficient to melt paraffin deposits, and (2) the rate of the exothermic reaction is properly controlled such that the maximum temperature of the fluid takes place right at the paraffin deposition area.

On the basis of these requirements, we selected an organic-based emulsion fluid system in the third quarter for the study of the dissolution of paraffin deposits. The components of this fluid system includes (1) oil phase: to dissolve the heated paraffin deposits such as heptane, (2) aqueous phase: to host the exothermic reaction, and (3) nonionic surfactant: such as the sorbitan mono-oleate surfactant to emulsify water and oil. The resultant fluids behave as water-in-oil emulsions with significant fractions of both oil phase and water phase. The exothermic reaction selected in this study is described below,



with the following enthalpy and specific heat of reaction

$$\begin{aligned} \Delta H_R &= -334.47 \text{ KJ} / \text{mol} \\ \Delta C_p &= 197.2 \text{ J} / (\text{mol} \cdot \text{K}) \end{aligned} \quad (18)$$

Before the dissolution of paraffin deposits, the reactants, ammonium chloride (NH<sub>4</sub>Cl) and sodium nitrite (NaNO<sub>2</sub>) are solubilized in two separate emulsion fluids. These two emulsion

fluids are injected simultaneously into the location where paraffin deposition occurs. As illustrated in Figure 70, immediately after emulsion fluids are co-injected, ammonium chloride and sodium nitrite start to mix with each other and conduct the exothermic reaction described in equation (17). Subsequently, the heat generated by this reaction melt and dissolve paraffin deposits.

This study demonstrates that paraffin deposits can be dissolved by a thermal treatment involving the in-situ generation of heat in organic-based reactive micellar fluids. Therefore, this approach might offer a feasible way alternative to hot-oiling in the dissolution of paraffin deposits occurred in the actual oil fields and pipelines. However, there might still exist some problems in this thermal treatment method. Namely, the amount of released heat is limited by the solubility of ammonium chloride and sodium nitrite in the aqueous phase. The side product nitrogen gas causes a tremendously expansion of the volume of reaction media. This side effect might increase difficulties during the operation of this treatment as well as reduce the effectiveness of this treatment on paraffin dissolution.

### 3.6 Kinetics of the exothermic reaction between $\text{NH}_4\text{Cl}$ and $\text{NaNO}_2$

The rate of the exothermic reaction between ammonium chloride and sodium nitrite is influenced by a number of factors, including the concentrations of ammonium chloride, sodium nitrite and the acid catalysis, e.g. acetic acid. In addition, because the exothermic reaction is conducted in the aqueous phase of the two emulsions after they are mixed, the rate of coagulation between these two types of emulsion droplets will also affect the rate of exothermic reaction. The rate of emulsion droplet coagulation can be controlled by the type and concentration of surfactant used for preparing the emulsions. Firstly, we investigated the kinetics of the exothermic reaction described by equation (17) using an adiabatic batch reactor described in Figure 71. During the reaction, solution temperature and reaction time were recorded for the kinetics analysis. The results are described in Figure 71.

**3.6.1 Effect of the Concentration of Acid Catalyst** : Studies on the kinetics of this exothermic reaction were carried out using the aqueous solution with the following composition:  $[\text{NH}_4\text{OH}]_0 = [\text{NaNO}_2]_0 = 1.347 \text{ M}$  (i.e. mole/dm<sup>3</sup>) and different concentrations of acetic acid,  $[\text{CH}_3\text{COOH}]$ . The temperature-time profiles at different acetic acid concentrations are illustrated in Figure 72. It shows that the rate of temperature increment increases with the acetic acid concentration, indicating that acetic acid offers proton to catalyze the reaction. Analysis of the experimental data in Figure 73 was performed by using the following equations:

$$[\text{NH}_4\text{Cl}](t) = [\text{NH}_4\text{Cl}]_0 - (T(t) - T_0) * C_{P,solution} / (-\Delta H_R) \quad (19)$$

$$\text{reaction rate} = -\frac{d[\text{NH}_4\text{Cl}]}{dt} \quad (20)$$

where  $T(t)$  and  $T_0$  are the temperature at time  $t$  and at the beginning of the reaction, respectively.  $C_{p,\text{solution}}$  is the heat capacity of the solution. The result of this analysis is highlighted in Figure 74 showing  $\text{NH}_4\text{Cl}$  concentration decreases with the reaction time and the reaction rate rises in the beginning of the reaction and declines subsequently due to the consumption of reactants.

In the analysis of the reaction dependence on the concentration of acid, a simpler analysis was conducted. Under adiabatic condition, the slope of temperature profiles,  $dT/dt$  ( $^{\circ}\text{C second}^{-1}$ ), is the rate of reaction on a relative scale. The slope of the temperature profile at the very early stage of the reaction where the ammonium chloride concentration was still close to  $[\text{NH}_4\text{OH}]_0$ , were used to analyze the reaction order with respect to the concentration of proton ( $\text{H}^+$ ) generated from acetic acid. The concentration of proton in the solution can be calculated by

$$[\text{H}^+] = \{1.76 \times 10^{-5} [\text{CH}_3\text{COOH}]\}^{1/2} \quad (21)$$

with  $1.76 \times 10^{-5}$  being the dissociation constant of acetic acid in water at  $25^{\circ}\text{C}$ . As illustrated in Figure 73 the logarithmic plot of the reaction rate ( $dT/dt$ ) vs.  $[\text{H}^+]$  displays a fairly linear relationship with the slope to be 1.6 in approximation. From this result, one can see that the rate of this exothermic reaction can be effectively controlled by the concentration of acetic acid.

**3.6.2 Effect of the Concentration of  $\text{NH}_4\text{Cl}$  Reactant** : Figure 75 illustrates the influence of the concentration of ammonium chloride on the temperature evolution of the aqueous reacting medium in the adiabatic reactor as the exothermic reaction is conducted. The concentration of ammonium chloride was varied from 0.1 M to 0.6 M while the concentration of sodium nitrite was kept excessively at 4.4 M. The concentration of the acid catalyst, acetic acid, also maintained constant at 1.07 M. As illustrated in Figure 75, the rate of temperature increment are increased with increasing the concentration of ammonium chloride. The slope of temperature profiles,  $dT/dt$  ( $^{\circ}\text{C second}^{-1}$ ), is the rate of reaction on a relative scale. The initial slope of the temperature profile was calculated and is plotted in Figure 76. It shows that the logarithmic scale of both the reaction rate and the concentration of ammonium chloride has a fairly linear relationship. From the slope of this linear curve, the order of the exothermic reaction with respect to the concentration of ammonium chloride was estimated to be approximately 1.2.

**3.6.3 Effect of the Concentration of  $\text{NaNO}_2$  Reactant** : Figure 77 shows the influence of the concentration of sodium nitrite on the temperature evolution of the reacting medium in the adiabatic reactor as the exothermic reaction is conducted. The concentration of sodium nitrite was changed from 0.1 M to 0.6 M, while the concentration of sodium nitrite was kept excessively at 4.5 M. The concentration of the acid catalyst, acetic acid, was also maintain

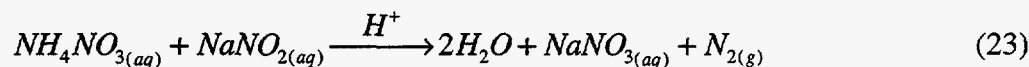
constant at 1.07 M. As illustrated in Figure 77, the rate of temperature increment are increased with increasing the concentration of sodium nitrite. The initial slope of the temperature profile,  $dT/dt$ , was calculated and is plotted in Figure 78. It shows that the logarithmic scale of both the reaction rate and the concentration of sodium nitrite has a fairly linear relationship. From the slope of this linear curve, the order of the exothermic reaction with respect to the concentration of sodium nitrite was estimated to be approximately 1.5.

The results shown above provide a complete analysis of the kinetics of the exothermic reaction described in equation (17). This analysis revealed that this reaction at 25°C can be described as:

$$-\frac{d[NH_4Cl]}{dt} = -\frac{d[NaNO_2]}{dt} = k[NH_4Cl]^{1.2}[NaNO_2]^{1.5}[H^+]^{1.6} \quad (22)$$

where  $[H^+]$  was calculated by equation (21).

**3.6.4 Application of Kinetics study to the  $NH_4NO_3$ - $NaNO_2$  Reaction:** : In this study, it was also found that ammonium nitrate,  $NH_4NO_3$ , can conduct an exothermic reaction with sodium nitrite as that of ammonium chloride. The reaction between ammonium nitrate and sodium nitrite is described below,



with the following enthalpy and specific heat of reaction

$$\begin{aligned} \Delta H_r &= -334.66 \text{ KJ / mol} \\ \Delta C_p &= 197.2 \text{ J / (mol.K)} \end{aligned} \quad (24)$$

One observes that the exothermic reactions described in equations (17) and (23) have the similar heat of reaction. This similarity indicates that both reactions are equally effective in the generation of heat to melt paraffin deposits. The kinetics of both reactions was studied in an adiabatic condition and is compared in Figure 79. It shows that in two sets of similar solution compositions, the temperature-time profiles in both reaction systems are nearly identical. On the basis of this observation, it is deduced that the kinetics of the reaction between ammonium nitrate and sodium nitrite should be similar to that between ammonium chloride and sodium nitrite described in equation (22).

Although ammonium chloride and ammonium nitrate react equally well with sodium nitrite, it appears that the solubility of ammonium chloride in water is significantly lower than those of ammonium nitrate and sodium nitrite. Therefore, the amount of heat generated in the fluid containing ammonium chloride and sodium nitrite is limited by the solubility of ammonium chloride, and the replacement of ammonium chloride with the more soluble ammonium nitrate allows a greater extent of exothermic reaction to generate more heat for the melting of paraffin

deposits. However, also note that care must be taken in the use of ammonium nitrate because it is a strong oxidizer and has been used as a component of explosive materials.

### 3.7 Other Factors: Surfactant and Oil

To study the effect of surfactant on the kinetics of the  $\text{NaNO}_2\text{-NH}_4\text{Cl}$  reaction in water/oil emulsions, an emulsion system was developed for the dissolution of paraffin deposits. The components of this system include (1) oil phase: to dissolve the heated paraffin deposits, such as heptane, (2) aqueous phase: to host the exothermic  $\text{NaNO}_2\text{-NH}_4\text{Cl}$  reaction, and (3) nonionic surfactant: to emulsify water and oil. In this study, two nonionic surfactants, sorbitan mono-oleate (SMO) and sorbitan mono-laurate (SML), and three oil media, heptane, dodecane and paraffin oil, were used. The temperature of emulsion fluids undergoing the exothermic  $\text{NaNO}_2\text{-NH}_4\text{Cl}$  reaction in a adiabatic reactor was measured during the reaction period. The exothermic rate of emulsion fluids was then quantified from the initial rate of increase of emulsion temperature.

**3.7.1 Effect of Type of Surfactant:** : Figure 80 shows the effect of surfactant type on the temperature evolution profiles of water/heptane solutions with a given reactant composition ( $\text{NH}_4\text{Cl}$ ,  $\text{NaNO}_2$  and acetic acid) and a given water-to-heptane volume ratio. Without any surfactant in the water/heptane mixture, the exothermic reaction is completed in 3 minutes as evidenced by a quick rise of the mixture temperature up to a final value at  $100^\circ\text{C}$ . Because water and heptane in this system are separated, the exothermic reaction is virtually carried out in pure aqueous medium. Three types of surfactant, pure SMO, pure SML and SMO/SML (2/1 weight ratio), were added by a concentration of 50 g/l to emulsify the water/heptane mixture. One observes the emulsification of water/heptane mixture in general slows down of  $\text{NaNO}_2\text{-NH}_4\text{Cl}$  reaction. The rate of temperature increase follows the order:  $\text{SMO} > \text{SMO/SML} > \text{SML}$ . That is, SML is apparently much more effective in decreasing the reaction rate of the system compared to SMO. This result is perhaps due to the different viscosities of water/heptane emulsions prepared by SML and SMO. The SML emulsion is more viscous and stable than the SMO emulsion. As a result, the rate of coagulation between aqueous droplets containing  $\text{NH}_4\text{Cl}$  and  $\text{NaNO}_2$  in SML emulsions is much smaller than that in SMO emulsions, resulting in a slower reaction in SML emulsions. In addition, the more viscous SML emulsion seems likely hold up more nitrogen produced by the reaction and becomes foam which may further retard the rate of contact and reaction between  $\text{NH}_4\text{Cl}$  and  $\text{NaNO}_2$ .

**3.7.2 Effect of the Water-to-Oil Volume Ratio** : Figures 81 to 83 show the effect of the water-to-oil volume ratio on the rate of the exothermic  $\text{NaNO}_2\text{-NH}_4\text{Cl}$  reaction in emulsions. As shown in Figure 81, for given amounts of water and SMO surfactant, the rate of temperature increase, i.e., the exothermic reaction rate, decreases with increasing the amount of heptane in the mixture.

A similar trend was also observed for SML surfactant as shown in Figure 82. Figure 83 also shows that for constant amount of heptane and SML, the reaction rate increases with increasing the amount of water in the mixture. To sum up the results shown in Figure 81 to 83, it is clear that the rate of the exothermic  $\text{NaNO}_2\text{-NH}_4\text{Cl}$  reaction increases with increasing the water-to-oil volume ratio. This trend indicates that a increase in the water-to-oil volume ratio enhances the rate of mixing between  $\text{NaNO}_2$  and  $\text{NH}_4\text{Cl}$  and therefore increases the  $\text{NaNO}_2\text{-NH}_4\text{Cl}$  reaction. In addition, a comparison between Figures 81 and 82 further verifies that the  $\text{NaNO}_2\text{-NH}_4\text{Cl}$  reaction in SMO emulsions is in general faster than that in SML emulsions.

**3.7.3 Effect of Surfactant Concentration:** : Figure 84 shows the temperature evolution profiles of water/heptane emulsions containing constant reactant concentrations but different concentrations of SML. It shows that the rate of temperature increment gradually decreases as the concentration of SML is increased. The initial slope ( $dT/dt$ ) of each profile, i.e., a relative scale of the  $\text{NaNO}_2\text{-NH}_4\text{Cl}$  reaction rate, was plotted in Figure 85. It is clear that the reaction rate,  $dT/dt$ , decreases significantly with increasing SML concentrations up to 0.02 M, and gradually levels out at higher SML concentrations. This trend indicates that a critical concentration of SML (ca. 0.02 M) is necessary to form stable water/heptane emulsions with a reduced rate of coagulation of aqueous emulsion droplets containing  $\text{NaNO}_2$  and  $\text{NH}_4\text{Cl}$ .

**3.7.4 Effect of Type of Oil:** : Figure 86 shows the temperature evolution profiles of emulsions containing different alkane solvents emulsified with a given amount of aqueous reactants by SMO surfactant. One observes that the rate of temperature increment for heptane and dodecane solvents seems higher than that for paraffin oil even though paraffin oil has the highest viscosity. This trend can be explained by the reduced stability of reactant-contained emulsion droplets in paraffin oil compared to that in heptane and dodecane.

**3.7.5 Effect of Acetic Acid Concentration:** : The effect of the acetic acid concentration on the  $\text{NaNO}_2\text{-NH}_4\text{Cl}$  reaction rate in pure aqueous media has been quantified as described in equations (21) and (22). Figure 87 shows the effect of acetic acid concentration on the rate of this exothermic reaction in water/heptane/SML emulsions. As the acid concentration greatly influences the aqueous reaction, so does it influence the emulsified reaction. It shows that as the acid concentration is increased, the reaction rate in emulsions also increases despite the hindrance to the coagulation of emulsion droplets containing  $\text{NaNO}_2$  and  $\text{NH}_4\text{Cl}$  reactants.

### 3.8 Experimental Investigation of Paraffin Dissolution in Pipelines

As shown schematically in Figure 88, a continuous-flow tubular reactor was used to further investigate the feasibility of dissolving paraffin deposits in pipelines. To prevent the severe heat loss, this tubular reactor was surrounded with a sheet of styrofoam. The reactants,  $\text{NH}_4\text{NO}_3$  and  $\text{NaNO}_2$ , were placed separately in two batches of two different oil/water emulsions.

The oil medium used to prepare emulsions was heptane (or xylene). A small amount of catalyst, acetic acid, was placed in the  $\text{NaNO}_2$  emulsion. These two emulsion fluids were subsequently pumped into a tubular reactor containing Jolliet paraffin deposits. Upon mixing at the reactor inlet, reactants in these emulsions started to react each other and generated heat which raised the temperature of fluid to dissolve paraffin deposits in the reactor. The temperature evolution profile at four positions along the tube were measured using thermocouples. The dissolution of paraffin deposits were recorded in-situ using video-enhanced microscopy which connected with a video cassette recorder.

Figure 89 shows a typical result of the temperature of the outer tube wall surface at four different axial positions along the tubular reactor. These four positions are illustrated in Figure 88. One observes that the temperature at all four positions rises steadily for the first 18 minutes. In this stage, the rate of heat generation from  $\text{NH}_4\text{NO}_3$ - $\text{NaNO}_2$  reaction is greater than the rate of heat loss from the reactor to the environment, leading to the increase of tube temperature. From 18 to 40 minutes, the temperature at each position becomes fairly constant. This result indicates that a steady state of tube temperature is reached as a result of the balance between heat generated by fluids and that lost to the environment. The steady temperature value is 50, 68, 88 and  $48^\circ\text{C}$  at positions 1 to 4, respectively. At about the 40th minute, the reactants are stopped pumping into the reactor, and the temperature of tube decreases gradually to room temperature due to the loss of heat to the environment.

It was observed that the paraffin deposits initially placed near position 3 started to melt and dissolved as the temperature at position 3 attained about  $60^\circ\text{C}$ . The rate of paraffin dissolution increases significantly with increasing the temperature. The process of paraffin dissolution in an another similar experiment is illustrated in Figures 90(a) to (d). This series of pictures shows clearly that the front face of paraffin deposits recedes significantly over a period of 2 minutes at a tube temperature of  $66^\circ\text{C}$ . The reddish brown trails and stains around the interface between fluid and deposit are paraffins undergoing dissolution and dispersion towards fluid.

**3.8.1 Evaluation of Effect of Evolved Nitrogen on Paraffin Removal:** : Our preliminary assessment indicates that nitrogen produced from the exothermic  $\text{NaNO}_2$ - $\text{NH}_4\text{Cl}$  reaction described in equation (17) can have the following effects on the treatment of paraffin deposits in oil pipelines with exothermic reactive emulsion fluids.

(1) Formation of oil/water/nitrogen foams: Nitrogen produced from the  $\text{NaNO}_2$ -  $\text{NH}_4\text{Cl}$  reaction can be easily entrapped in emulsions to form a foam flow in pipelines. The resulting foam complicates the kinetics of the exothermic reaction between  $\text{NaNO}_2$  and  $\text{NH}_4\text{Cl}$  because of the change in the rate of molecular contact among reactants.

(2) Increase of the fluid volume and reduction of heat loss to the environment: The incorporation of nitrogen into the initial emulsion fluids creates foams with an expanded fluid volume. As a result, the speed of exothermic fluid traveling in pipelines increases dramatically, and the time for exothermic fluids to reach the paraffin deposition zone is reduced correspondingly. Due to decreased travel time, the exothermic fluid loses less heat to the environment surrounding pipelines and thus maintains higher temperatures to consequently melt paraffin deposits more effectively.

(3) Increase of pressure in pipelines: Nitrogen generated in emulsions can also increase the pressure in oil pipelines if pipelines are completely plugged up by the down-stream paraffin deposits. The elevated pressure provides an extra mechanical means to rupture paraffin deposits. However, if this pressure becomes too high (pipelines can withstand up to 2500 psi of pressure generally), it may damage the pipeline itself, particularly the junction between pipes.

### 3.9 Simulation of Exothermic Reactive Fluid Flow inside Pipelines

**3.9.1 Model Description :** A computational fluid dynamics model was developed to simulate the flow of a reactive aqueous fluid containing  $\text{NaNO}_2$  and  $\text{NH}_4\text{Cl}$  inside pipelines. This flow system involves both the  $\text{NaNO}_2$ - $\text{NH}_4\text{Cl}$  reaction which generates heat to raise the fluid temperature and the loss of heat from pipe to the surrounding environment. Hence, this simulation takes into account not only the governing equations of mass and momentum balance but also those of the enthalpy energy balance and the species conservation of  $\text{NaNO}_2$  and  $\text{NH}_4\text{Cl}$  as listed below

[Momentum Balance]

$$\frac{Dv^*}{Dt^*} = -\nabla^* P^* + \frac{1}{\text{Re}} \nabla^* v^* + \frac{1}{Fr} \frac{G}{g} \quad (25)$$

[Energy Balance]

$$\frac{DT^*}{Dt^*} = \frac{1}{\text{Re} \cdot \text{Pr}} \nabla^{*2} T^* + \frac{Br}{\text{Re} \cdot \text{Pr}} \Phi^* + \frac{D}{V(T_1 - T_0)} (S_{\text{reaction}} - Q_{\text{ext}}) \quad (26)$$

[Species Conservation]

$$\frac{DC^*}{Dt^*} = \frac{1}{\text{Re}} \left( \frac{1}{Sc_m} + \frac{1}{Sc_t} \right) \nabla^{*2} C^* + \frac{1}{\text{Re} \cdot Sc^T} \frac{D}{(C_{i1} - C_{i0})} \nabla^* T^* + \frac{D}{V(C_{i1} - C_{i0})} R_j, \quad (27)$$

where

$$R_{j,k} = n_{j,k} \cdot T^{\beta_k} \cdot A_k \cdot \exp(-E_k / RT) \cdot \prod_{j' \text{ reactants}} C_{j'}^{\alpha_{j',k}} \quad (28)$$

$$S_{\text{reaction}} = \sum_j [h_j^o + \int_{T_{\text{ref}}}^T C_{p,j} dT] \cdot R_j \quad (29)$$

$$Q_{\text{ext}} = Ua(T - T_a) \quad (30)$$



$$\mu = \mu(T) = 2.67 \times 10^{-6} \frac{\sqrt{MT}}{\sigma^2 \Omega_u} \quad (31)[15]$$

$$D_{ij} = D_{ij}(T) = 0.0188 \frac{\sqrt{T^3 (1/M_i + 1/M_j)}}{P \cdot \sigma_{ij}^2 \cdot \Omega_D} \quad (32)[15]$$

$$D_i^T = -2.59 \times 10^{-7} \cdot T^{0.659} \left[ \frac{M_i^{0.511} \cdot X_i}{\sum_{i=1}^n M_i^{0.511} \cdot X_i} - m_i \right] \cdot \left[ \frac{\sum_{i=1}^n M_i^{0.511} \cdot X_i}{\sum_{i=1}^n M_i^{0.489} \cdot X_i} \right] \quad (33)[15]$$

with

$$\begin{aligned} v^* &= \frac{v}{V}, p^* = \frac{(p-p_o)}{\rho \cdot V^2}, t^* = \frac{t \cdot V}{D}, T^* = \frac{T-T_o}{T_1-T_o}, C^* = \frac{C-C_o}{C_1-C_o} \\ x^* &= \frac{x}{D}, y^* = \frac{y}{D}, z^* = \frac{z}{D}, \frac{D}{Dt^*} = \left(\frac{D}{V}\right) \frac{D}{Dt} \\ \nabla^* &= D\nabla = (\delta_1 \frac{\partial}{\partial x^*} + \delta_2 \frac{\partial}{\partial y^*} + \delta_3 \frac{\partial}{\partial z^*}) \\ \nabla^{*2} &= D^2\nabla^2 = (\delta_1 \frac{\partial^2}{\partial x^{*2}} + \delta_2 \frac{\partial^2}{\partial y^{*2}} + \delta_3 \frac{\partial^2}{\partial z^{*2}}) \end{aligned}$$

where D is the pipe diameter, V is the average velocity, T<sub>o</sub> is the reference temperature, T<sub>1</sub> is the initial temperature, C<sub>o</sub> is the reference concentration, C<sub>1</sub> is the initial concentration, and p<sub>o</sub> is the reference pressure.

The kinetics of NaNO<sub>2</sub>-NH<sub>4</sub>Cl reaction in aqueous media containing acetic acid catalyst was measured previously in an adiabatic batch study. This reaction kinetics was used in this simulation, as shown below

$$-r_{[NH_4Cl]} = -r_{[NaNO_2]} = A_1 C_{[NH_4Cl]}^{1.2} C_{[NaNO_2]}^{1.5} C_{[H^+]}^{1.6} \quad (34)$$

where  $C_{[H^+]} = [1.76 \times 10^{-5} C_{[CH_3COOH]}]^{0.5}$ . The rate constant equation in this reaction is

$$A = A_0 \exp[(E/R)(1/T_1 - 1/T)] \quad (35)$$

where E/R = 8000 K, R = ideal gas constant and A<sub>0</sub> = 2.1 (l<sup>3.3</sup>/mol<sup>3.3</sup> s) with T<sub>1</sub> = 298 K, which were measured from the Arrhenius plot of experimental data.

The governing equations were solved by a simulation package, FLUENT\* (version 4.32), using a control volume-based finite difference method [16]. These equations were discretized into their finite-difference analogs on a curvilinear grid to enable computations in the complex and irregular geometric domain [17-19]. The resulting finite-difference equations were then integrated in time implicitly over the computational cells into which the domain was divided. After the integration, the resulting algebraic equations were solved by a semi-implicit iterative

\*FLUENT is a general-purpose computational fluid dynamics package suited for incompressible and mildly compressible flows. It is available from Fluent Inc, NH. More information is available at their website <http://www.fluent.com>.

scheme which started from arbitrary initial conditions (except at the boundaries) and converged to the correct solution (i.e. that which satisfied the governing equations) after performing a number of iterations. The detailed iteration procedure is illustrated in Figure 91.

This simulation study considers the cases where both  $\text{NaNO}_2$  and  $\text{NH}_4\text{Cl}$  aqueous fluids were injected into an elbow-shaped pipe simultaneously or sequentially for a period of time. The geometry and grid layout of this pipe are illustrated in Figure 92. For the case of simultaneous injection of  $\text{NaNO}_2$  and  $\text{NH}_4\text{Cl}$ , the boundary conditions are

$$v(0, t) = 0.05 \text{ m/s}$$

$$C_{\text{NaNO}_2}(0, 0 < t < 2 \text{ sec.}) = 1.45 \text{ mol/l (i.e., 0.1 in mass fraction)}$$

$$C_{\text{NaNO}_2}(0, t > 2 \text{ sec.}) = 0.0 \text{ mol/l}$$

$$C_{\text{NH}_4\text{Cl}}(0, 0 < t < 2 \text{ sec.}) = 1.85 \text{ mol/l (i.e., 0.1 in mass fraction)}$$

$$C_{\text{NH}_4\text{Cl}}(0, t > 2 \text{ sec.}) = 0.0 \text{ mol/l}$$

$$T(0, t) = 298 \text{ K}$$

$$T_a(x, t) = 273 \text{ K, } Q_a = Ua(T - T_a)$$

For the case of sequential slug injection, the boundary condition is

$$v(0, t) = 0.05 \text{ m/s}$$

$$C_{\text{NaNO}_2}(0, 0 < t < 2 \text{ sec.}) = 1.45 \text{ mol/l (i.e., 0.1 in mass fraction)}$$

$$C_{\text{NaNO}_2}(0, t > 2 \text{ sec.}) = 0.0 \text{ mol/l}$$

$$C_{\text{NH}_4\text{Cl}}(0, 7 < t < 9 \text{ sec.}) = 1.85 \text{ mol/l (i.e., 0.1 in mass fraction)}$$

$$C_{\text{NH}_4\text{Cl}}(0, t > 9 \text{ and } 0 < t < 7 \text{ sec.}) = 0.0 \text{ mol/l}$$

$$T(0, t) = 298 \text{ K, } T_a(x, t) = 273 \text{ K}$$

### 3.9.2 Simulation Results

**3.9.2.1 Simultaneous Injection:** Figures 93 and 94 show the concentration profiles of  $\text{NaNO}_2$  and  $\text{NH}_4\text{Cl}$  inside the pipe, respectively. In both figures, the concentration of reactant in the pipe is illustrated by a spectrum of colors. The correspondence of color to the mass fraction of reactant in fluid (i.e., g of reactant/ g of fluid) is shown in a scale bar at the left side of the figure. Because the concentration of  $\text{NH}_4\text{Cl}$  flown into the pipe, 1.85 mol/l, is larger than that of  $\text{NaNO}_2$ , 1.45 mol/l,  $C_{\text{NH}_4\text{Cl}}$  always remains higher than  $C_{\text{NaNO}_2}$ . Figure 93 shows that the concentration of  $\text{NaNO}_2$  is peaked at the center of the elbow-shaped pipe as  $\text{NaNO}_2$  is almost consumed up. Meanwhile, as illustrated in Figure 94, the concentration distribution of  $\text{NH}_4\text{Cl}$  ranges up to  $3.08 \times 10^{-3}$  in mass fraction. Figure 95 illustrates the fluid temperature ranges from 273 K on the pipe wall to 321 K (i.e., 48°C) at the center of the pipe. This simulation provides the detailed information of the distribution of reacting species concentrations and temperature in the pipe, which cannot be measured easily in experiment.

**3.9.2.2 Sequential Slug Injection.** The simulation of sequential slug injection of  $\text{NaNO}_2$  and  $\text{NH}_4\text{Cl}$  into an elbow-shaped pipe was performed. Figures 96 and 97 show the concentration profiles of  $\text{NaNO}_2$  and  $\text{NH}_4\text{Cl}$  inside the pipe, respectively. At the time of injection equal to 10 seconds,  $\text{NaNO}_2$  in the first injected fluid has traveled down to the pipeline by approximately a third of pipeline length as demonstrated by the reddish contour (Figure 96), whereas  $\text{NH}_4\text{Cl}$  in the second injected fluid is still near the entrance of the pipe (Figure 97). The axial dispersion of  $\text{NaNO}_2$  and  $\text{NH}_4\text{Cl}$  inside the pipe causes these two reacting species to mix and react exothermically with each other. Therefore, one observes that the maximum fluid temperature (red spot in Figure 98) is located at a position between those of  $\text{NaNO}_2$  and  $\text{NH}_4\text{Cl}$  concentrations (red spots in Figures 96 and 97, respectively). This dispersion and mixing of reacting species suggests that a desired temperature profile may be achievable by controlling the scheme of injection of reacting species,  $\text{NaNO}_2$  and  $\text{NH}_4\text{Cl}$ .

**3.9.2.3 Comparison of Simultaneous and Sequential Injection.** The temperature profiles along the pipe center line at different times were plotted in Figures 99 and 100 for simultaneous and sequential injection cases, respectively. As shown in Figure 99, the simultaneously injected  $\text{NaNO}_2$  and  $\text{NH}_4\text{Cl}$  react with each other very quickly at the inlet region, leading to a drastic increase of fluid temperature up to  $370^\circ\text{C}$  at 2-5 seconds at about 0.25m from the pipe entrance. As the fluid travels downstream along the pipe, the temperature peak also move forward; however, the temperature peak gradually becomes broader and the maximum temperature decreases to  $300^\circ\text{C}$  at 40 seconds at 2m from the pipe inlet. This decrease of temperature peak can be attributable to the heat loss to the pipe wall being larger than the heat generated by the  $\text{NaNO}_2$ - $\text{NH}_4\text{Cl}$  reaction due to their gradual consumption.

Figure 100 shows that the sequential injection of  $\text{NaNO}_2$  and  $\text{NH}_4\text{Cl}$  can only bring about a small temperature increment to  $320^\circ\text{C}$  in the initial injection time period compared with that (e.g.,  $370^\circ\text{C}$ ) of the simultaneous injection. This trend is due to the fact that a slug of fluid which separates the sequentially injected  $\text{NaNO}_2$  and  $\text{NH}_4\text{Cl}$  delays the axial mixing and reaction between  $\text{NaNO}_2$  and  $\text{NH}_4\text{Cl}$ . Nevertheless, this exothermic reaction is still sufficiently fast to generate heat to elevate the fluid temperature. However, similar to the simultaneous injection case, during the later stage of reaction, the maximum temperature also decreases gradually, for example, to  $300^\circ\text{C}$  at 40 seconds at 2m from the pipe inlet.

The comparison of the performance of simultaneous and sequential injection of  $\text{NaNO}_2$  and  $\text{NH}_4\text{Cl}$  is also illustrated by the temperature evolution at the position 2m from the pipe inlet. As shown in Figures 101 and 102, for both simultaneous and sequential injection cases the temperature increases gradually from the wall temperature  $275^\circ\text{C}$  to  $300^\circ\text{C}$ . The similarity of temperature evolution between these two cases implies a similar performance of these two injection schemes.

The time evolution of  $\text{NaNO}_2$  concentrations at the position 2m from the pipe inlet for both simultaneous and sequential injection cases is also plotted in Figures 103 and 104, respectively. In this simulation study,  $\text{NaNO}_2$  is the limiting reactant because the concentration of  $\text{NaNO}_2$ , 1.45 mol/l flown into the pipe is smaller than that of  $\text{NH}_4\text{Cl}$ , 1.85 mol/l. As shown in Figure 103, for the simultaneous flow case the  $\text{NaNO}_2$  mass fraction reaches a maximum of  $4 \times 10^{-5}$  at 30 seconds of reaction, whereas for the sequential flow case, shown in Figure 104, the  $\text{NaNO}_2$  mass fraction reaches a significantly higher maximum of  $1.3 \times 10^{-3}$ . Taking into account the dispersion of fluids, we found that  $\text{NaNO}_2$  is almost completely consumed in the simultaneous flow case but there still remains 30% of  $\text{NaNO}_2$  unreacted in the sequential flow case. This incompleteness of  $\text{NaNO}_2$ - $\text{NH}_4\text{Cl}$  reaction indicates that the strategy of reactant injection can be further improved in order to achieve both a complete usage of reactants and a temperature of fluids sufficiently high for paraffin dissolution in pipelines.

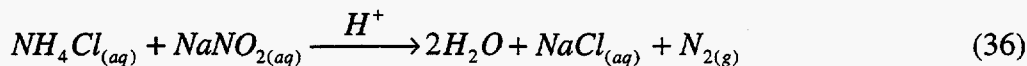
### 3.10 Simulation of Exothermic Reactive Fluid Flow in a Pipeline

An exothermic reaction between  $\text{NH}_4\text{Cl}$  and  $\text{NaNO}_2$  that is catalyzed by  $\text{H}^+$ -ion takes place inside a pipeline modeled as a tubular reactor with dispersion. Because the ocean floor is at  $5^\circ\text{C}$ , the reaction mixture is cooled as it flows through the pipeline. In order to deliver the heat release at long distances from the pipeline entrance, pulses of the reactants separated by an inert may be injected as shown in Figure 105a and 105b.

The objective is to compute the average temperature of one set of pulses as a function of the location inside the pipeline and to investigate the effect of pulse width on the extent of delay in the reaction. The reaction system is as shown below:



An example is the aqueous exothermic reaction between  $\text{NH}_4\text{Cl}$  (or  $\text{NH}_4\text{NO}_3$ ) and  $\text{NaNO}_2$  which can be catalyzed by acids, such as acetic acid, as shown below (Ashton *et al.*, 1989):



$$\Delta H_R = -334.47 \text{ kJ/mol}$$

The kinetics of this exothermic reaction were investigated in the laboratory whereby temperature-time profile was recorded as the reaction proceeded adiabatically in a well-mixed batch reactor. Results show that the reaction kinetics can be expressed by the following power law rate equation:

$$-r_{\text{NH}_4\text{Cl}} = -r_{\text{NaNO}_2} = k[\text{NH}_4\text{Cl}]^{1.2}[\text{NaNO}_2]^{1.5}[\text{H}^+]^{1.6} \quad (37)$$

The rate constant  $k$  can be expressed in an Arrhenius' form as shown below

$$k = k_1 \exp\left[\frac{E}{R}\left(\frac{1}{T_1} - \frac{1}{T}\right)\right] \quad (38)$$

where  $k_1 = 2.1 \text{ (dm}^3/\text{mol)}^{3.3} \text{ s}^{-1}$ ,  $\frac{E}{R} = 8000 \text{ K}$ ,  $T_1 = 298 \text{ K}$

If acetic acid is used as a catalyst then  $\text{H}^+$ -ion concentration can be expressed as

$$\text{H}^+ = (1.76 \times 10^{-5} [\text{CH}_3\text{COOH}])^{1/2} \text{ mol/dm}^3$$

Other parameters (typical for subsea pipelines) are as follows:

Diameter of the Pipeline, $d_i = 0.3 \text{ m}$
Length of the Pipeline, $L = 30000 \text{ m}$
Average Velocity, $u = 1 \text{ m/s}$
Fluid Density, $\rho = 1000 \text{ kg/m}^3$
Fluid Viscosity, $\mu = 0.001 \text{ Pa s}$
$C_p = 4.18 \text{ kJ/kg}$
Inlet Temperature, $T_0 = 25 \text{ }^\circ\text{C}$
Surrounding Temperature, $T_{oc} = 5 \text{ }^\circ\text{C}$
Average Overall Heat Transfer Coefficient, $U = 20 \text{ W/m}^2\text{K}$
Reynolds Number, $\text{Re} = \frac{d_i u \rho}{\mu} = 3 \times 10^5$

Sodium nitrite also reacts with acetic acid; however the rate of this side reaction is negligible as compared to the reaction between ammonium chloride and sodium nitrite. In order to minimize the reaction between sodium nitrite and acetic acid, acetic acid is mixed in the pulse of ammonium chloride.

**3.10.1 Governing Differential Equations** : A dispersed plug flow model (Fogler, 1992) is used to solve this problem. The simplified governing equations of mass and energy balance in Lagrangian coordinates are as follows:

Dimensionless Mass Balance Equation

$$\frac{DC_i^*}{D\theta} = Pe_m \frac{\partial^2 C_i^*}{\partial z^2} + \frac{L}{uC_{i0}} (r_i), \quad i = 1, 2, 3 \quad (39)$$

where  $i=1$  represents  $\text{NH}_4\text{Cl}$ ;  $i=2$  represents  $\text{NaNO}_2$ ;  $i=3$  represents  $\text{CH}_3\text{COOH}$ ;  $C_i^* = C_i/C_{i0}$ , is the dimensionless concentration and  $C_{i0}$  is the concentration at the entrance;  $L$  is the total length of the pipeline;  $u$  is the average velocity inside the pipeline;  $\theta = tu/L$ , is the dimensionless time;  $z = x/L$ , is the dimensionless distance;  $r_i$  is the rate of reaction with respect to the species  $i$ ; since  $\text{CH}_3\text{COOH}$  is a catalyst  $r_3 = 0$ ;  $Pe_m = D_e/uL$ , is the Peclet number for mass transfer and  $D_e$  is the material dispersion coefficient;  $\frac{D}{D\theta} = \left( \frac{\partial}{\partial \theta} + \frac{\partial}{\partial z} \right)$  is the time derivative in Lagrangian coordinates.

### Dimensionless Energy Balance Equation

$$\frac{DT^*}{D\theta} = Pe_t \frac{\partial^2 T^*}{\partial z^2} + \frac{L(\Delta H_A \times r_A)}{\rho C_p u (T_o - T_{oc})} - \frac{4UL}{\rho C_p u d_i} T^* \quad (40)$$

where  $T^* = (T - T_{oc}) / (T_o - T_{oc})$ , is a dimensionless temperature having  $T_o$  and  $T_{oc}$  as the inlet temperature and ocean temperature respectively;  $\rho$  is the density of the liquid;  $C_p$  is the heat capacity of the liquid;  $d_i$  is the diameter of the pipeline;  $U$  is the overall heat transfer coefficient for the heat transfer through the pipe wall;  $\Delta H_A$  is the heat of reaction per mole of A reacted;  $r_A$  is the rate of reaction of A;  $Pe_t = \alpha_t / uL$  is the Peclet number for heat transfer and  $\alpha_t$  is the thermal dispersion coefficient.

For  $Re = 3 \times 10^5$  (turbulent flow), the Peclet number (for material dispersion) is given as (Levenspiel, 1958)

$$\frac{D_e}{ud_i} = 0.21, \Rightarrow Pe_m = \frac{D_e}{uL} = \frac{D_e}{ud_i} \times \frac{d_i}{L} = 2.1 \times 10^{-6} \quad (41)$$

In the case of turbulent flow, the Peclet number for thermal dispersion is assumed equal to that for material dispersion (Bird *et al.*, 1960).

$$Pe_t = \frac{\alpha_t}{uL} = Pe_m = 2.1 \times 10^{-6} \quad (42)$$

**3.10.2 System of Single Set of Pulses :** The schematic of the system of single set of pulses is shown in Figure 106a having the inlet conditions

$$C_{A0} = 7.5 \times 10^3 \text{ mol/m}^3$$

$$C_{B0} = 12.5 \times 10^3 \text{ mol/m}^3$$

$$T = T_m$$

The governing equations were discretized into their finite-difference analogs. The resulting finite-difference equations were then implicitly solved.

**3.10.2.1 Effect of Spacing.** Figures 106a and 106b show the maximum temperature trajectory inside the pipeline for different widths of inert spacing. Increase in inert spacing delays the reaction because increase in inert spacing delays the mixing of the two reactants. Increase in the inert spacing also decreases the concentration of the reactants before their mixing because of axial dispersion of the reactants. This decrease in concentration of reactants decreases the maxima of maximum temperature with increase in inert spacing.

**3.10.2.2 Effect of Inlet Temperature.** Figures 107a and 107b show the maximum temperature trajectory inside the pipeline for different values of inlet temperatures. The maxima of the maximum temperature trajectory decreases with a decrease in inlet temperature. As the rate of reaction is small at low temperatures, the delay of the reaction increases with a decrease in inlet temperature.

Figures 108a and 108b show the temperature trajectory at two different locations inside the pipeline for the case when  $A=125\text{m}$ ,  $B=75\text{ m}$ ,  $S=375\text{ m}$  and  $T_{in}=25^\circ\text{C}$ . Temperature at a particular location remains essentially same except when the pulses of reactants reach that location. Figures 109a and 109b show the distribution of temperature and concentration of the reactants in the pulses of reactants and inert after 30 km of travel by these pulses.

**3.10.3 System of Multiple Set of Pulses :** The schematic of the system of single set of pulses is shown in Figure 44b having the following boundary conditions

$$C_1^* = C_3^* = 1, \quad \text{at } z = 0, \quad \text{for } n\tau \times \left(\frac{u}{L}\right) \leq \theta < (n+0.25)\tau \times \left(\frac{u}{L}\right)$$

$$C_1^* = C_3^* = 0, \quad \text{at } z = 0, \quad \text{for } (n+0.25)\tau \times \left(\frac{u}{L}\right) \leq \theta < (n+1)\tau \times \left(\frac{u}{L}\right)$$

$$C_2^* = 1, \quad \text{at } z = 0, \quad \text{for } (n+0.5)\tau \times \left(\frac{u}{L}\right) \leq \theta < (n+0.75)\tau \times \left(\frac{u}{L}\right)$$

$$C_2^* = 0, \quad \text{at } z = 0, \quad \text{for } n\tau \times \left(\frac{u}{L}\right) \leq \theta < (n+0.5)\tau \times \left(\frac{u}{L}\right)$$

$$\text{and } (n+0.75)\tau \times \left(\frac{u}{L}\right) \leq \theta < (n+1)\tau \times \left(\frac{u}{L}\right)$$

$$T^* = 1, \quad \text{at } z = 0, \quad \text{for all } \theta$$

where  $\tau$  is the injection time period for one set of pulses (e.g. AIBI) and  $n=0, 1, 2, \dots, N$  represents the count on the set of pulses being injected in the pipeline. The widths of all pulses of the different materials,  $w$ , are assumed to be the same and are directly related to the injection time period for one set of pulses,  $\tau$ , as follows

$$w = \frac{\tau \times u}{4} \tag{43}$$

The governing equations are four simultaneous coupled nonlinear partial differential equations for the dependent variables  $C_1^*$ ,  $C_2^*$ ,  $C_3^*$ , and  $T^*$  as a function of independent variables  $\theta$  and  $z$ . These partial differential equations are discretized in the finite difference equations and solved using an implicit technique.

**3.10.4 Results and Discussions** : The movement of the system of pulses inside the pipeline can be visualized as the propagation of a temperature wave whose maxima and minima can respectively be expected to occur at the maximum and minimum overlap of the concentration waves of the reactants inside the pipeline. In order to describe the propagation of reactant concentration waves and temperature wave inside the pipeline, let us consider a particular case of the pulse flow having  $C_{10} = C_{20} = 7 \text{ mol/dm}^3$ ,  $C_{30} = 1 \text{ mol/dm}^3$ , and a pulse size 30 m.

Figures 110 through 114 show the local concentration and temperature profiles when the center of the inert spacer reaches 0 km, 3 km, 5 km, 10 km, and 20 km respectively from the entrance of the pipeline. All sets of pulses (e.g. BIAIB) are identical as far as the temperature and concentration waves are concerned. Hence, the control volume for these concentration and temperature waves (in Figures 110 through 114) consists of half pulse width of A ( $\text{NH}_4\text{Cl}$  and  $\text{CH}_3\text{COOH}$ ), one pulse width of inert, and half pulse width of B ( $\text{NaNO}_2$ ). Hence, only one half of the concentration wave (i.e. between adjacent maxima and minima) are shown in these figures.

Figure 110 shows dimensionless concentration profiles for  $\text{NH}_4\text{Cl}$ ,  $\text{NaNO}_2$ , and  $\text{CH}_3\text{COOH}$  and temperature profile at the entrance of the pipeline. Two distinct non-overlapping half pulses of the reactants separated by an inert spacer can be seen in this figure showing a constant temperature profile of  $25^\circ\text{C}$ . Figure 111 shows dimensionless concentration and temperature profiles when the center of the inert spacer is at 3 km. The reaction zone where the two reactants are mixed is primarily between 2.98 km and 3.02 km. The maxima in the temperature profile shows the extent of heat release in the reaction zone. The dimensionless concentration profile for the catalyst  $\text{CH}_3\text{COOH}$  (i.e.  $C_3$ ) is higher than that of the reactant  $\text{NH}_4\text{Cl}$  (i.e.  $C_1$ ) because of the consumption of the reactants during the reaction.

Figure 112 and 113 show dimensionless concentration and temperature profiles when the center of the inert spacer is at 5 km and 10 km respectively. It can be observed that there is a smaller degree of overlap between the two reactant concentration profiles at these locations as compared to that at 3 km (i.e. Figure 111). The reason is that the temperature at these locations is relatively higher than that at 3 km which increases the reaction rate such that it becomes almost instantaneous. An overlap of the reactant concentration profiles is not possible for an instantaneous reaction. It can also be observed that the amplitude of the temperature wave decreases as the system moves from 5 km to 10 km which indicates the existence of thermal dispersion.



Figure 114 shows dimensionless concentration and temperature profiles at a time when the center of the inert spacer is at 20 km. The flat temperature profile indicates that the system is in the state of complete thermal mixing. However, the reactant concentration profiles are distinct from each other and their magnitude is less than 4% of the initial value. The reaction is almost complete at this location, hence the system will be cooled down by the surrounding sea water (at 5°C) while traveling from 20 km to 30 km (i.e. exit of the pipeline).

In order to compare the results for various cases, an average temperature of the thermal wave is computed at various locations of the pipeline. The average temperature of one set of pulses is the volume average temperature defined as:

$$T_{av} = \frac{\int_0^{4w} T dx}{4w} \quad (44)$$

**3.10.4.1 Effect of Pulse Width.** The reaction between aqueous  $\text{NH}_4\text{Cl}$  and  $\text{NaNO}_2$  pulses flowing inside the pipeline was simulated and studied for various pulse widths (sizes). Figure 115 shows the average temperature  $T_{av}$  at various locations in the pipeline. All temperatures are reported as the volume average temperature as defined previously. The solid line shows the drop in the fluid temperature that would occur in the absence of reaction. For a pulse width of 10 m (i.e. 10 m  $\text{NH}_4\text{Cl}$  and  $\text{CH}_3\text{COOH}$ , 10 m inert, 10 m  $\text{NaNO}_2$ ) the maximum average temperature is reached very close to the entrance and then drops due to the cooling of the fluid as it moves through the pipeline. As the pulse width is increased, the time required for the reactants to mix is increased thereby delaying the reaction. The longer the delay in the reaction, the higher is the heat loss to the surrounding before the system reaches the location of maximum average temperature. Hence, the maximum average temperature reached in the pipeline decreases with increasing pulse width. However, the average temperature reached at large distances from the inlet (e.g. 25 km) increases with increasing the pulse width.

**3.10.4.2 Effect of Concentration of Reactants.** Figure 116 shows the average temperature trajectories for various concentrations of reactants keeping all other parameters constant. The higher the reactant concentration, the higher is the heat release. Hence, average temperature trajectory for a higher reactant concentration shows higher average temperatures throughout the entire pipeline.

**3.10.4.3 Effect of Concentration of Catalyst.** Figures 117 and 118 show the average temperature trajectories for various concentrations of catalyst (acetic acid) keeping all other parameters same. The lower the acid concentration, the slower will be the reaction rate. Hence, average temperature trajectory for lower catalyst concentration exhibits larger delay in the heat

release. Higher catalyst concentration shows a sharper increase in the average temperature inside the pipeline.

**3.10.4.4 Dispersion of the Molten Wax.** The above results show that this technique is successful in delaying the reaction and supplying heat to those segments of the pipeline which are highly susceptible to wax deposition. These results also show that the heat of reaction is sufficient to melt the wax deposited on the wall of the pipeline. But, in order to effectively disperse the molten wax and avoid its re-deposition, a certain amount of surfactant or dispersant should also be added in the fluid.

### **3.11 Simulation of $\text{NaNO}_2$ - $\text{NH}_4\text{Cl}$ Reaction (in Water/Oil Emulsion) in a Pipeline**

This section focuses on the reaction between emulsified  $\text{NaNO}_2$  and  $\text{NH}_4\text{Cl}$  flowing inside the pipeline.

**3.11.1 Determination of Kinetics** : A reactive W/O emulsion system was prepared for the dissolution of paraffin deposited on the wall of pipelines. The components of this system include (1) Heptane, the continuous oil phase, (2) dispersed aqueous droplets: to host the exothermic  $\text{NaNO}_2$ - $\text{NH}_4\text{Cl}$  reaction, and (3) sorbitan mono-laurate (SML), a nonionic surfactant: to provide steric stability to the emulsion. In this study, two separate emulsions having aqueous ionic phases of the two different reactants, were separately prepared by stirring the mixture of two phases at 5000 rpm for five minutes. These two emulsions were mixed in an adiabatic reactor and the temperature of emulsion mixture was measured during the reaction period. The kinetics of  $\text{NaNO}_2$ - $\text{NH}_4\text{Cl}$  reaction in W/O emulsions was then quantified from the initial rate of increase of emulsion temperature.

**3.11.1.1 Effect of Stirring Rate.** Figures 119 to 124 show the effect of stirring rate on the temperature evolution profiles of water/heptane solutions with the given reactant and surfactant compositions ( $\text{NH}_4\text{Cl}$ ,  $\text{NaNO}_2$  acetic acid and SML) and 1:1 volume ratio of aqueous solution and heptane. In the initial phase of reaction (temperature below  $35^\circ\text{C}$ ), there is no effect of stirring rate on the temperature evolution profiles. Deviations for higher temperatures is because of the fact that higher stirring rate departs the system from perfect adiabatic conditions. Nonlinear regression of the points below  $40^\circ\text{C}$  gives the kinetics of the reaction in W/O emulsion rate.

**3.11.1.2 Effect of Surfactant Concentration.** Figure 125 shows the temperature evolution profiles of water/heptane emulsions containing constant reactant concentrations but different concentrations of SML. The initial rate of temperature increment decreases as the concentration of SML is increased. The kinetics of the initial reaction rate shows that the pre-

exponential factor decreases by a factor of 0.011 and 0.009 for 1% and 2% (v/v) SML concentration respectively.

Rate Law from Nonlinear Regression :

$$r_A = -f \times k [NH_4Cl]^{1.2} [NaNO_2]^{1.5} [H^+]^{1.6} \quad (45)$$

where

$$f = 0.011 \quad \text{for 1\% SML}$$

$$= 0.009 \quad \text{for 2\% SML}$$

Other features of the rate law were found to be same as given in equation (21). The factor  $f$  decreases with an increase in SML concentration.

**3.11.2 Simulation of Alternate Pulse Flow of the Emulsions in a Pipeline :** A simplified computational fluid dynamics model is developed to simulate the flow of alternate pulses of emulsions, consisting one of the aqueous reactant solutions stabilized in heptane using surfactant (SML). The emulsified aqueous droplets having different reactants are expected to collide after dispersing through the pulses of each other providing a delay in the chemical reaction. The delay is required so as to provide heat to the regions further down the pipeline where paraffin plugging takes place. The exothermicity of the reaction raises the fluid temperature, but at the same time it also increases the loss of heat from the pipe to the surroundings (ocean). It is assumed that these droplets do not coalesce because of the generation of nitrogen gas. Hence, when the two droplets of different reactants collide, the reactants diffuse from one droplet to another and then they get separated because of the gas generation. It is also assumed that these droplets are monodisperse and do not change sizes during collision. The governing material and energy balance equations are solved using the finite-difference method.

Species Conservation :

$$\frac{\partial C_i}{\partial \theta} = -\frac{\partial C_i}{\partial z} + \frac{\alpha_i}{uL} \nabla C_i + \frac{L}{u} (r_A) \quad (46)$$

Energy Balance :

$$\frac{\partial T^*}{\partial \theta} = -\frac{\partial T^*}{\partial z} + \frac{D_e}{uL} \nabla^2 T^* + \frac{L}{\rho C_p u} (\Delta H^* r_A) - \frac{4uL}{\rho C_p u d_i} T^* \quad (47)$$

where

$$T^* = (T - T_{ocean}), \quad T_{ocean} = 5^{\circ} C$$

$$\theta = \frac{ut}{L}, \quad \nabla^2 = \frac{\partial^2}{\partial z^2}, \quad z = \frac{x}{L}$$

$$u = 0.75 \text{ m/s}, \quad L = 30,000 \text{ m}$$

$$\Delta H = -334.47 \text{ kJ/mol}$$

$$D_e = \alpha_t = 0.094 \text{ m}^2/\text{s}, \quad d_i = 0.3 \text{ m}$$

$$r_A = -k[NH_4Cl]^{1.2}[NaNO_2]^{1.5}[H^+]^{1.6}$$

$$k = k_1 \exp\left[\frac{E}{R}\left(\frac{1}{T_1} - \frac{1}{T}\right)\right], \quad H^+ = (1.76 * 10^{-5}[CH_3COOH])^{1/2}$$

$$\frac{E}{R} = 8000 \text{ K}$$

$$T_1 = 298 \text{ K}$$

(48)

The governing equations were discretized into their finite-difference analogs. The resulting finite-difference equations were then implicitly solved. The propagation of pulses correspond to the movement of thermal wave inside the pipeline. The average temperature is an average throughout the whole temperature wave.

### 3.11.3 Simulation Results

**3.11.3.1 Effect of Pumping Mixture of the Two Emulsions.** Figure 126 shows the temperature trajectory inside the pipeline for different concentration of the reactants when an instant mixture of the two emulsions is fed in the pipeline. Each emulsion is 1:1 in heptane and aqueous phase, concentration of each reactants is the same in both of the aqueous solutions, and 2% surfactant (SML) is added to provide the steric stability to the aqueous droplets inside the emulsions. In all cases of the concentrations considered here, the location of the maximum temperature is within 4 miles. Hence, this will be ineffective if the paraffin plugging is at 15-20 miles away from the pipe entrance. In order to study the delay in the reaction, the flow of alternate pulses of the two emulsions is simulated. The system of alternate pulses of the reactive emulsions delays the reaction by delaying the mixing of the two reactants.

**3.11.3.2 Propagation of the Temperature Wave in the Pipeline.** Figures 127 shows a sketch of the pipeline having a continuous system of alternate pulses of the two emulsions (A and B) being injected at the entrance. The width of each pulse is 200 m, concentration of the reactants in the aqueous phases is  $4 \text{ kmol/m}^3$ , and 2% surfactant (SML) is used to stabilize the aqueous droplets. Figures 128-131 show the temperature waves at the location of 5 km, 10 km, 20 km, and 30 km respectively inside the pipeline. The peak of the temperature wave almost remains at the junction of the two different emulsion pulses. On the other hand, the lowest point of the temperature wave remains close to the mid point of each pulse. It can also be observed that the amplitude of the temperature wave is small for the locations which are away from the pipe entrance because the mixing of the two emulsion pulses increases as the system moves inside the pipeline.

**3.11.3.3 Effect of Pumping Alternate Pulses of the Two Emulsions.** Figure 132 shows the average temperature trajectory inside the pipeline for the cases of the reactant concentrations 4, 4.5 and  $5 \text{ kmol/m}^3$ . Comparison between figure 126 and figure 132 shows that this technique is effective in supplying heat further down the pipeline where paraffin plugging is more likely to take place.

### **3.12 Encapsulation of the Catalyst**

The catalyst of the reaction between  $\text{NaNO}_2$  and  $\text{NH}_4\text{Cl}$  is an acid. Acid anhydride is encapsulated in gelatin capsules and added to the reactive mixture of the two reactants. The reaction takes place only when the gelatin capsule is dissolved and acid anhydride gets into contact with water. Hydrolysis of acid anhydride gives acid which catalyses the reaction. The preliminary experimental results are shown in the figure 133. The desired delay in the reaction can be achieved by knowing the dissolution kinetics of gelatin. Then the thickness of the capsule will accordingly be designed.

### 3.13. Nomenclature for Sections 3.1 through 3.9

$a$  = heat transfer area per unit volume

$A$  = rate constant

$A_o$  = pre-exponential factor

$C_1$  = initial concentration

$C_i$  = concentration of  $i$ -component

$C_o$  = reference concentration

$C_{pi}$  = specific heat at constant pressure of species  $i$ '

$D$  = pipe diameter

$D_{ij}$  = diffusion coefficient

$E$  = activation energy

$h$  = enthalpy

$M$  = molecular weight

$m_{j'}$  = mass fraction of species  $j$ '

$n_{j,k}$  = stoichiometric coefficient for species  $j$ ' in reaction  $k$

$p_o$  = reference pressure

$Q_{ext}$  = the heat rate by external boundary

$R$  = gas constant

$r$  = reaction rate

$R_{j'}$  = the mass rate of creation or depletion by chemical reaction

$S_{reaction}$  = rate of heat production by chemical reaction

$t$  = time

$T_1$  = initial temperature

$T_a$  = external temperature

$T_o$  = reference temperature

$V$  = average velocity

$v$  = velocity

$X_{j'}$  = mole fraction of species  $j$ ' in the mixture

$x$  =  $x$ -coordinate

$y$  =  $y$ -coordinate

$z$  =  $z$ -coordinate

$\alpha_{j,k}$  = exponent on the concentration of reactant  $j$ ' in reaction  $k$

$\beta_k$  = temperature exponent

$\rho$  = density

$\mu$  = viscosity

$\sigma$  = Lennard-Jones parameter

$\Omega_{\mu}$  = reduced collision integral

$\Omega_D$  = collision integral

$$Re = \text{Reynolds number} = \frac{D \cdot V \cdot \rho}{\mu}$$

$$Fr = \text{Froude number} = \frac{V^2}{g \cdot D}$$

$$Sc_m = \text{Schmidt number based on molecular diffusion} = \frac{\mu}{\rho \cdot D_{AB}}$$

$$Sc_t = \text{Schmidt number based on turbulent diffusion} = \frac{\mu}{\rho \cdot D_t}$$

$$Sc^T = \text{Schmidt number based on solet diffusion} = \frac{\mu}{\rho \cdot D^T}$$

$$Pr = \text{Prandtl number} = \frac{C_p \cdot \mu}{k}$$

$$Br = \text{Brinkman number} = \frac{\mu \cdot V^2}{k(T_1 - T_0)}$$

$\Phi^*$  = Dissipation function

### 3.14. Nomenclature for Sections 3.10 through 3.12

$C_i^*$  = dimensionless concentration of  $i$ -component,  $i = 1$  means  $\text{NH}_4\text{Cl}$ ,  $i = 2$  means  $\text{NaNO}_2$ , and  
 $i = 3$  means  $\text{CH}_3\text{COOH}$

$C_{i0}$  = initial concentration of  $i$ th component

$C_p$  = heat capacity of the fluid

$d_i$  = pipe diameter

$D_e$  = dispersion coefficient

$E$  = activation energy

$k$  = rate constant

$n_i$  = number concentration of  $i$ -droplets

$n_{i0}$  = initial number concentration of  $i$ -droplets

$Pe_t$  = Peclet number for thermal dispersion

$Pe_m$  = Peclet number for material dispersion

$r_i$  = reaction rate with respect to species  $i$

$r_A$  = reaction rate of reactant A

$R$  = universal gas constant

$Re$  = Reynolds number

$t$  = time  
 $\tau$  = injection time period for one set of pulses  
 $T_o$  = initial temperature of the fluid  
 $T_{oc}$  = temperature of the surroundings (ocean)  
 $T_{av}$  = average temperature of a single set of pulses  
 $u$  = average velocity  
 $U$  = overall heat transfer coefficient  
 $L$  = length of the pipeline  
 $\alpha_t$  = thermal dispersion coefficient  
 $\rho$  = density of the fluid  
 $w$  = pulse width



#### 4. References

1. Jiang, T.S., Kawanaka, S., Mansoori, G.A., "Asphaltene Deposition and its Role in Petroleum Production and Processing", *Arabian J. Sc. Eng.*, 13(1), 17-34, 1988.
2. Haskett, C.E., Tartera, M., "A Practical Solution to the Problem of Asphaltene Deposits-Hassi Messaoud Field, Algeria", SPE 994, 1965.
3. Lichaa, P.M., Herrera, L., "Electrical and Other Double Effects Related to the Formation and Prevention of Asphaltene Deposition: Problem in Venezuela Crudes", SPE 5304, 1975.
4. Bungler, J.W., Li, N.C., Eds., "Advances in Chemistry Series, Vol.195: Chemistry of Asphaltenes", ACS, Washington D.C., 1981.
5. Speight, J.G., "The Chemistry and Technology of Petroleum", 2nd.Ed., Chapter 11, Marcel Dekker, NY, 1991.
6. Jacobs, I.C., Thorne, M.A., "Asphaltene Precipitation During Acid Stimulation Treatment", SPE 14823, 1986.
7. Rogacheva, O.V. et al., "Study of Surfactant Acitivity of Asphaltenes in Petroleum Residues", *Colloid J. USSR*, 42(3), 586-89, 1980.
8. *ASTM D2007-80*, "Standard test method for characteristic groups in rubber extender and processing oils by the clay-gel adsorption chromatographic method", 1983 ASTM Annual Book of ASTM Standards, 05.01, ASTM, Philadelphia, PA.
9. *ASTM D664-81* "Standard test method for neutralization number by potentiometric titration", 1983 ASTM Annual Book of ASTM Standards, 05.01, ASTM, Philadelphia, PA.
10. Chang, Chia Lu, Fogler, H.S., "Stabilization of Asphaltenes in Aliphatic Solvents Using Alkylbenzene-Derived Amphiphiles. 1. Effect of the Chemical Structure of Amphiphiles on Asphaltene Stabilization", *Langmuir*, 10, 1749-57, 1994.
11. Chang, Chia Lu, Fogler, H.S., "Stabilization of Asphaltenes in Aliphatic Solvents Using Alkylbenzene-Derived Amphiphiles. 2. Study of the Asphaltene-Amphiphile Interactions and Structures Using Fourier Transform Infrared Spectroscopy and Small Angle X-Ray Scattering Techniques", *Langmuir*, 10, 1758-66, 1994.
12. Fogler, H.S., "Elements of Chemical Reaction Engineering", 2nd. Ed., Chapter 10, Prentice-Hall, NJ, 1992.
13. Jacobs, I.C., "Chemical Systems for the Control of Asphaltene Sludge During Oilwell Acidizing Treatments", SPE 18475, 1989.
14. Fredd, C.N., Fogler, H.S., "Alternative Stimulation Fluids and Their Impact on Carbonate Acidizing", SPE 31074, 1996.

15. Hirsch, J.O., Curtiss, C.F., Bird, R.B., "Molecular Theory of Gases and Liquids", John Wiley & Sons, New York, NY, 1954.
16. Fluent Incorporated, "FLUENT User's Guide", Fluent Inc., January 1995.
17. Acharya, S., Moukalled, F.H., "Improvements to Incompressible Flow Calculation on a Nonstaggered Curvilinear Grid," *Numer. Heat Transfer B*, 15(2), 131-152, June 1989.
18. Patankar, S.V., "Numerical Heat Transfer and Fluid Flow," Hemisphere Publishing Corp., Washington D.C., 1980.
19. Paric, M., Kessler, R., Scheuerer, G., "Comparison of Finite-Volume Numerical Methods with Staggered and Collocated Grids," *Comput. Fluids*, 16(4), 389-403, 1988.
20. Brown, T.S., Niesen, V.G., Erickson, D.D., "Measurement and Prediction of the Kinetics of Paraffin Dissolution", SPE 26548, 1993.
21. de Boer, R.B. et al., "Screening of Crude Oils for Asphalt Precipitation: Theory, Practice, and the Selection of Inhibitors, SPE 24987, 1992.
22. Permsukarome, Pornruedee, Chang, Chialu, Fogler, H. Scott, "Kinetic study of asphaltene dissolution in amphiphile/alkane solutions, *Ind. & Eng. Chem. Res.*, 36, 3960-67, 1997.

## 5. Tables and Figures

Table 1. Asphaltenes used in this study.

Asphaltene Name	Preparation	Company
Mobil #0	Precipitated from crude	Mobil
Venezuela	Precipitated from crude	INTEVEP
Villano Field	Precipitated from crude	ARCO
Kuparuk Residual	Precipitated from residual oil	ARCO
West Sak	Precipitated from crude	ARCO

Table 2. Alkylbenzene-derived amphiphiles used in this study




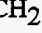
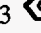



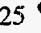


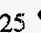
Name	Abbrev.	Chemical structure	Source	M.W.	Purity (wt %)
p-Cresol	C	CH <sub>3</sub>  OH	Aldrich	108.14	99
Ethyl phenol	EP	C <sub>2</sub> H <sub>5</sub>  OH	Aldrich	122.17	99
n-butyl phenol	BP	n-C <sub>4</sub> H <sub>9</sub>  OH	Kodak	150.22	97
sec-Butyl phenol	SBP	(CH <sub>3</sub> ) <sub>2</sub> CHCH <sub>2</sub>  OH	Aldrich	150.22	96
n-Hexyl phenol	HP	n-C <sub>6</sub> H <sub>13</sub>  OH	Kodak	178.28	97
n-octyl phenol	OP	n-C <sub>8</sub> H <sub>15</sub>  OH	Kodak	206.33	97
tert-Octyl phenol	TOP	(CH <sub>3</sub> ) <sub>3</sub> CCH <sub>2</sub> C(CH <sub>3</sub> ) <sub>2</sub>  OH	Aldrich	206.33	95
n-Nonyl phenol	NP	n-C <sub>9</sub> H <sub>19</sub>  OH	Aldrich	220.36	
n-Dodecyl phenol	DP	n-C <sub>12</sub> H <sub>25</sub>  OH	Pfaltz	262	96.5
n-Nonyl benzene	NB	n-C <sub>9</sub> H <sub>19</sub>  OH	Fluka	204.36	97
n-Nonyl benzene di-oxyethylene	NBDO	n-C <sub>9</sub> H <sub>19</sub>  (OC <sub>2</sub> H <sub>4</sub> ) <sub>2</sub> OH	Aldrich	308.47	97
n-Dodecyl benzene sulfonic acid	DBSA	n-C <sub>12</sub> H <sub>25</sub>  SO <sub>3</sub> H	Pfaltz	326	97

Table 3. List of the amphiphiles' functional groups used for quantifying amphiphile concentrations by FTIR spectroscopy

Amphiphile	Wavenumber (cm <sup>-1</sup> )	Band assignment	Quantification method
NB	697	out-of-plane bending vibration of the mono-substituted benzene ring	Peak area
NBDO	1516	semi-circle stretching of para-di-substituted benzene ring	Peak area
DBSA	1173	symmetric SO <sub>2</sub> stretching	Peak height
Alkyl phenol	1516	same as above	Peak area

Table 4. List of the experimental conditions conducted in this study.

Variable evaluated	Amphiphiles	Solvents	Amphiphile Concentration (wt%)	Temperature (°C)	Flow rate (ml/min)
Concentration	NP	C7, C12	2, 4, 7, 10, 20, 30	22	1
	DBSA	C7, C12	1, 3, 5, 10, 20	22	1
Solvent	NP	C6,C7,C10,C12,C16			
	DBSA	C6,C7,C10,C12,C16			
Flow rate	NP	C7	20	22	0.1,1
Temperature	NP	C12	20	6, 22, 58	1
	DBSA	C12	5	6, 22, 58	1

Table 5. List of  $K_S$  and  $k_\infty$  values.

Amphiphile/alkane Soln.	$k_\infty$ (mole of amphiphile/l)	$K_S$ ( $\text{min}^{-1}$ )
NP/heptane	0.263	0.25
NP/dodecane	0.296	0.11
DBSA/heptane	0.110	0.12
DBSA/dodecane	0.037	0.11

Table 6. Amount of asphaltene dissolved using different good solvents and flow rates.

Solvent	1 ml / min	5 ml / min
5% NP / Heptane	0.3756 g/ml	0.3986 g/ml
7% NP / Heptane	0.4192 g/ml	0.6783 g/ml
13% NP / Heptane	0.4898 g/ml	0.4918 g/ml
20% NP / Heptane		0.8241 g/ml
5% DBSA / Heptane	0.2701 g/ml	0.1727 g/ml
10% DBSA / Heptane	0.4072 g/ml	0.2937 g/ml
20% DBSA / Heptane	0.8290 g/ml	0.5952 g/ml

Table 7. Elemental Analysis of asphaltenes precipitated in the presence and absence of ferric iron

Type of Asphaltene	% C (wt)	%H (wt)	%N (wt)	C:H molar ratio
Asphaltene from Venezuela crude (addition of heptane)	77.66	7.99	1.40	0.810
Asphaltene from Venezuela crude (addition of ferric iron)	79.76	7.33	1.63	0.907

Table 8. BET Surface areas and specific reaction rate constants for dissolution of fractions from Mobil #0 crude oil precipitate

Asphaltene	BET surface area, m <sup>2</sup> /g	Reaction rate constant, k (min <sup>-1</sup> )	Specific rxn rate constant, k <sub>sp</sub> (g.m <sup>2</sup> .min <sup>-1</sup> )
Unfractionated	0.3743	0.4702	1.2562
F1	1.4765	0.0730	0.0494
F4	7.0726	2.1169	0.2993

Table 9. Heteroatom analysis for fractions from sludge and directly from crude oil

Metal	Conc, ppm for asphaltene from crude by heptane	Conc, ppm for F30/70	Conc, ppm for F10/90	Conc, ppm for asph. from acid	Conc, ppm for asph. from acid+Fe <sup>3+</sup>
Ba	20	10	20	20	30
Cd	10	10	10	10	10
Fe	0.02	0.03	0.01	0.04	1.91
Mn	10	10	10	10	60
Ni	260	330	260	210	190
V	1300	1600	1300	1000	820
Zn	240	200	680	30	50

Table 10. List of the measured cloud point temperatures of Joliet wax and hexatriacontane in solutions containing inhibitor candidates

Wax	Joliet Wax (1 wt.%)				Hexatriacontane (1 wt.%)			
Inhibitor conc.(wt%)	1	2	4	8	1	2	4	8
Inhibitor Name	Cloud Point Temp. (°C)				Cloud Point Temp.(°C)			
Arachidyl Alcohol	30.5	31.0	33.5	37.0	28.0	32.0	36.0	39.0
Behanic Acid	31.0	31.0	32.0	35.0	28.0	33.0	39.0	44.0
Poly(ethylene vinyl acetate)	27.0	27.0	27.0	26.0	23.0	26.0	27.0	29.0
Poly(octadecene maleic anhydride)	31.0	32.0	32.0	34.0	28.0	28.0	27.0	27.0
Without inhibitors	30.0				27.0			

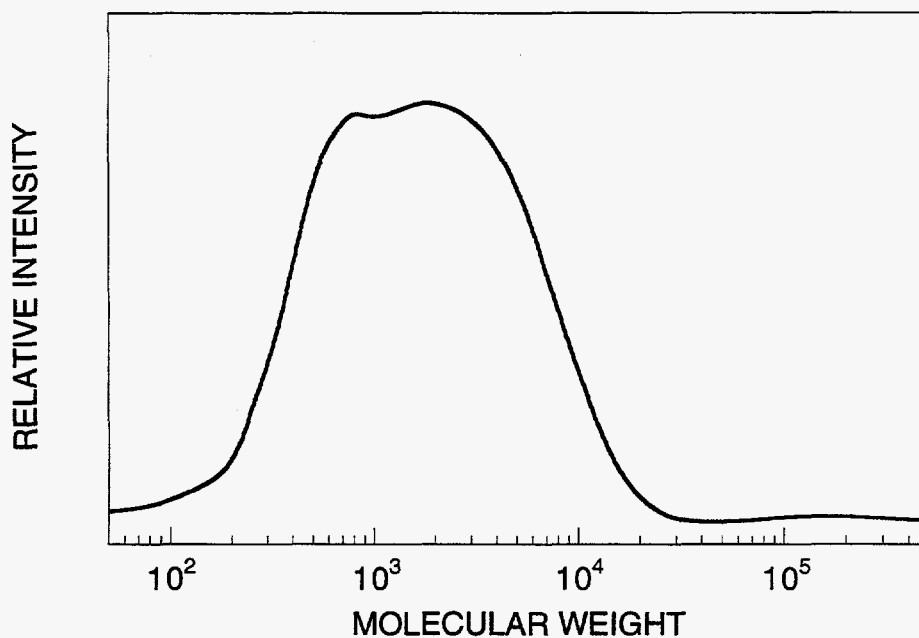


Figure 1. Molecular weight distribution of Mobil asphaltene measured by size exclusion chromatography.

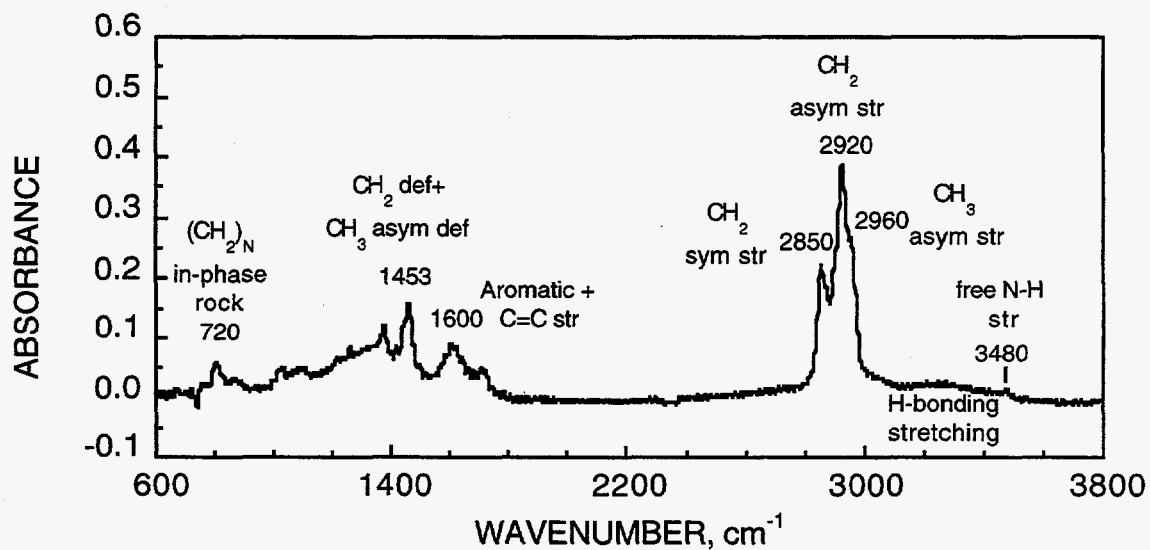


Figure 2. FTIR spectrum of Mobil asphaltene [in  $\text{CCl}_4$  (above  $1400\text{ cm}^{-1}$ ) and  $\text{CS}_2$  (below  $1400\text{ cm}^{-1}$ )].



Figure 4. Light microscopic graph of Mobil asphaltene precipitates.  
(picture dimension = 275  $\mu\text{m}$  x 165  $\mu\text{m}$ ).

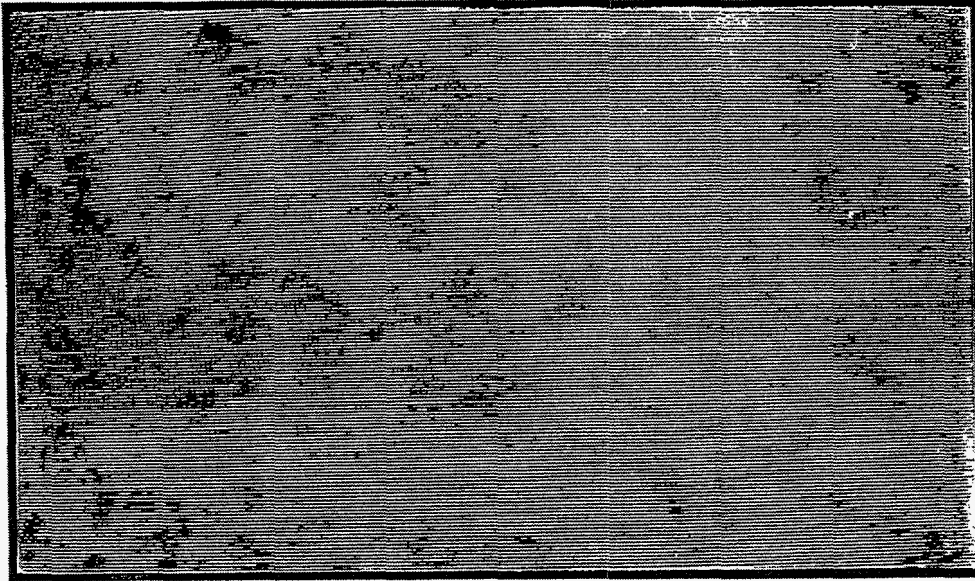
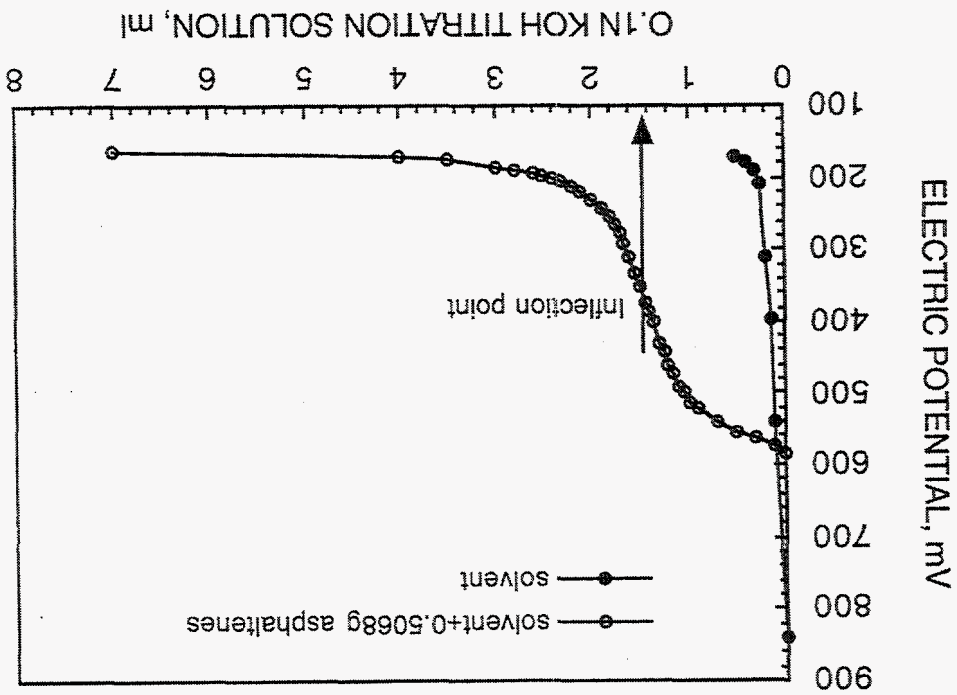


Figure 3. Potentiometric titration of the acid quantity of Mobil asphaltenes.



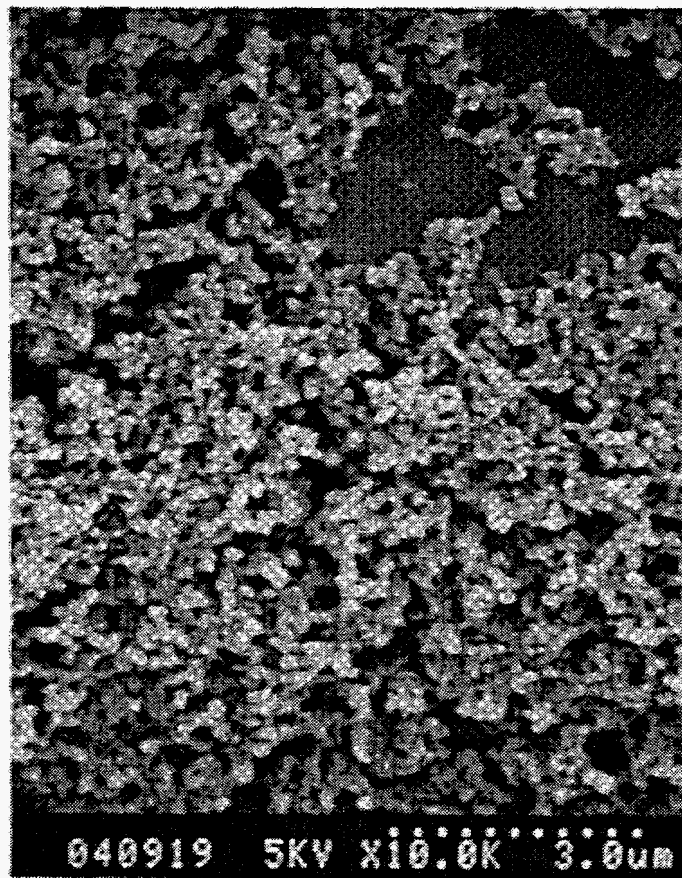


Figure 5. Scanning electron micrograph of Mobil asphaltene precipitates.

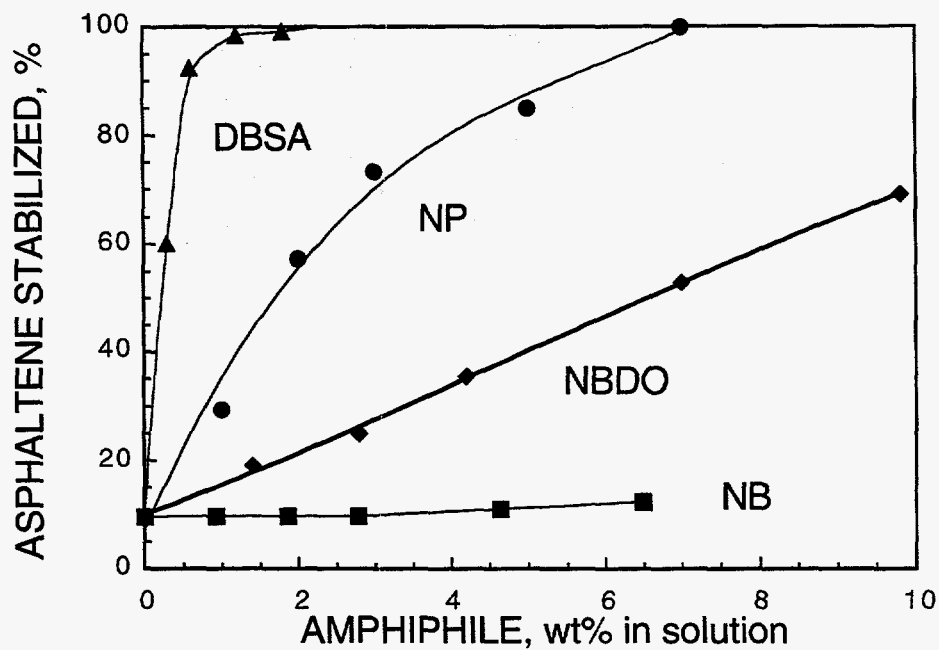


Figure 6. Asphaltenes stabilized in heptane solutions containing amphiphiles with different head groups.

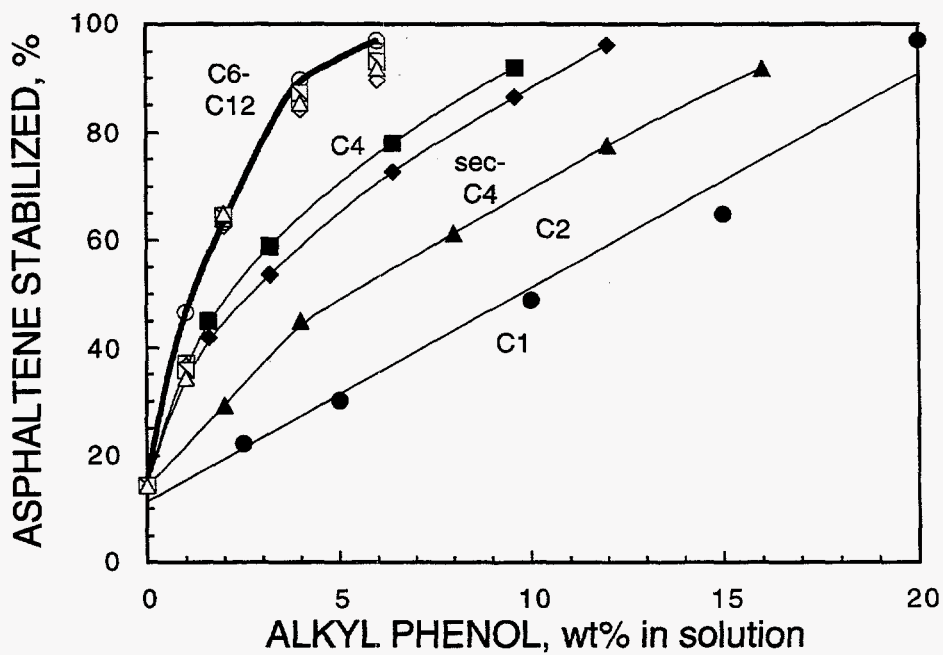


Figure 7. Asphaltenes stabilized in heptane solutions containing alkyl phenol amphiphiles with different tail lengths ( $C_n$ ,  $n$  = carbon number of the alkyl tail).

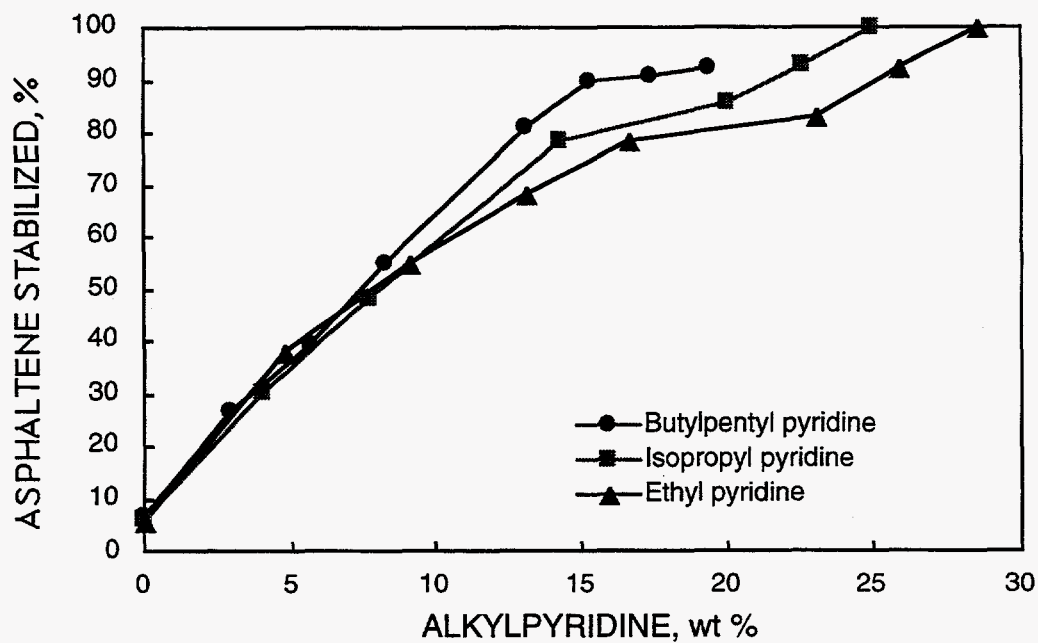


Figure 8. Kuparuk asphaltenes stabilized in heptane solution containing alkylpyridine amphiphiles.

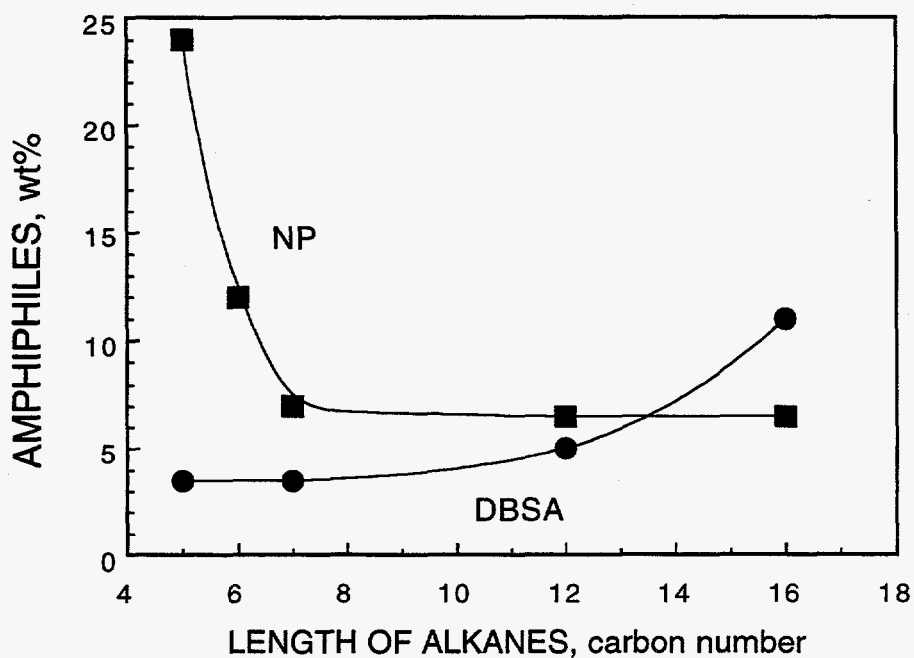


Figure 9. Minimum amount of nonyl phenol (NP) and dodecyl benzene sulfonic acid (DBSA) for completely dissolving 1 wt% asphaltenes in different alkanes.

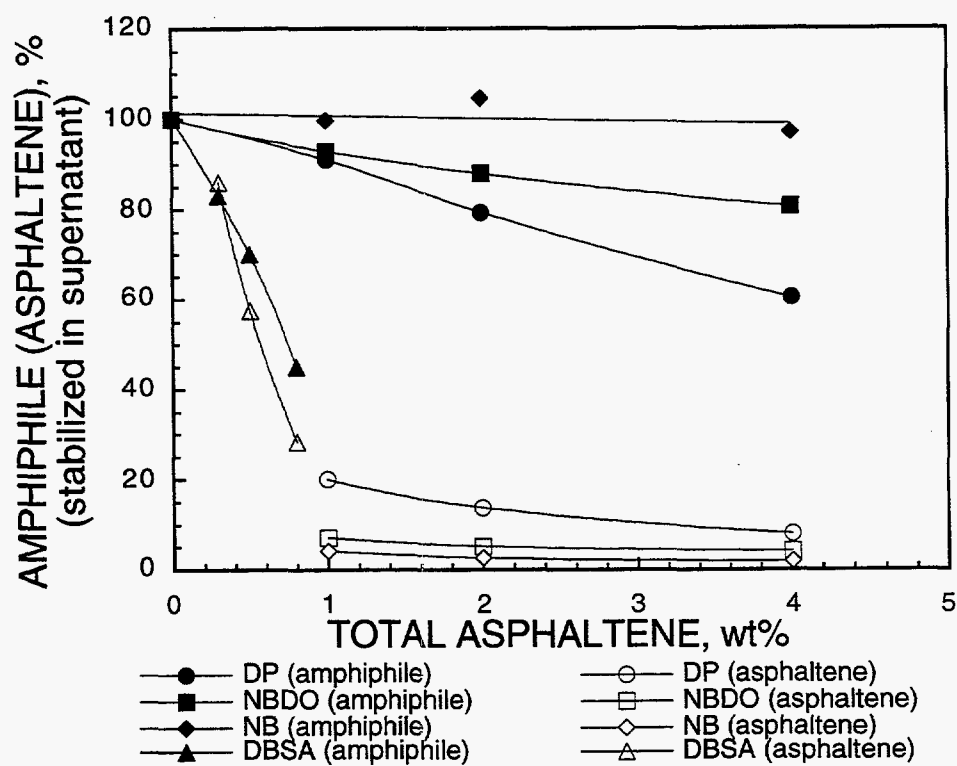


Figure 10. Amphiphiles with different head groups (and asphaltenes) remaining in the supernatant after centrifuging the amphiphile/decane solutions containing different amounts of asphaltenes.

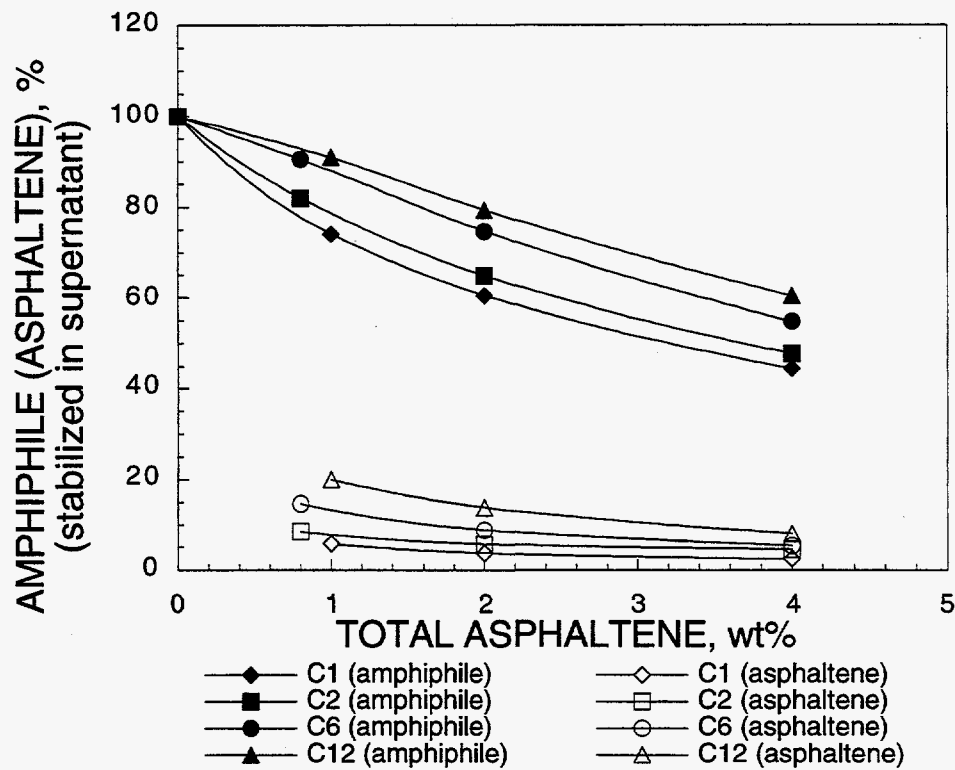


Figure 11. FTIR spectra of alkyl phenol amphiphiles with different tail lengths in the supernatant after centrifuging the amphiphile/decane solutions containing different amounts of asphaltenes (C<sub>n</sub>, n = carbon number of the alkyl tail).

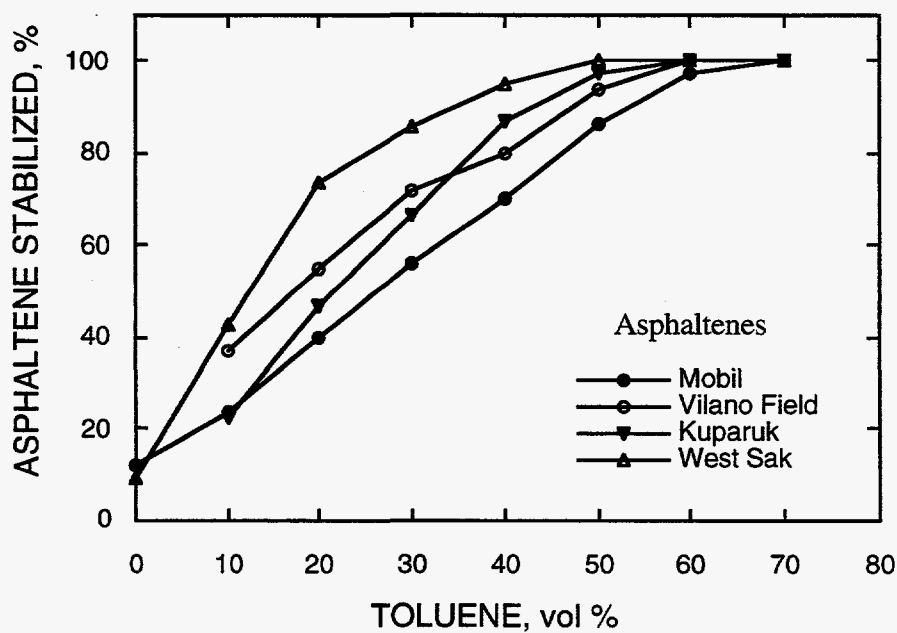


Figure 12. Asphaltene stabilized in the binary heptane-toluene solution.

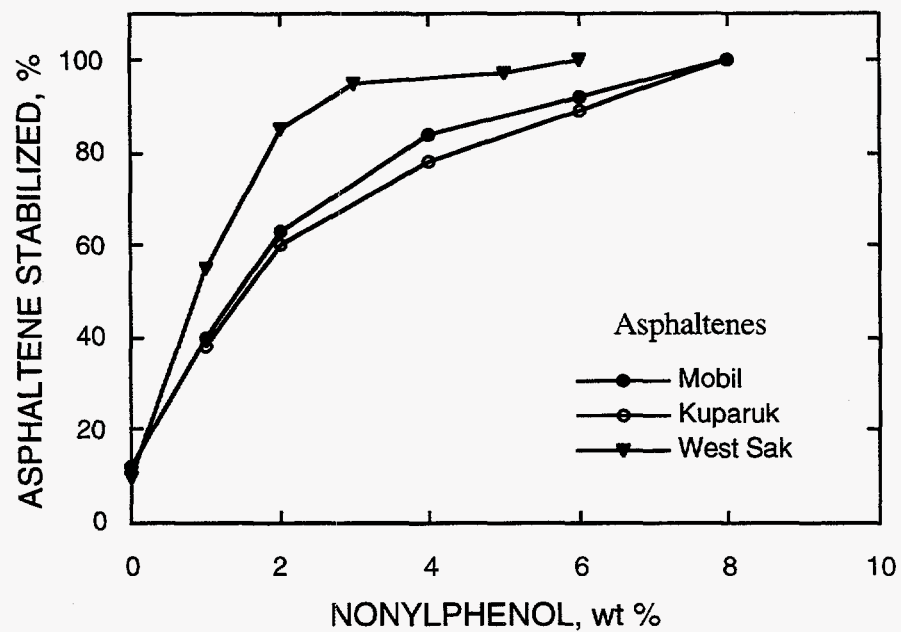


Figure 13. Asphaltenes stabilized in heptane solution with nonylphenol.

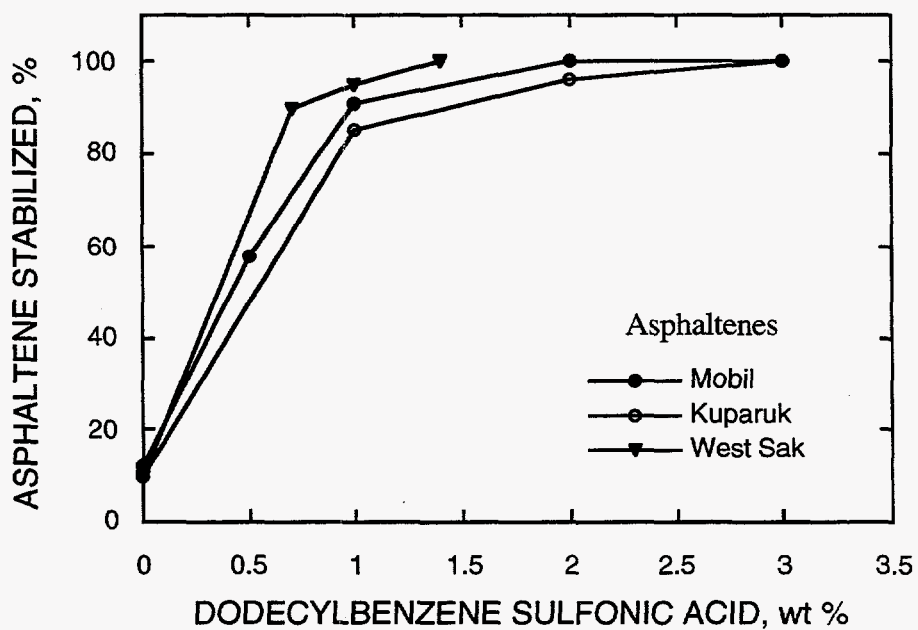


Figure 14. Asphaltenes stabilized in heptane solution with dodecylbenzene sulfonic acid.

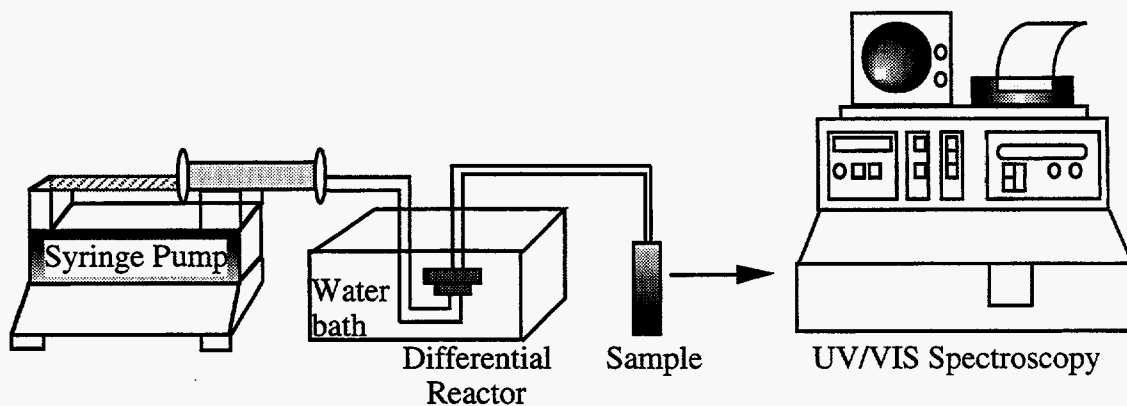


Figure 15. A schematic illustration of the experimental setup used for the kinetic study of asphaltene dissolution.

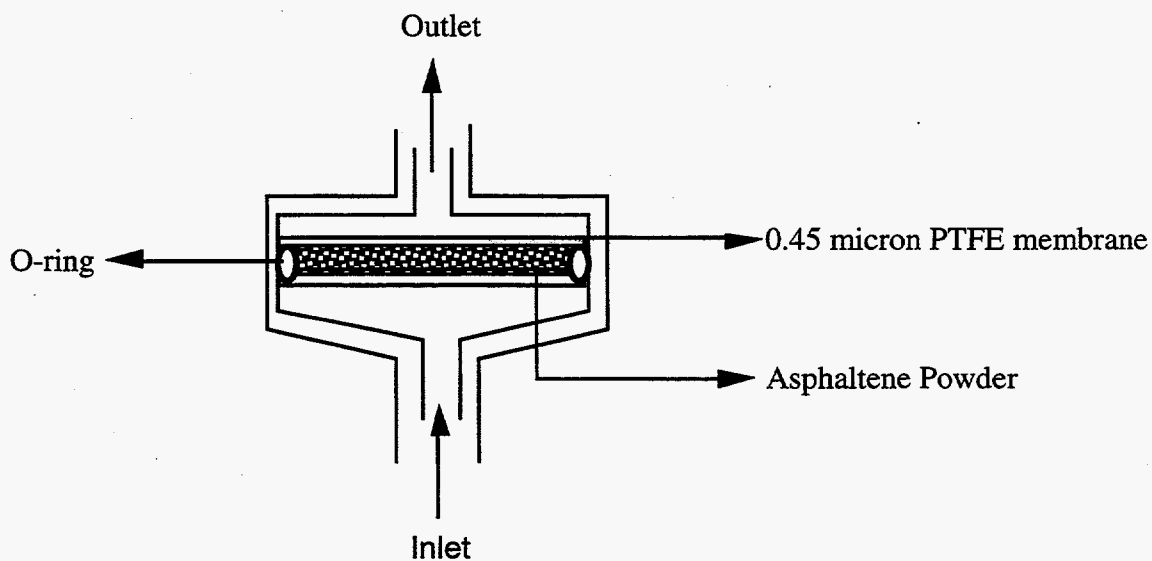


Figure 16. Detailed schematic of the differential reactor used in this study.



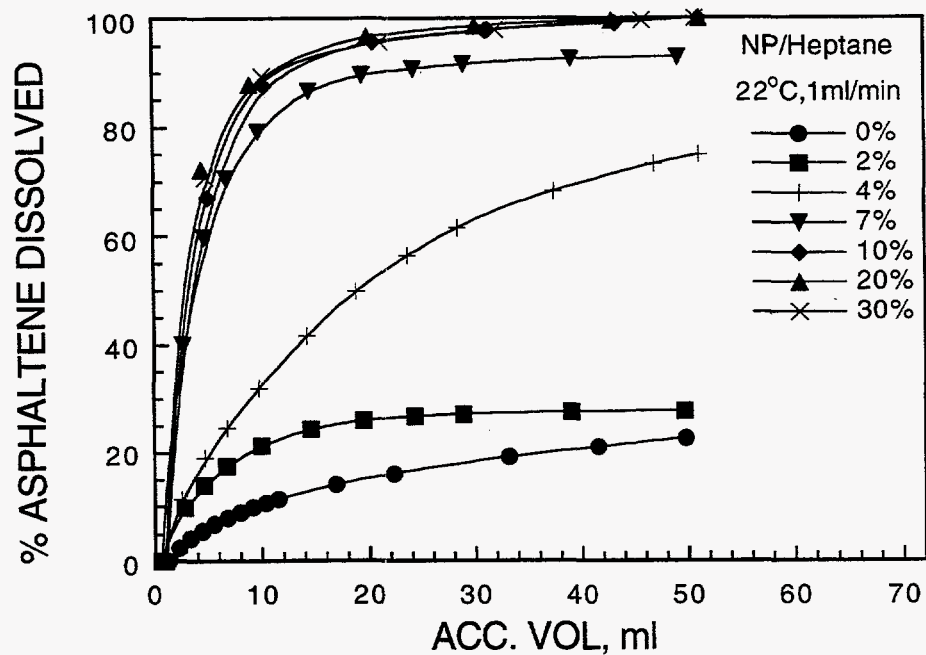


Figure 17. Profile of asphaltene dissolution by heptane-based fluids containing different concentrations of NP.

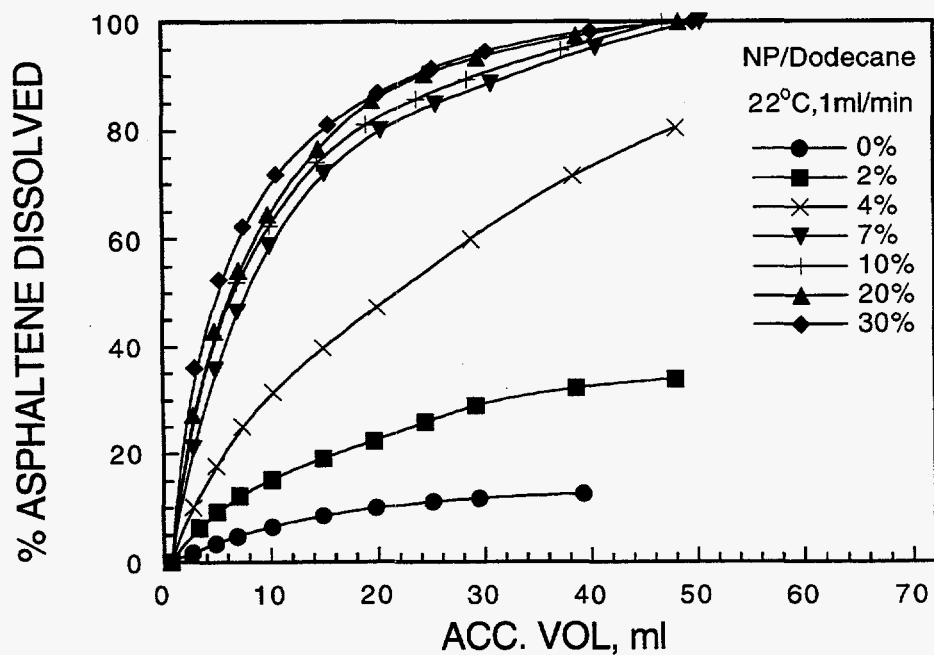


Figure 18. Profile of asphaltene dissolution by dodecane-based fluids containing different concentrations of NP.

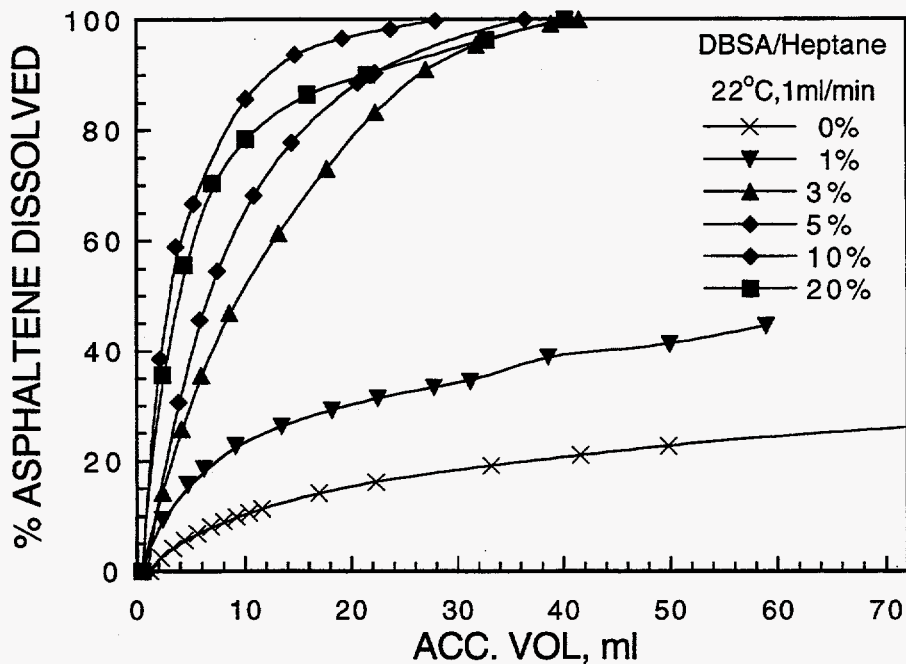


Figure 19. Profile of asphaltene dissolution by heptane-based fluids containing different concentrations of DBSA.

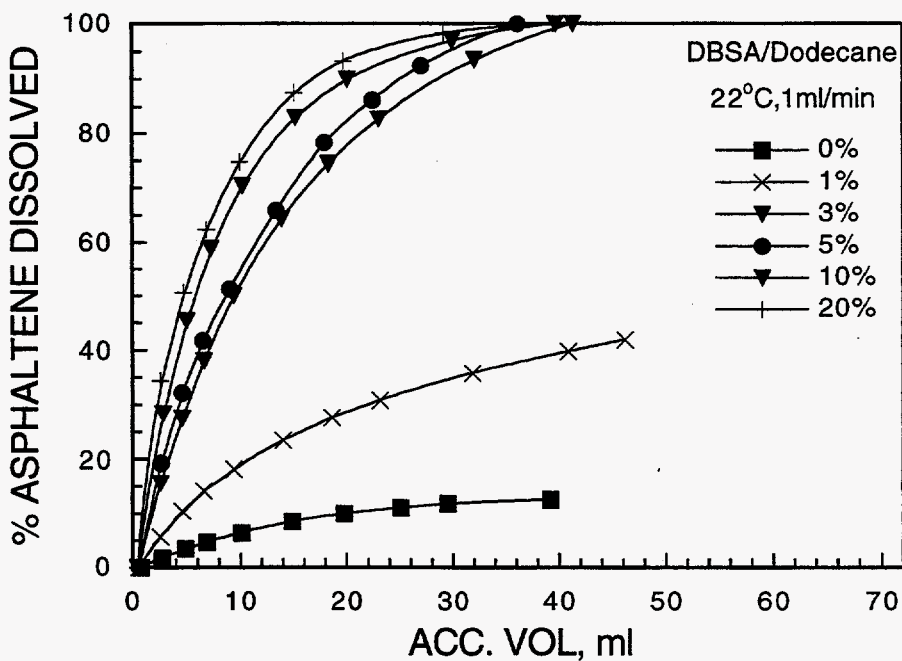


Figure 20. Profile of asphaltene dissolution by dodecane-based fluids containing different concentrations of DBSA.

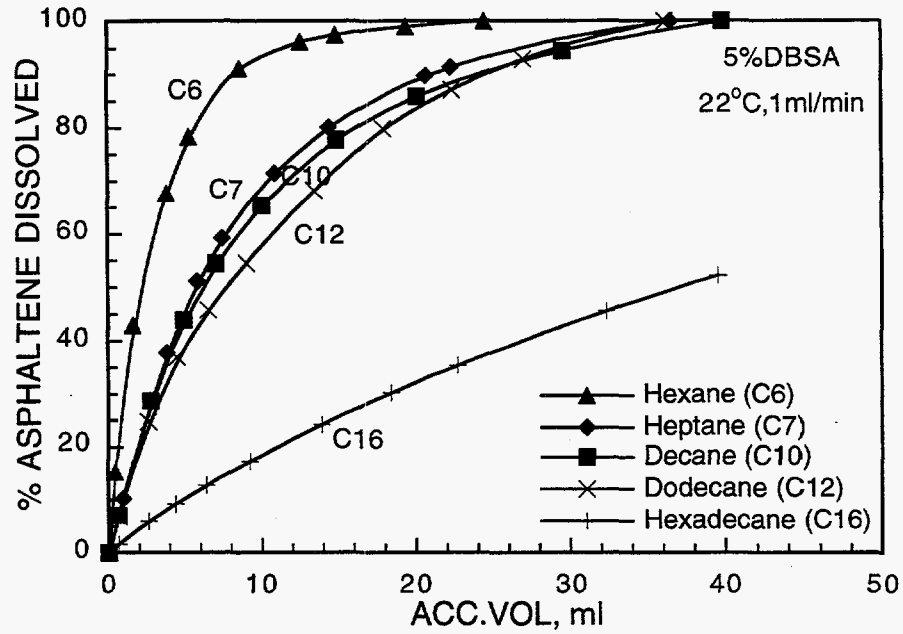


Figure 21. Asphaltene dissolution in 5% DBSA amphiphile solutions containing different types of alkane solvents.

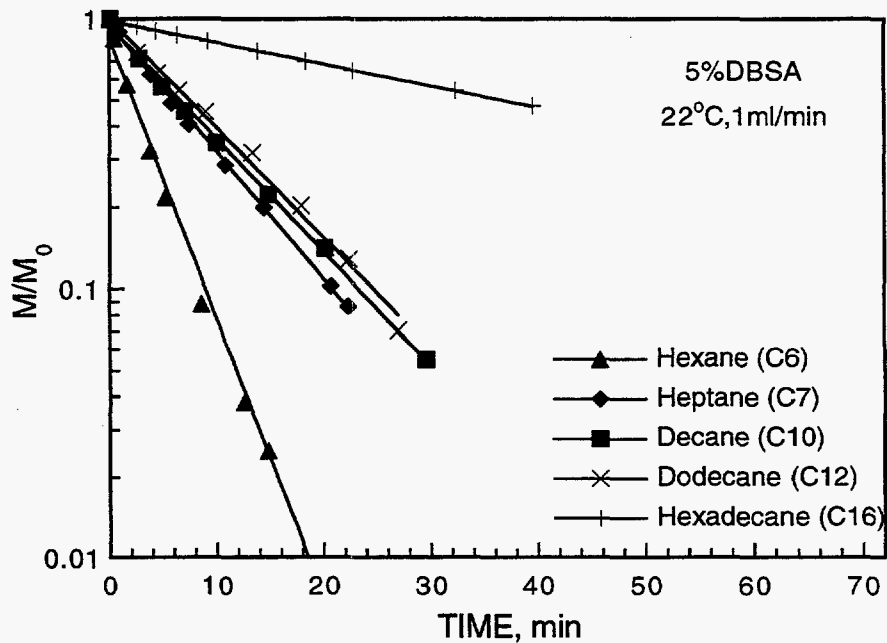


Figure 22. Kinetic analysis of asphaltene dissolution in 5% DBSA amphiphile solutions containing different types of alkane solvents.

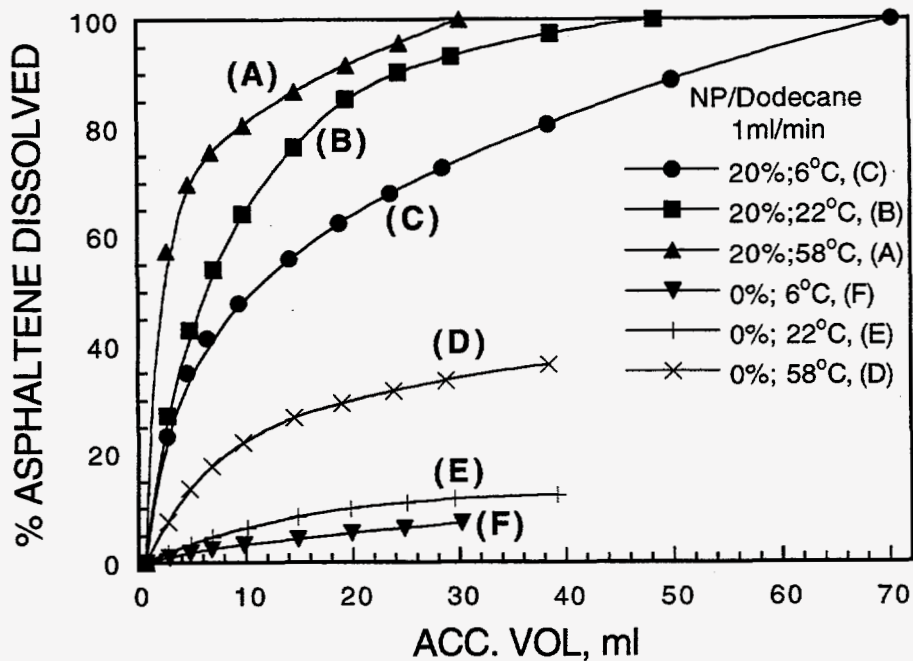


Figure 23. Asphaltene dissolution at different temperatures by the dodecane-based fluid containing 20 wt% of NP.

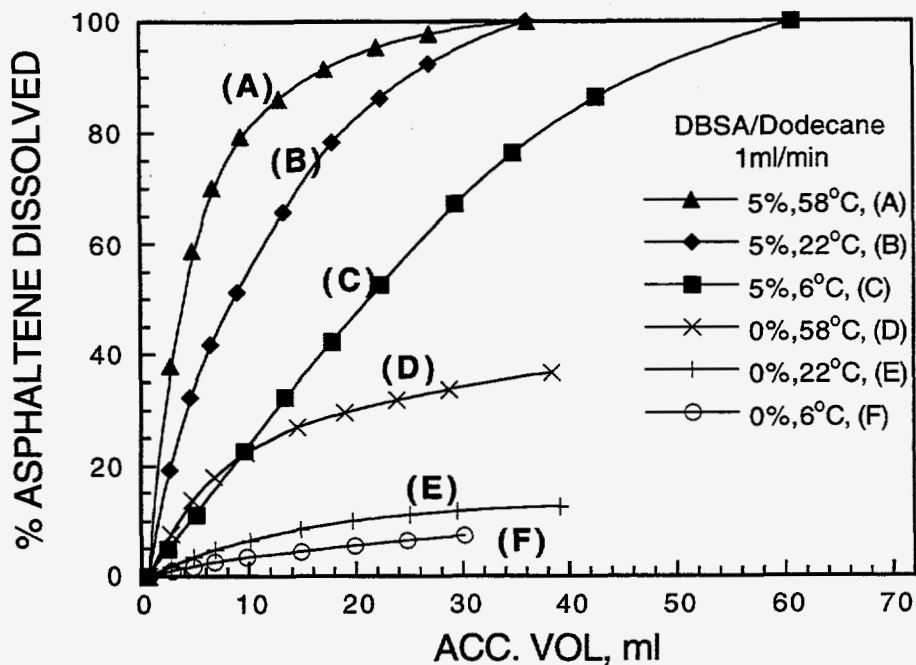


Figure 24. Asphaltene dissolution at different temperatures by the dodecane-based fluid containing 5 wt% of DBSA.

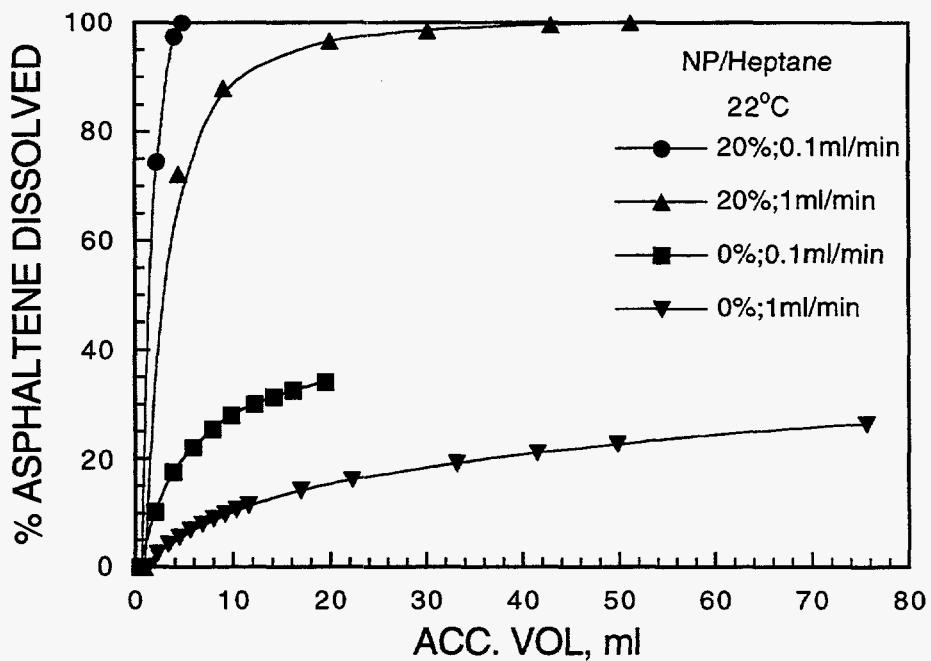
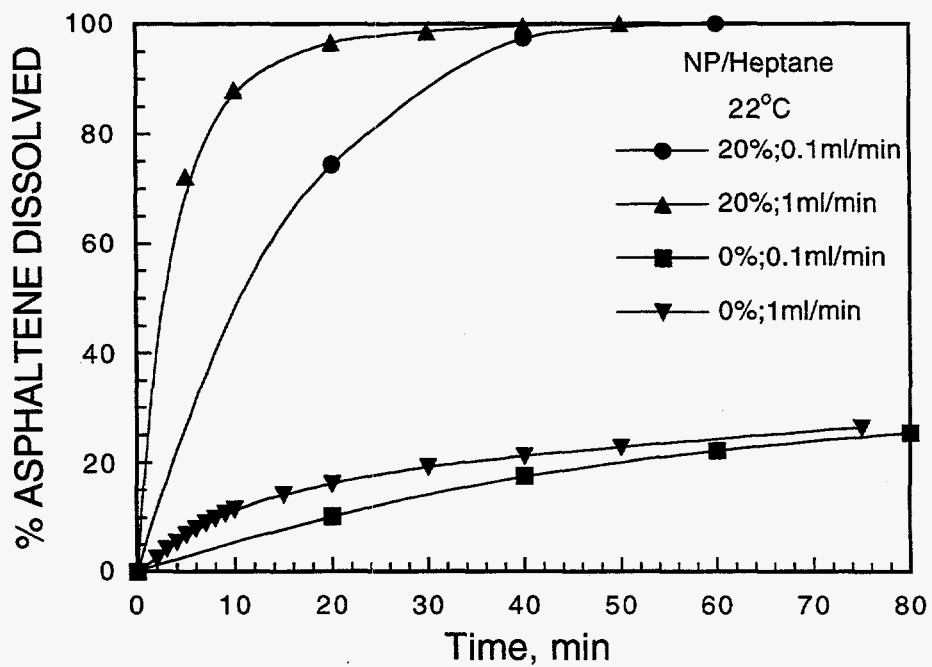


Figure 25. Asphaltene dissolution by heptane-based fluid containing 20 wt% of NP at different flow rates. The dissolution profile is plotted as a function of both the time of dissolution (top) and the accumulated volume of effluent (bottom).

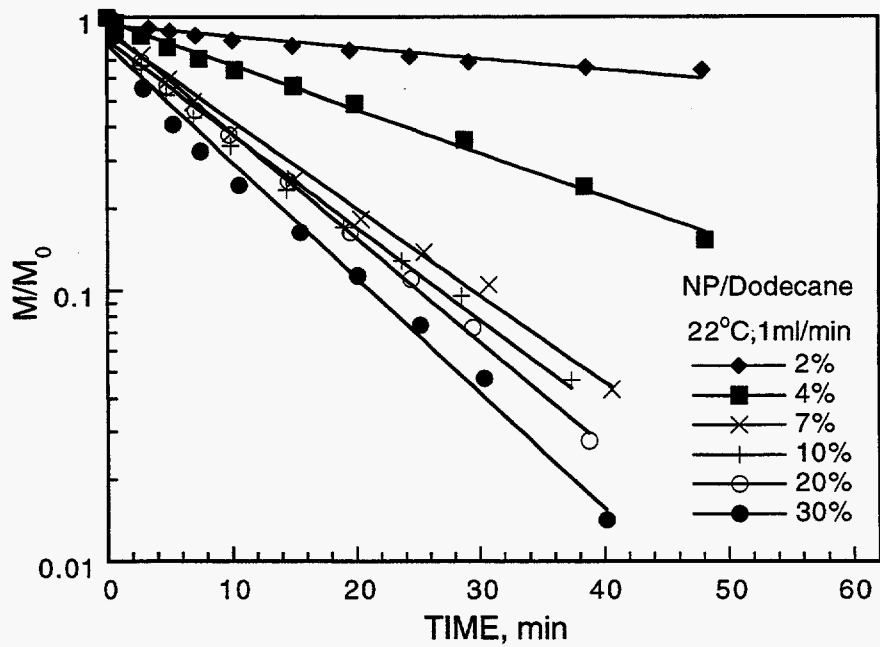


Figure 26. Kinetic analysis of asphaltene dissolution in NP/dodecane solutions containing different concentrations of NP.

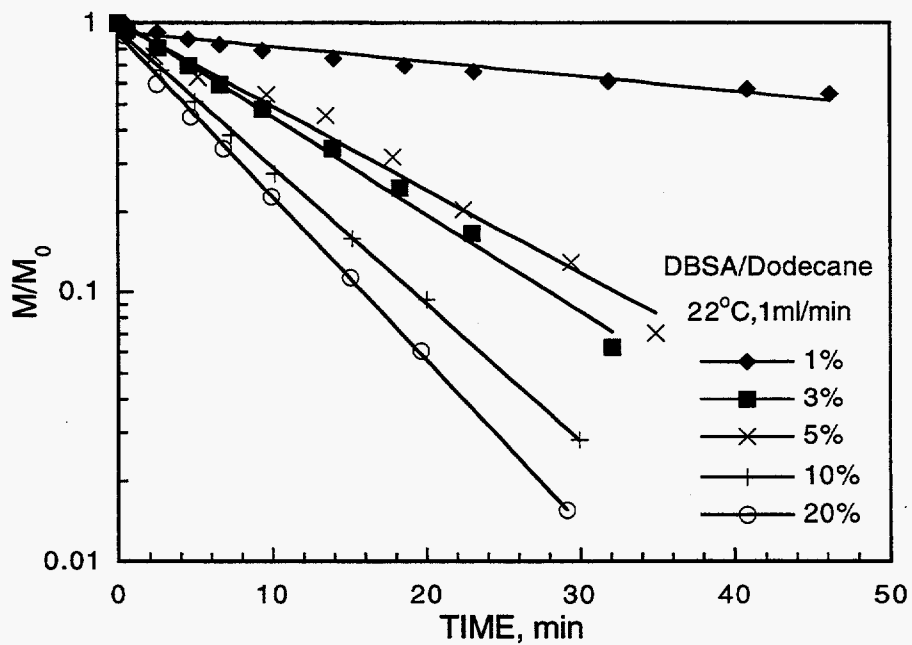


Figure 27. Kinetic analysis of asphaltene dissolution in DBSA/dodecane solutions containing different concentrations of DBSA.

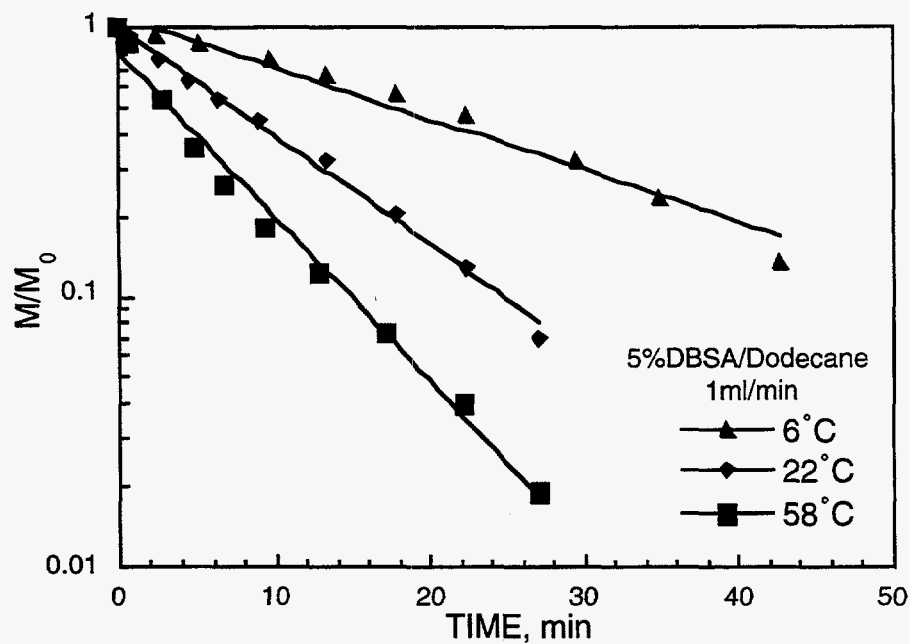


Figure 28. Kinetic analysis of asphaltene dissolution in 5% DBSA/dodecane solutions at different temperatures.

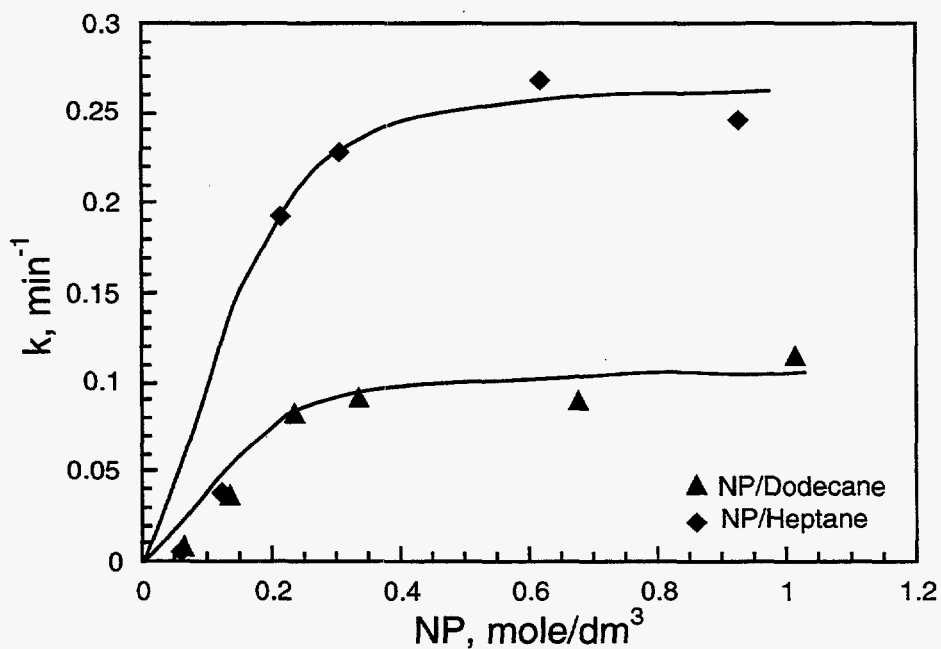


Figure 29. Specific dissolution rate constant,  $k$ , as a function of the NP concentration in solutions.

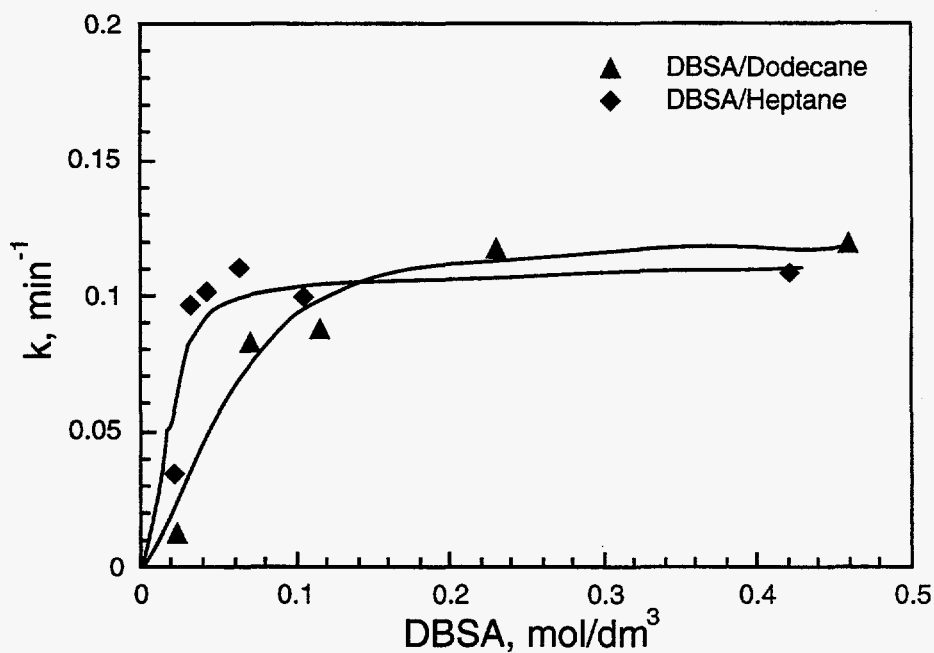


Figure 30. Specific dissolution rate constant,  $k$ , as a function of the DBSA concentration in solutions.

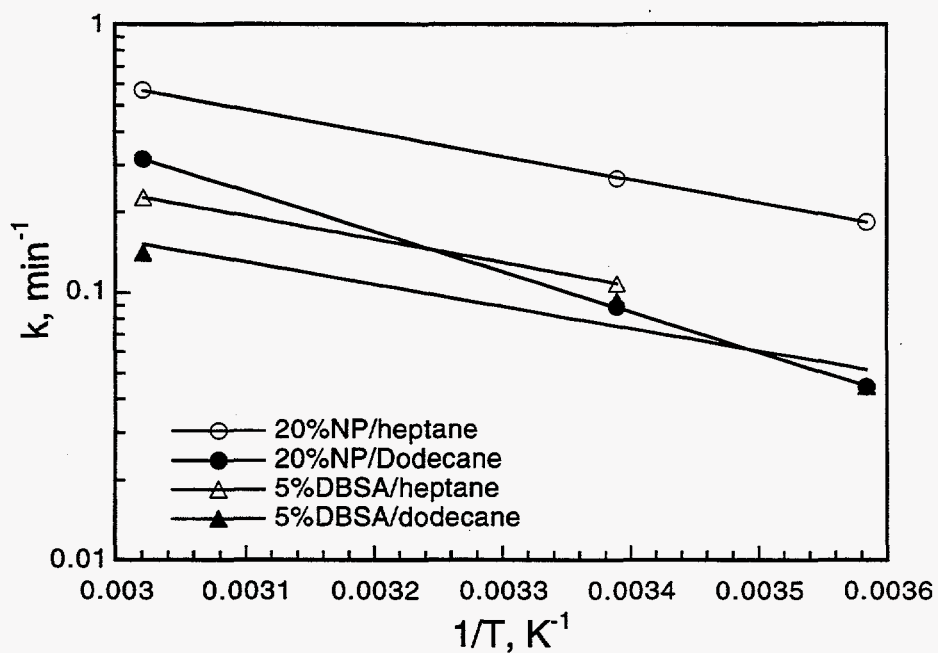


Figure 31. Specific dissolution rate constant,  $k$ , as a function of the solution temperature.



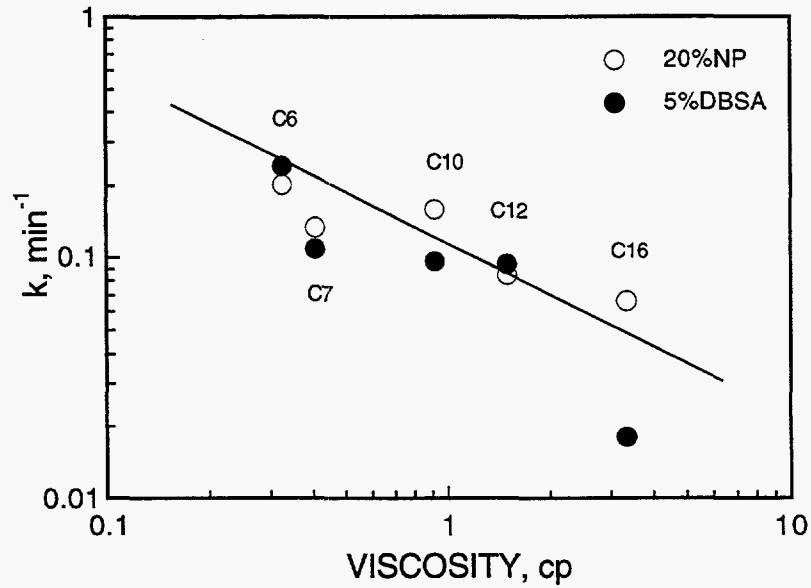


Figure 32. Specific dissolution rate constant,  $k$ , as a function of the viscosity of alkane solvents used in amphiphile solutions.

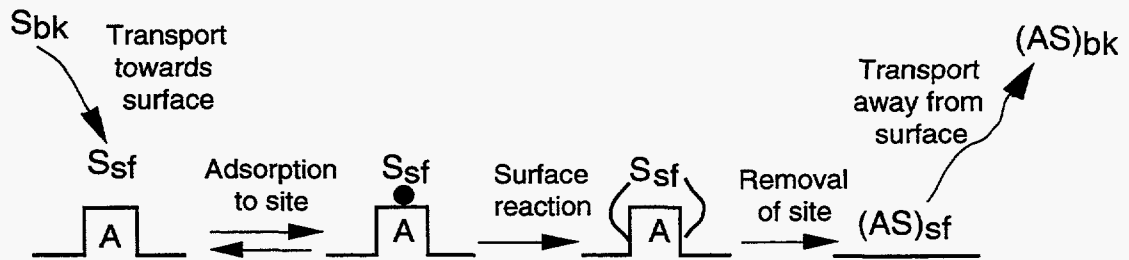


Figure 33(a). Schematic of dissolution of asphaltene deposits by amphiphile/alkane fluids.

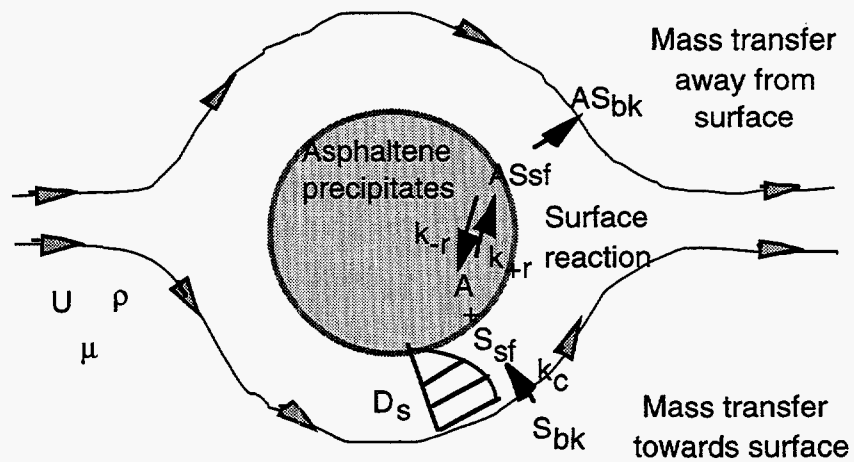


Figure 33(b). Schematic of the mass transfer process in asphaltene dissolution.

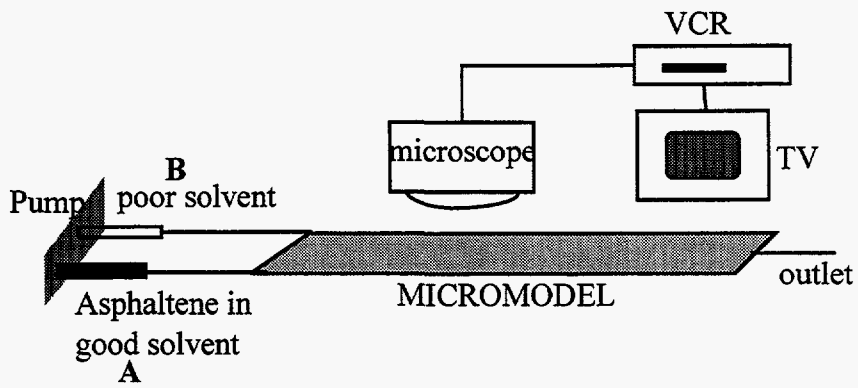


Figure 34. Schematic of a glass micromodel apparatus.

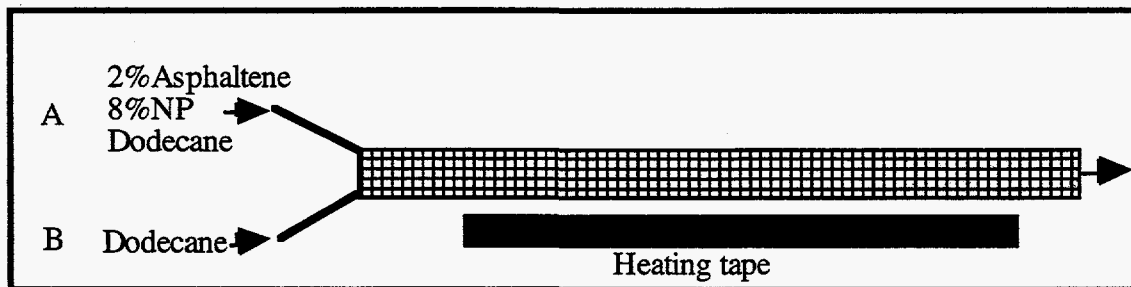
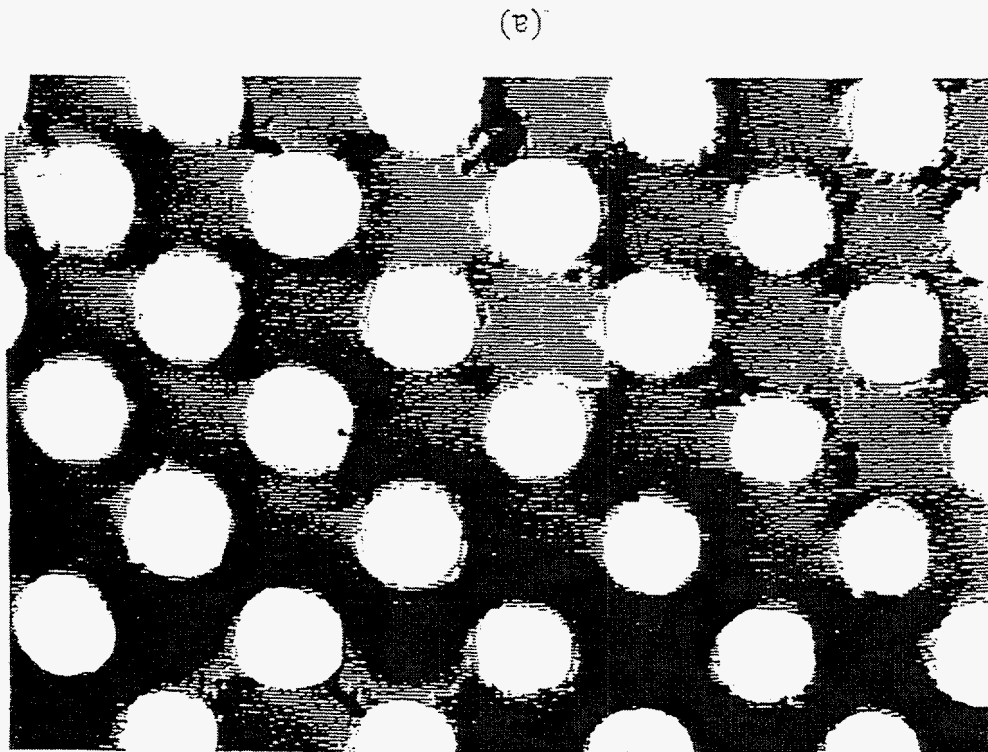
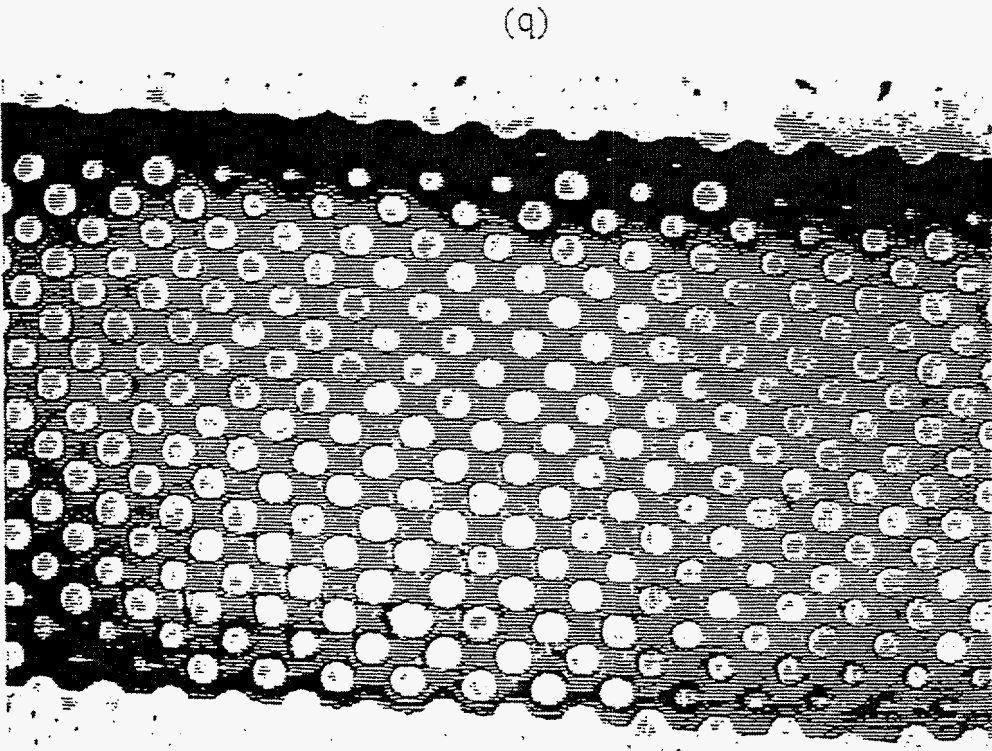
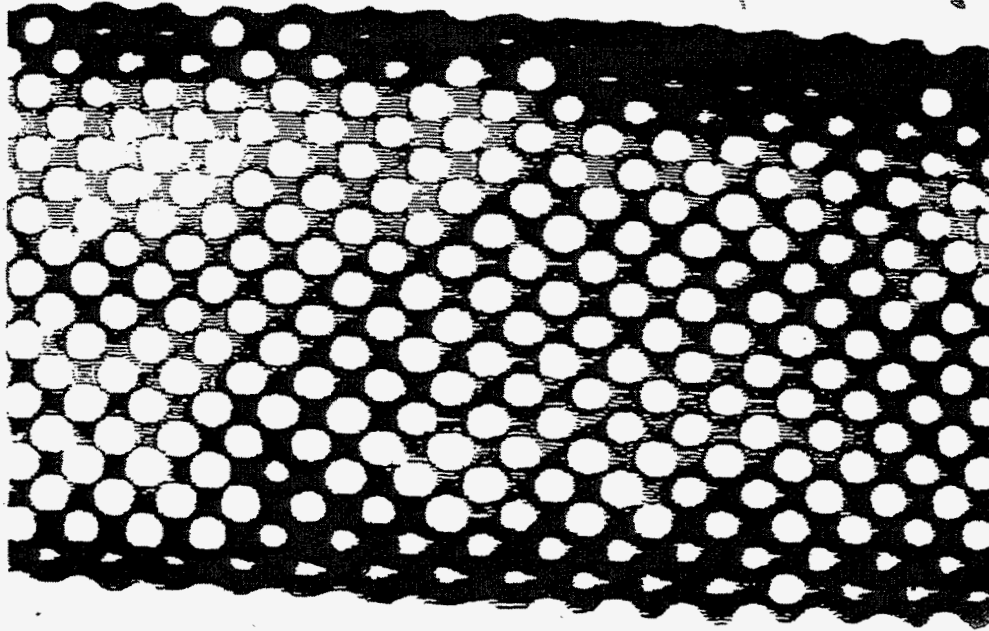


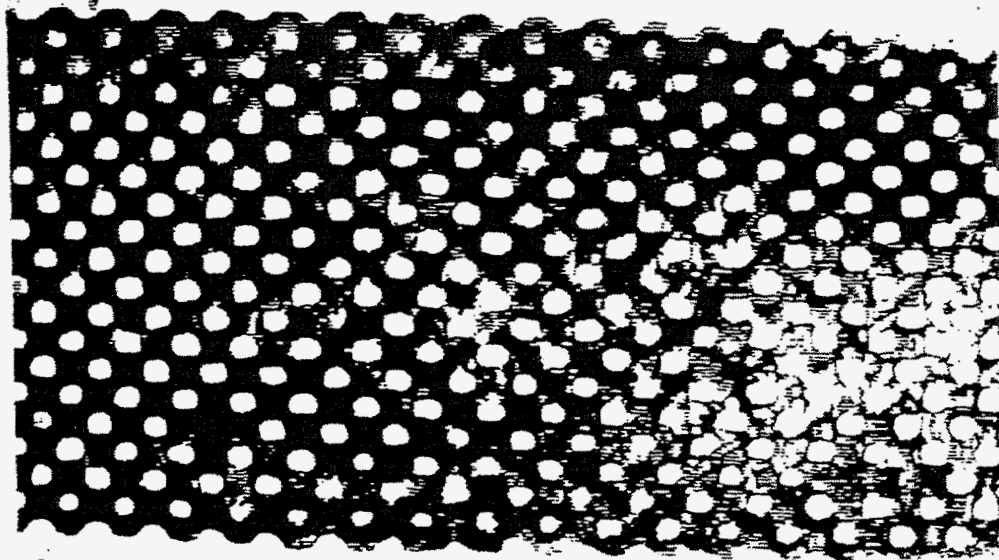
Figure 35. Experimental setup for the asphaltene precipitation and plugging in the micromodel.

Figure 36. Microscopic images showing asphaltene deposition and plugging in the micromodel. (a) Asphaltenes deposit at pore throats. (b) Micromodel at the initial stage of asphaltene plugging.





(c)



(d)

Figure 36. (c) Micromodel at the middle stage of asphaltene plugging. (d) Micromodel is completely plugged by deposited asphaltenes.

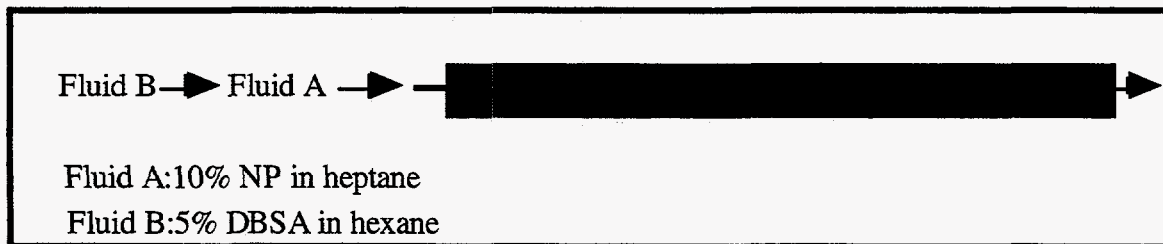


Figure 37. Experiment setup for the dissolution of asphaltene in the micromodel.

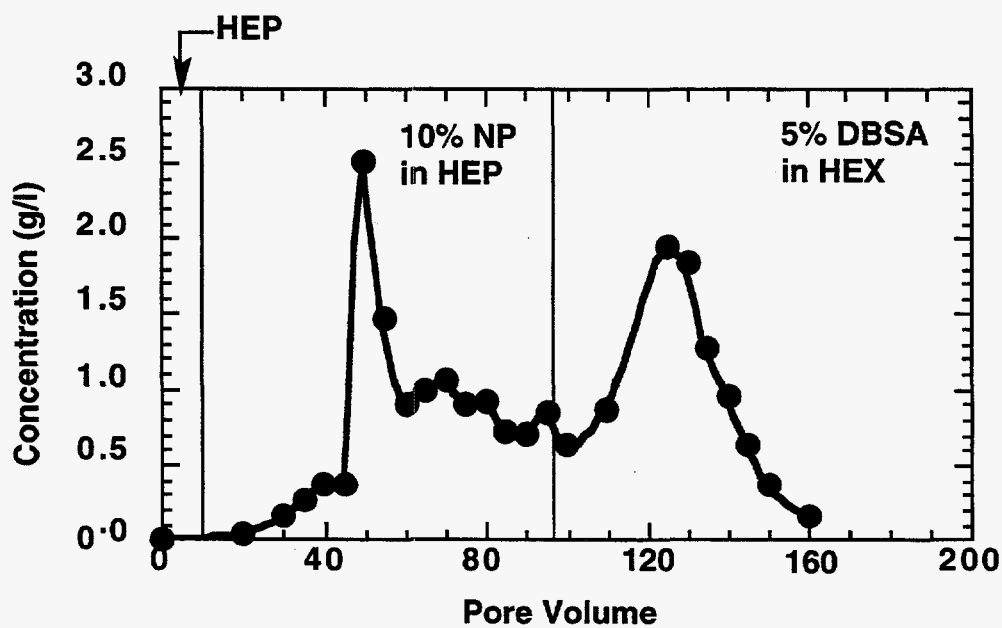
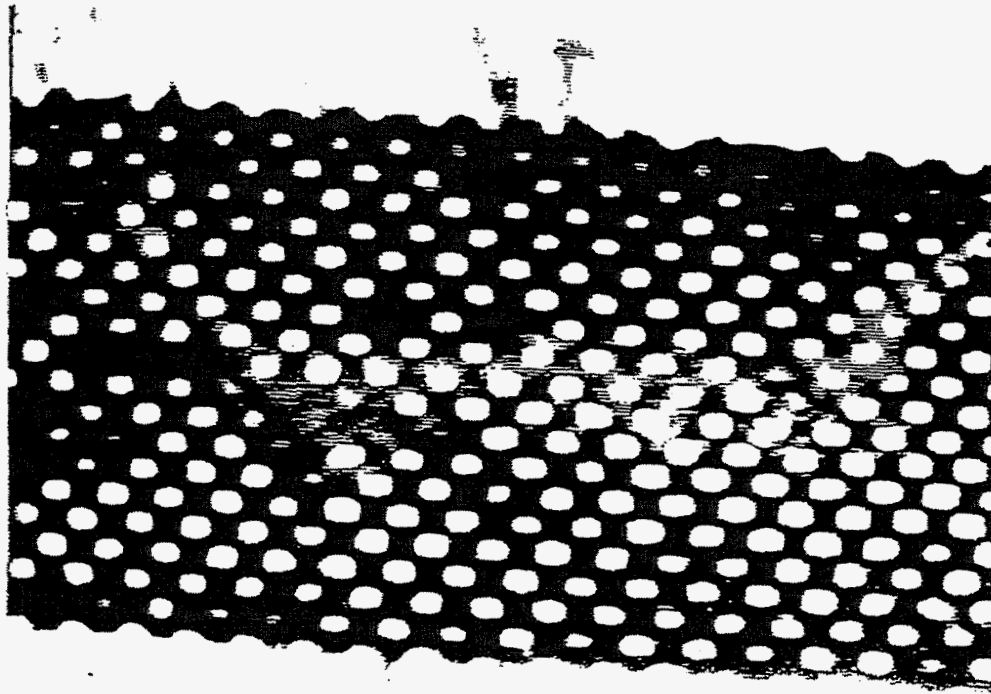
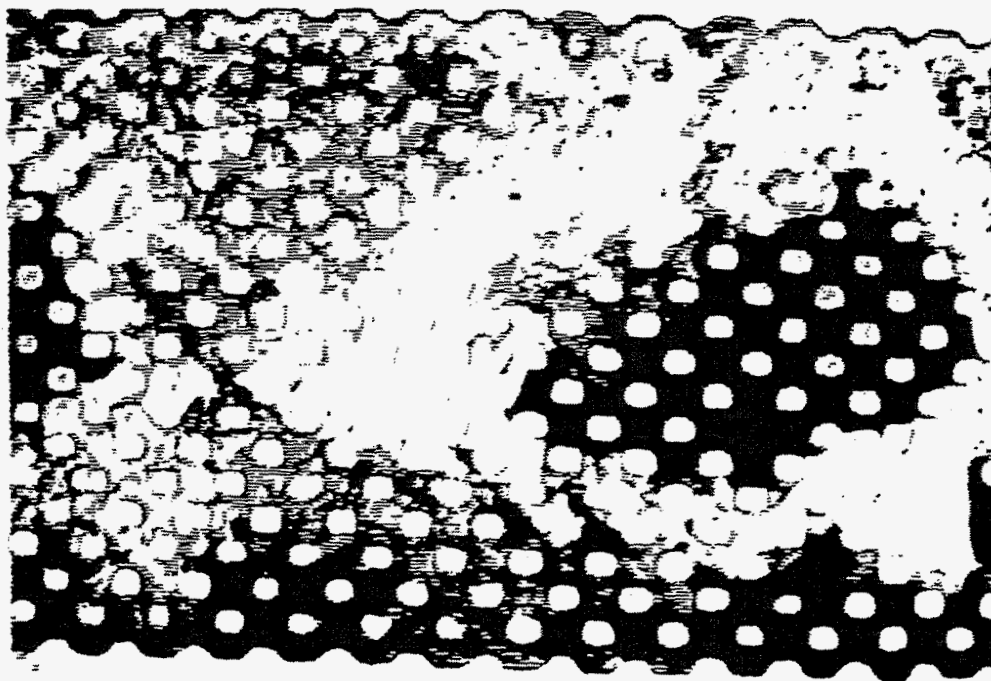


Figure 38. Concentration of asphaltenes in the effluent as a function of the elution time.

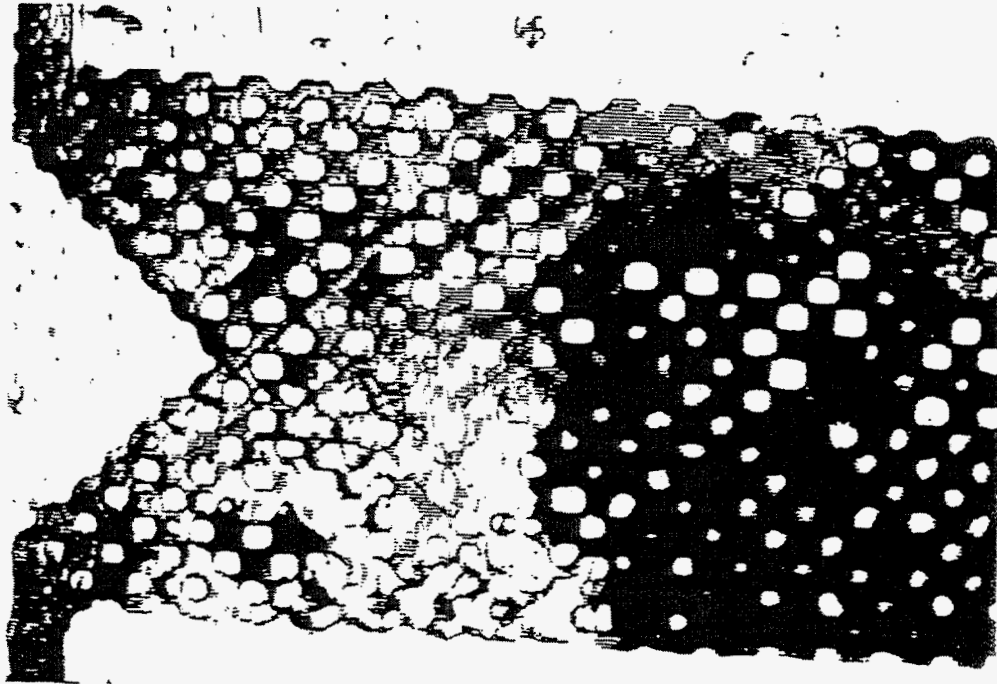


(a)

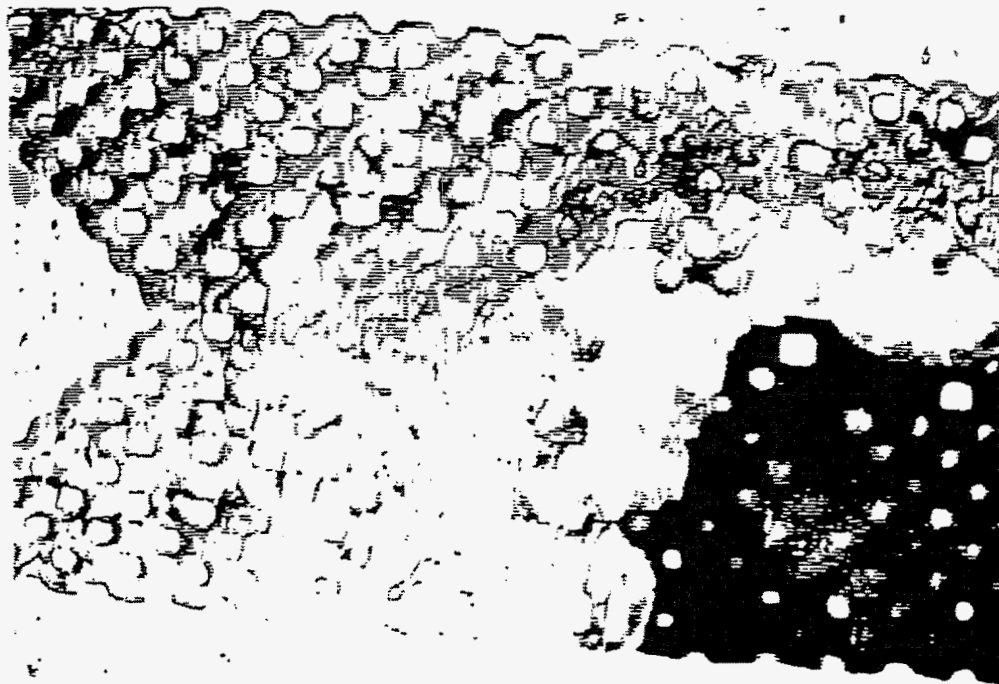


(b)

Figure 39. Microscopic images showing asphaltene dissolution in the micromodel by the 10 wt.% NP/heptane solution. (a) Micromodel at the initial stage of asphaltene dissolution. A wormhole-like flow channel is clearly seen. (b) Micromodel at the middle stage of asphaltene dissolution.



(c)



(d)

Figure 39. (c) Inlet region of micromodel before the dissolution of asphaltenes. (d) Inlet region of micromodel during the dissolution of asphaltenes. (b) and (d) show that the island-like asphaltene deposits are dissolved while the cluster-like deposits are left behind without dissolution.

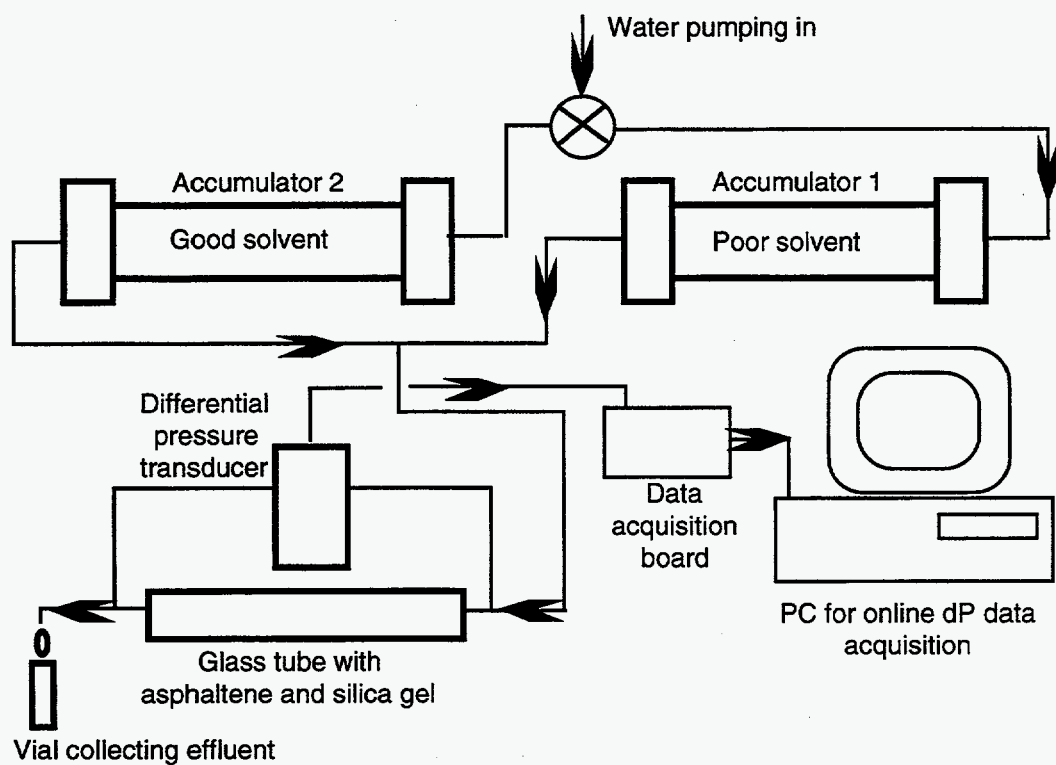


Figure 40. Schematic of the pack-bed experimental setup.



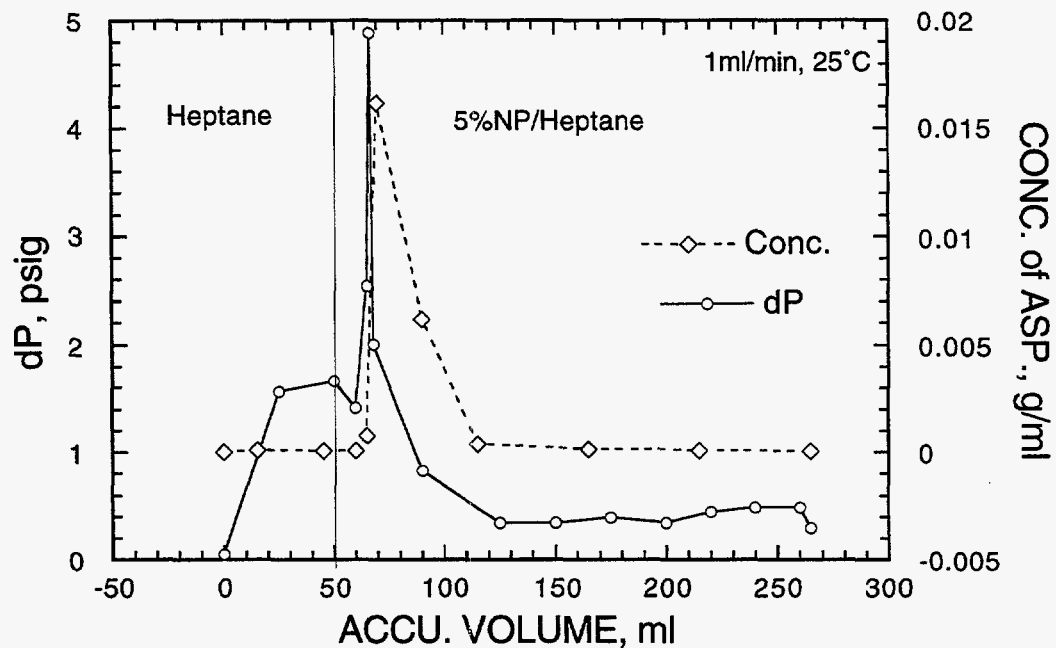


Figure 41. Differential pressure profile and concentration profile for asphaltene dissolution in packed bed.

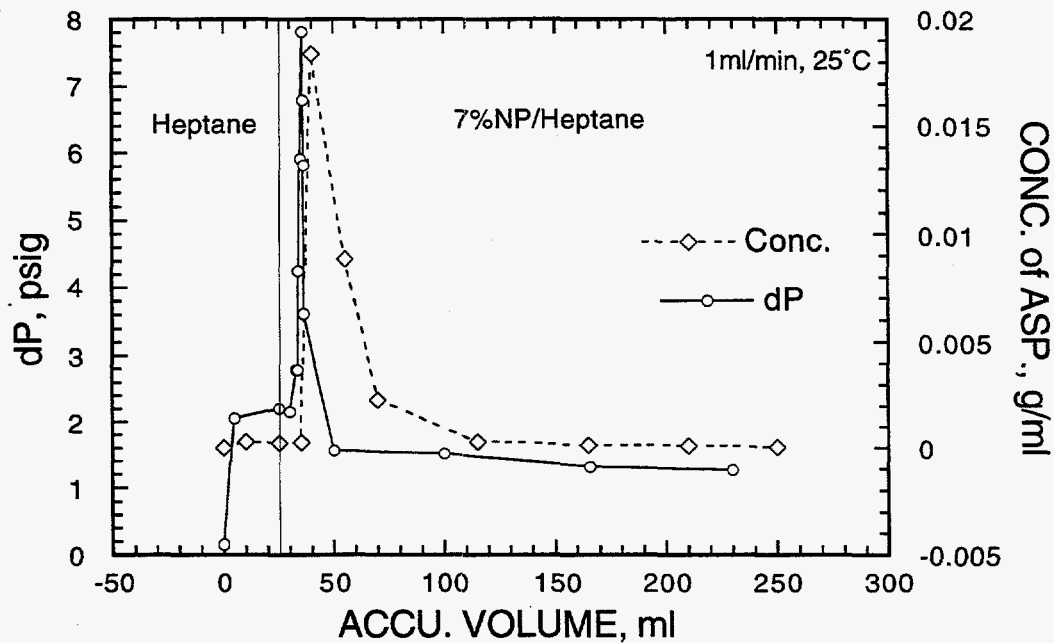


Figure 42. Differential pressure profile and concentration profile for asphaltene dissolution in packed bed.

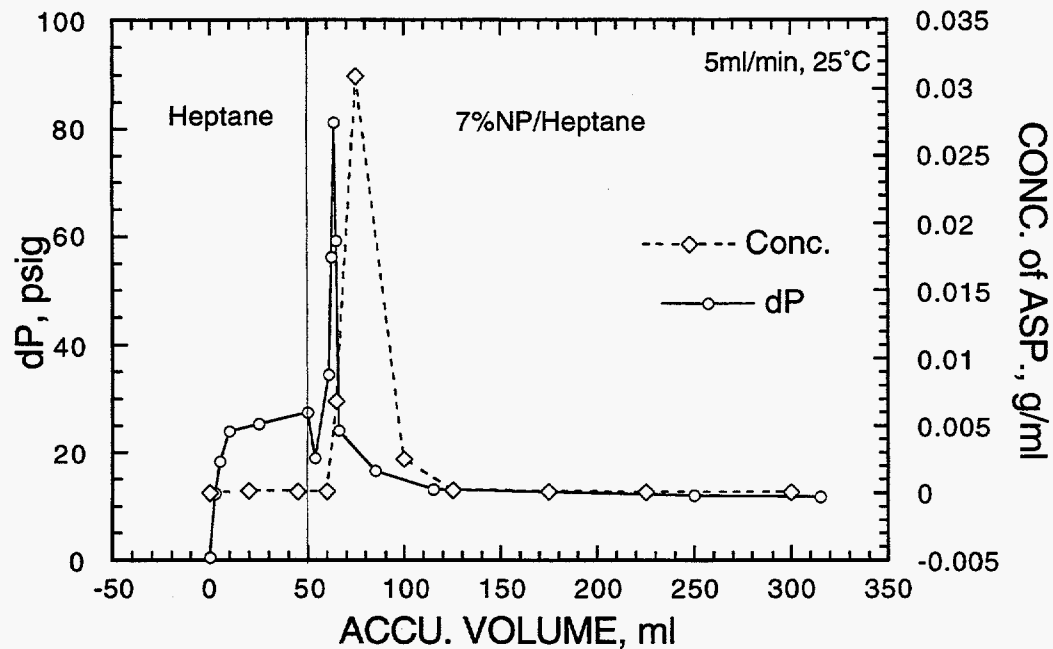


Figure 43. Differential pressure profile and concentration profile for asphaltene dissolution in packed bed.

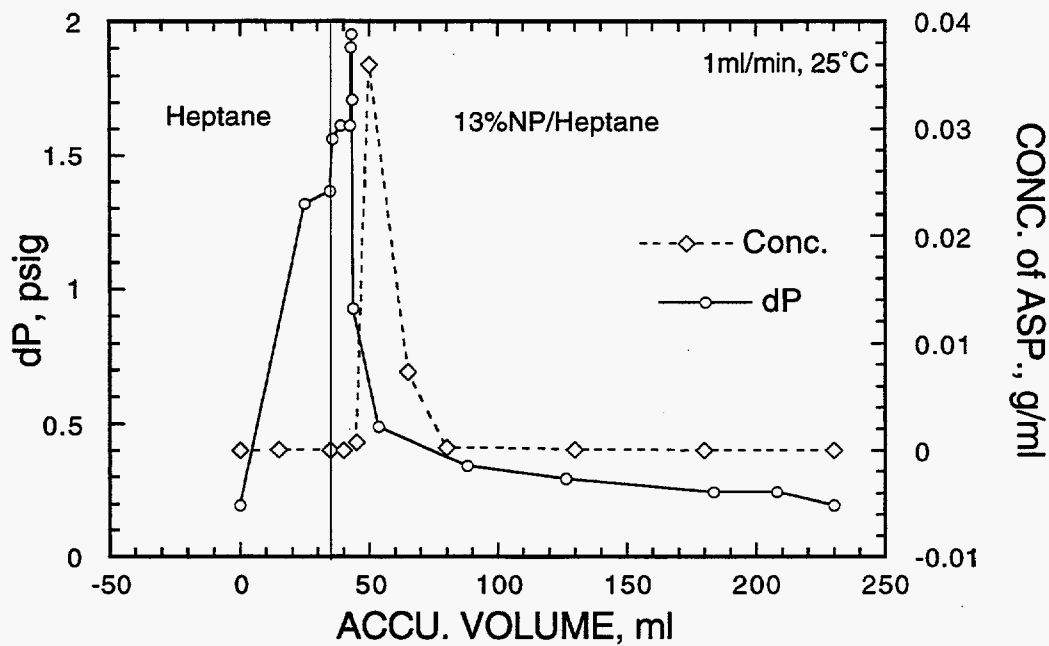


Figure 44. Differential pressure profile and concentration profile for asphaltene dissolution in packed bed.

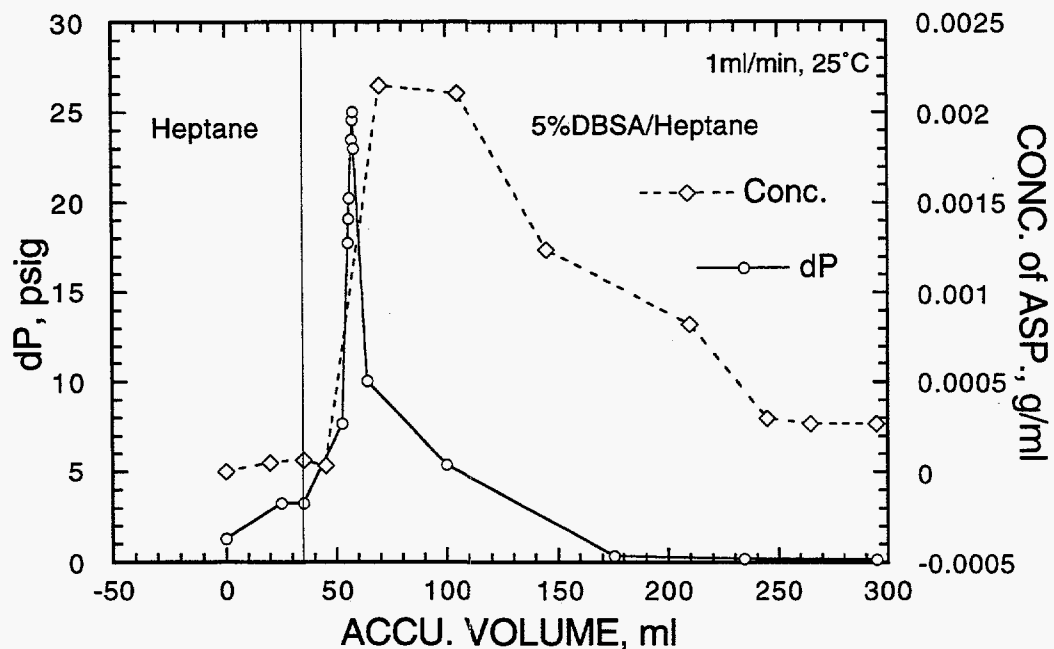


Figure 45. Differential pressure profile and concentration profile for asphaltene dissolution in packed bed.

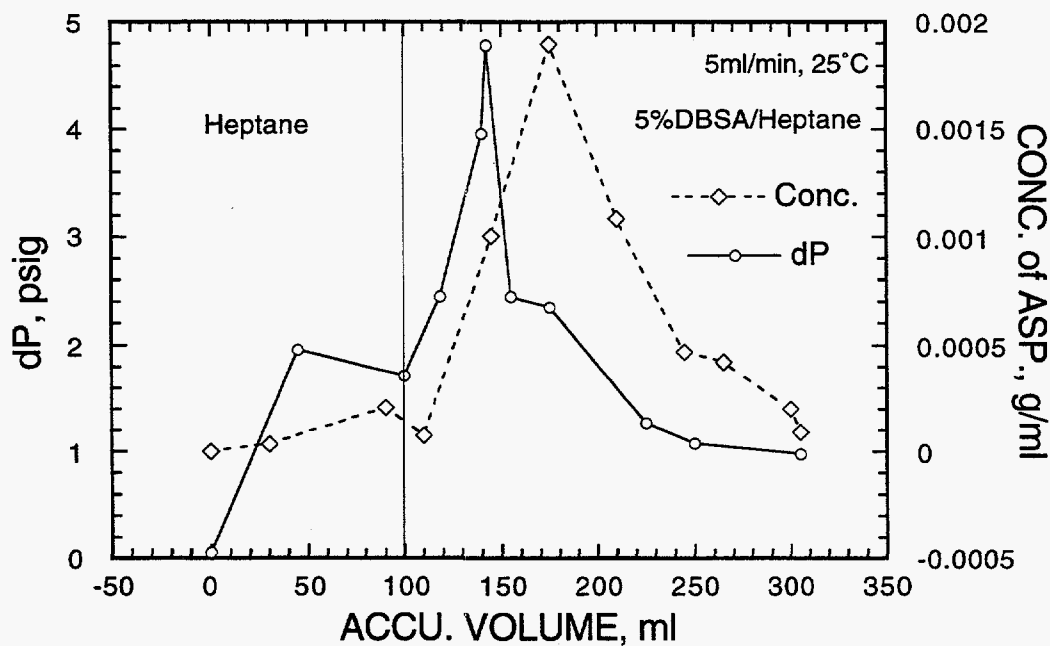


Figure 46. Differential pressure profile and concentration profile for asphaltene dissolution in packed bed.

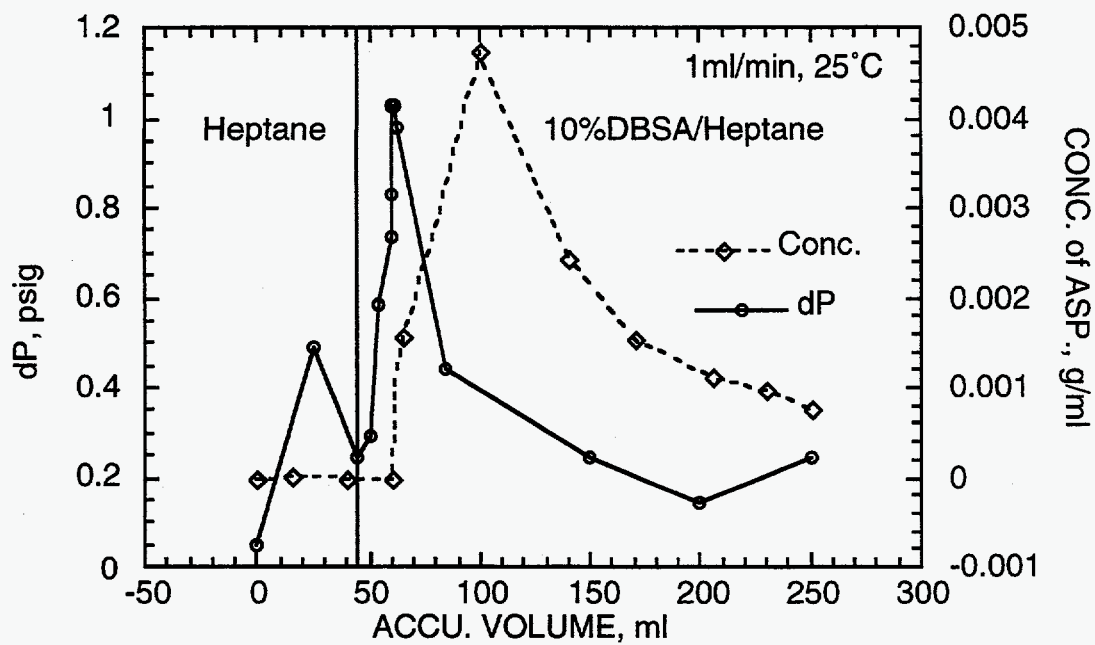


Figure 47. Differential pressure profile and concentration profile for asphaltene dissolution in packed bed.

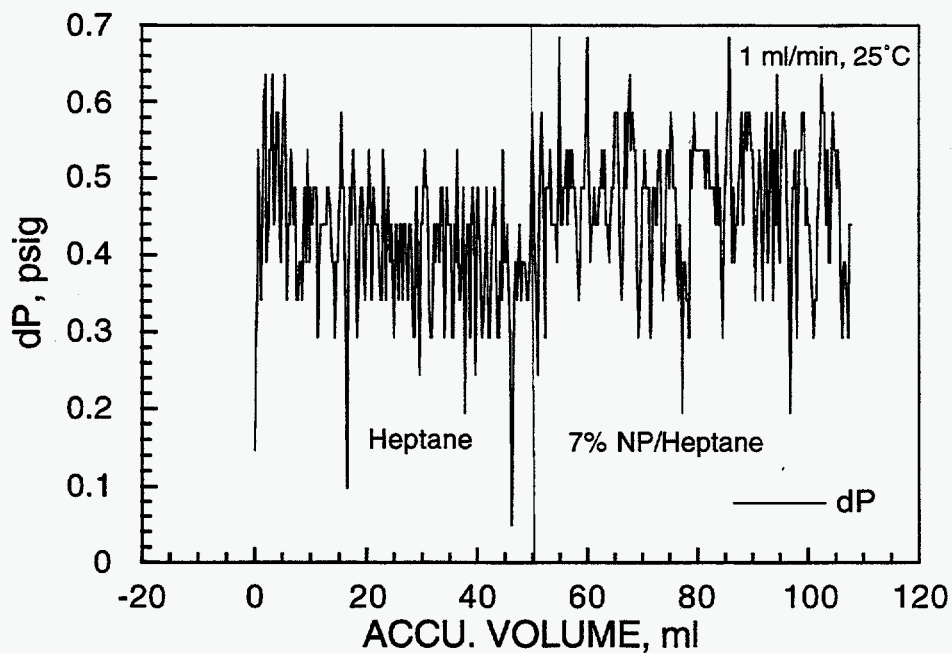


Figure 48. Differential pressure profile for silica gel in packed bed.

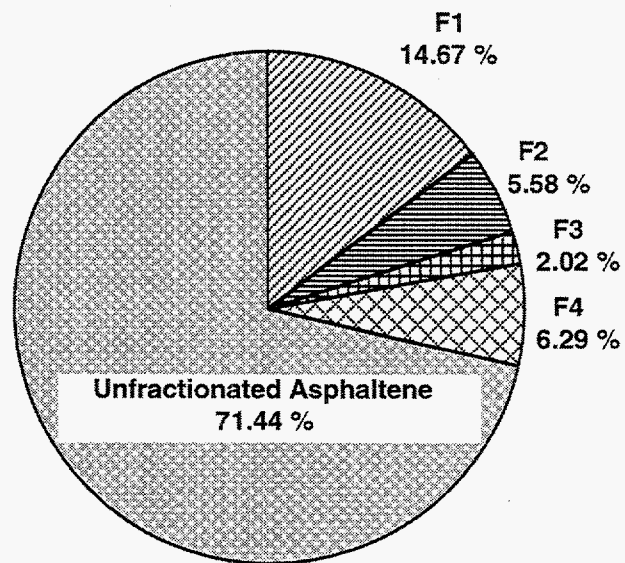


Fig 49. Yield of asphaltene fractions as wt % of asphaltenes originally dissolved in  $\text{CH}_2\text{Cl}_2$ .

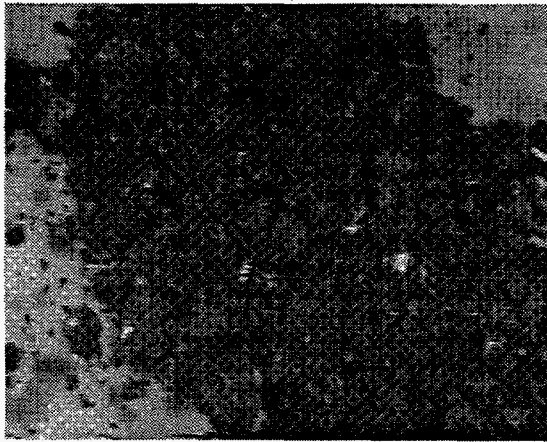


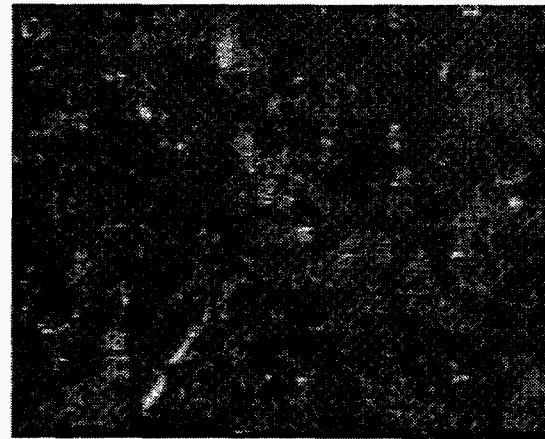
Fig 50(a) Unfractionated Asphaltene



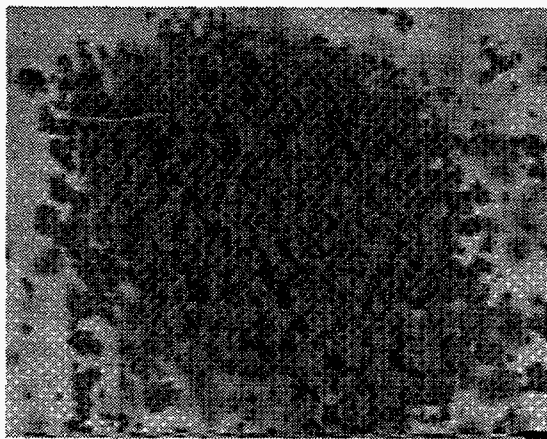
(b) Close-up of unfractionated asphaltene



(c) Asphaltene Fraction F1



(d) Close-up of F1



(e) Asphaltene Fraction F4



(f) Close-up of F4

Fig 50. Light microscope pictures of unfractionated asphaltene and fractions F1 and F4.

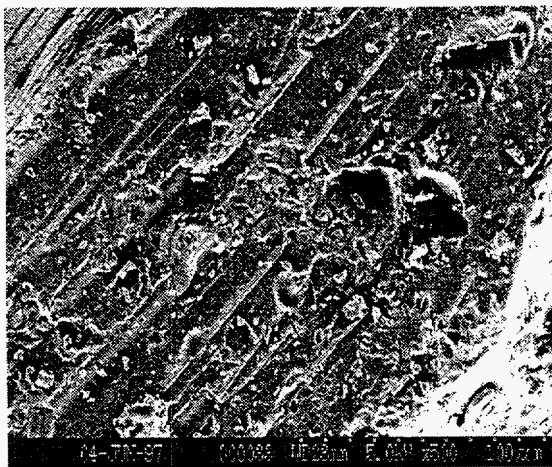
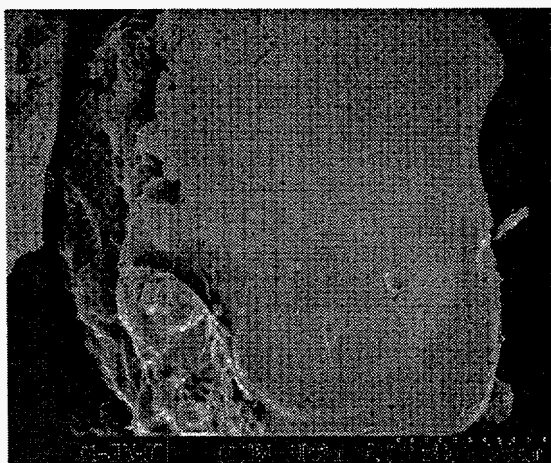
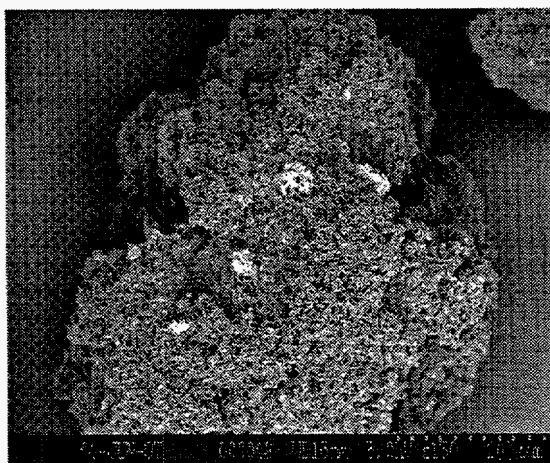


Fig 51 (a) SEM of unfractionated asphaltene



(b) SEM of fraction F1



(c) SEM of fraction F4

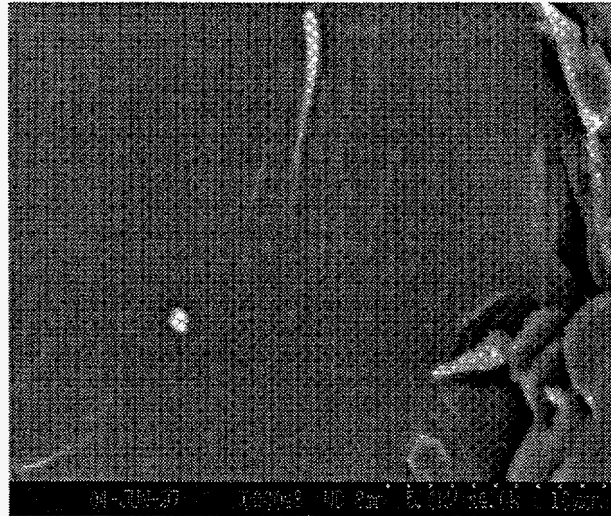


Fig 52 (a) SEM of F1 (higher magnification)

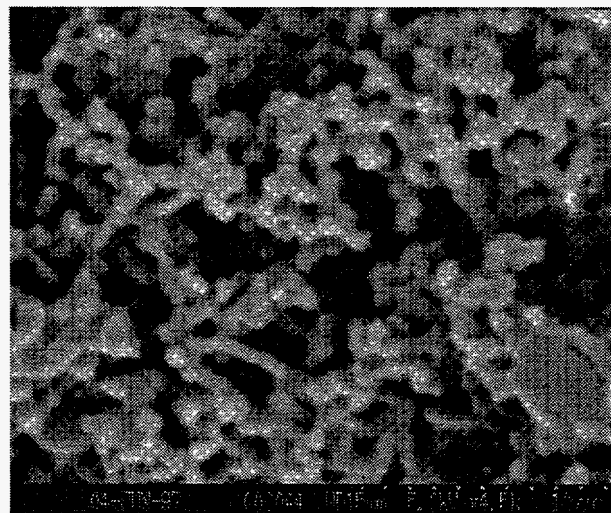


Fig 52 (b) SEM of F4 (higher magnification)



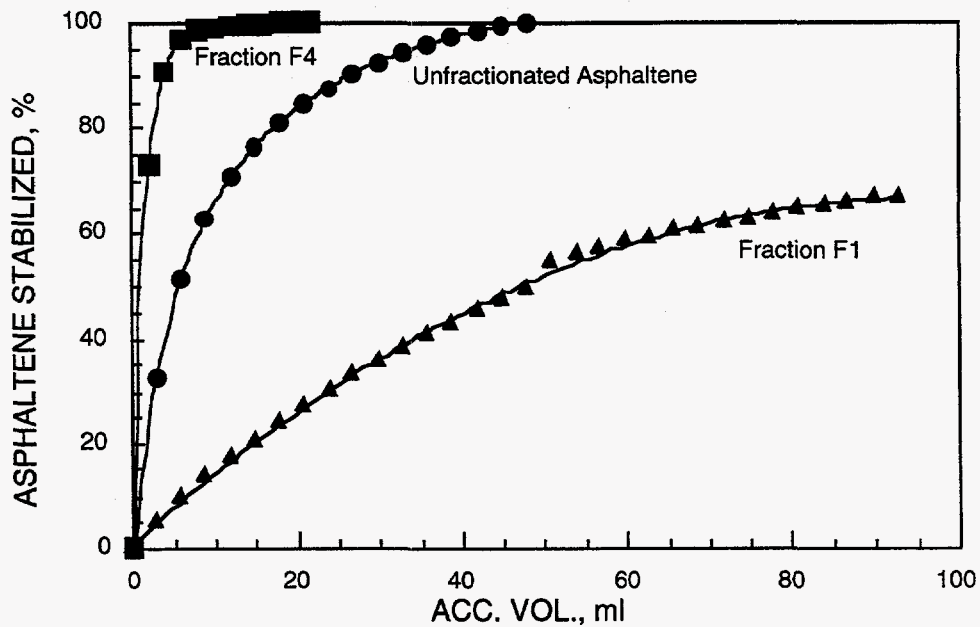


Figure 53. Comparative dissolution curves for asphaltene fractions and unfractionated asphaltene.

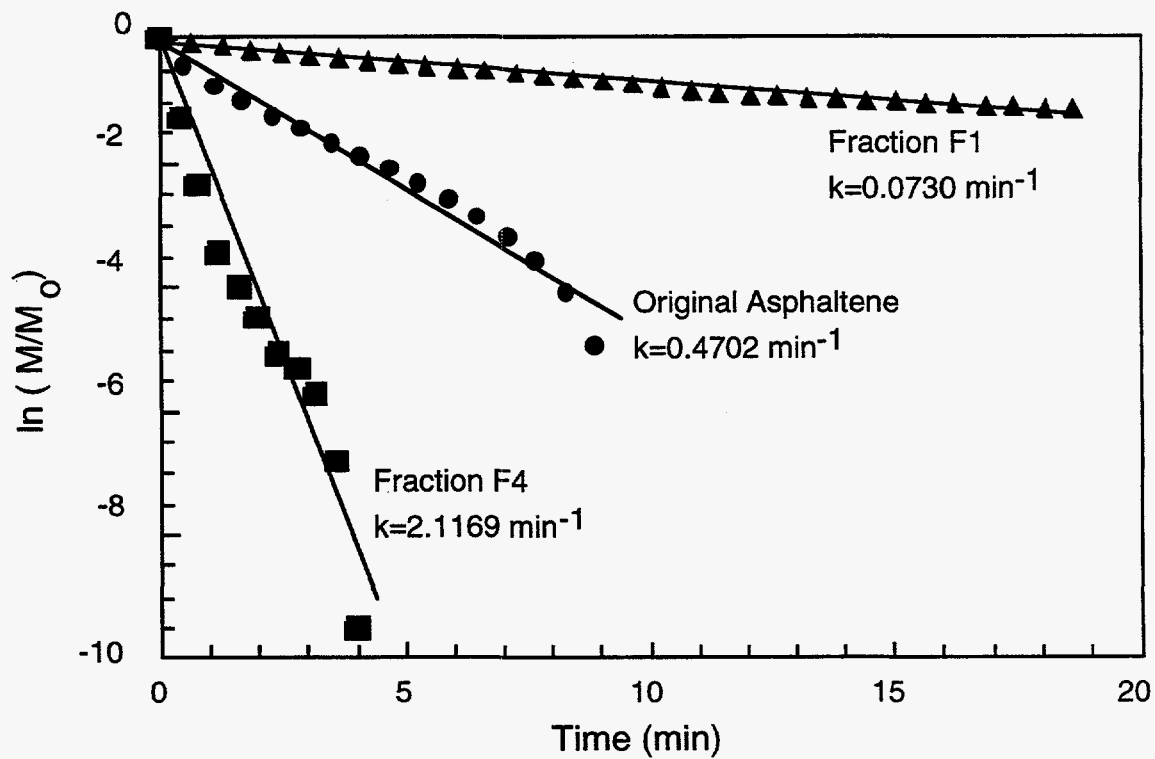


Figure 54. Kinetic analysis of dissolution rates of fractions and unfractionated asphaltene.

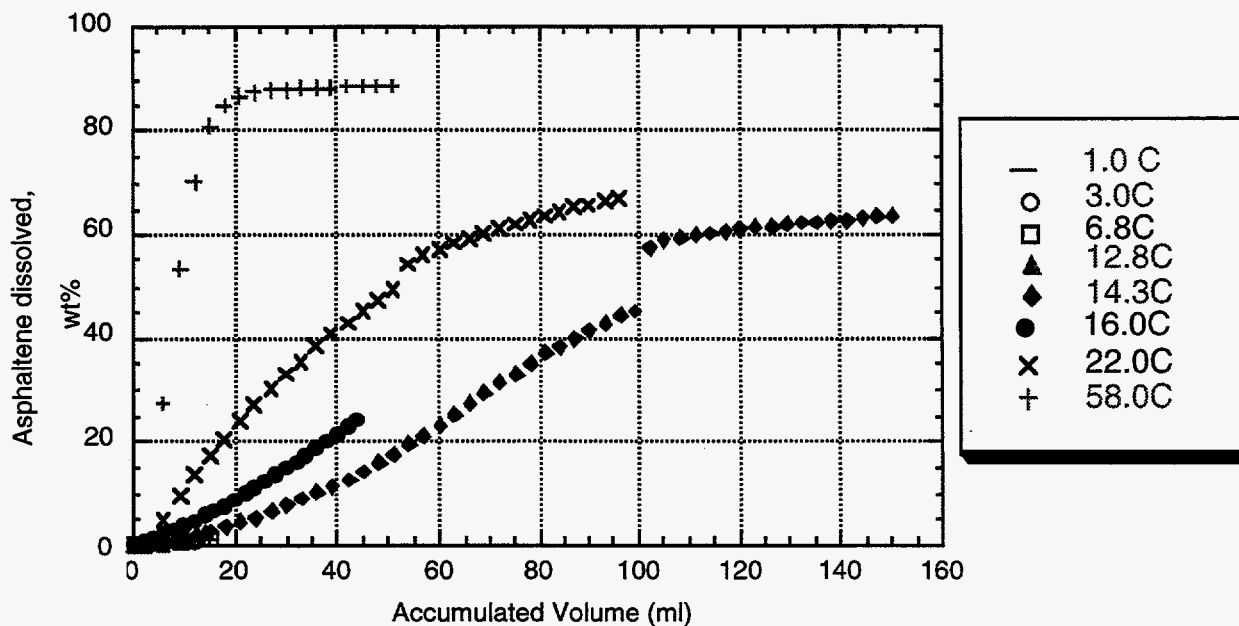


Figure 55. Dissolution curves for fraction F1 using 10 wt% DBSA in heptane at a flow rate of 5 ml / min. There is no dissolution at 1 & 3°C. The breaks in the curves for 14.3 and 22°C is due to extra residence time introduced while changing the syringe.

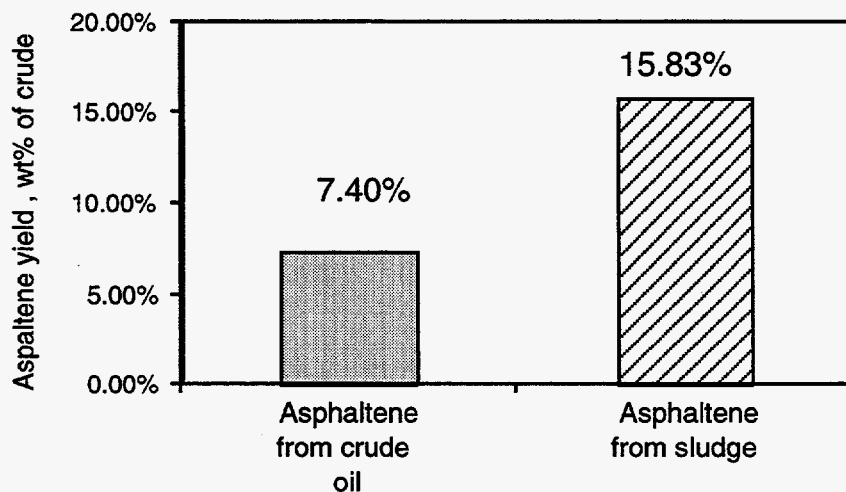


Figure 56. Asphaltene yield with and without the presence of ferric iron. The asphaltenes from sludge indicate the asphaltenes precipitated in the presence of ferric iron.

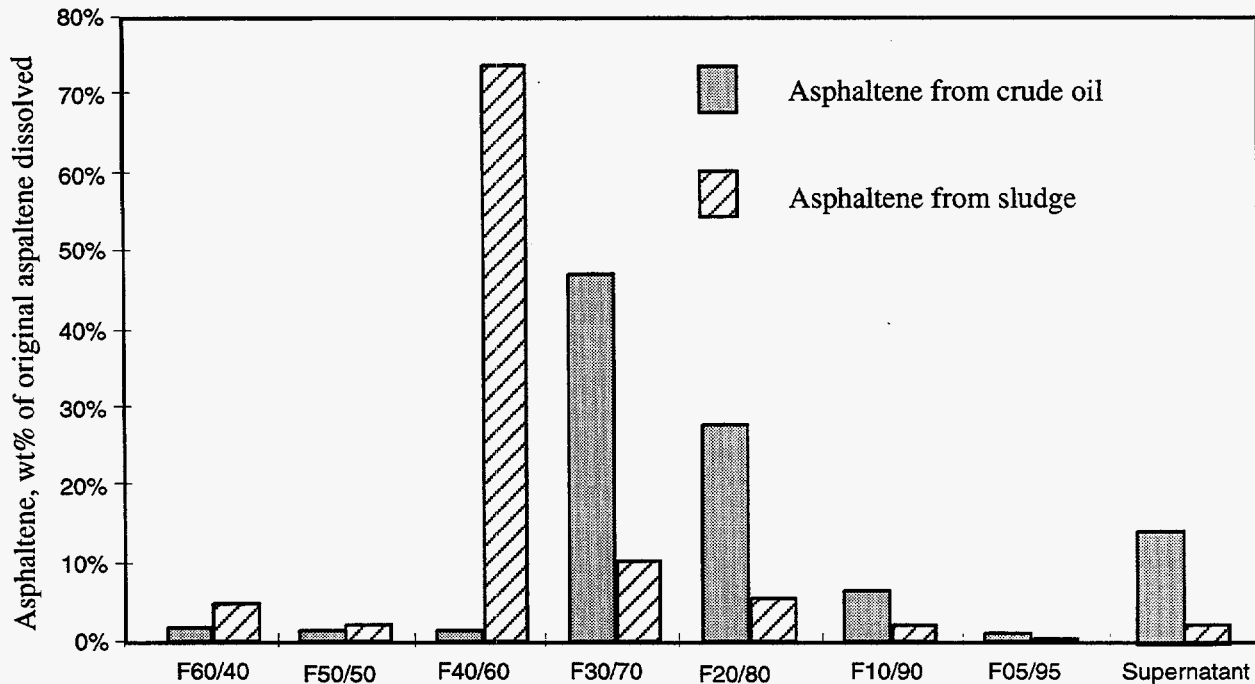


Figure 57. Distribution of fractions precipitated from crude oil and from sludge.

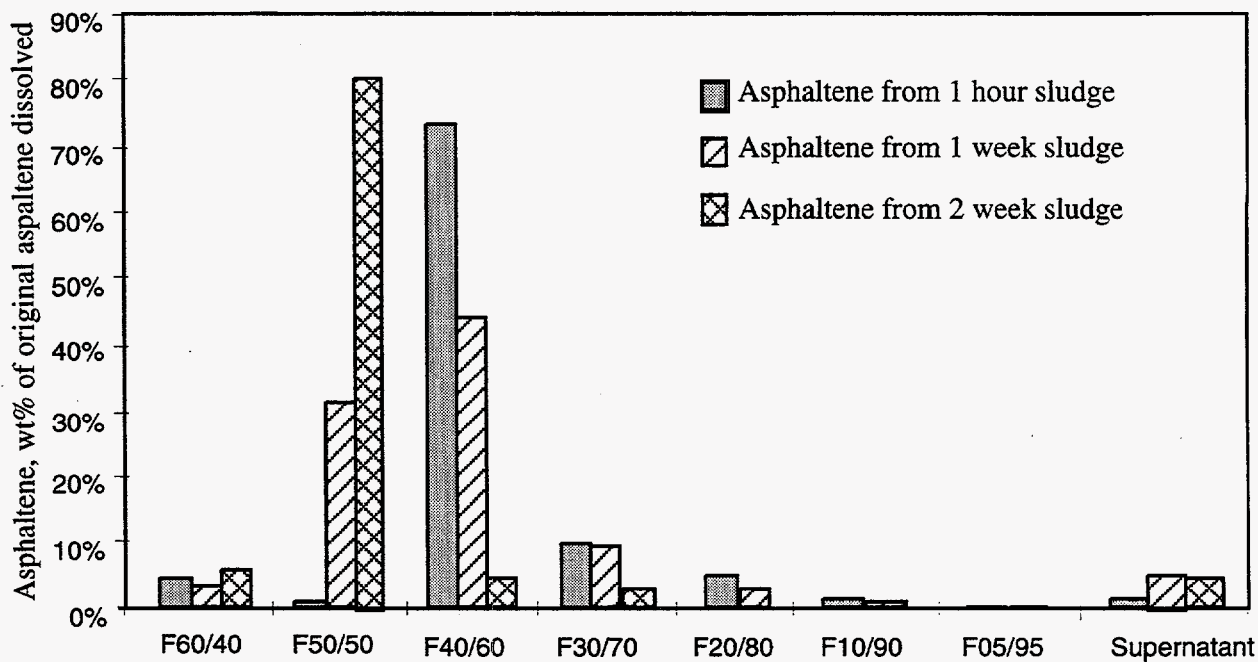


Figure 58. Effect of aerobic aging on the distribution of fractions from sludge. The aging process involved exposure of the sludge to air at room temperature.

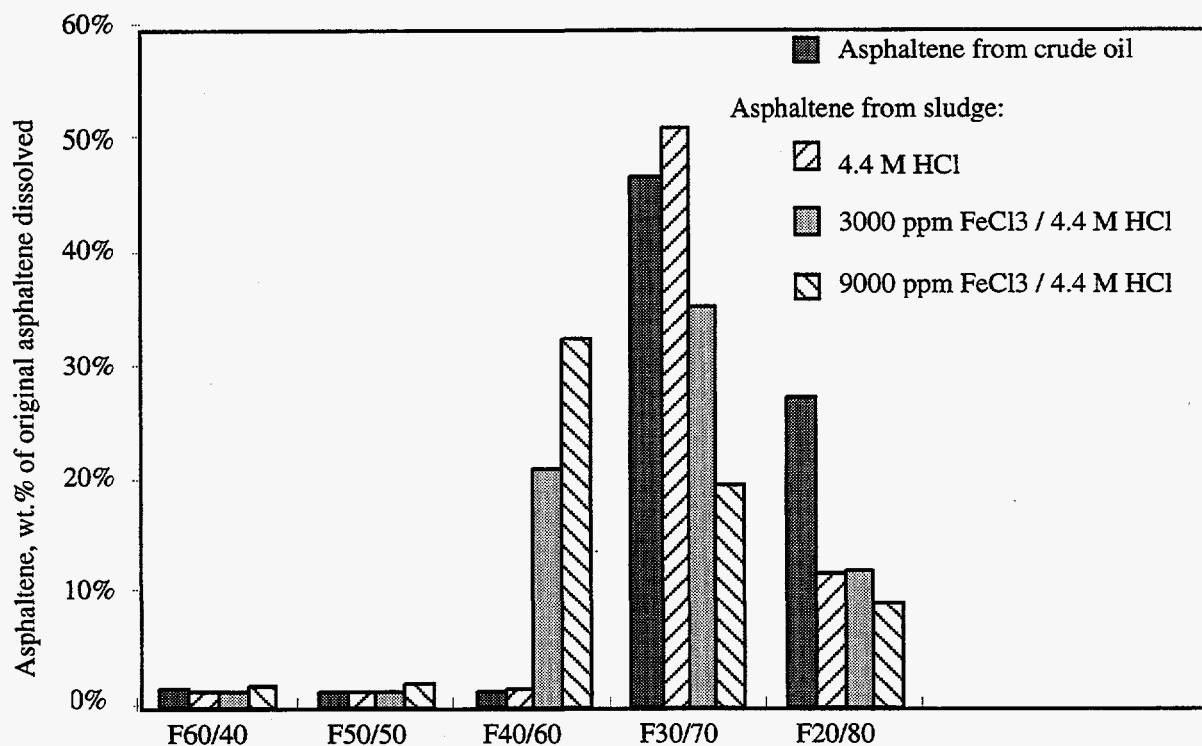


Figure 59. Effect of ferric ion concentration on fraction yield from sludge.

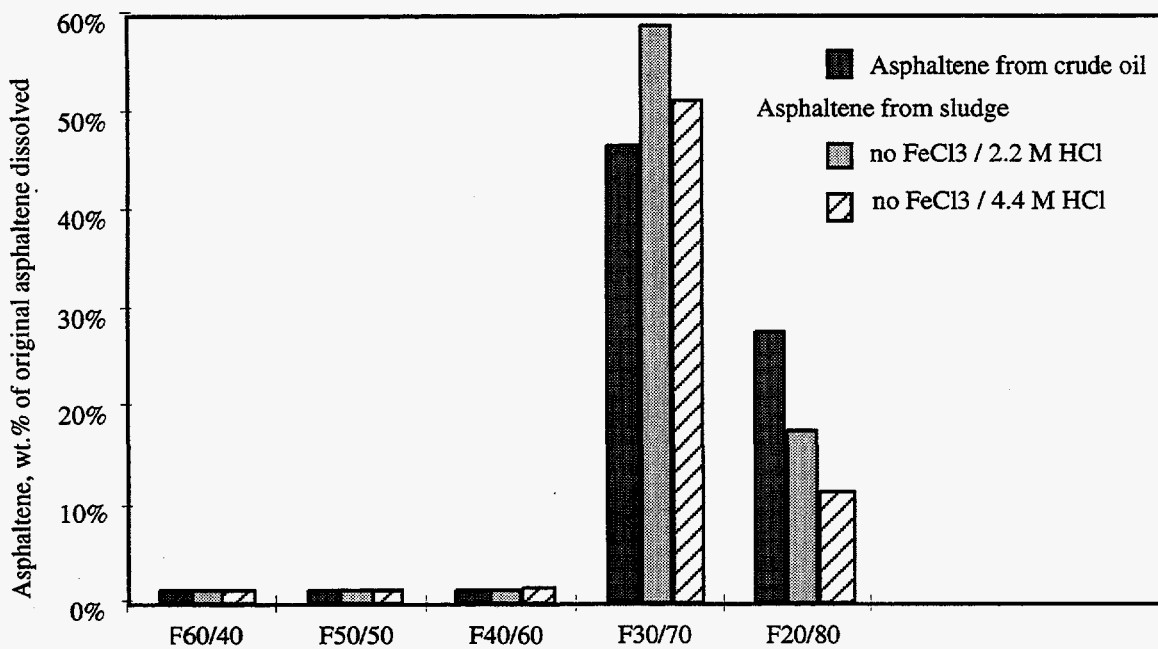


Figure 60. Effect of acid concentration on the fraction yield in the absence of ferric ions.

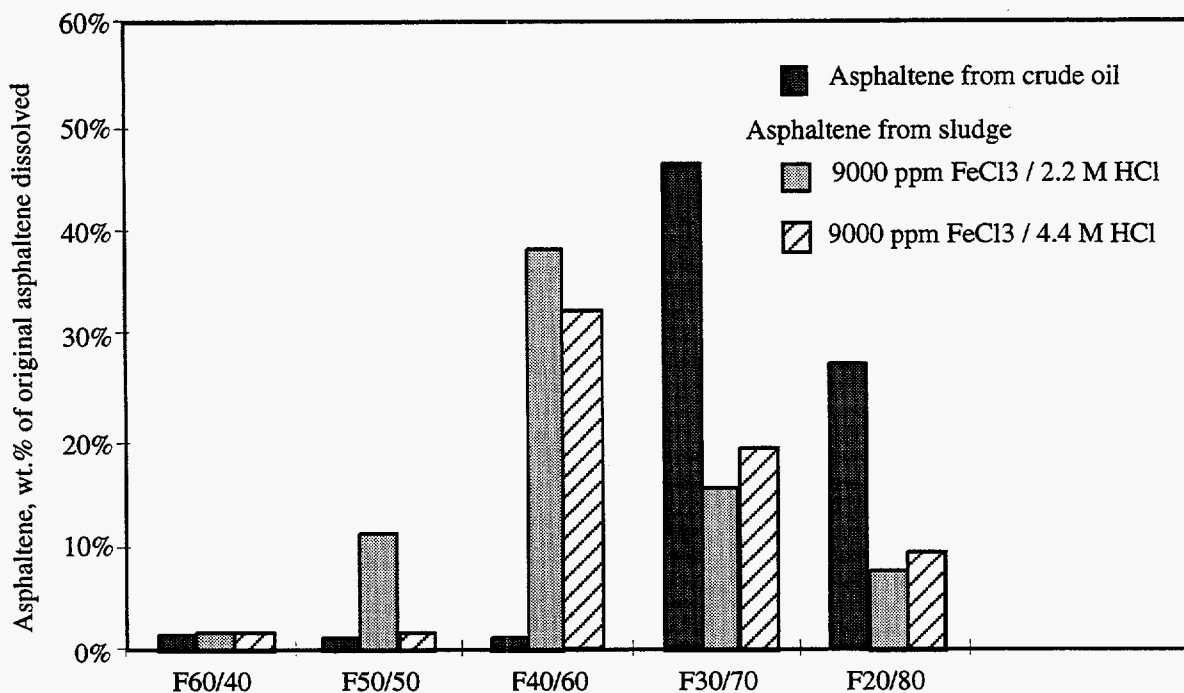


Figure 61. Effect of acid concentration on the fraction yield in the presence of ferric ions.

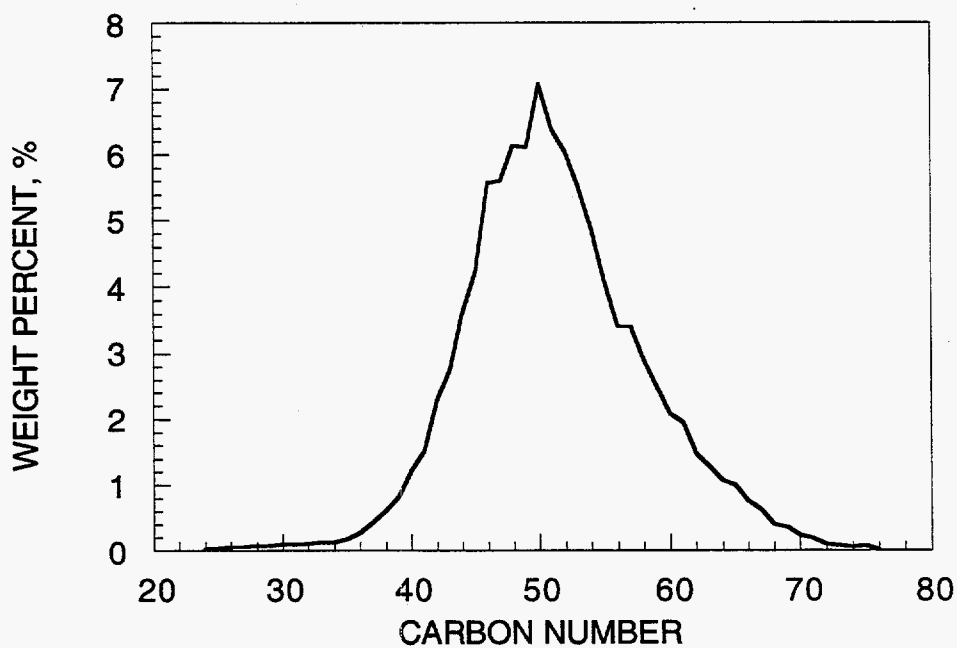


Figure 62. Molecular weight distribution of Joliet wax measured by high temperature gas chromatography.

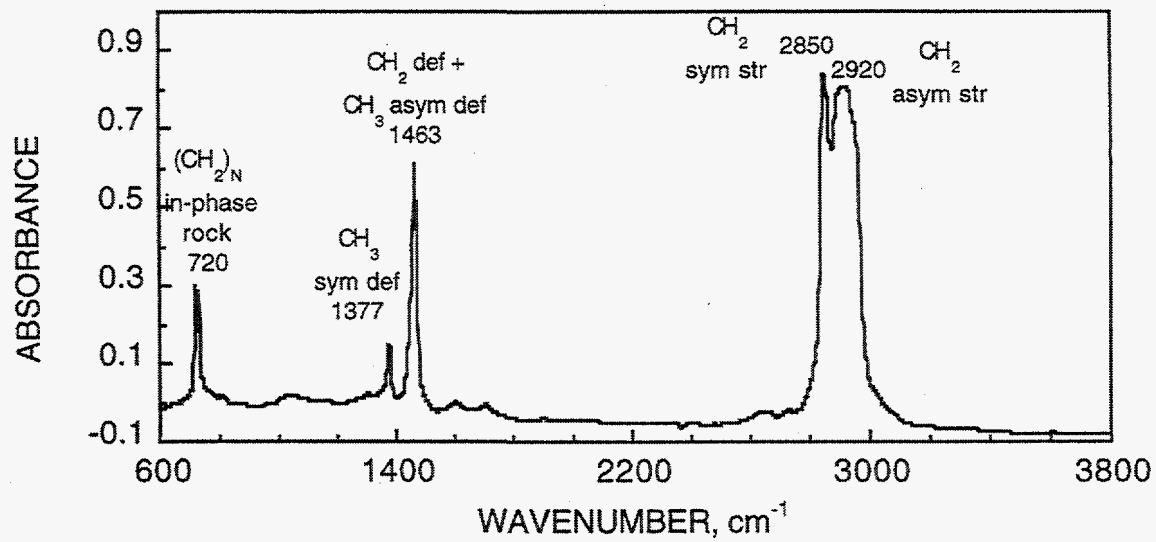


Figure 63. FTIR spectrum of Jolliet wax [prepared by casting wax film on an NaCl window].

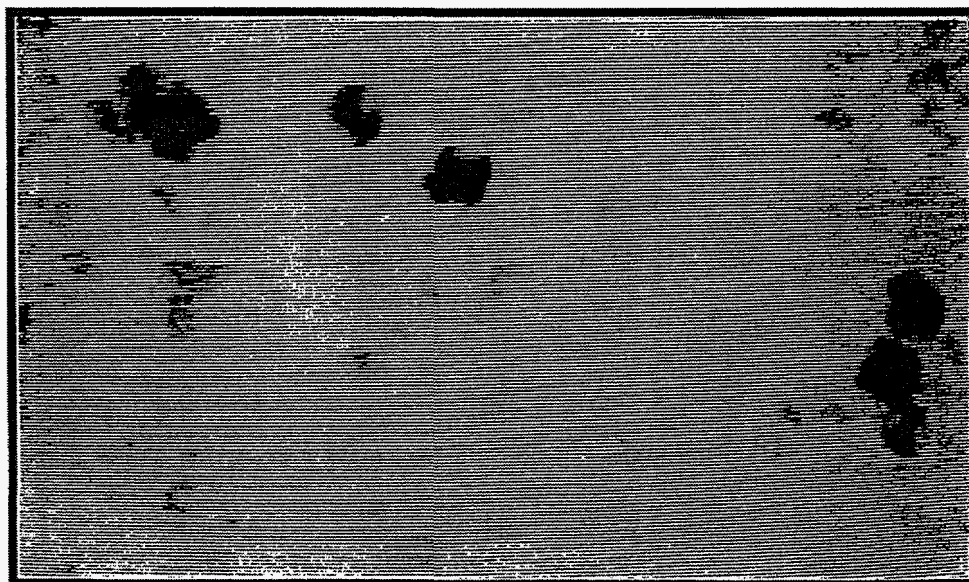


Figure 64. Light microscopic graph of Jolliet wax precipitates.  
(picture dimension =  $275 \mu\text{m} \times 165 \mu\text{m}$ )

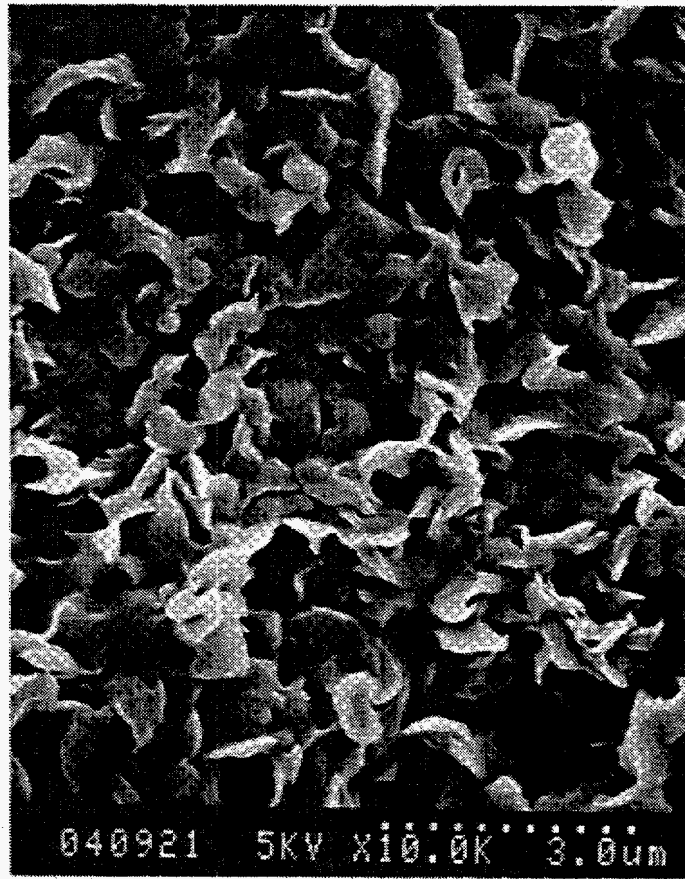


Figure 65. Scanning electron microscopic graph of Joliet wax precipitates.

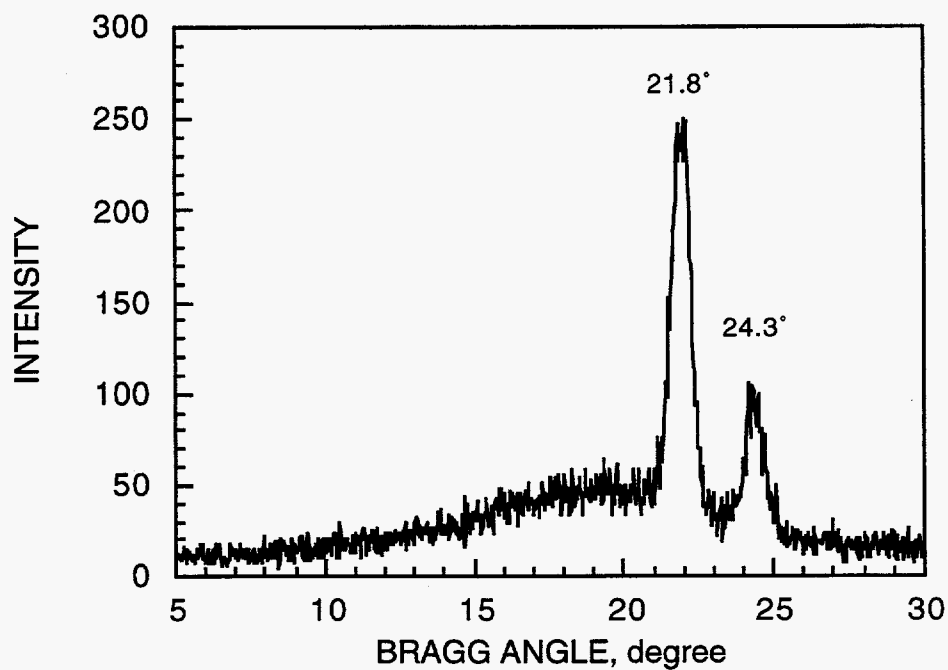


Figure 66. X-ray diffraction profiles of Joliet wax precipitates.

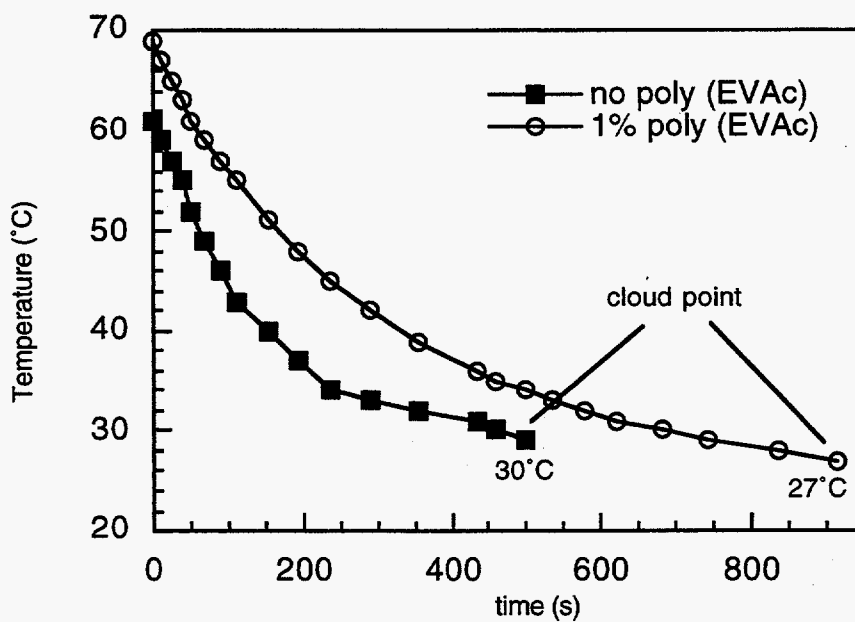


Figure 67. Cooling temperature profiles of heptane solution containing 1% Joliet wax (with or without poly (ethylene vinyl acetate)).



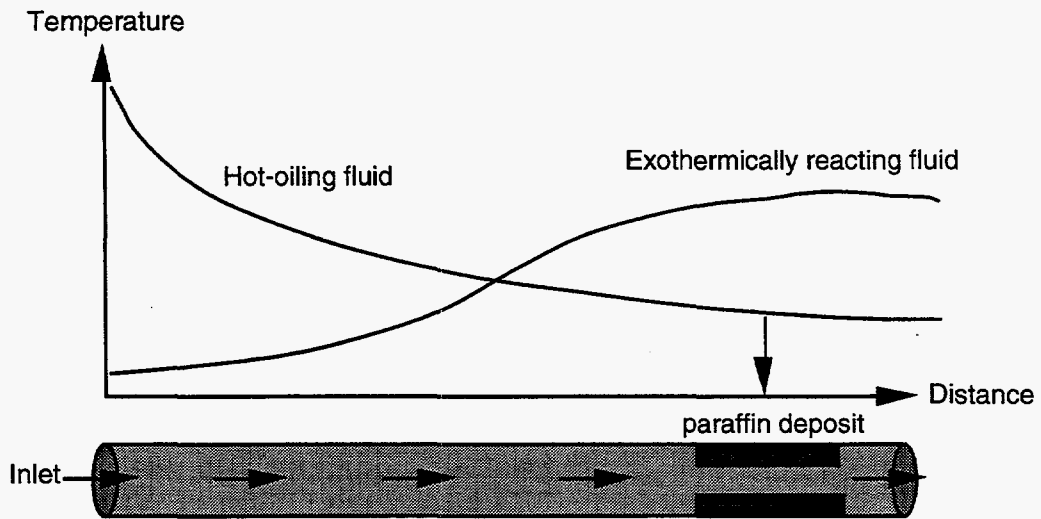


Figure 68. Schematic comparison of the temperature profile of hot-oiling fluids with that of exothermically reacting fluids when both fluids are injected into the pipeline for dissolving paraffin deposits.

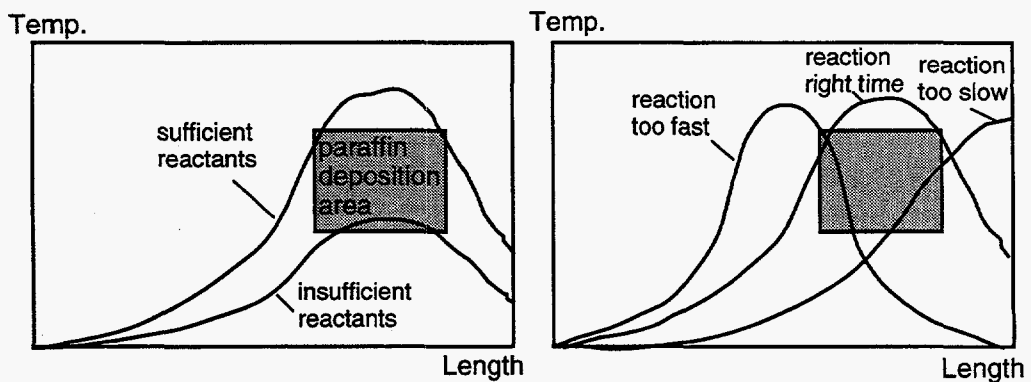


Figure 69. Schematic of the criteria of the effective dissolution of paraffin deposits using in-situ exothermic reactions conducted in the cleaning fluid.

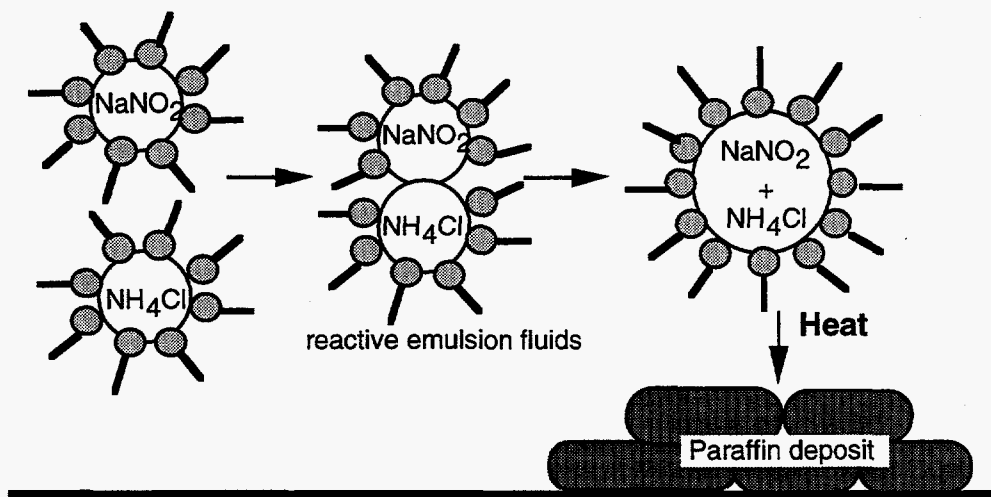


Figure 70. Schematic of the process of the exothermic reaction between  $\text{NH}_4\text{Cl}$  and  $\text{NaNO}_2$  conducted in the water-in-oil emulsion fluid.

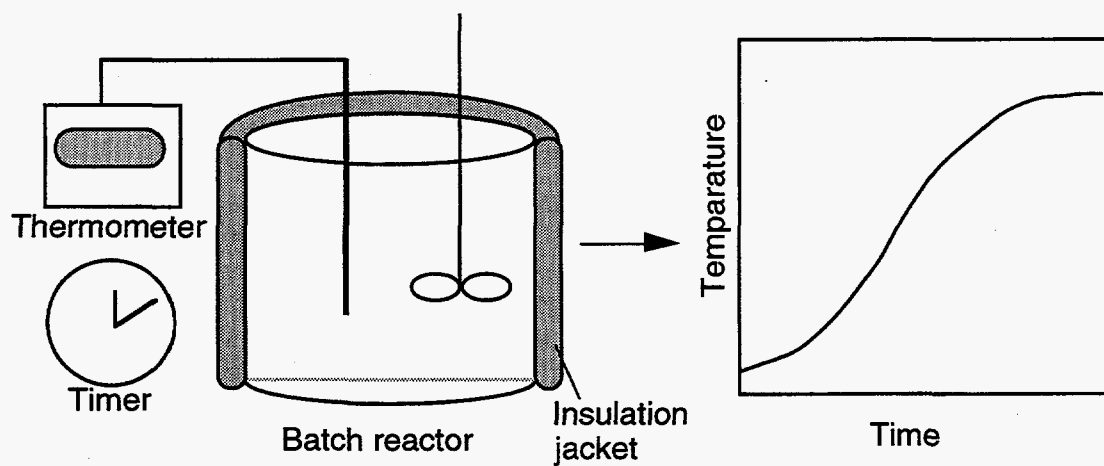


Figure 71. Schematic of the adiabatic batch reactor for studying the exothermic reaction kinetics.

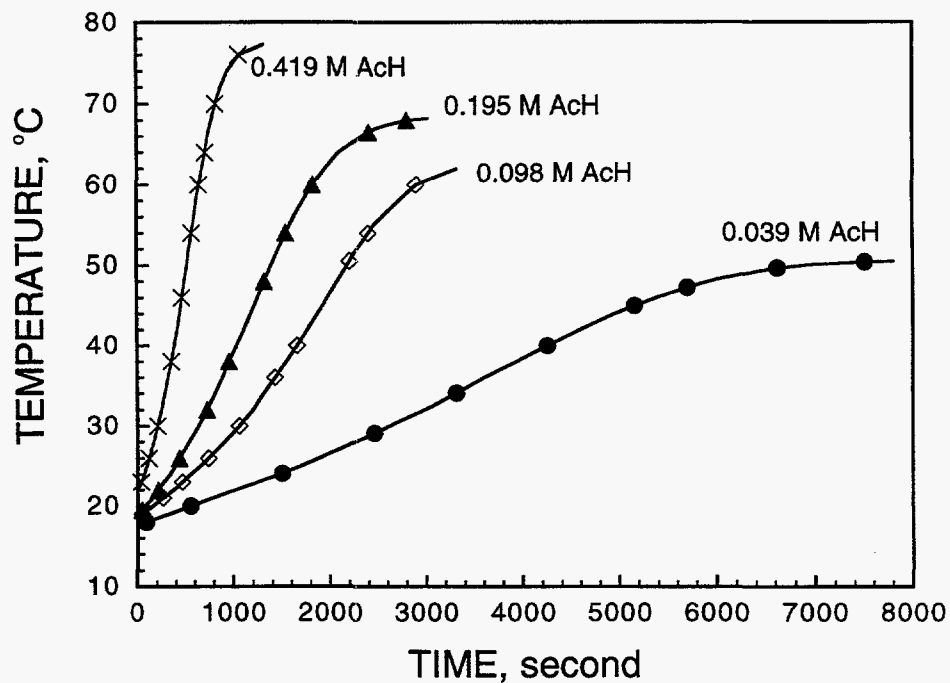


Figure 72. Effect of acetic acid (ac) concentration on the evolution of temperature in the adiabatic batch reactor during the exothermic reaction.

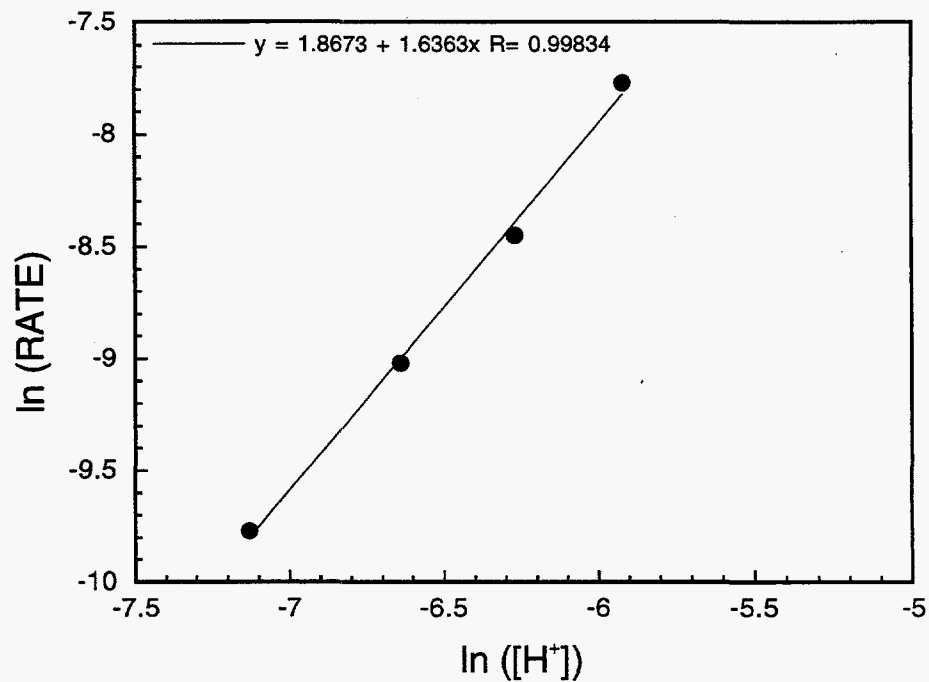


Figure 73. Rate of the exothermic reaction as a function of proton concentration. The slope of the fitting line, 1.6, is the reaction order with respect of the proton concentration.

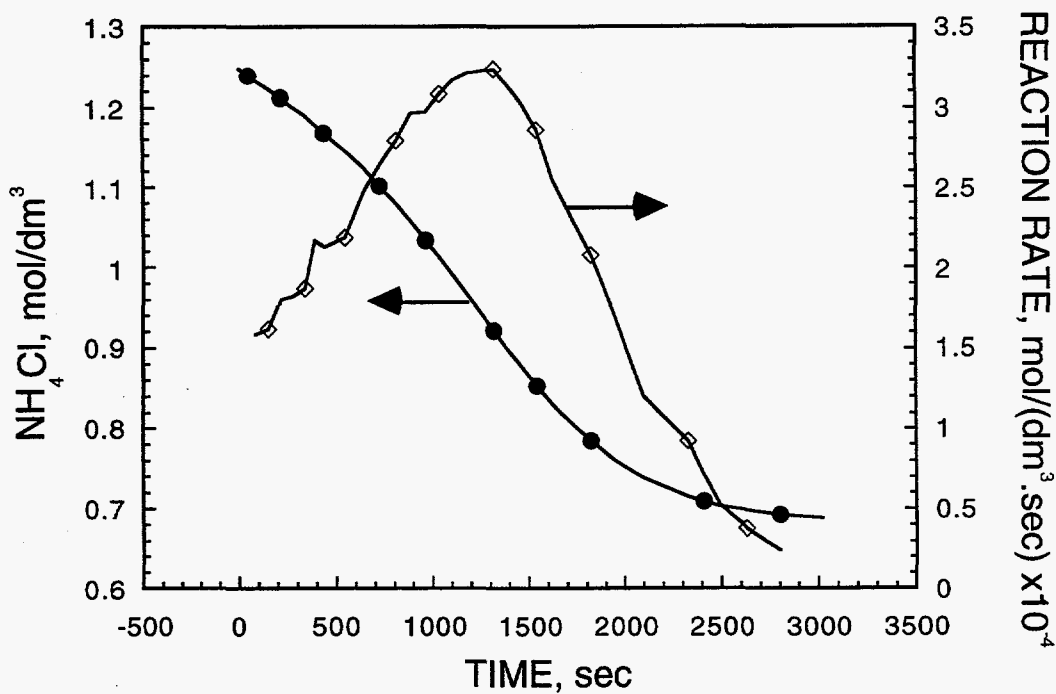


Figure 74.  $\text{NH}_4\text{Cl}$  concentration and the reaction rate deduced from data in Figure 73 (0.195 M ac) using equations (18) and (19), respectively.

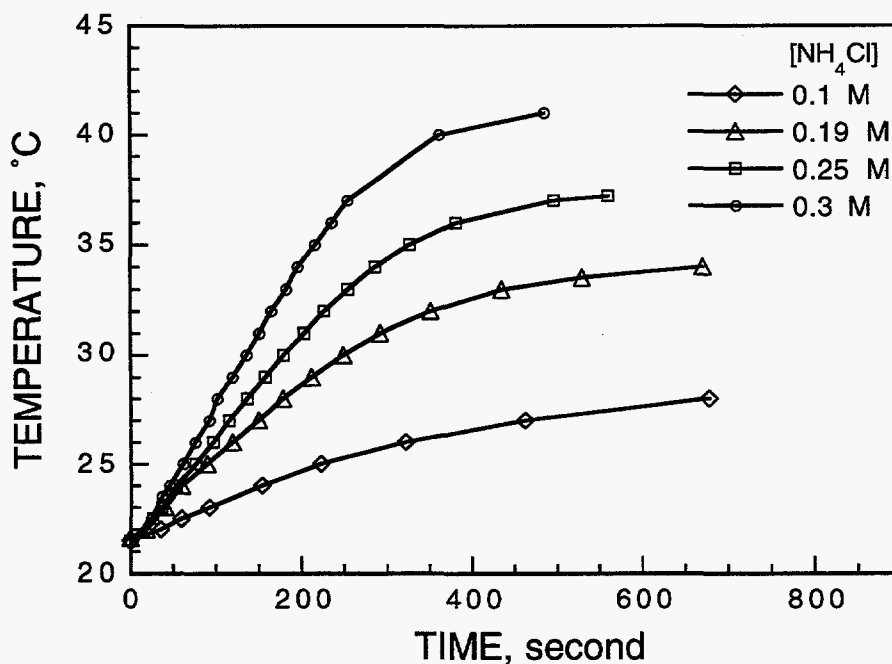


Figure 75. Temperature profile of aqueous solutions conducting the exothermic reaction between  $\text{NH}_4\text{Cl}$  and  $\text{NaNO}_2$  under adiabatic conditions. The concentration of  $\text{NH}_4\text{Cl}$  is varied as shown in the figure while those of  $\text{NaNO}_2$  and  $\text{CH}_3\text{COOH}$  are kept at 4.38 M and 1.02 M, respectively.

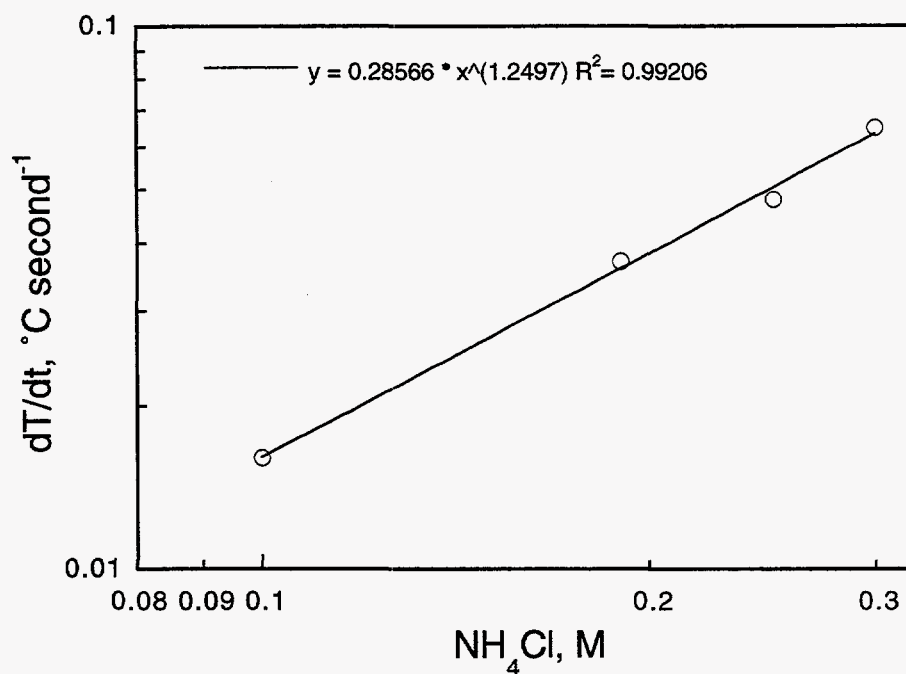


Figure 76. Rate of the exothermic reaction as a function of the concentration of  $\text{NH}_4\text{Cl}$ . The slope of the fitting line, 1.2, is the reaction order with respect of the  $\text{NH}_4\text{Cl}$  concentration.

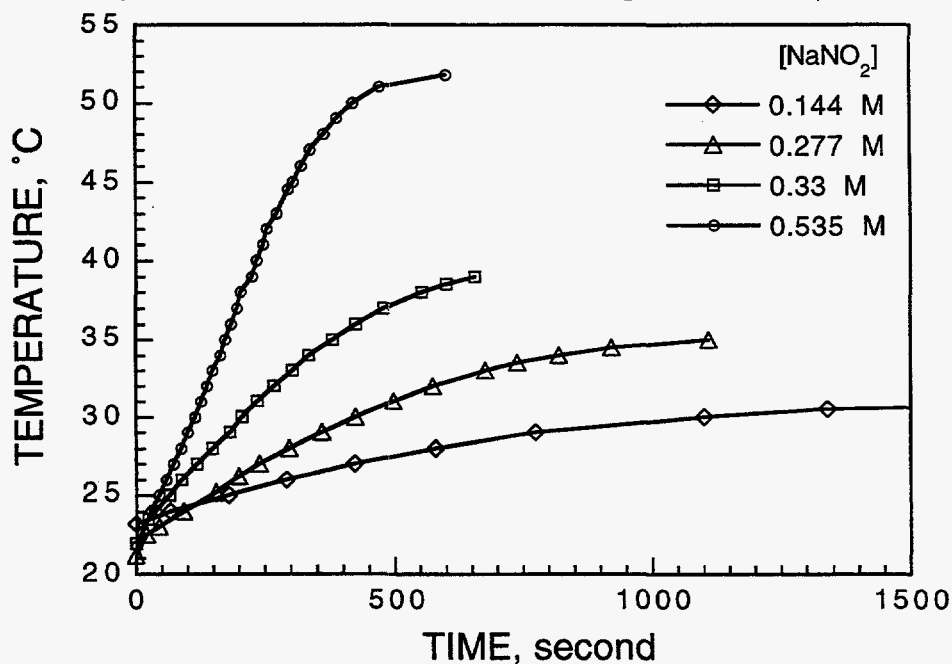


Figure 77. Temperature profile of aqueous solutions conducting the exothermic reaction between  $\text{NH}_4\text{Cl}$  and  $\text{NaNO}_2$  under adiabatic conditions. The concentration of  $\text{NaNO}_2$  is varied as shown in the figure while those of  $\text{NH}_4\text{Cl}$  and  $\text{CH}_3\text{COOH}$  are kept at 4.6 M and 1.08 M, respectively.

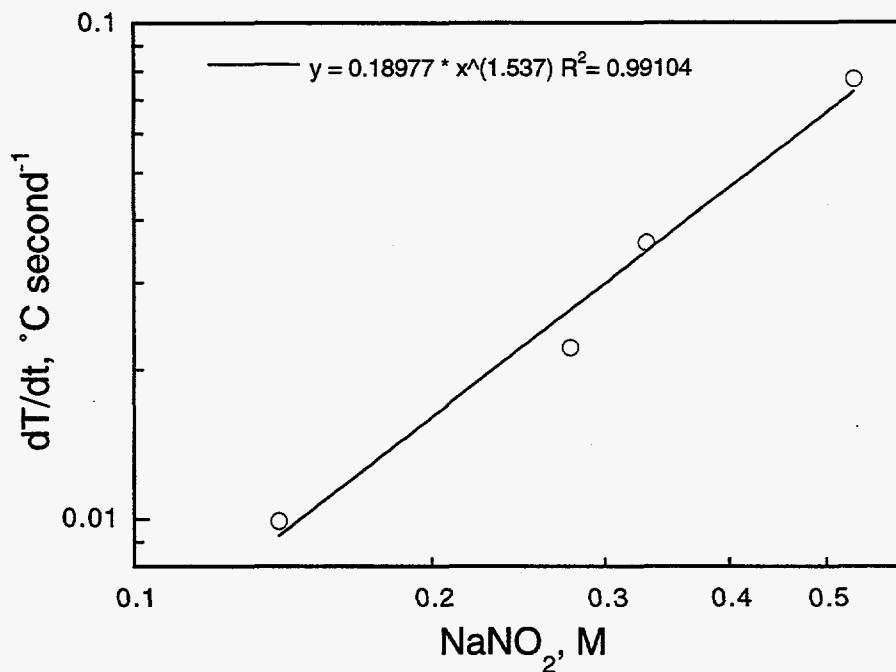


Figure 78. Rate of the exothermic reaction as a function of the concentration of  $\text{NaNO}_2$ . The slope of the fitting line, 1.5, is the reaction order with respect to  $\text{NaNO}_2$  concentration.

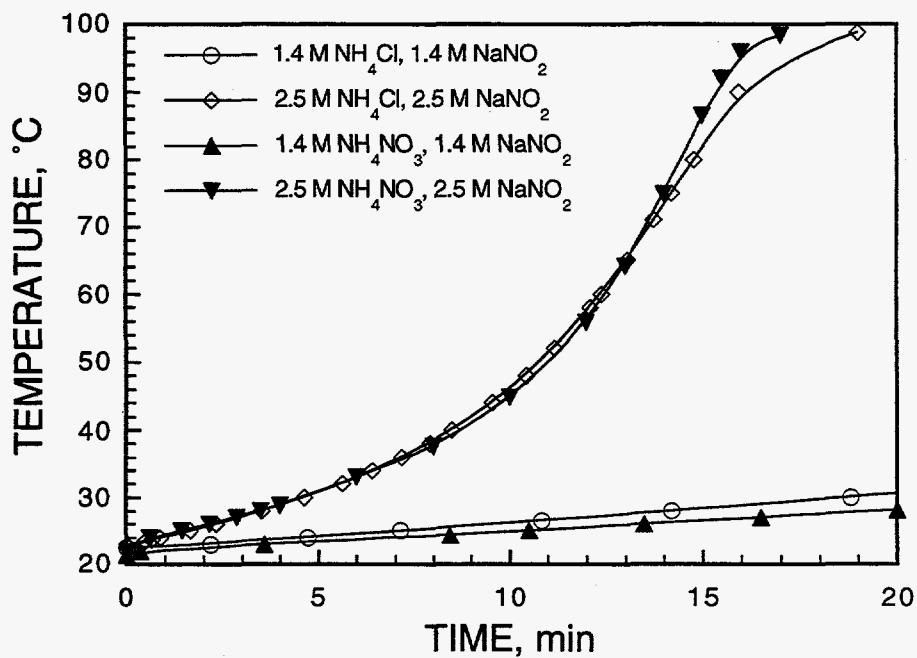


Figure 79. Temperature profile of aqueous solutions conducting the  $\text{NH}_4\text{Cl}-\text{NaNO}_2$  reaction and the  $\text{NH}_4\text{NO}_3-\text{NaNO}_2$  reaction under adiabatic conditions.

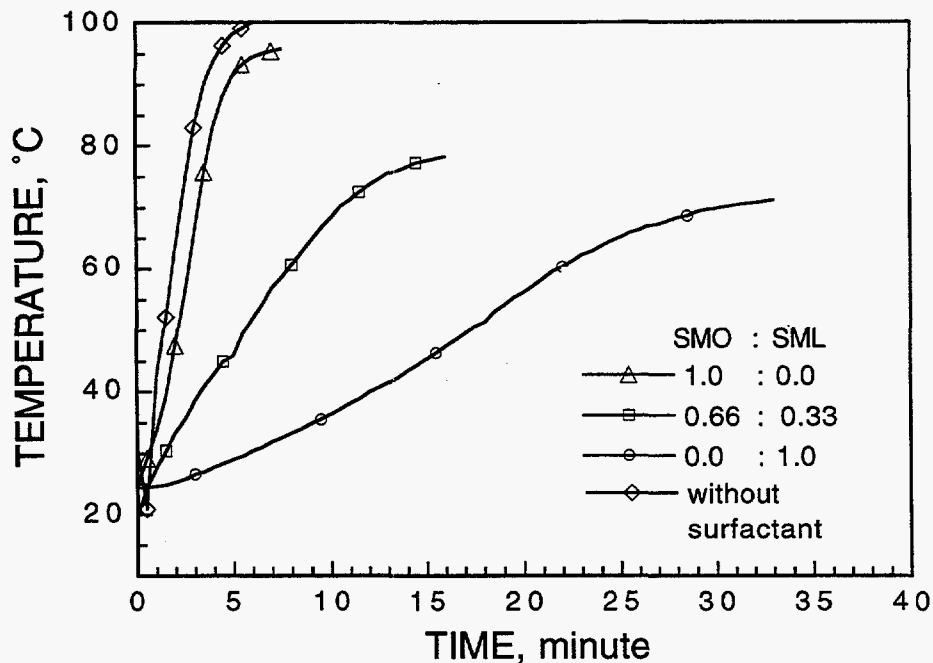


Figure 80. Temperature profiles of water/heptane emulsions containing SMO and SML by different proportions during the reaction between  $\text{NaNO}_2$  and  $\text{NH}_4\text{Cl}$ .

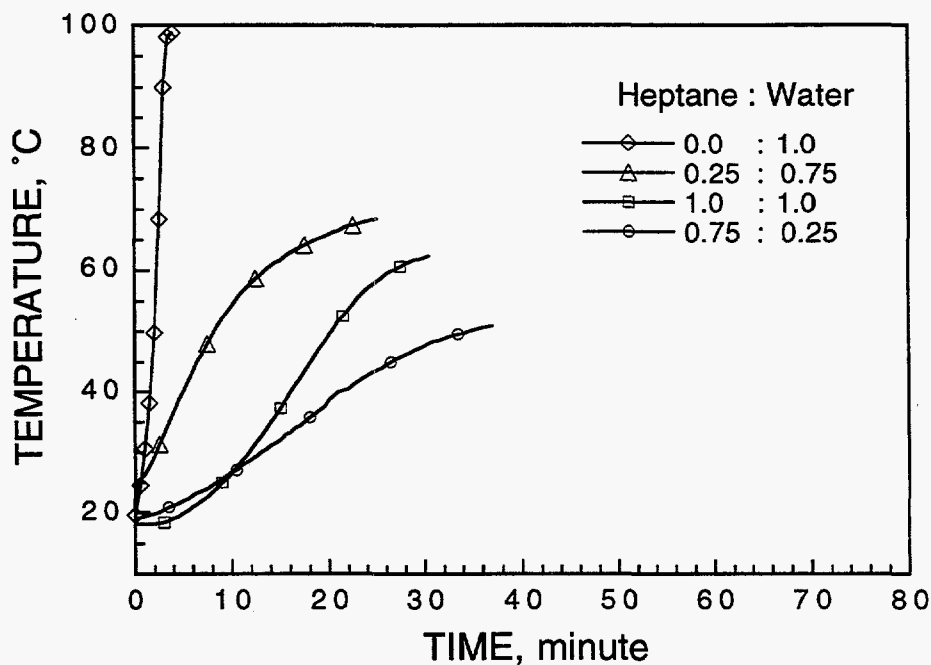


Figure 81. Temperature profiles of SMO emulsions containing different proportions of water and heptane during the reaction between  $\text{NaNO}_2$  and  $\text{NH}_4\text{Cl}$ .

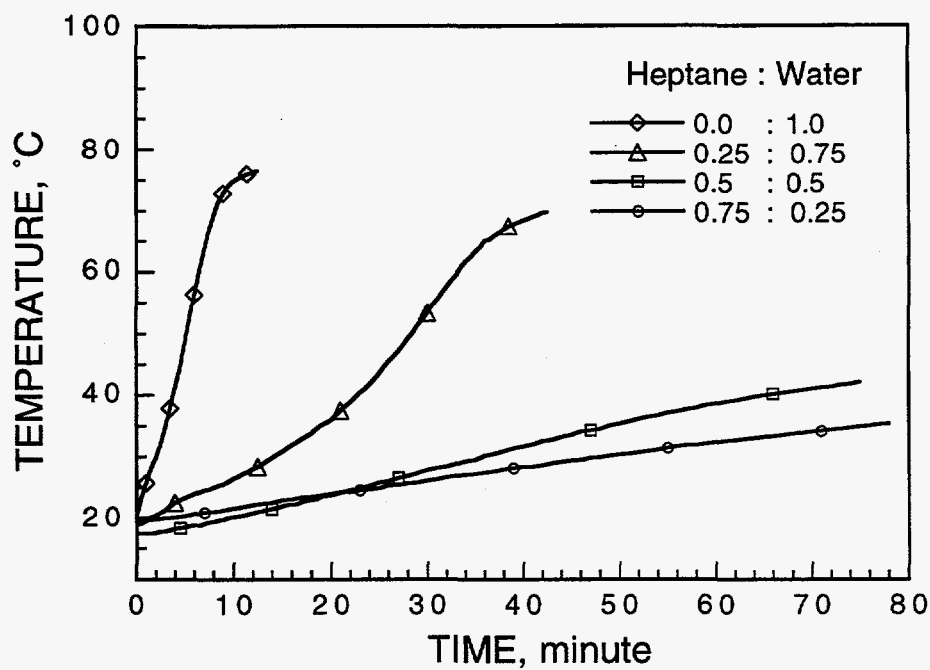


Figure 82. Temperature profiles of SML emulsions containing different proportions of water and heptane during the reaction between  $\text{NaNO}_2$  and  $\text{NH}_4\text{Cl}$ .

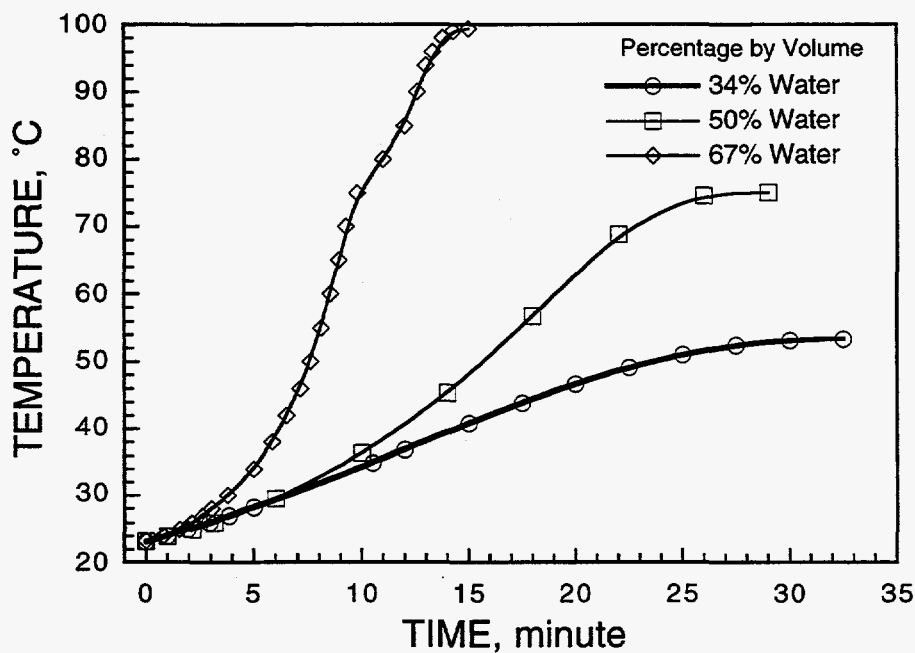


Figure 83. Temperature profiles of SML emulsions containing different proportions of water and heptane during the reaction between  $\text{NaNO}_2$  and  $\text{NH}_4\text{Cl}$ .



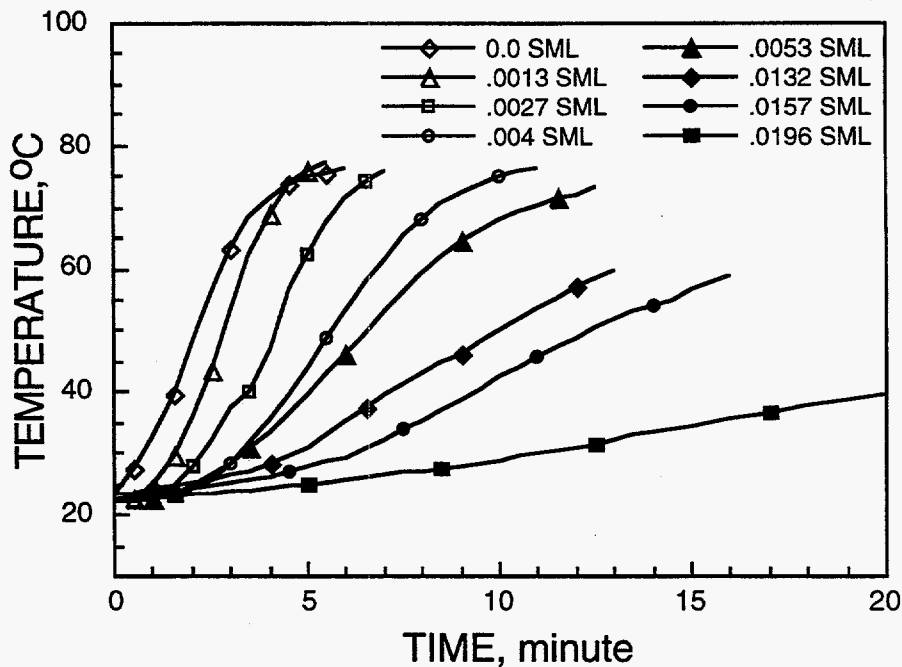


Figure 84. Temperature profiles of water/heptane emulsions containing different concentrations of SML during the reaction between  $\text{NaNO}_2$  and  $\text{NH}_4\text{Cl}$ .

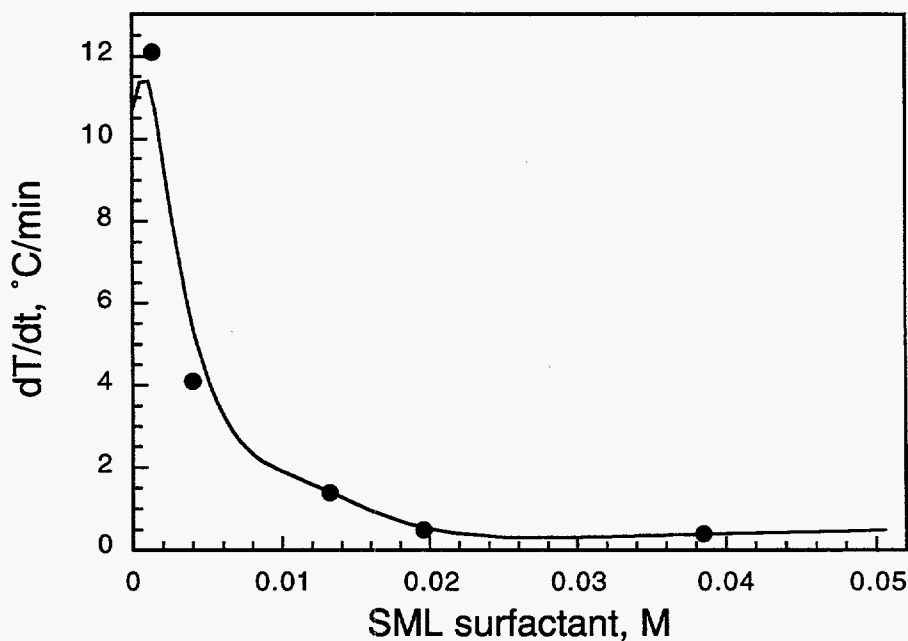


Figure 85. Rate of  $\text{NaNO}_2$ - $\text{NH}_4\text{Cl}$  reaction,  $dT/dt$ , as a function of the concentration of SML surfactant in water/heptane emulsions.

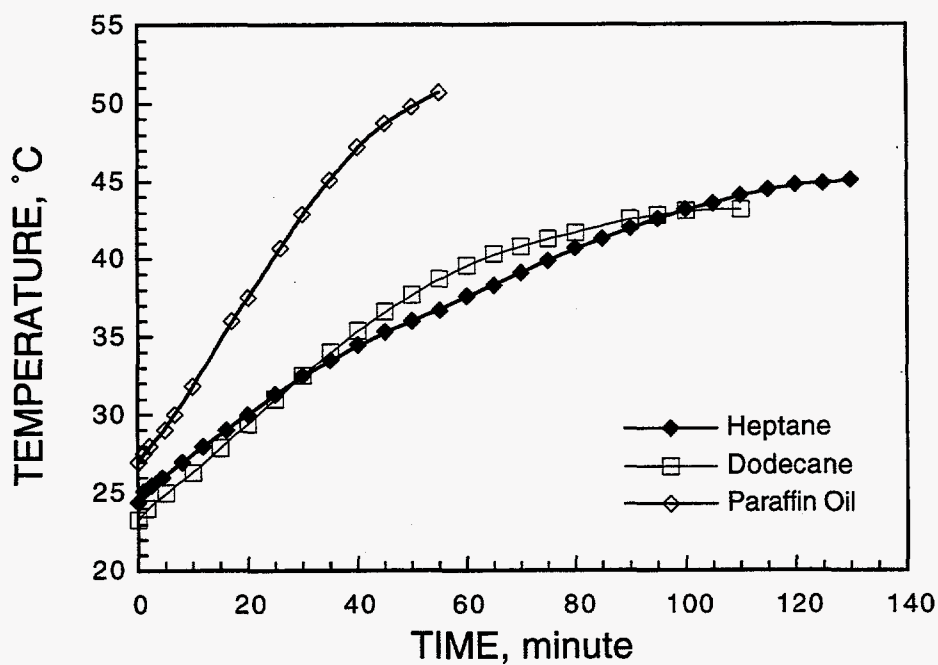


Figure 86. Temperature profiles of SMO emulsions containing different types of alkane during the reaction between  $\text{NaNO}_2$  and  $\text{NH}_4\text{Cl}$ .

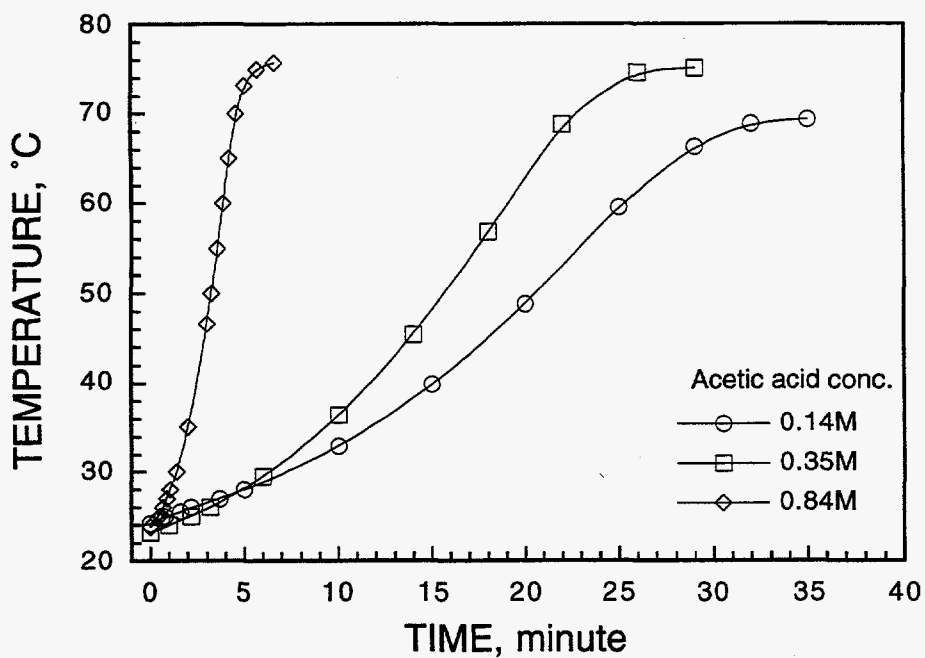


Figure 87. Temperature profiles of water/heptane/SML emulsions containing different concentrations of acetic acid during the reaction between  $\text{NaNO}_2$  and  $\text{NH}_4\text{Cl}$ .

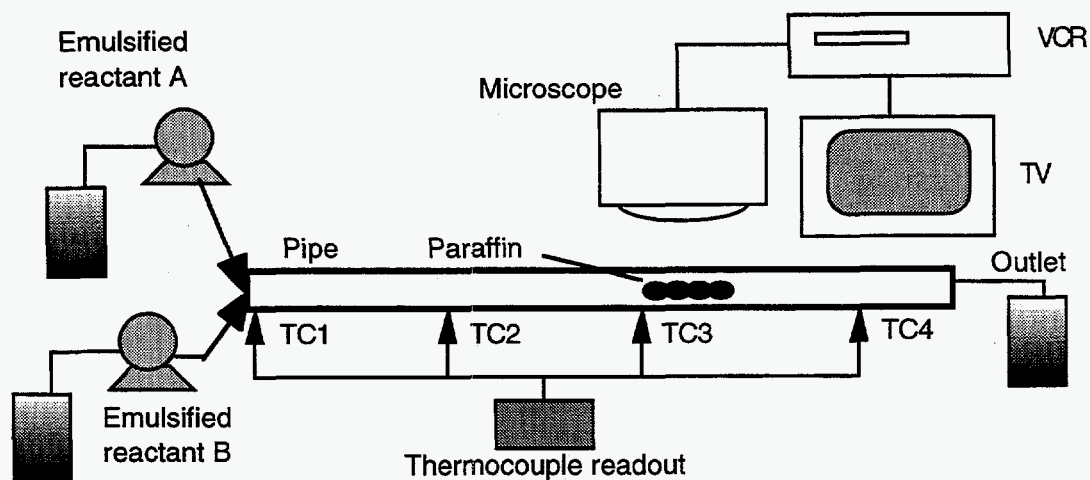


Figure 88. Schematic of the pipe flow experimental setup.

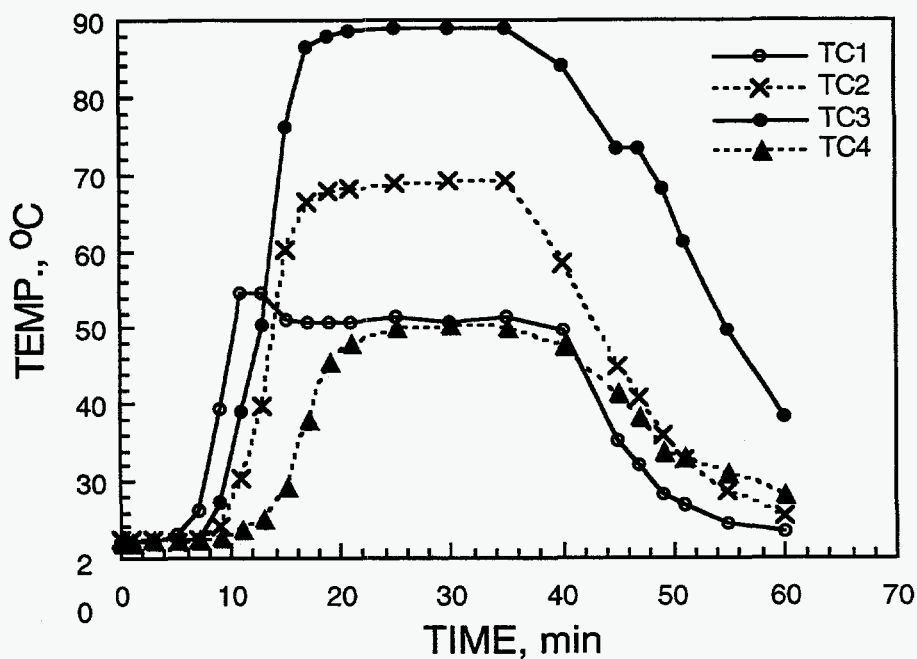


Figure 89. Temperature of pipe walls at four different positions (see Figure 88) during the flow of  $\text{NaNO}_2$  and  $\text{NH}_4\text{NO}_3$ .



Fig. 90 (a) Paraffin in pipeline, 38 min. 41 sec.,  $T=66^{\circ}\text{C}$ .



Fig. 90(b) Paraffin in pipeline, 39 min. 53 sec.,  $T=66^{\circ}\text{C}$ .

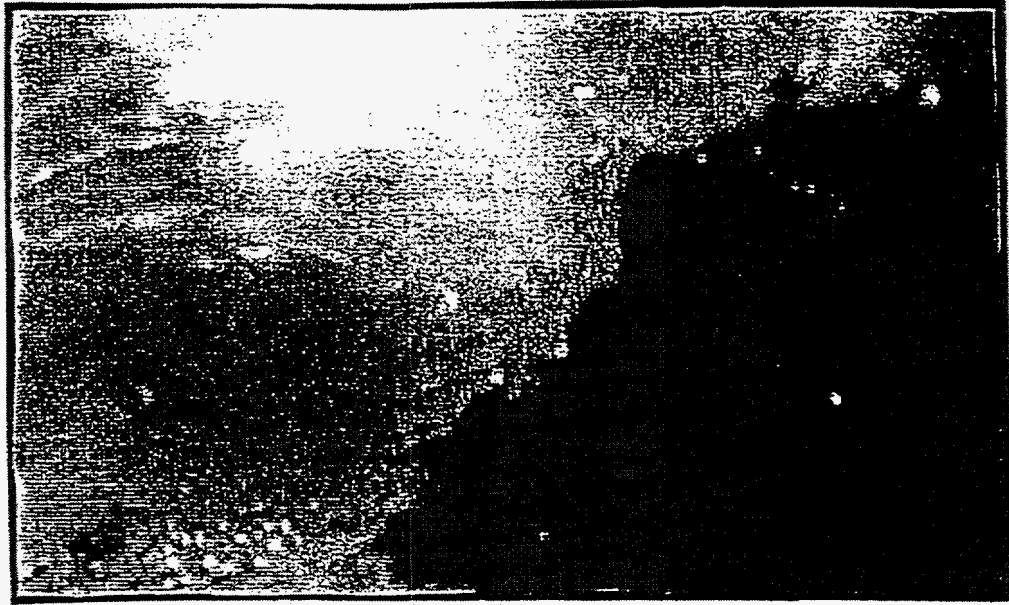


Fig. 90(c) Paraffin in pipeline, 40 min. 15 sec.,  $T=65^{\circ}\text{C}$ .

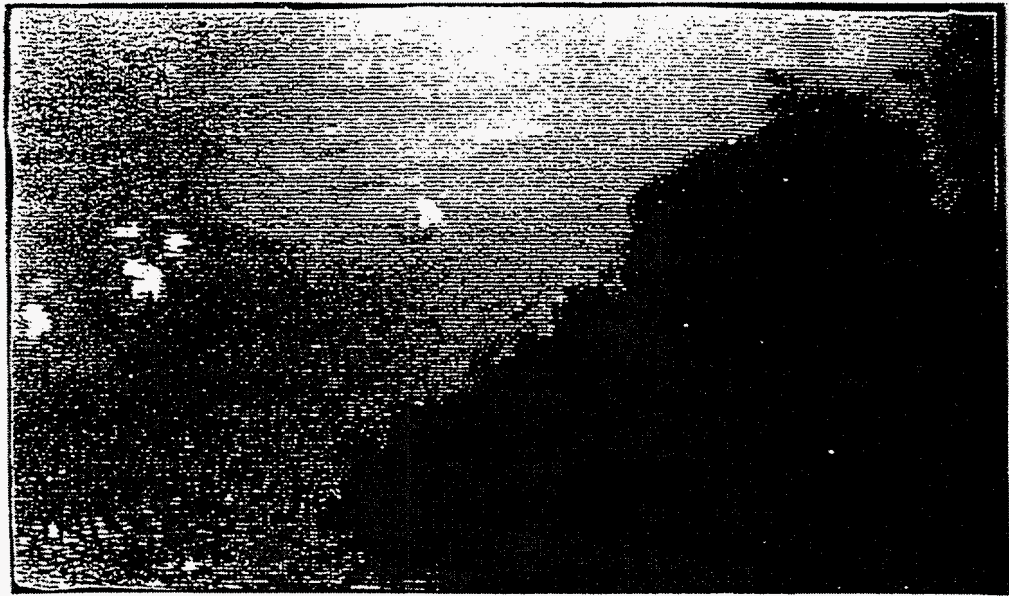


Fig. 90(d) Paraffin in pipeline, 40 min. 20 sec.,  $T=65^{\circ}\text{C}$ .

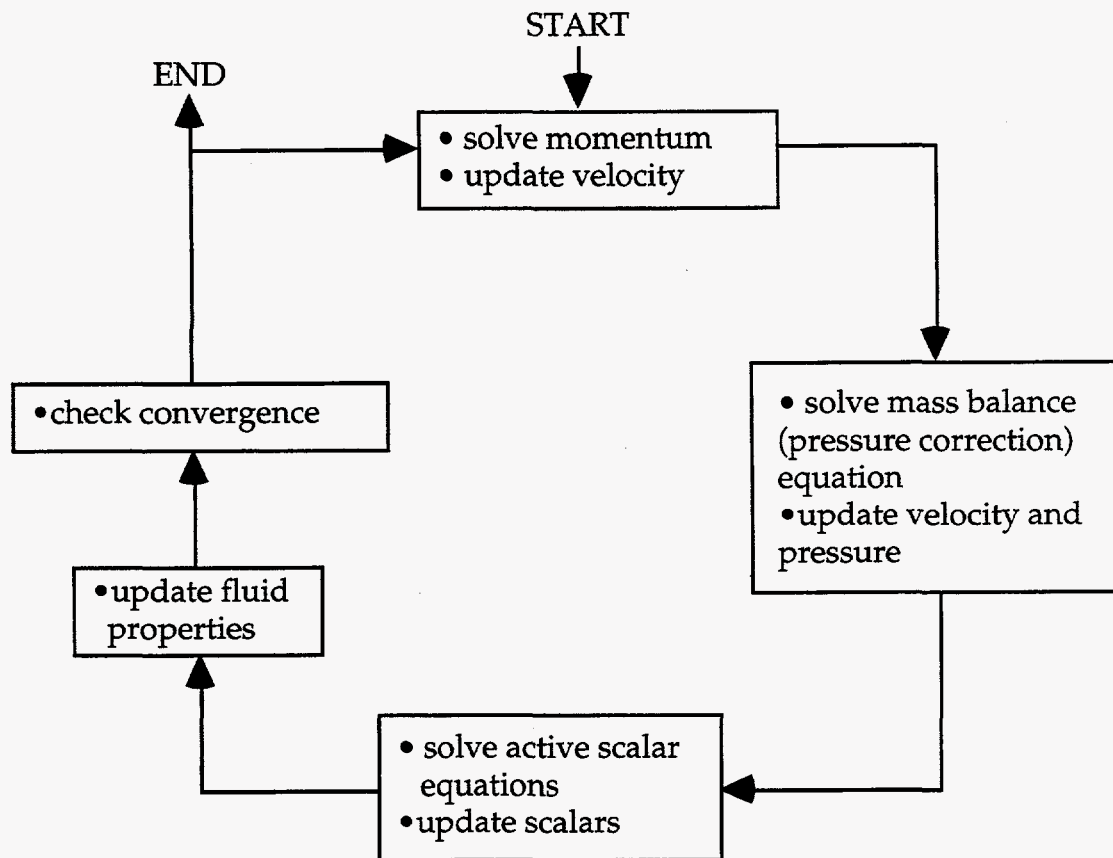


Figure 91. Overall view of the solution process.

6.40E+01  
 6.18E+01  
 5.96E+01  
 5.74E+01  
 5.52E+01  
 5.30E+01  
 5.08E+01  
 4.86E+01  
 4.63E+01  
 4.41E+01  
 4.19E+01  
 3.97E+01  
 3.75E+01  
 3.53E+01  
 3.31E+01  
 3.09E+01  
 2.87E+01  
 2.65E+01  
 2.43E+01  
 2.21E+01  
 1.99E+01  
 1.77E+01  
 1.54E+01  
 1.32E+01  
 1.10E+01  
 8.83E+00  
 6.62E+00  
 4.41E+00  
 2.21E+00  
 .00E+00

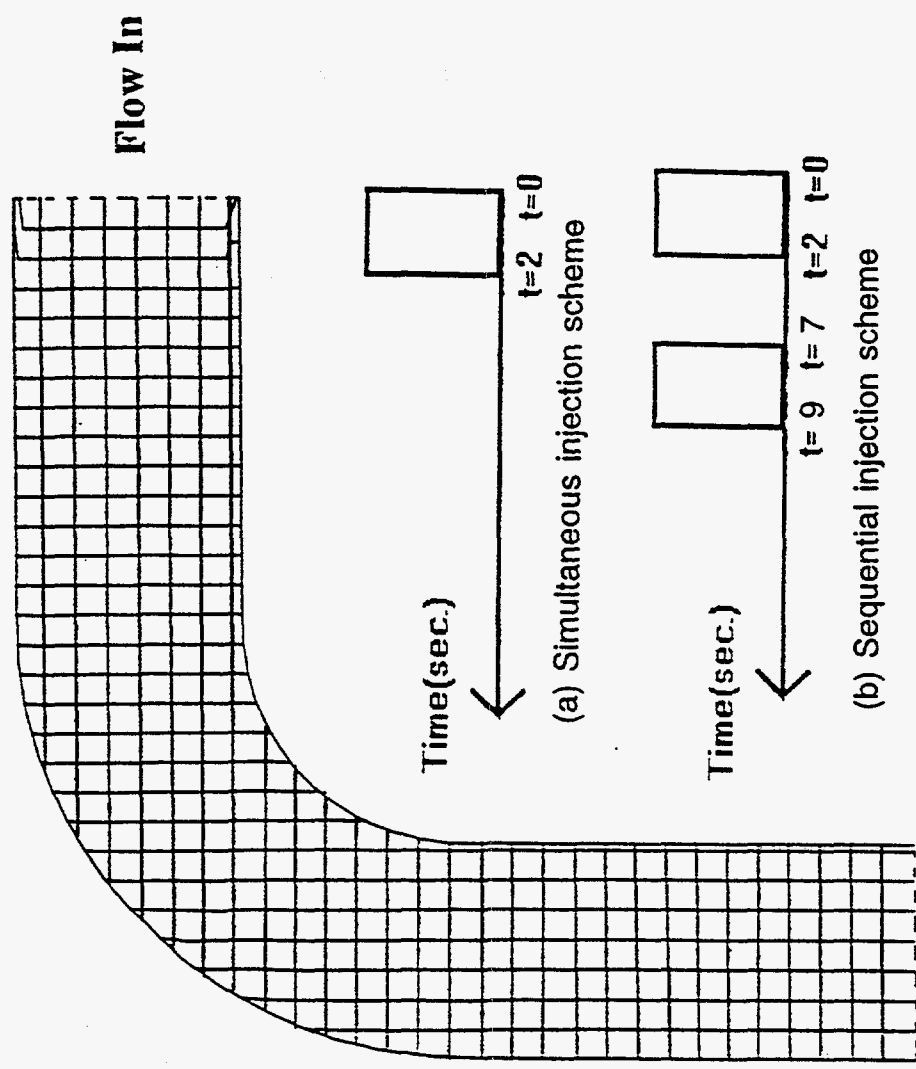
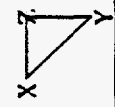


Figure 92. Two different injection cases.

Fluid Flow and Heat Transfer in a Mixing Elbow  
 X-Position (Inches) Max = 6.400E+01 Min = .000E+00  
 Y-Position (Inches) Max = 6.400E+01 Min = .000E+00



1.99E-14  
 1.93E-14  
 1.86E-14  
 1.79E-14  
 1.73E-14  
 1.66E-14  
 1.59E-14  
 1.53E-14  
 1.46E-14  
 1.39E-14  
 1.33E-14  
 1.26E-14  
 1.20E-14  
 1.13E-14  
 1.06E-14  
 9.96E-15  
 9.30E-15  
 8.63E-15  
 7.97E-15  
 7.31E-15  
 6.64E-15  
 5.98E-15  
 5.31E-15  
 4.65E-15  
 3.98E-15  
 3.32E-15  
 2.66E-15  
 1.99E-15  
 1.33E-15  
 6.64E-16  
 0.00E+00



Figure 93. Concentration profile of  $\text{NaNO}_2$  in simultaneous injection model.



Jun 03 1996  
 Fluent 4.32  
 Fluent Inc.

Fluid Flow and Heat Transfer in a Mixing Elbow  
 $\text{NaNO}_2$  Mass Fraction  
 Max = 1.992E-14 Min = 0.000E+00 Time = 2.100E+01



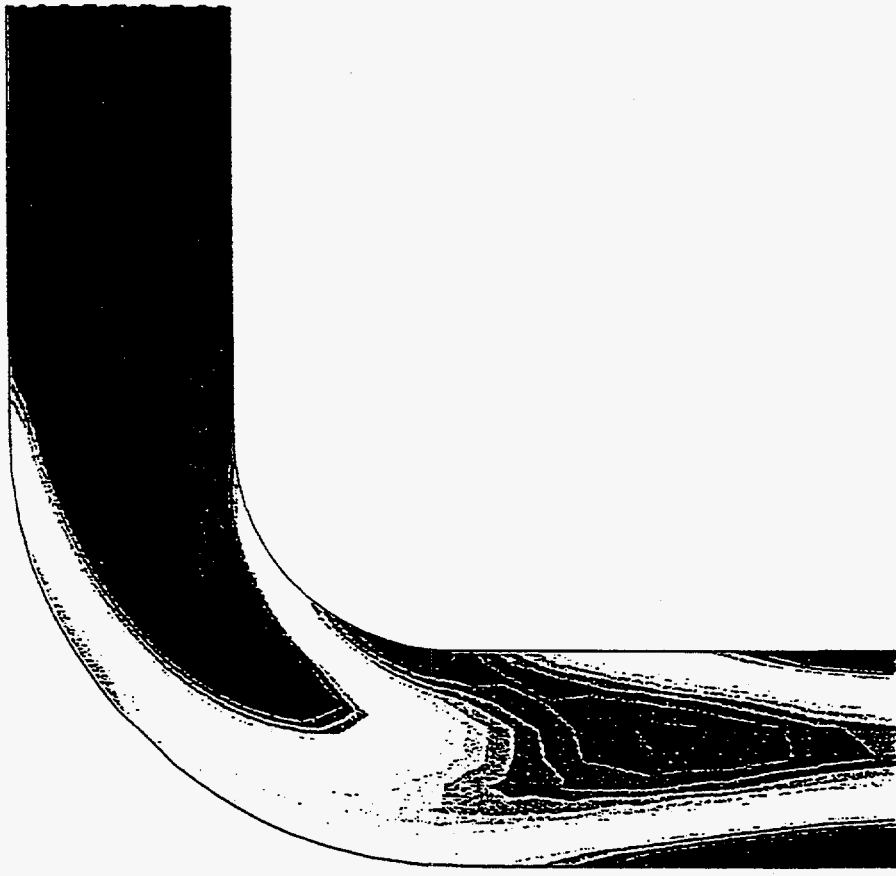
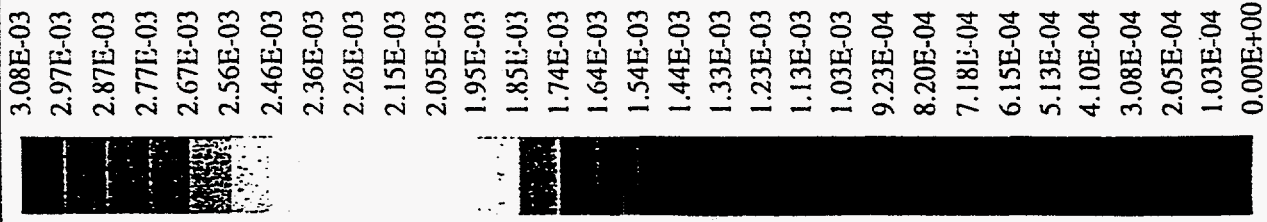


Figure 94. Concentration profile of  $\text{NH}_4\text{Cl}$  in simultaneous injection model.

Fluid Flow and Heat Transfer in a Mixing Elbow

$\text{NH}_4\text{Cl}$  Mass Fraction

Jun 03 1996

Fluent 4.32

0.000E+00 Time 2.100E+01

Fluent Inc

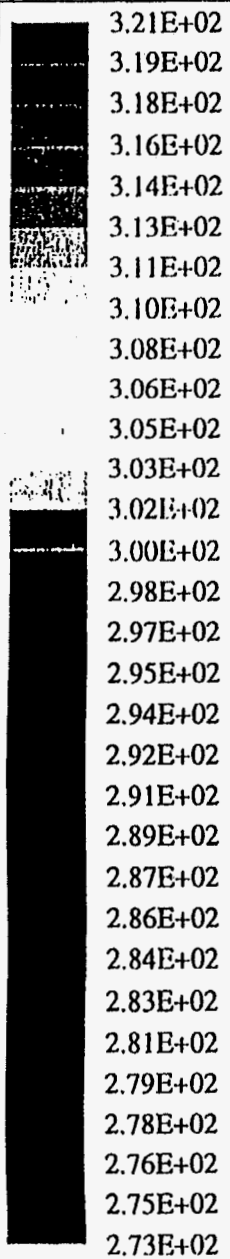
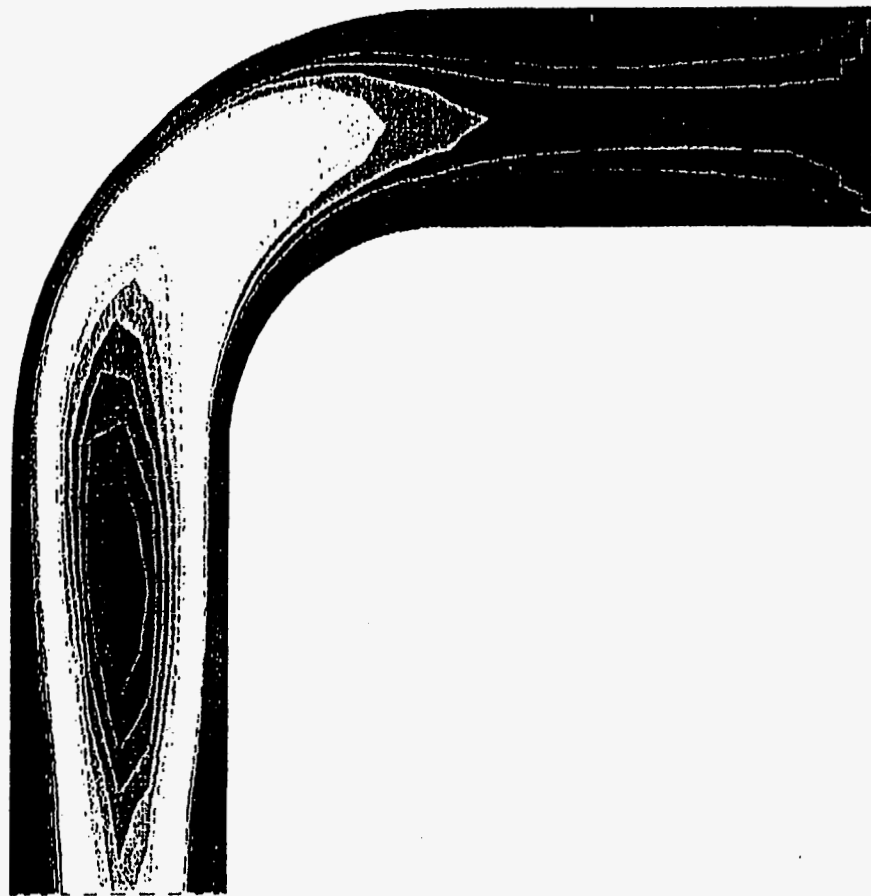


Figure 95. Temperature profile in simultaneous injection model.



Fluid Flow and Heat Transfer in a Mixing Elbow

Temperature (K)

Max = 3.208E+02 Min = 2.730E+02 Time = 2.100E+01

Jun 03 1996

Fluent 4.32

Fluent Inc.

5.74E-03  
 5.55E-03  
 5.36E-03  
 5.17E-03  
 4.98E-03  
 4.79E-03  
 4.59E-03  
 4.40E-03  
 4.21E-03  
 4.02E-03  
 3.83E-03  
 3.64E-03  
 3.45E-03  
 3.25E-03  
 3.06E-03  
 2.87E-03  
 2.68E-03  
 2.49E-03  
 2.30E-03  
 2.11E-03  
 1.91E-03  
 1.72E-03  
 1.53E-03  
 1.34E-03  
 1.15E-03  
 9.57E-04  
 7.66E-04  
 5.74E-04  
 3.83E-04  
 1.91E-04  
 .00E+00

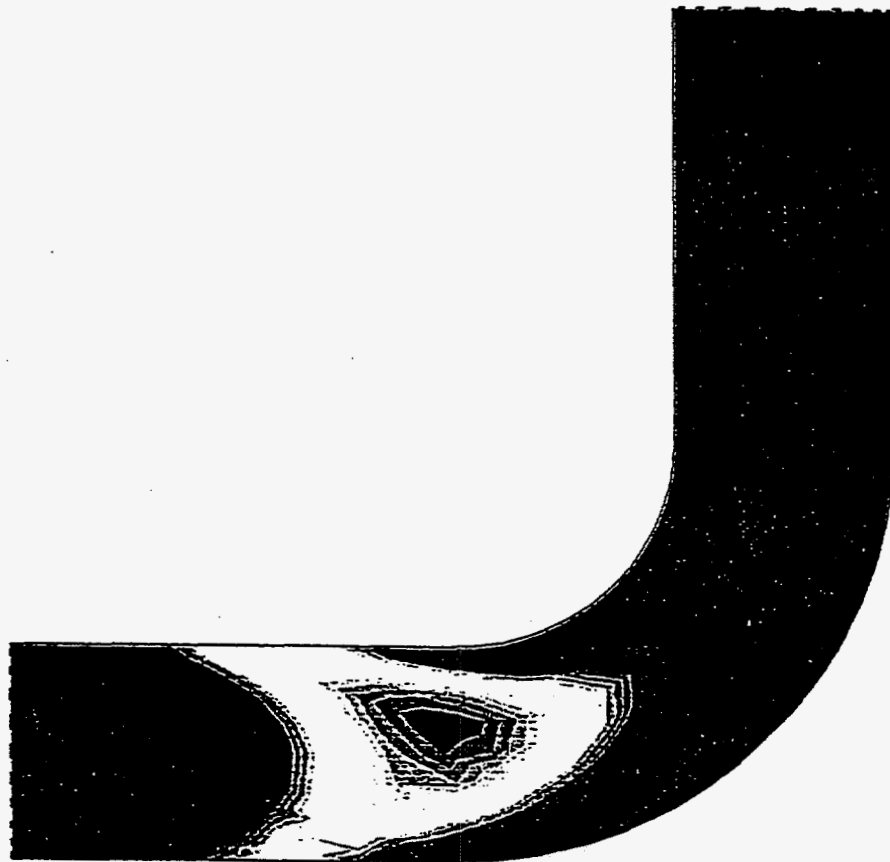


Figure 96. Concentration profile of NaNO<sub>2</sub> in sequential injection model. NaNO<sub>2</sub> was injected from 0 to 2 seconds.

Fluid Flow and Heat Transfer in a Mixing Elbow

Nano2 Mass Fraction

Max = 5.742E-03 Min = .000E+00 Time = 1.000E+01

Sep 03 1996  
 Fluent 4.32  
 Fluent Inc.

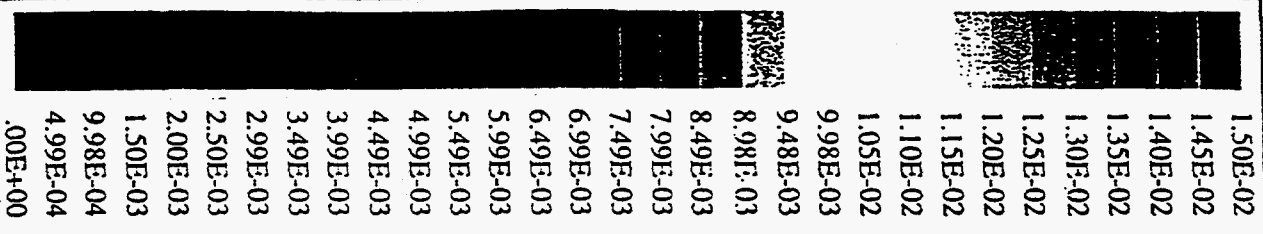
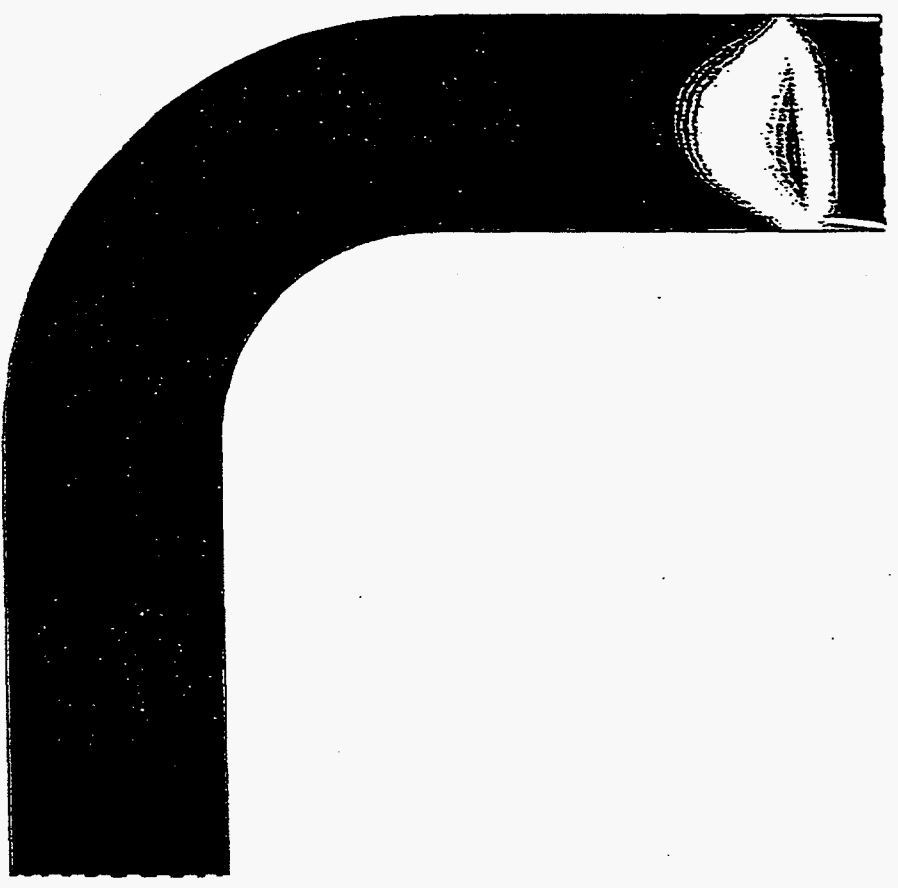


Figure 97. Concentration profile of  $NH_4Cl$  in sequential injection model.  $NH_4Cl$  was injected from 5 to 7 seconds.



Fluid Flow and Heat Transfer in a Mixing Elbow

$NH_4Cl$  Mass Fraction

Max = 1.497E-02 Min = .000E+00 Time = 1.000E+01



Sep 03 1996  
Fluent 4.32  
Fluent Inc.

3.35E+02  
 3.33E+02  
 3.31E+02  
 3.29E+02  
 3.27E+02  
 3.25E+02  
 3.22E+02  
 3.20E+02  
 3.18E+02  
 3.16E+02  
 3.14E+02  
 3.12E+02  
 3.10E+02  
 3.08E+02  
 3.06E+02  
 3.04E+02  
 3.02E+02  
 3.00E+02  
 2.98E+02  
 2.96E+02  
 2.94E+02  
 2.92E+02  
 2.90E+02  
 2.87E+02  
 2.85E+02  
 2.83E+02  
 2.81E+02  
 2.79E+02  
 2.77E+02  
 2.75E+02  
 2.73E+02

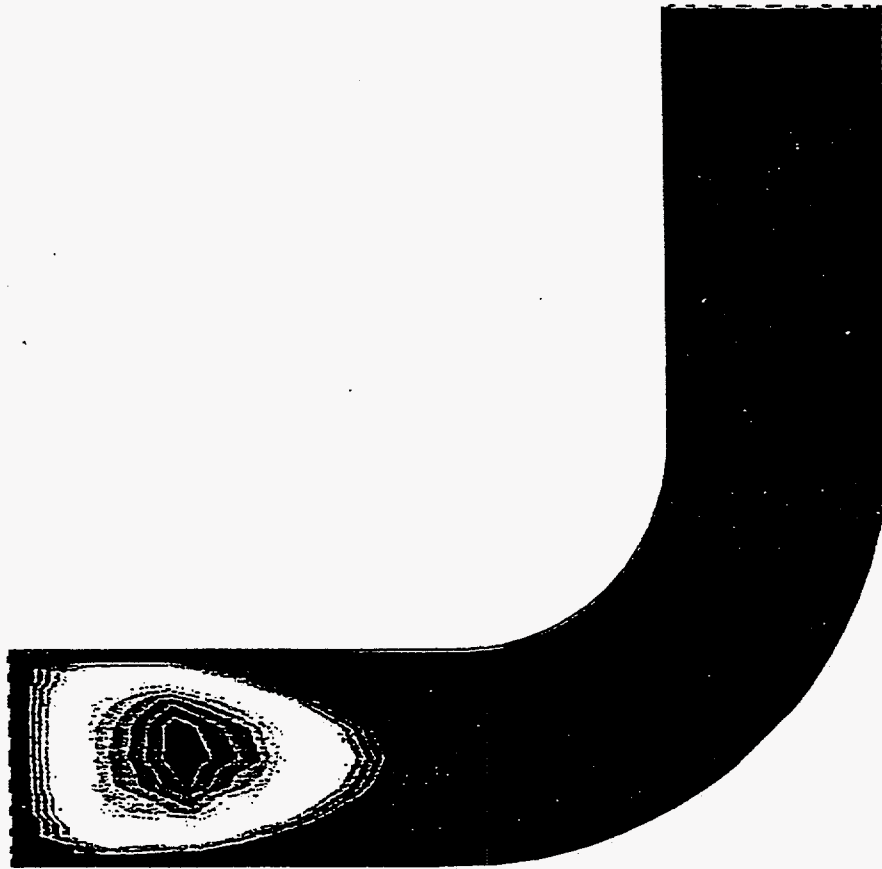


Figure 98. Temperature profile in a sequential injection model.

Aug 30 1996  
 Fluent 4.32  
 Fluent Inc.

Fluid Flow and Heat Transfer in a Mixing Elbow

Temperature (K)

Max = 3.348E+02 Min = 2.730E+02 Time = 1.000E+01

7 Y

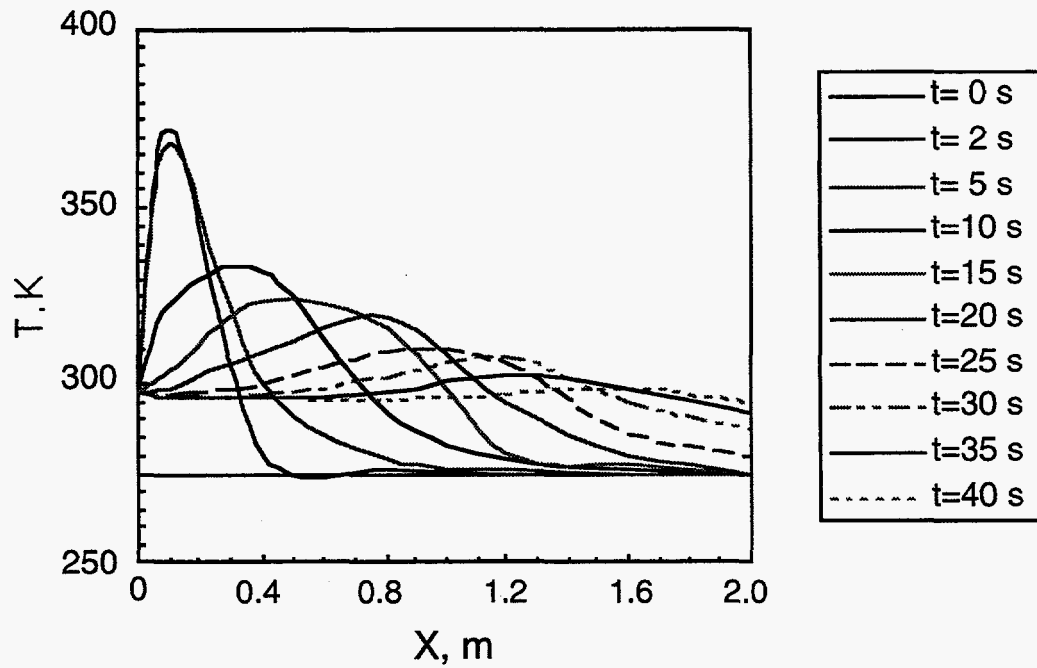


Figure 99. Fluid temperature along the center line of the pipe with a simultaneous injection of  $\text{NaNO}_2$  and  $\text{NH}_4\text{Cl}$ .

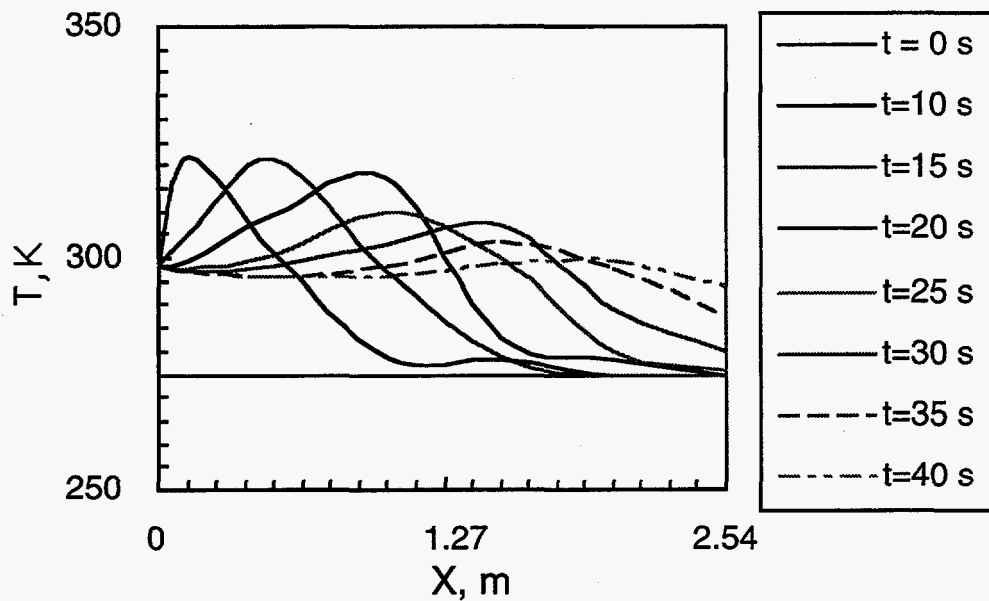


Figure 100. Fluid temperature along the center line of the pipe with a sequential injection of  $\text{NaNO}_2$  and  $\text{NH}_4\text{Cl}$  along with a liquid spacer.

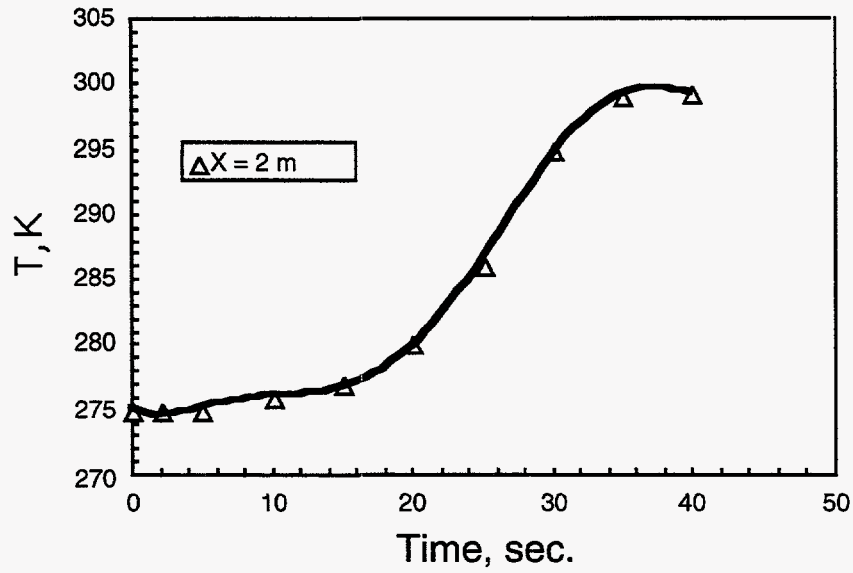


Figure 101. Temperature evolution of fluid at the position 2m from the pipe inlet for the simultaneous injection case.

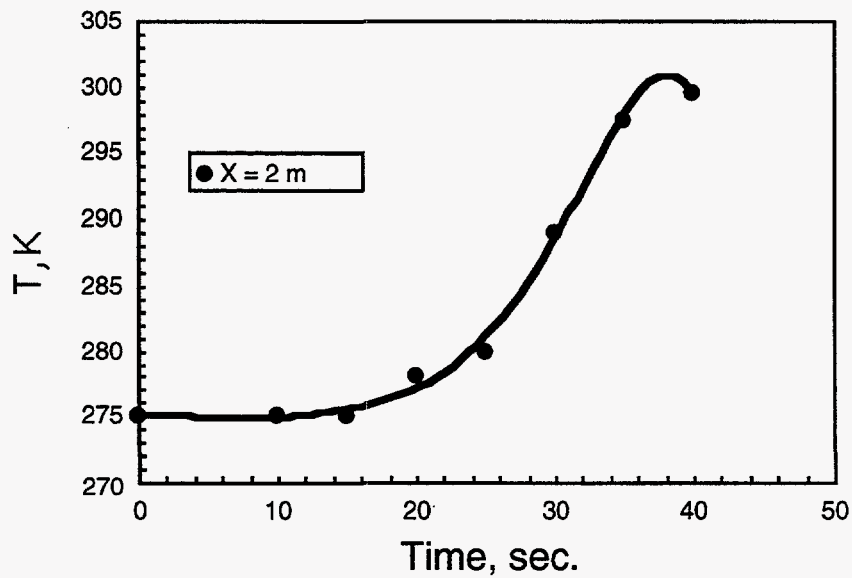


Figure 102. Temperature evolution of fluid at the position 2m from the pipe inlet for the sequential injection case.

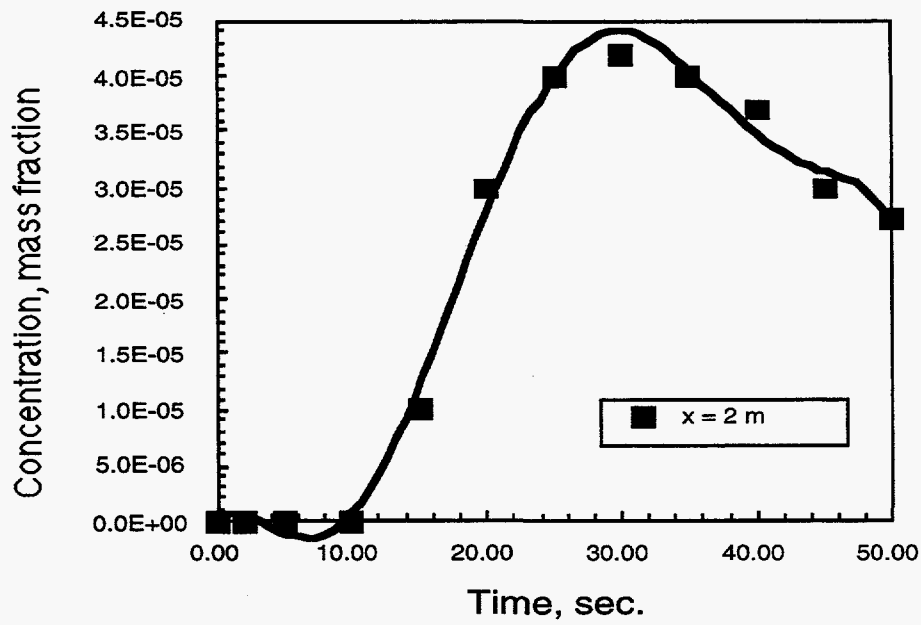


Figure 103.  $\text{NaNO}_2$  concentration profile at the position 2m from the pipe inlet for the simultaneous injection case.

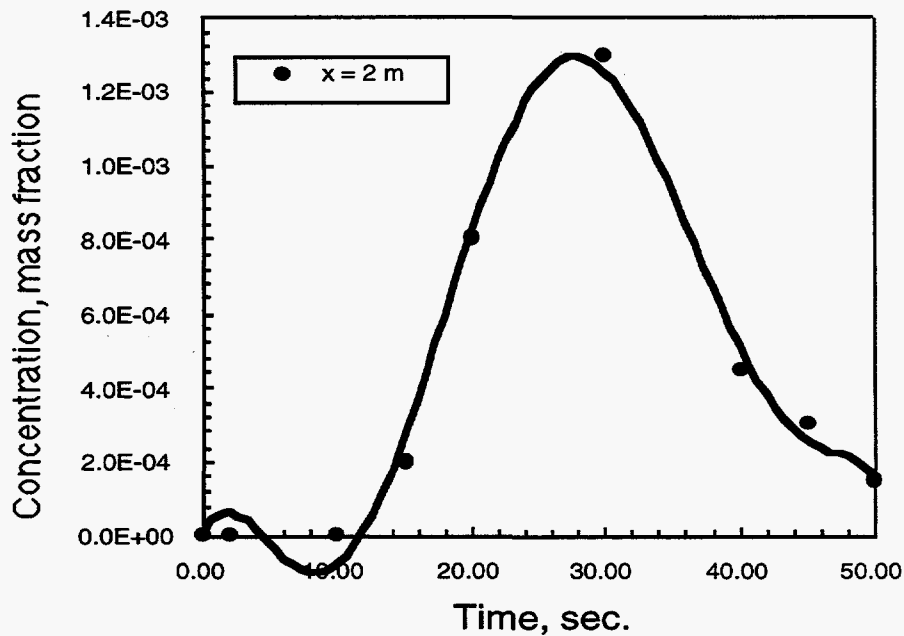


Figure 104.  $\text{NaNO}_2$  concentration profile at the position 2m from the pipe inlet for the sequential injection case.



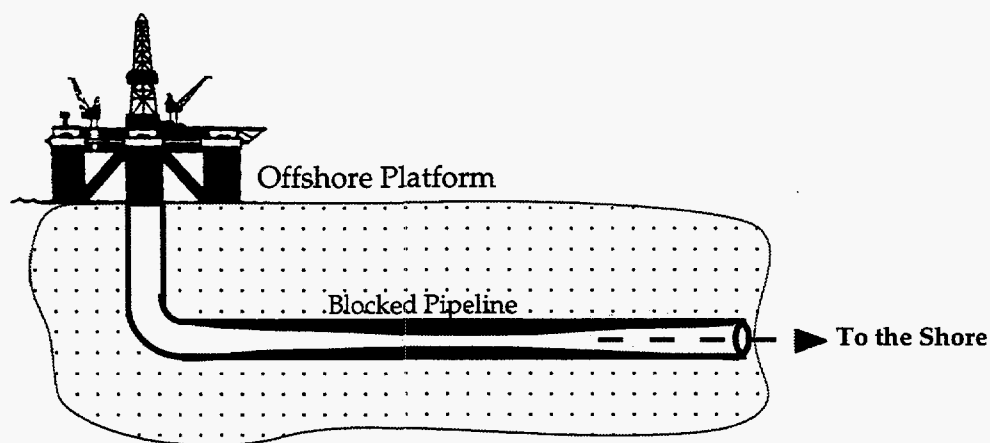


Figure 105a: Schematic of an offshore platform with a pipeline which is partially plugged by wax deposition.

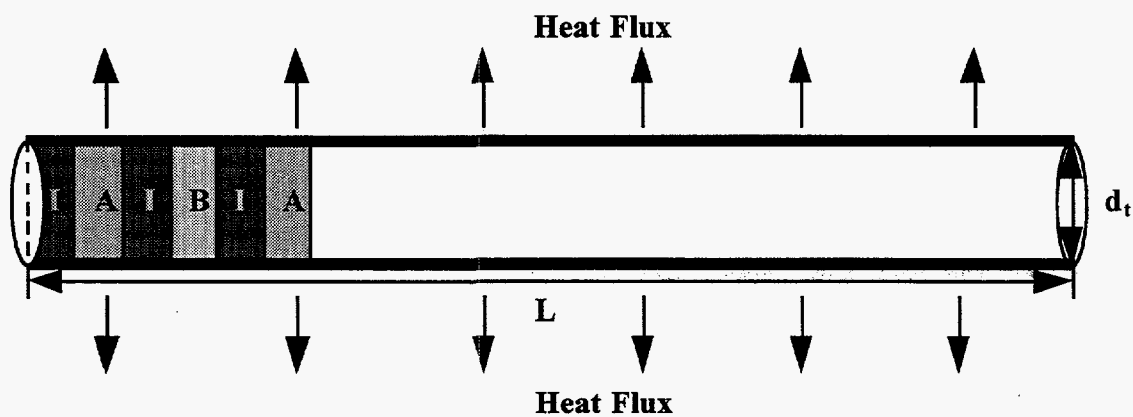


Figure 105b: Schematic of a tubular reactor with system of pulses having the two reactants and the inert spacer denoted as A, B, and I respectively.

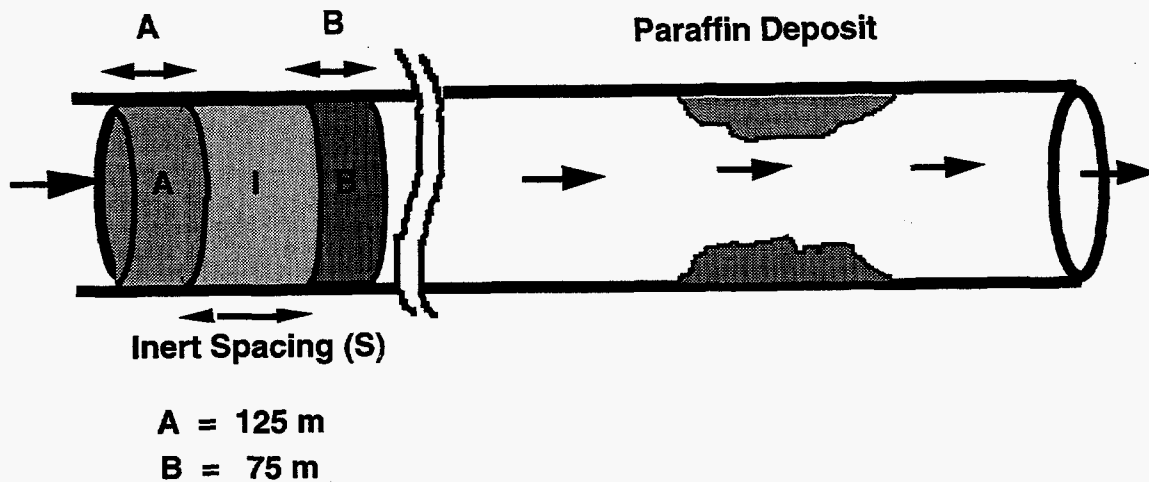


Figure 106a: Schematic of the pipeline with the pulses of reactants (the values of A and B were used for results in Figure 106b).

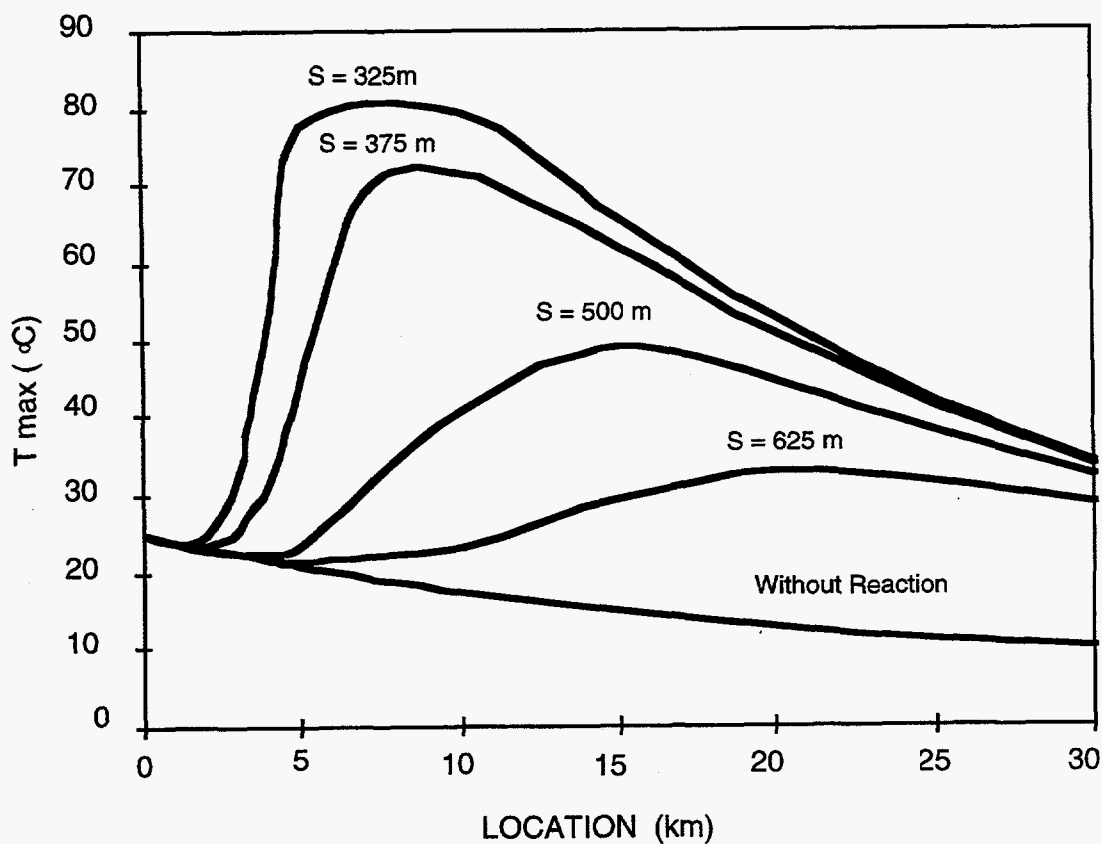


Figure 106b. Effect of length of inert spacing on the plot of maximum temperature vs location inside the pipeline during the reaction between  $\text{NaNO}_2$  and  $\text{NH}_4\text{Cl}$  in aqueous phase.

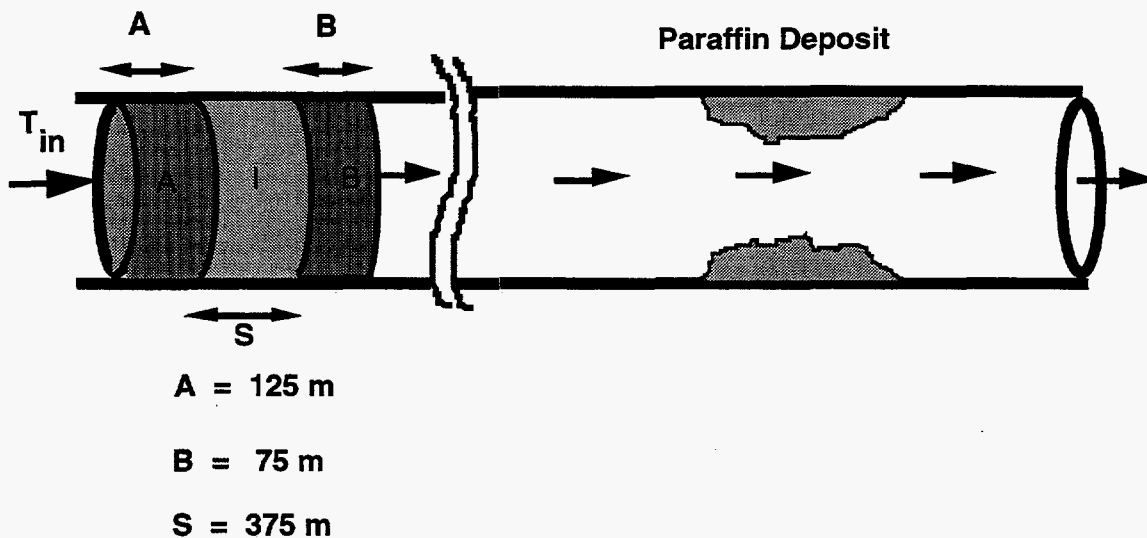


Figure 107a: Schematic of the pipeline with the pulses of reactants (the values of A, B and S were used for results in Figure 107b).

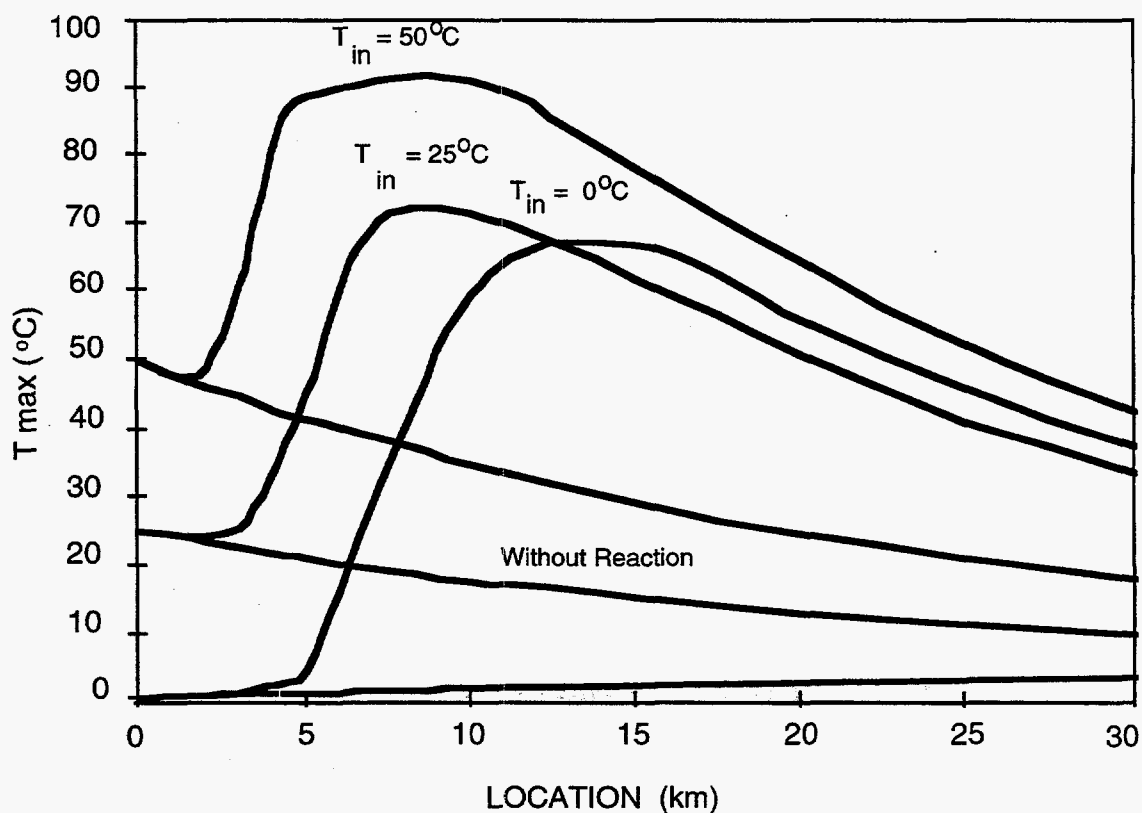
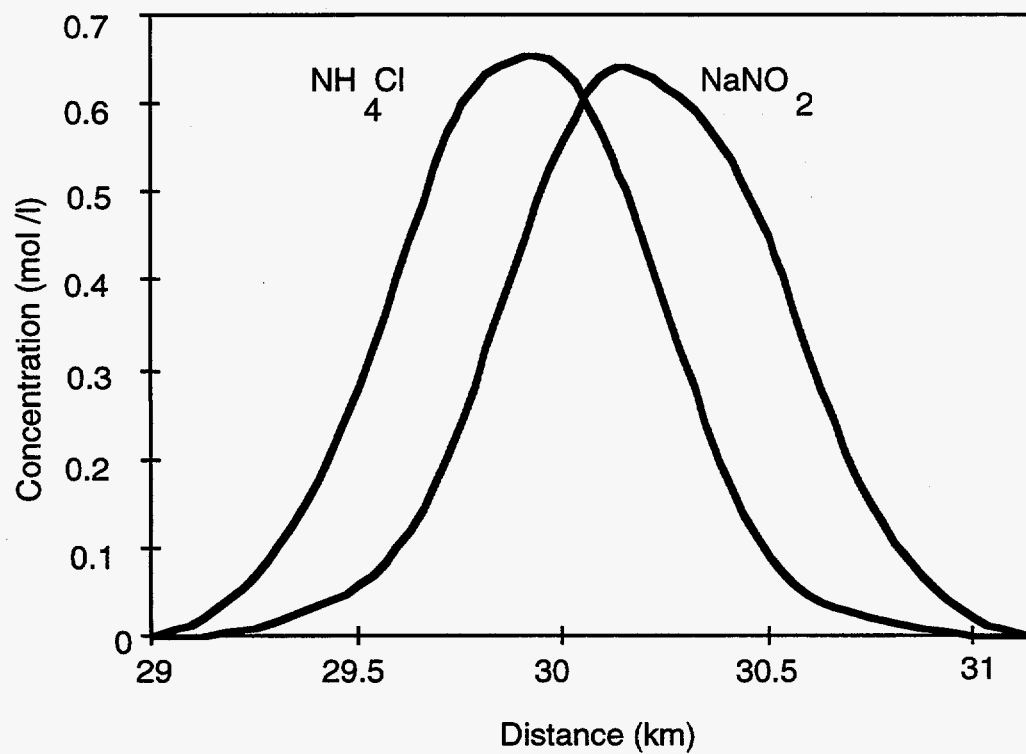
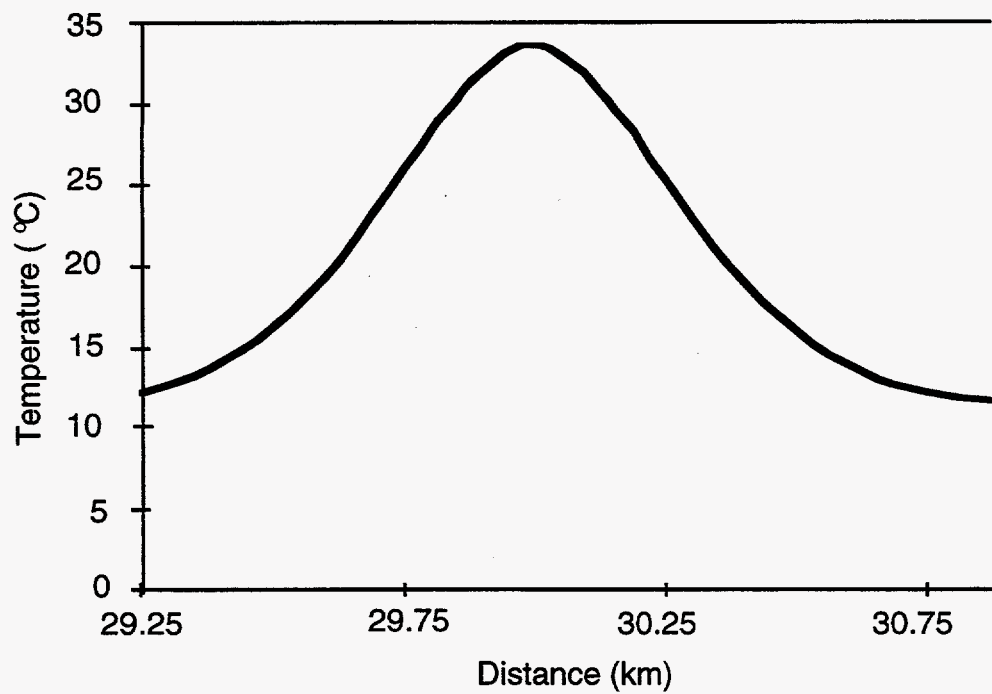
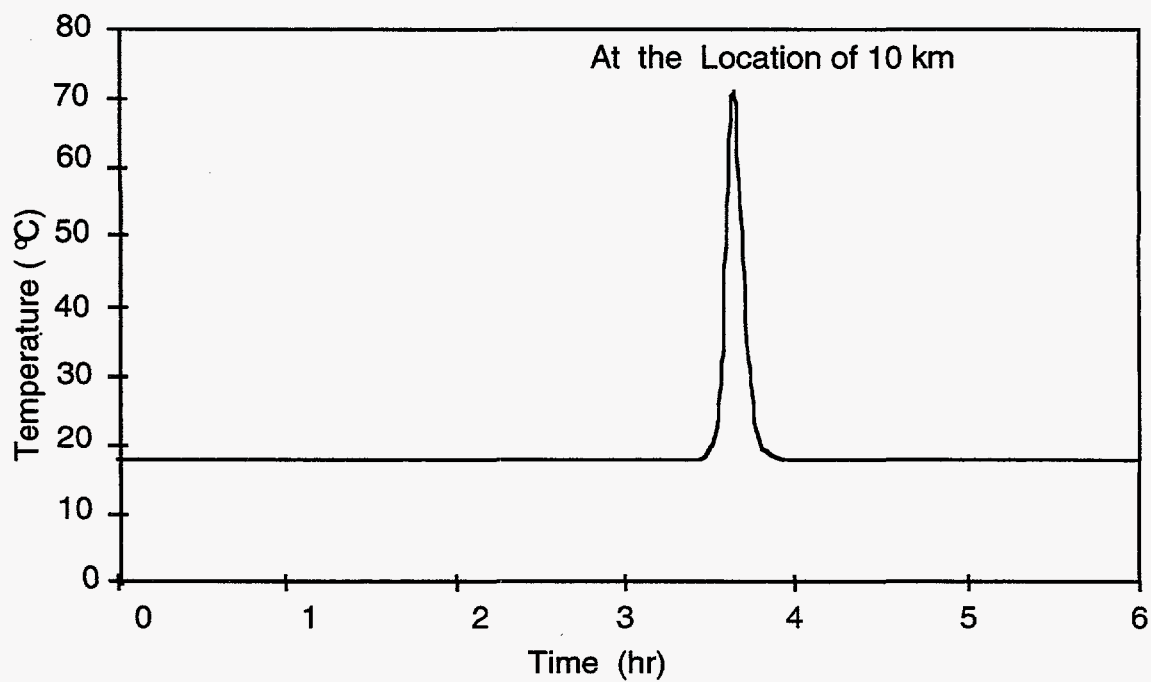
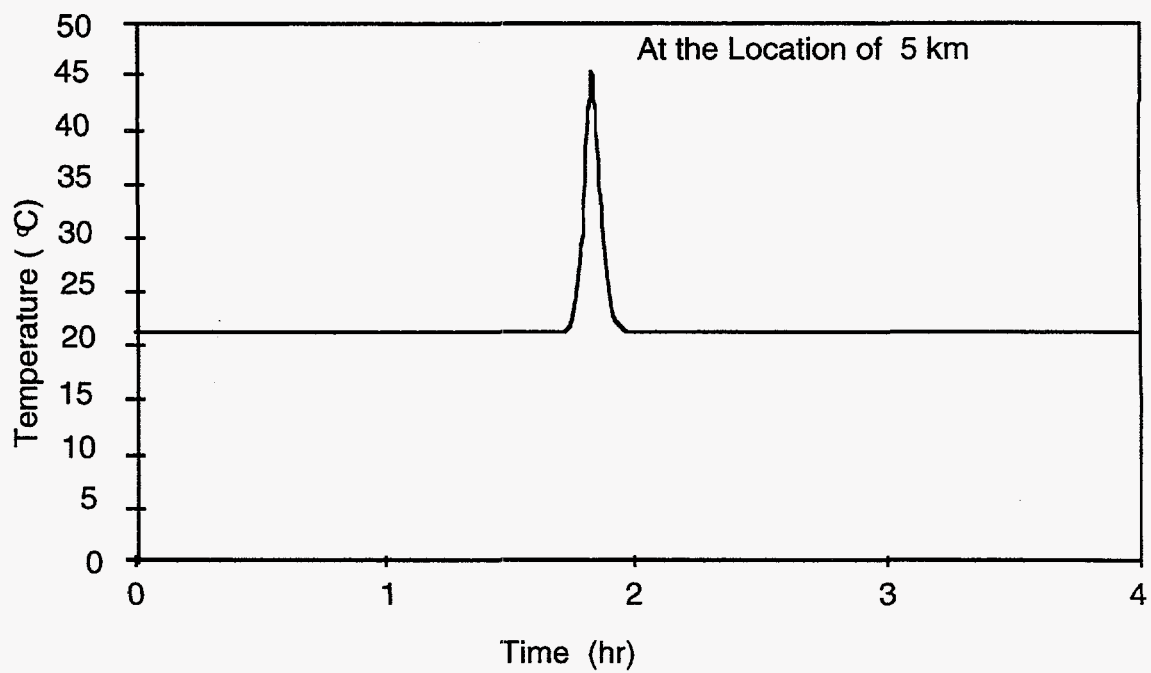


Figure 107b. Effect of inlet temperature on the maximum temperature vs location inside the pipeline during the reaction between  $\text{NaNO}_2$  and  $\text{NH}_4\text{Cl}$  in aqueous phase with 375 m inert spacing.



Figures 108a,b. Temperature trajectory at the location of 5 and 10 km from the inlet end inside the pipeline during the reaction between  $\text{NaNO}_2$  and  $\text{NH}_4\text{Cl}$  in aqueous phase when  $A=125\text{m}$ ,  $B=75\text{ m}$ ,  $S=375\text{ m}$  and  $T_{\text{in}}=25\text{ }^\circ\text{C}$ .



Figures 109a,b. Distribution of temperature and concentration of the reactants after the entire system has travelled 30 km when  $A=125$  m,  $B=75$  m,  $S=375$  m and  $T_{in}=25$  °C.

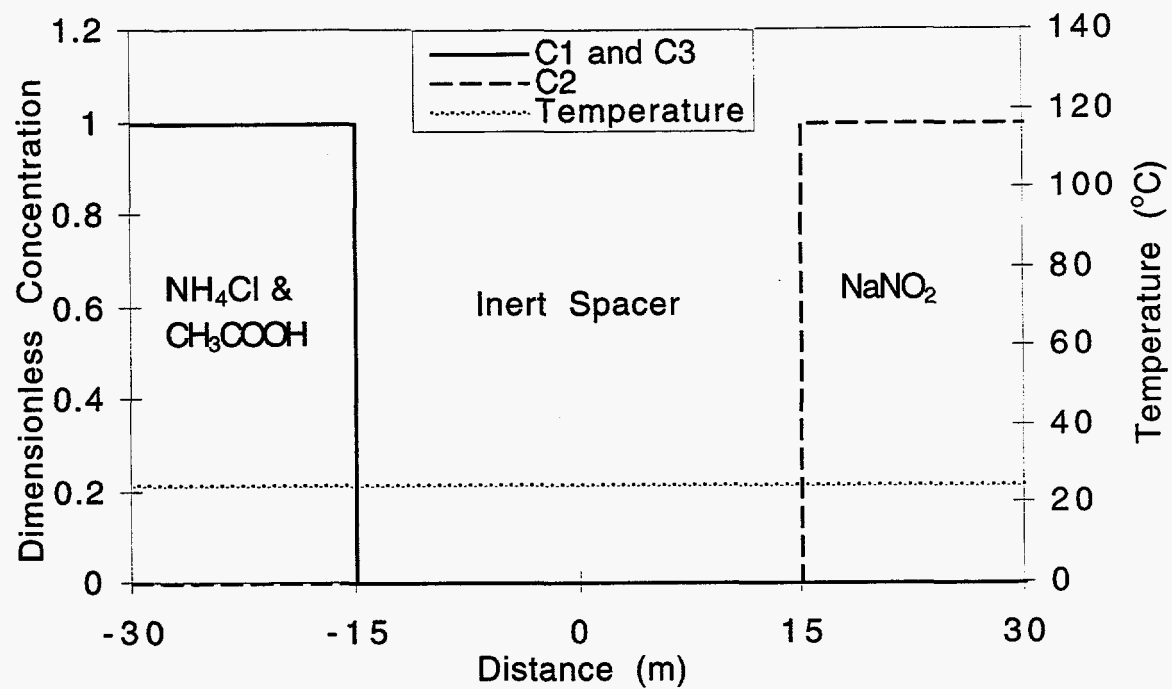


Figure 110: Local dimensionless concentration and temperature profiles at the entrance of the pipeline for a pulse width 30 m,  $C_{1o} = C_{2o} = 7 \text{ mol/dm}^3$ , and  $C_{3o} = 1 \text{ mol/dm}^3$ .

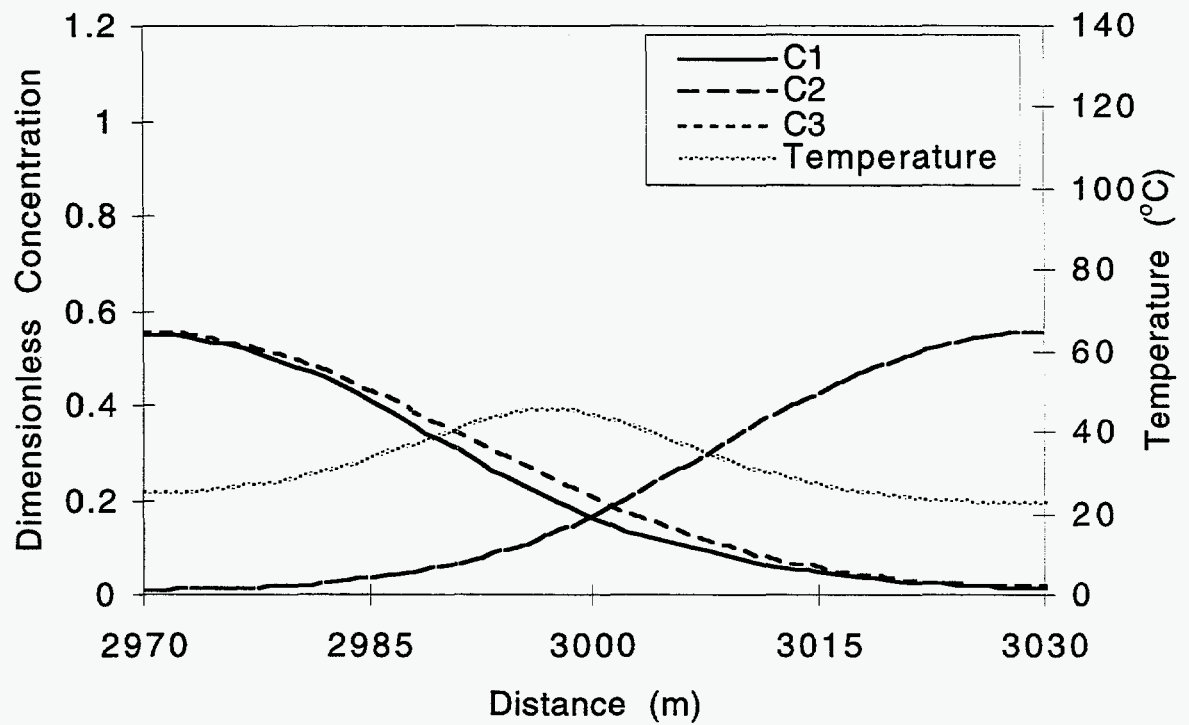


Figure 111: Local dimensionless concentration and temperature profiles at a location of 3 km from the entrance of the pipeline for a pulse size 30 m,  $C_{10} = C_{20} = 7 \text{ mol/dm}^3$ , and  $C_{30} = 1 \text{ mol/dm}^3$ .

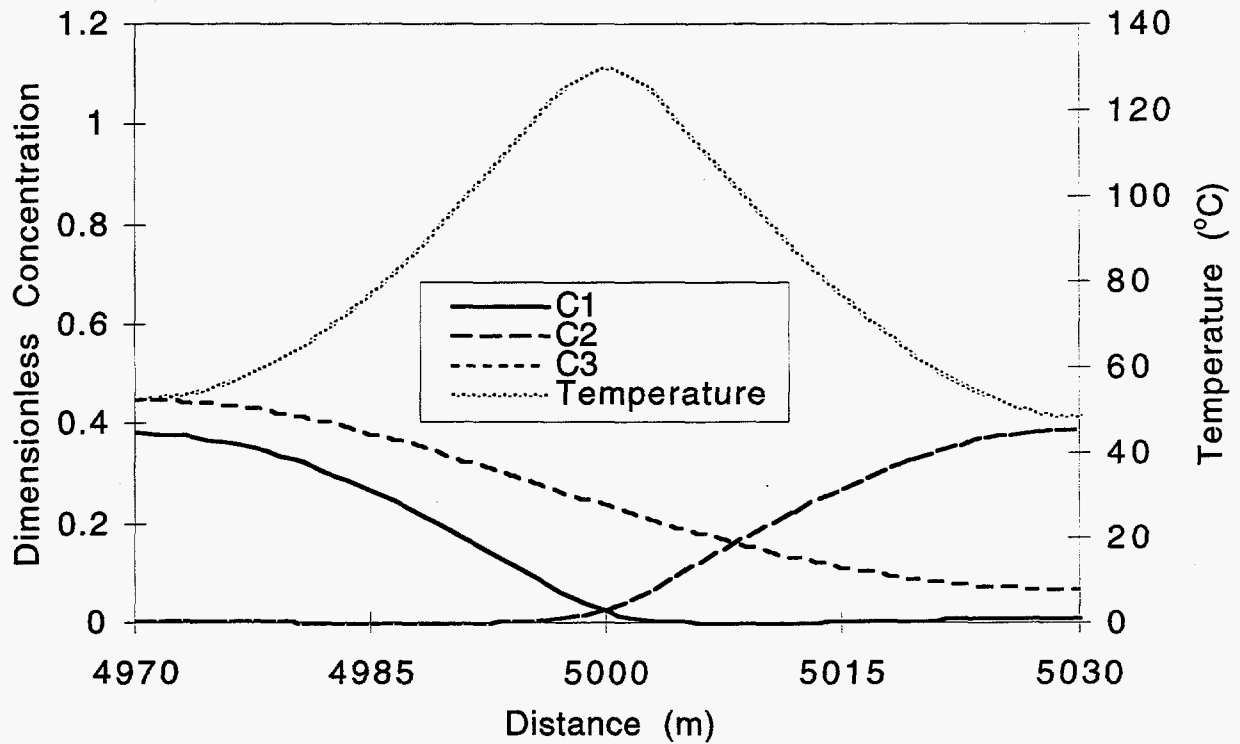


Figure 112: Local dimensionless concentration and temperature profiles at a location of 5 km from the entrance of the pipeline for a pulse size 30 m,  $C_{10} = C_{20} = 7 \text{ mol/dm}^3$ , and  $C_{30} = 1 \text{ mol/dm}^3$ .



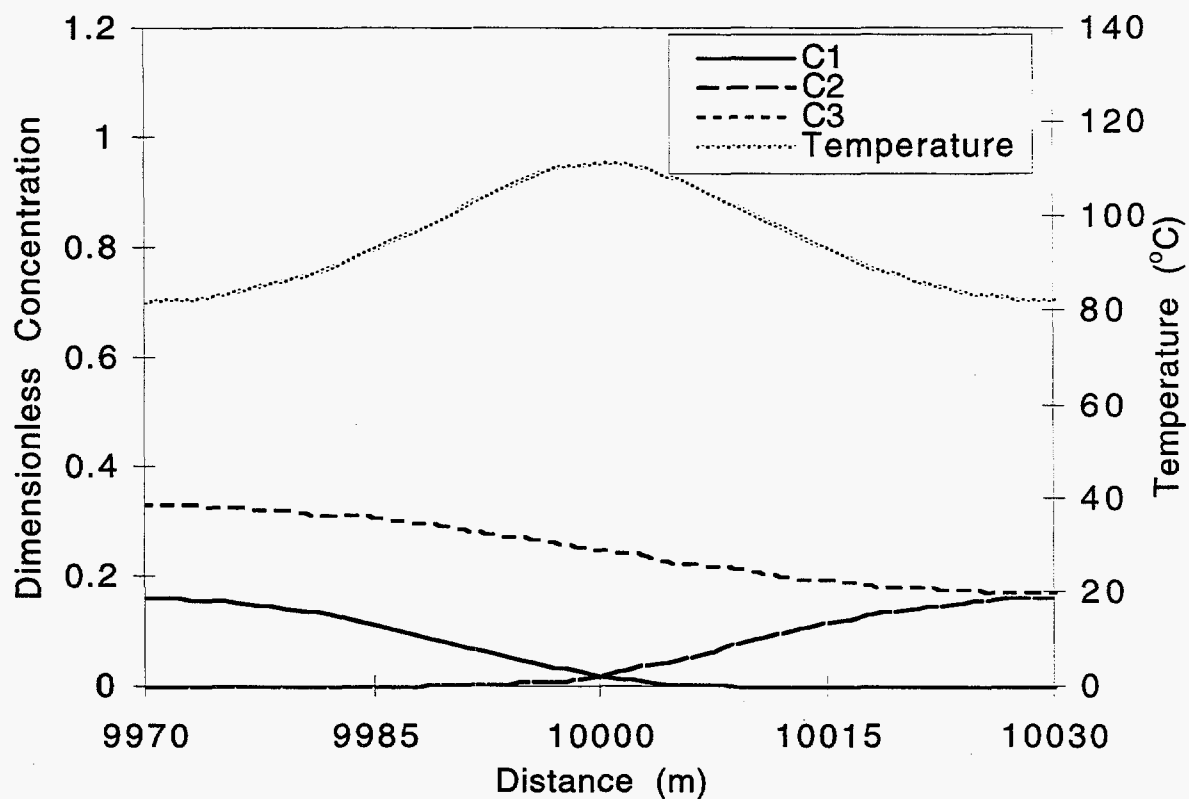


Figure 113: Local dimensionless concentration and temperature profiles at a location of 10 km from the entrance of the pipeline for a pulse size 30 m,  $C_{10} = C_{20} = 7 \text{ mol/dm}^3$ , and  $C_{30} = 1 \text{ mol/dm}^3$ .

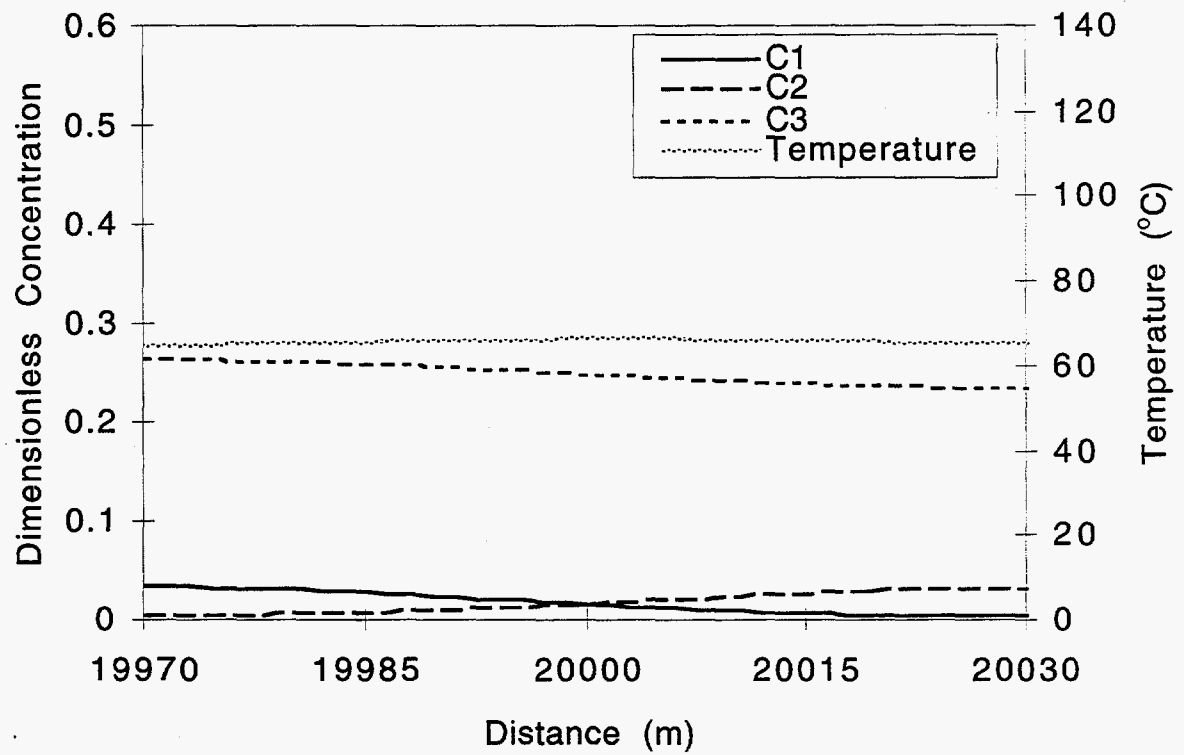


Figure 114: Local dimensionless concentration and temperature profiles at a location of 20 km from the entrance of the pipeline for a pulse size 30 m,  $C_{10} = C_{20} = 7 \text{ mol/dm}^3$ , and  $C_{30} = 1 \text{ mol/dm}^3$ .

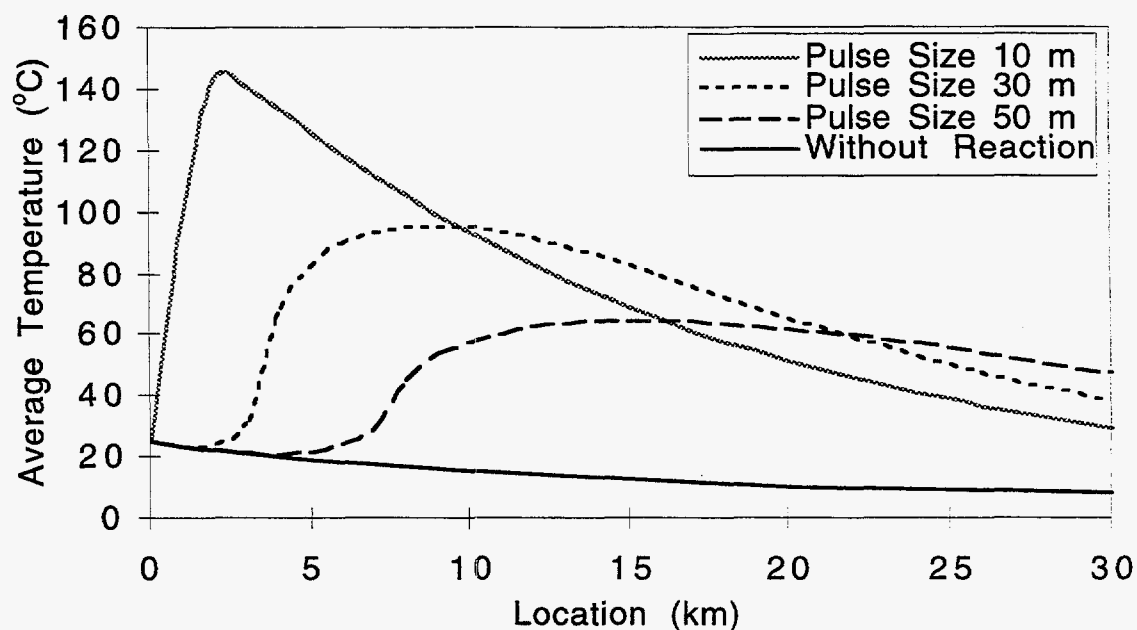


Figure 115: Volume average temperature as a function of location down the pipeline for various pulse sizes keeping  $C_{10} = C_{20} = 7 \text{ mol/dm}^3$  and  $C_{30} = 1 \text{ mol/dm}^3$ .

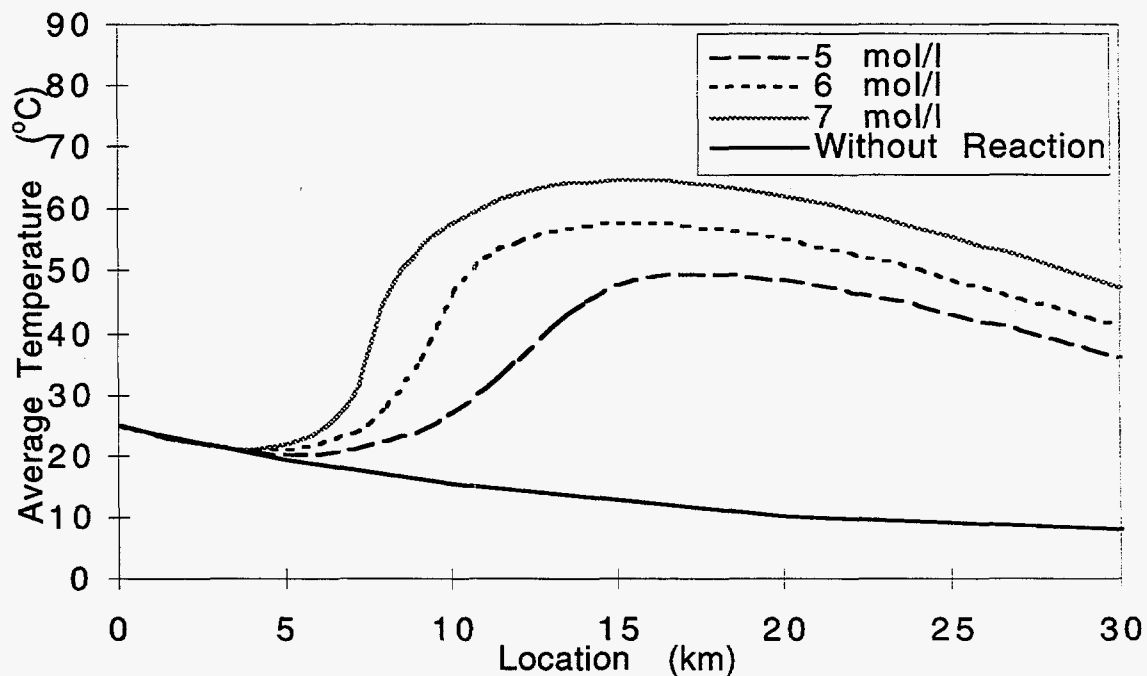


Figure 116: Volume average temperature as a function of location down the pipeline for various reactant concentrations keeping  $C_{30} = 1 \text{ mol/dm}^3$  and a pulse size 50 m.

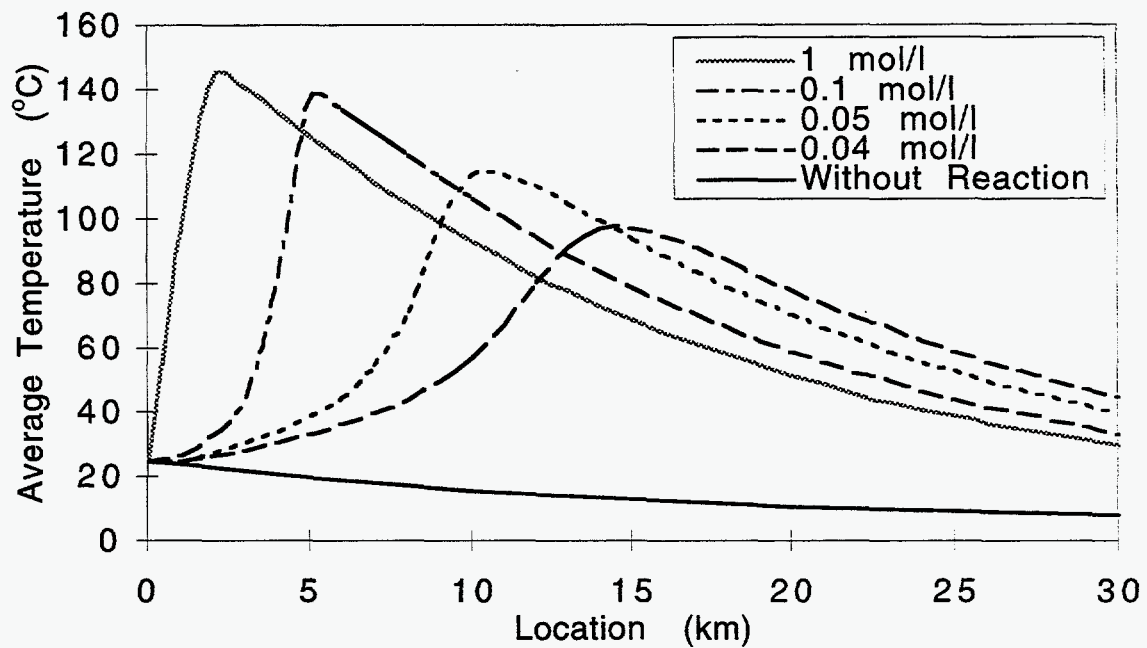


Figure 117: Volume average temperature as a function of location down the pipeline for various catalyst concentrations keeping  $C_{1o} = C_{2o} = 7 \text{ mol/dm}^3$  and a pulse size 10 m.

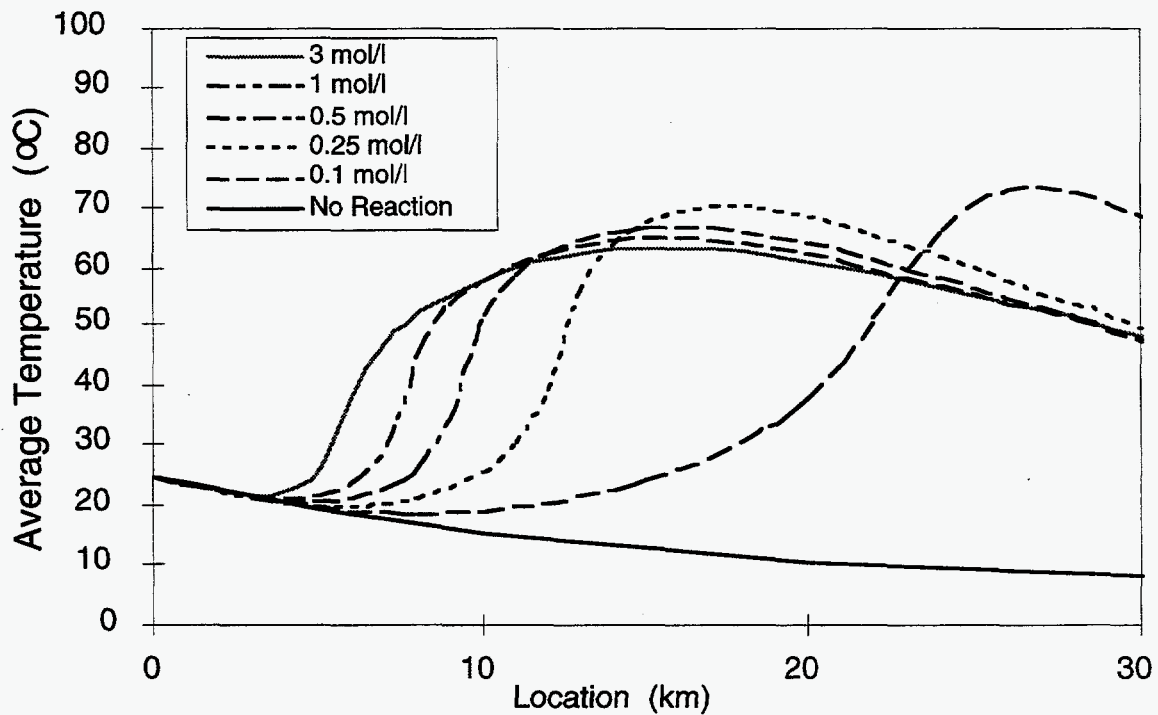


Figure 118: Plots of average temperature of one set of pulses vs. location inside the pipeline for various concentrations of catalyst keeping  $C_{1o} = C_{2o} = 7 \text{ mol/l}$  and pulse size 30 m.

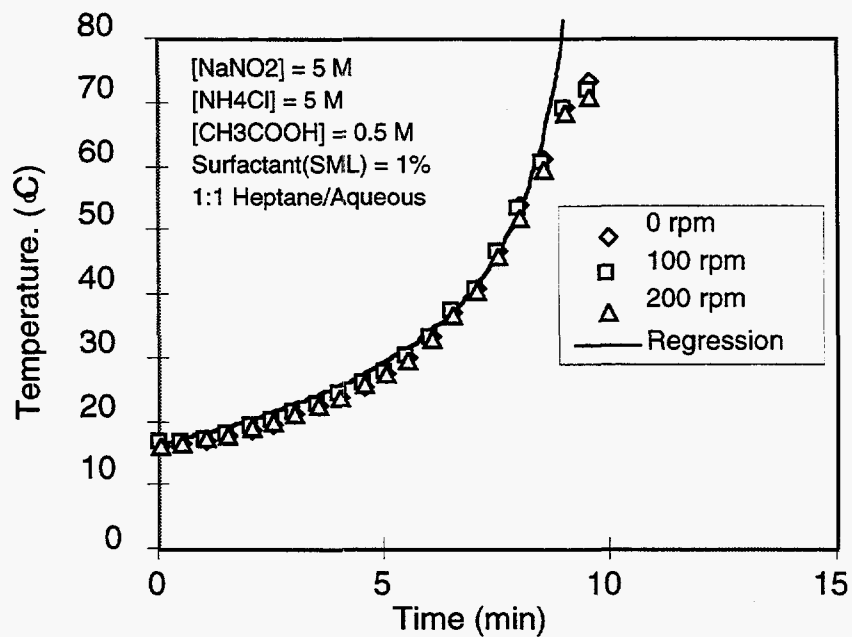


Figure 119. Temperature profiles of water/heptane emulsions containing SML during the reaction between  $\text{NaNO}_2$  and  $\text{NH}_4\text{Cl}$  for different stirring rates.

j

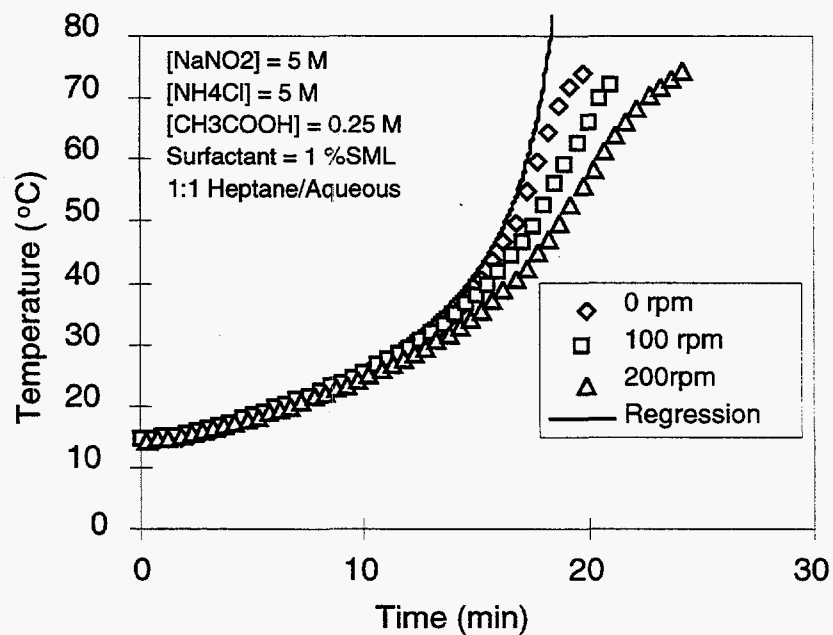


Figure 120. Temperature profiles of water/heptane emulsions containing SML during the reaction between  $\text{NaNO}_2$  and  $\text{NH}_4\text{Cl}$  for different stirring rates.

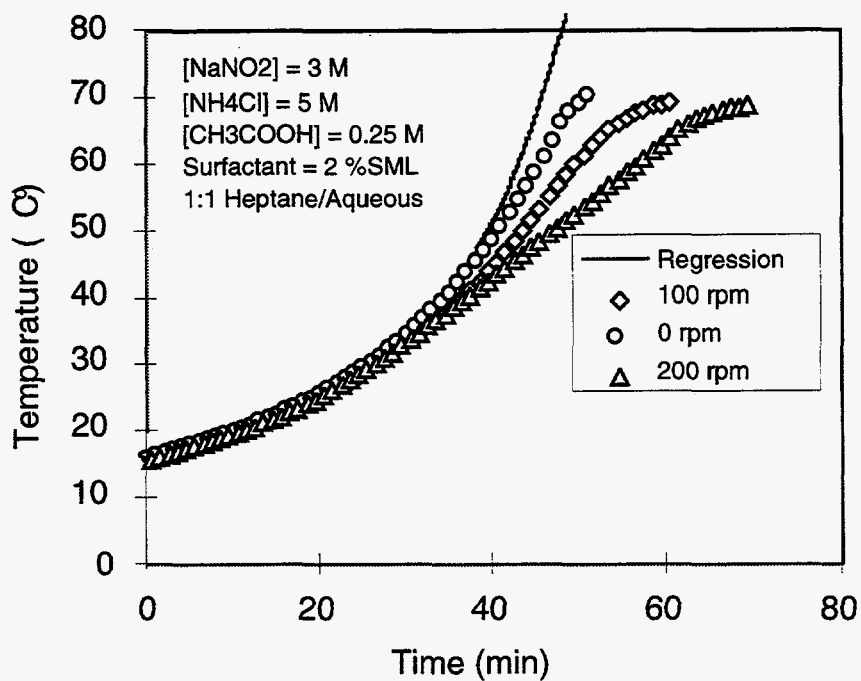


Figure 121. Temperature profiles of water/heptane emulsions containing SML during the reaction between  $\text{NaNO}_2$  and  $\text{NH}_4\text{Cl}$  for different stirring rates.

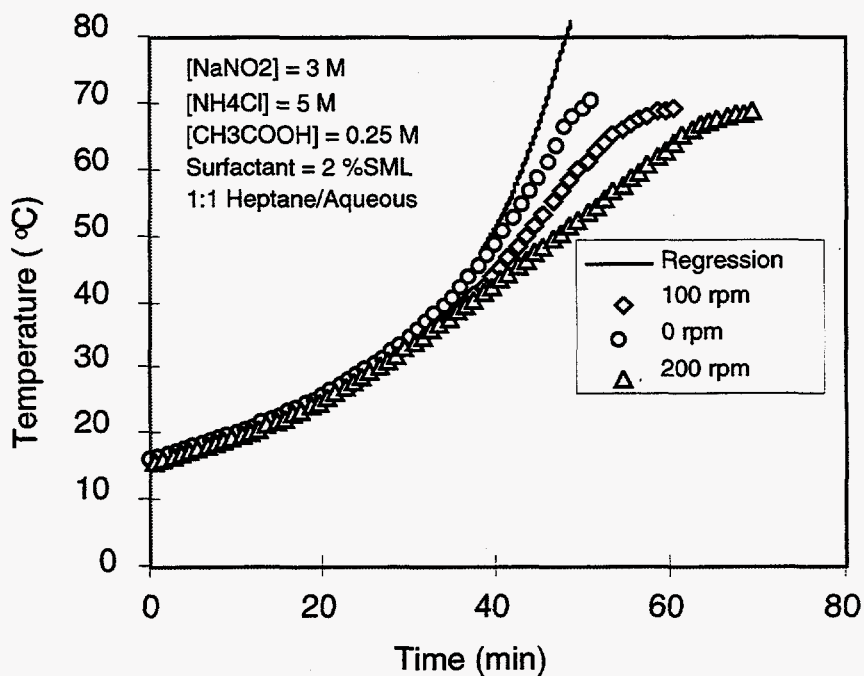


Figure 122. Temperature profiles of water/heptane emulsions containing SML during the reaction between  $\text{NaNO}_2$  and  $\text{NH}_4\text{Cl}$  for different stirring rates.

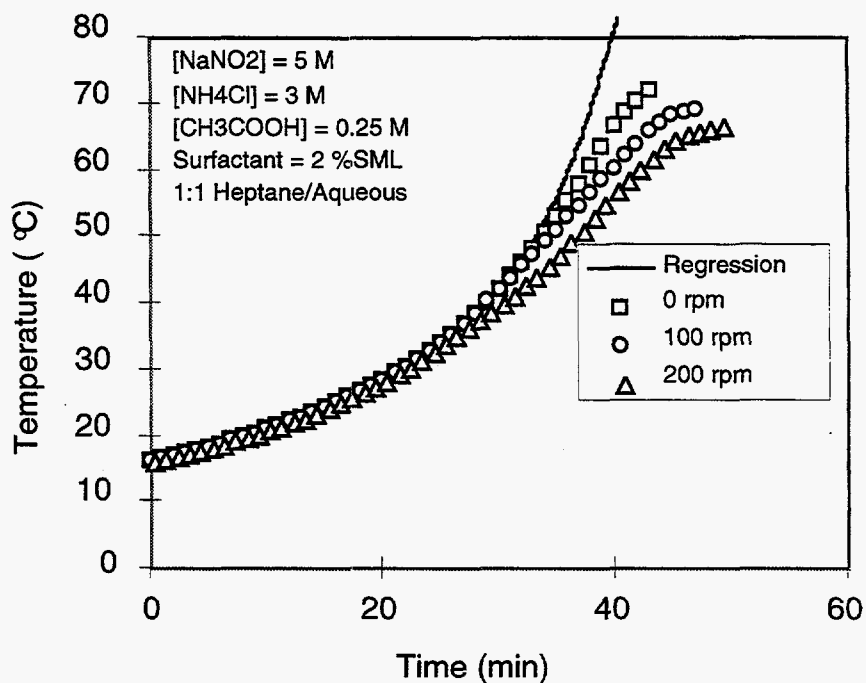


Figure 123. Temperature profiles of water/heptane emulsions containing SML during the reaction between  $\text{NaNO}_2$  and  $\text{NH}_4\text{Cl}$  for different stirring rates.

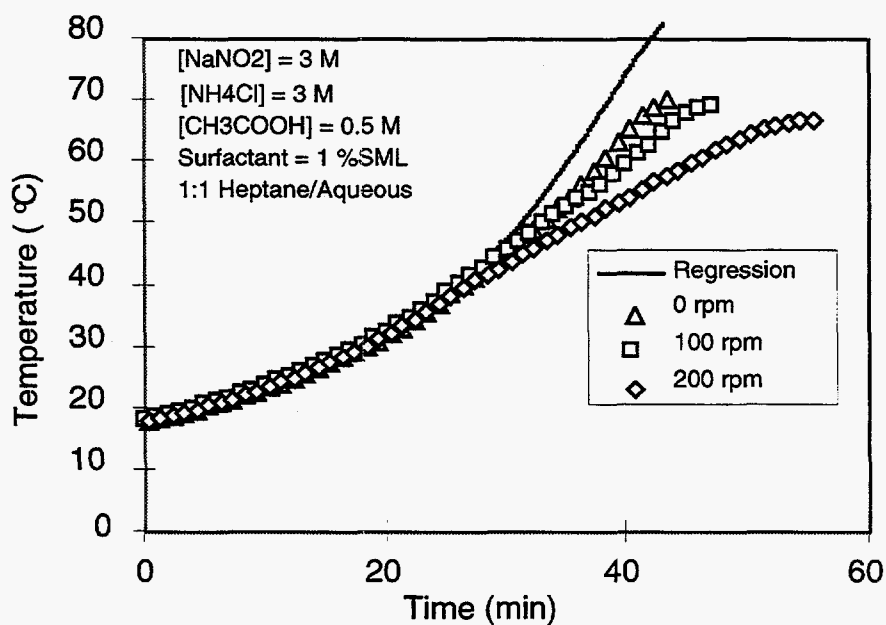


Figure 124. Temperature profiles of water/heptane emulsions containing SML during the reaction between  $\text{NaNO}_2$  and  $\text{NH}_4\text{Cl}$  for different stirring rates.

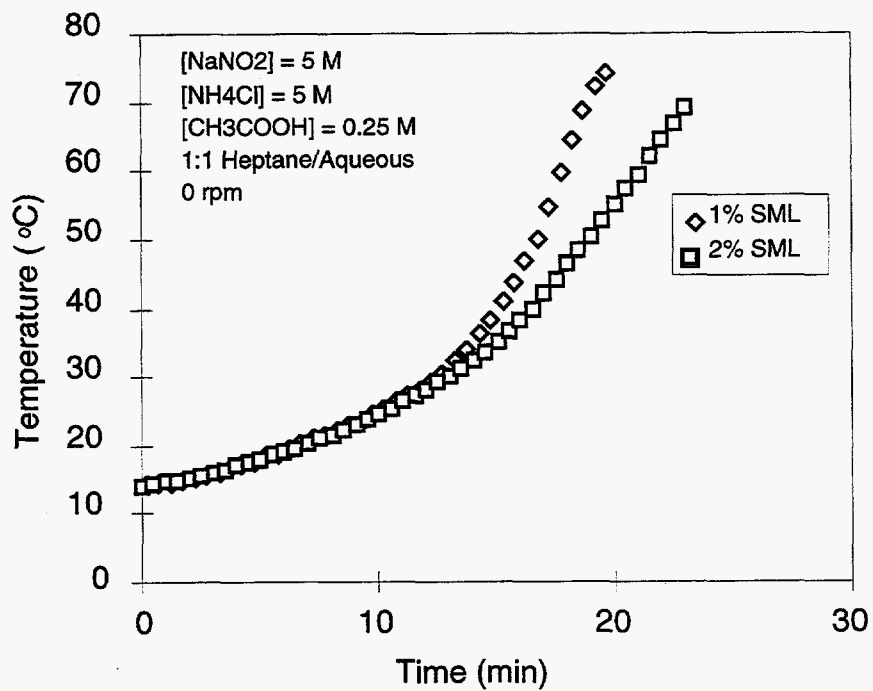


Figure 125. Temperature profiles of water/heptane emulsions containing SML during the reaction between NaNO<sub>2</sub> and NH<sub>4</sub>Cl for no stirring.



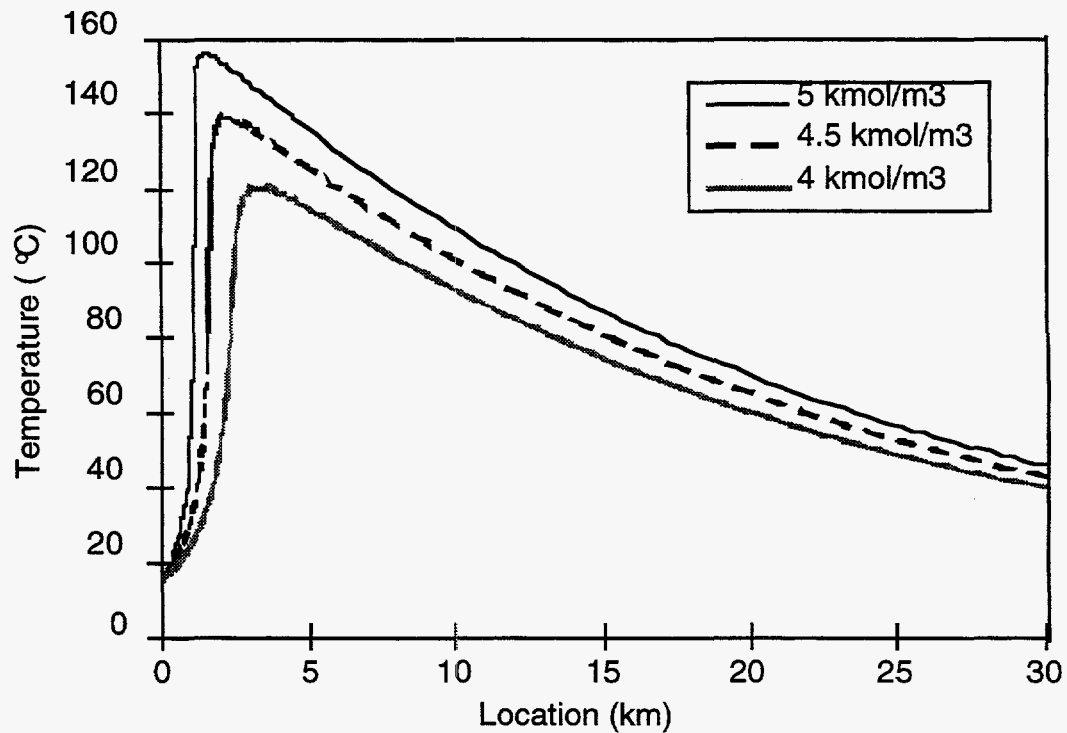


Figure 126: Temperature profiles of the mixture of the two emulsions flowing inside the pipeline for the cases when concentrations of both reactants are  $5 \text{ kmol/m}^3$ ,  $4.5 \text{ kmol/m}^3$ , and  $4 \text{ kmol/m}^3$ .

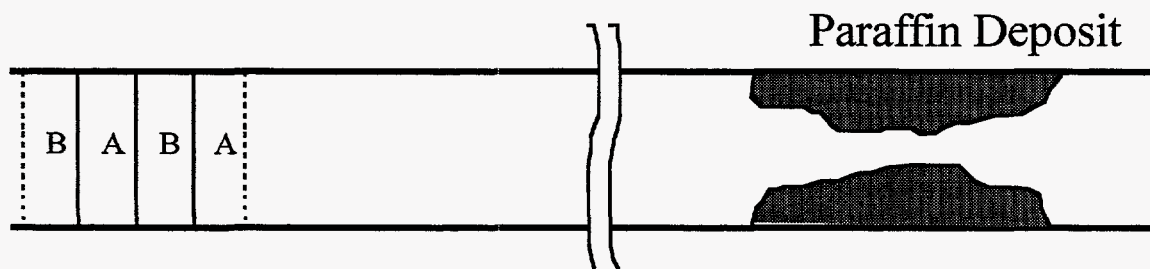


Figure 127: Schematic of the pipeline with the continuous alternate pulses of the emulsions of the two aqueous reactants where width of each pulse is 200 m.

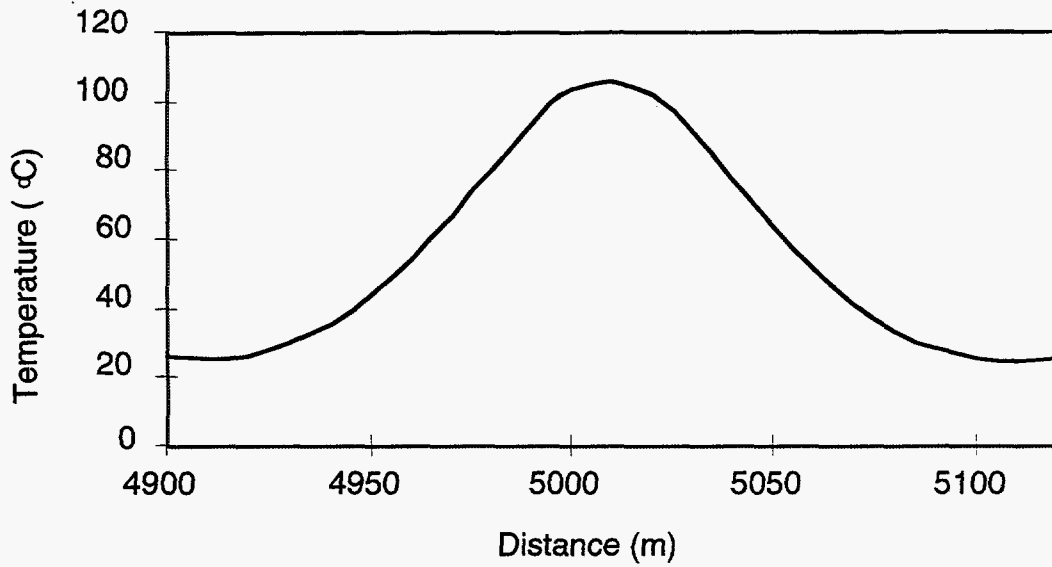


Figure 128: Local temperature wave inside the pipeline due to dispersion and reaction at the location of 5000 m for the case when the concentration of the two reactants is  $4 \text{ kmol/m}^3$  and width of each pulse is 200 m.

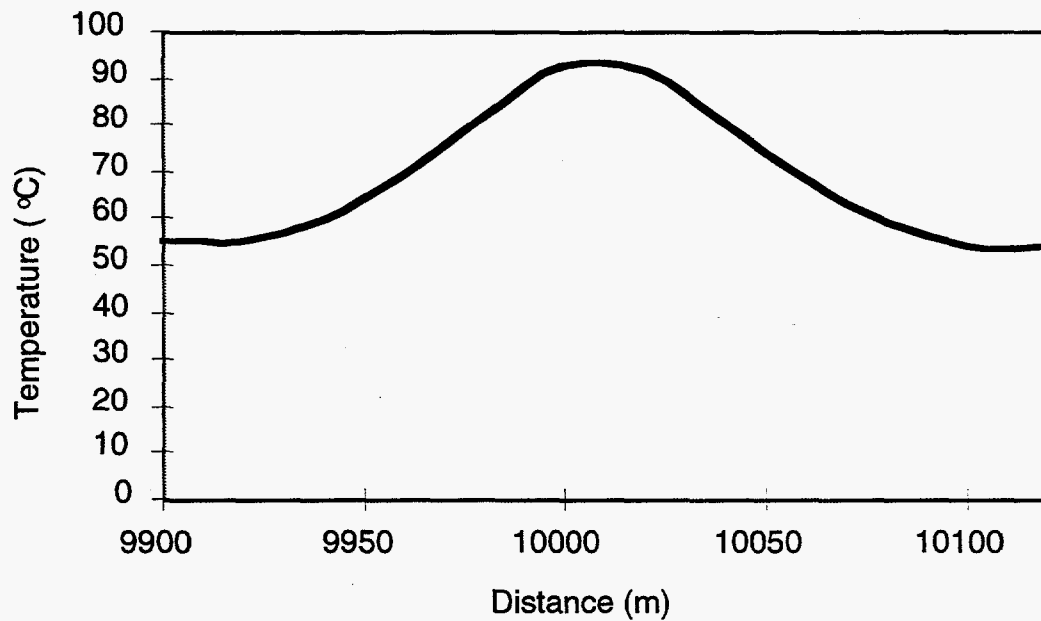


Figure 129: Local temperature wave inside the pipeline due to dispersion and reaction at the location of 10000 m for the case when the concentration of the two reactants is  $4 \text{ kmol/m}^3$  and width of each pulse is 200 m.

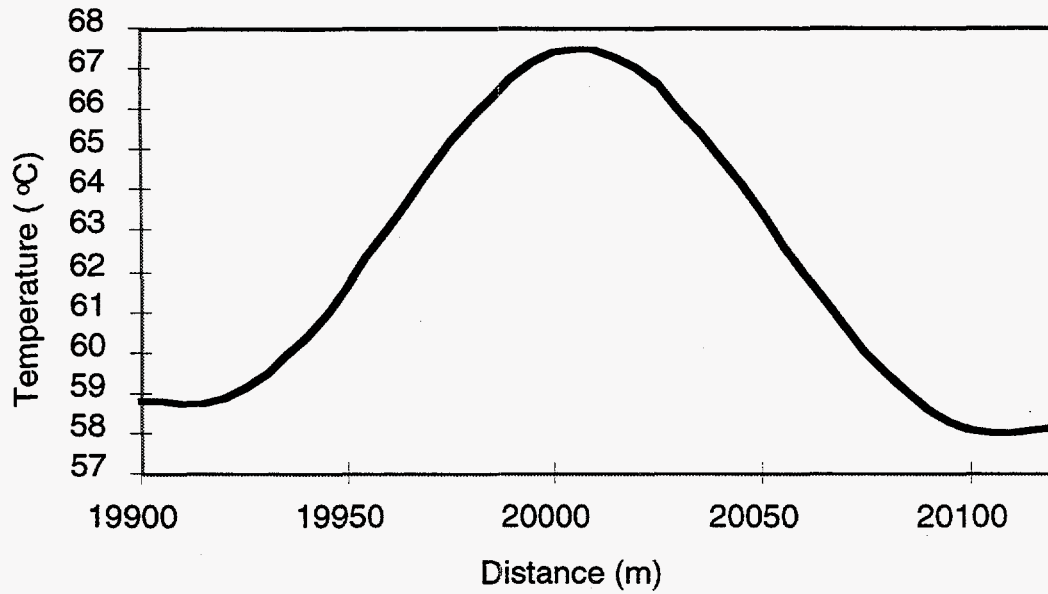


Figure 130: Local temperature wave inside the pipeline due to dispersion and reaction at the location of 20000 m for the case when the concentration of the two reactants is  $4 \text{ kmol/m}^3$  and width of each pulse is 200 m.

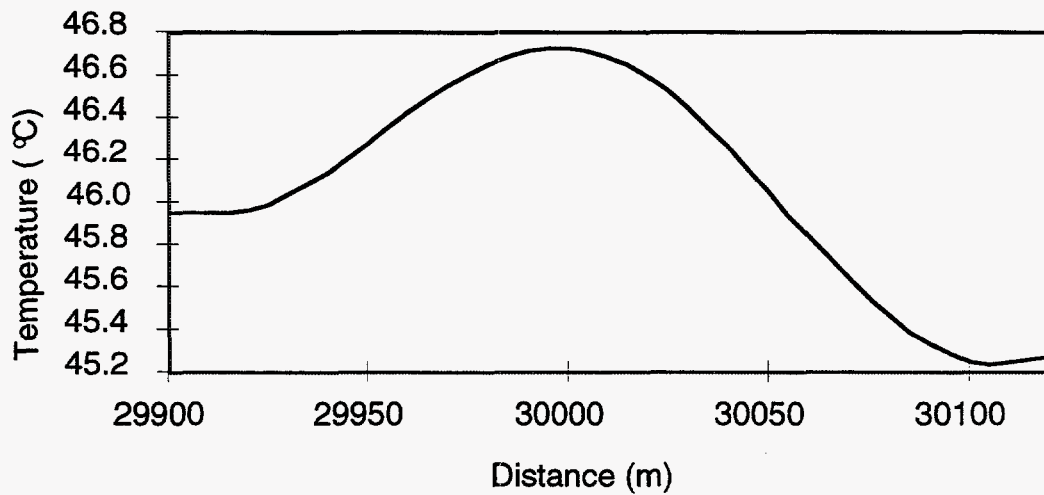


Figure 131: Local temperature wave inside the pipeline due to dispersion and reaction at the location of 30000 m for the case when the concentration of the two reactants is  $4 \text{ kmol/m}^3$  and width of each pulse is 200 m.

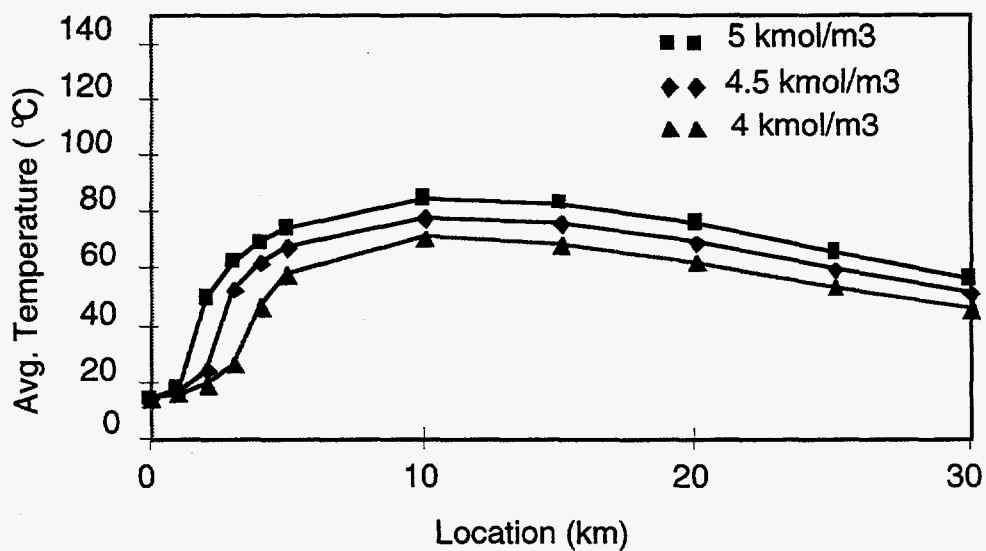


Figure 132: Average temperature profile inside the pipeline when continuous alternate pulses of the two emulsions are injected, the width of each pulse is 200 m, and the concentration of the two reactants is 4 kmol/m<sup>3</sup>, 4.5 kmol/m<sup>3</sup>, and 5 kmol/m<sup>3</sup>.

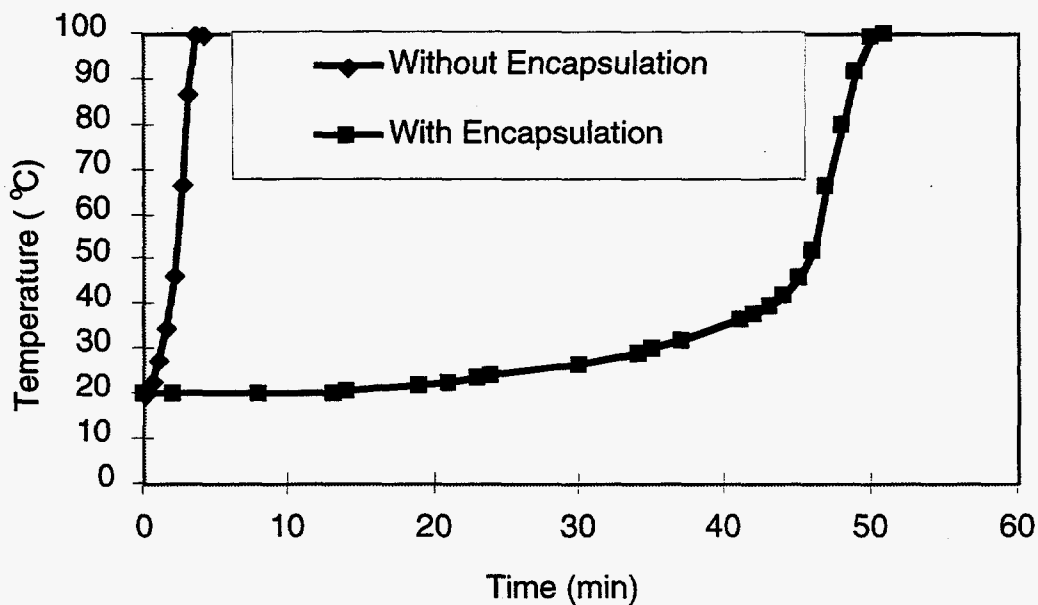


Figure 133: Temperature-time trajectory for encapsulated catalyst.